Group III Nitr

31. Group III Nitrides

Romualdo A. Ferreyra, Congyong Zhu, Ali Teke, Hadis Morkoç

Optical, electrical, mechanical, and thermal properties of group III nitrides, inclusive of AlN, GaN, InN and their ternary and quaternary alloys, are discussed. The driving force for group III nitride semiconductors is their important applications in optoelectronics, microwave amplifiers, and high voltage power switches. Owing to the aforementioned applications, the fundamental properties of each III nitride binary, as well as the alloys that have been acquired, are discussed in this chapter. In general, an appropriate assessment of the material properties for any material is not straightforward to begin with and the nitride family is no exception, particularly considering that group III nitrides are prepared on foreign substrates as low-cost native substrates are not yet available. Understandably, precise measurements of the mechanical, thermal, electrical and optical properties of the semiconductor nitride family are imperative for further advances. Notwithstanding the great progress that has already been made to further understand and exploit group III nitrides, especially GaN, reliable data for AlN and InN are still in the state of evolution, and naturally the subject of some controversy. This is, in part, a consequence of measurements having been performed on samples of widely varying quality. When possible, the spurious discrepancies have been disregarded. For some materials, too few measurements are available to yield a consensus, in which case the available data are simply reported. Defects in group III nitrides as well as GaN-based nanostructures are also discussed.

31.1 **Crystal Structures of Nitrides** 745
31.2 **Lattice Parameters of Nitrides** 746
31.3 **Mechanical Properties of Nitrides** 748
31.4 **Thermal Properties of Nitrides** 752
31.4.1 Thermal Expansion Coefficients 752
31.4.2 Thermal Conductivity 753
31.4.3 Specific Heat 756
31.5 **Electrical Properties of Nitrides** 757
31.5.1 Low Field Transport 758
31.5.2 High Field Transport 766
31.6 **Optical Properties of Nitrides** 769
31.6.1 Gallium Nitride 769
31.6.2 Aluminum Nitride 777
31.6.3 Indium Nitride 781
31.7 **Properties of Nitride Alloys** 782
31.8 **Doped GaN** 786
31.8.1 n-Type Doping 787
31.8.2 p-Type Doping 787
31.9 **Defects in GaN** 789
31.9.1 Points Defects 789
31.9.2 Extended Defects 792
31.10 **GaN-Based Nanostructures** 794
31.10.1 Quantum Wells 794
31.10.2 Quantum Dots 796
31.10.3 Vertical Cavities 796
31.10.4 Nitride Nanorods 799
31.11 **Summary and Conclusions** 801
References 802

During the last three decades, developments in the field of group III nitrides have been spectacular, with major breakthroughs taking place in the 1990s. They have been viewed as a highly promising material system for electronic and optoelectronic applications. As members of the group III nitrides family, AlN and GaN and their alloys with InN are all wide-bandgap materials (except for InGaN with very high In content) and can crystallize in both wurtzite and zincblende polytypes. The bandgaps of the wurtzite polytypes are direct and range from a possible value of ≈ 0.8 eV for InN, to 3.4 eV for GaN, and to 6.1 eV for AlN. GaN alloyed with AlN and InN may span a continuous range of direct-bandgap energies throughout much of the visible spectrum, well into ultraviolet (UV) wavelengths. This makes the nitride system attractive for optoelectronic applications, such as light-emitting diodes (LEDs), laser diodes (LDs), and UV detectors. Commercialization of bright

© Springer International Publishing AG 2017
S. Kasap, P. Capper (Eds.), *Springer Handbook of Electronic and Photonic Materials*, DOI 10.1007/978-3-319-48933-9_31

blue and green LEDs and the possibility of yellow LEDs paved the way for developing full-color displays. If the three primary-color LEDs, including red, produced by the InGaAlAs system are used in place of incandescent light bulbs in some form of a color-mixing scheme, they would provide not only compactness and longer lifetime, but also lower power consumption for the same luminous flux output. Additional possible applications include use in agriculture as light sources for accelerated photosynthesis, and in health care for diagnosis and treatment. Unlike display and lighting applications, digital information storage and reading require coherent light sources because the diffraction-limited optical storage density increases approximately quadratically with decreasing wavelength. The nitride material system, when adapted to semiconductor lasers in blue and UV wavelengths, offers increased data storage density, possibly as high as 50 Gb per disc with 25 Gb promised soon in the blu-ray system. Other equally attractive applications envisioned include printing and surgery. When used as UV sensors in jet engines, automobiles, and furnaces (boilers), the devices would allow optimal fuel efficiency and control of effluents for a cleaner environment. Moreover, visible-blind and solar-blind nitride-based photodetectors are also an ideal candidate for a number of applications including early missile-plume detection, UV astronomy, space-to-space communication, and biological effects. Another area gaining a lot of attention for group III–V nitrides is high-temperature/high-power electronic applications, such as radar, missiles, and satellites as well as in low-cost compact amplifiers for wireless base stations and high-voltage power switches, due to their excellent electron transport properties, including good mobility and high saturated drift velocity. The strongest feature of the group III nitrides compared to other wide-bandgap counterparts is the heterostructure technology that it can support. Quantum wells, modulation-doped heterointerfaces, and heterojunction structures can all be made in this system, giving access to new spectral regions for optical devices and new operational regimes for electronic devices. Other attractive properties of the nitrides include high mechanical and thermal stability, and large piezoelectric constants.

One of the main difficulties that has hindered group III nitride research is the lack of a lattice-matched and thermally compatible substrate material. A wide variety of materials have been studied for nitride epitaxy, including insulating metal oxides, metal nitrides, and other semiconductors. In practice, properties other than the lattice constants and thermal compatibility, including the crystal structure, surface finishing, composition, reactivity, and chemical and electrical properties, are also important in determining suitability as a substrate. The substrate employed determines the crystal orientation, polarity, polytype, surface morphology, strain, and the defect concentration of the epitaxial films. The most promising results on more conventional substrates so far have been obtained on sapphire, and SiC, however, accelerating progress has been made on Si substrates due to marketing issues, such as low-cost and compatibilities with Si processes. Also coming on the scene are thick freestanding GaN templates. Group III–V nitrides have been grown on Si, NaCl, GaP, InP, SiC, W, ZnO, $MgAl_2O_4$, TiO_2, and MgO. Other substrates have also been used for nitride growth, including Hf, $LiAlO_2$ and $LiGaO_2$. Lateral (lattice constant a) mismatched substrates lead to substantial densities of misfit and threading dislocations in broad-area epitaxially deposited GaN on foreign substrate, in the range $10^9-10^{10}\,cm^{-2}$. An appropriate surface preparation such as nitridation, deposition of a low-temperature (LT) AlN or GaN buffer layer, selective epitaxy followed by a type of coalescence called lateral epitaxial overgrowth (LEO) or epitaxial lateral overgrowth (ELOG) can reduce dislocation densities down to $10^6\,cm^{-2}$. However, these numbers are still high compared to extended-defect densities of essentially zero for silicon homoepitaxy, and $10^2-10^4\,cm^{-2}$ for gallium arsenide homoepitaxy. Vertical (lattice constant c) mismatch creates additional crystalline defects besetting the layers, including inversion domain boundaries and stacking faults. In addition, mismatch of thermal expansion coefficients between the epitaxial films and the substrate induces stress, which can cause crack formation in the film and substrate for thick films during cooling from the deposition temperature. A high density of defects, which increases the laser threshold current, causes reverse leakage currents in junctions, depletes sheet charge-carrier density in heterojunction field-effect transistors, reduces the charge-carrier mobility and thermal conductivity, and is detrimental to device applications and the achievement of their optimal performance. Thus, substrates capable of supporting better-quality epitaxial layers are always needed to realize the full potential of nitride-based devices. Nearly every major crystal-growth technique has been developed, including molecular beam epitaxy (MBE), hydride vapor-phase epitaxy (HVPE), and metalorganic chemical vapor deposition (MOCVD), in relation to nitride semiconductors. Several modifications to the conventional MBE method have been implemented for group III nitride growth: growth with ammonia or hydrazine (the latter is not attractive due to safety reasons and success of ammonia), plasma-assisted MBE (PAMBE), metalorganic MBE (MOMBE), pulsed laser deposition (PLD), and so on. Among other methods, radio-frequency (RF) and

electron-cyclotron resonance (ECR) plasma sources are the most commonly employed devices to activate the neutral nitrogen species in the MBE environment. Although all of these epitaxial methods contend with problems related to the lack of native GaN substrates, and difficulty with nitrogen incorporation, remarkable progress in the growth of high-quality epitaxial layers of group III nitrides by a variety of methods has been achieved. Additionally, growth of bulk GaN substrates by HVPE and ammonothermal methods have made tremendous progress in terms of dislocation density, impurities, growth speed, and so on.

Although many applications based on nitride semiconductors have emerged, and some of them are commercially available, as discussed throughout this chapter, there are many contradictions in identification of the basic physical properties of these materials. In this respect, they are not yet mature. Additionally, knowledge of the fundamental properties is crucial not only from the physics point of view but also when understanding and optimizing the device structures for better performance. In this chapter, therefore, we present the updated fundamental properties of GaN, AlN and InN, including structural, mechanical, thermal, electrical, and optical properties. The aim is to assist readers newly entering this field and other interested researchers in accessing the most recent available data. The reader is also urged to peruse the following publications for more detailed information on several aspects of ongoing research in group III nitrides. These consist of handbooks [31.1–3], and regular and review papers [31.4–31].

31.1 Crystal Structures of Nitrides

The group III nitrides share three crystal structures, which are wurtzite, zincblende, and rocksalt, where the thermodynamical stable phase is wurtzite for bulk AlN, GaN, and InN, and the cohesive energy per bond for the wurtzite phase is 2.88 eV (63.5 kcal/mol), 2.20 eV (48.5 kcal/mol), and 0.67 eV (15.5 kcal/mol) for AlN, GaN, and InN respectively [31.32]. The calculated energy difference between wurtzite and zincblende is small, which is -18.41 meV/atom for AlN, -9.88 meV/atom for GaN, and -11.44 meV/atom for InN; however, the wurtzite phase is energetically favorable for all three nitrides compared to zincblende. Being in the space group of $P6_3mc$, the wurtzite structure has a hexagonal unit cell with the a and c lattice parameters in the ratio of $c/a = \sqrt{8/3} = 1.633$. The wurtzite structure is composed of two interpenetrating hexagonal close-packed (hcp) sublattices, but displaced with respect to each other along the three-fold c-axis by an amount of $u = 3/8 = 0.375$, where each sublattice consists of four atoms per unit cell and every group III atom is surrounded tetrahedrally by four nitrogen atoms, or vice versa, these being located at the edges of a tetrahedron. The actual nitrides deviate from the above-mentioned ideal structure, which is signified by the c/a ratio or the u value [31.33]. These deviations come with the feature that the u parameter increases when the c/a ratio decrease while the four tetrahedral distances remain nearly constant through a distortion of the tetrahedral angles due to long-range polar interactions. These two slightly different bond lengths will be equal if the following equation holds

$$u = \left(\frac{1}{3}\right)\left(\frac{a^2}{c^2}\right) + \frac{1}{4} . \qquad (31.1)$$

The c/a ratio also depends on the dispersion in the electronegativities of the two constituents in group III nitrides with larger differences resulting in larger departures from an ideal c/a ratio [31.34]. These two parameters can be measured by using the four-circle diffractometry technique. In the case of GaN, the c/a ratio and the u parameter are measured as 1.627 and 0.377, respectively, which are close to the ideal values [31.35], while the available AlN deviates significantly from ideal parameters: $c/a = 1.601$ and $u = 0.382$. Thus, the interatomic distance and angles differ by 0.01 Å and 3°, respectively. Due to the lack of suitable size single-crystal InN for single-crystal diffractometry measurement, reported values are rare and may not be reliable. One popularly cited c/a value is 1.611 [31.36], which is consistent with data reported later in InN crystalline films grown by MBE [31.37] and MOCVD [31.38].

A phase transition to the rocksalt (NaCl) structure in group III nitrides can take place at very high external pressures due to the reduction of the lattice dimensions, which causes inter-ionic Coulomb interaction to favor ionicity over covalent nature. The structural phase transition was observed to occur at the following pressure values: 22.9 GPa for AlN [31.39], 52.2 GPa for GaN [31.40], and 12.1 GPa for InN [31.41]; however, the rocksalt structure of group III nitrides is not stable during epitaxial growth. With a six-fold coordinated structure, the rocksalt type of structure belongs to space-group symmetry of $Fm3m$.

The zincblende structure can be stabilized only by heteroepitaxial growth on cubic structure substrates, such as cubic SiC [31.42], Si [31.43], MgO [31.44], and GaAs [31.45]; however, they are metastable and tend to

form the wurtzite phase due to the inherent tendency. Thus in the case of highly mismatched substrates, there can be a certain amount of zincblende phase of nitrides separated by crystallographic defects from the wurtzite phase. However, over the years with considerably improved preparation techniques, this polyphase issue has substantially diminished. The crystal structure of the zincblende structure is composed of two interpenetrating face-centered cubic (fcc) sublattices displaced by one quarter of a body diagonal, which belongs to the space group of $F\bar{4}3m$. The unit cell is composed of four atoms, where every atom of one type is tetrahedrally coordinated with four atoms of other type, and vice versa. The overall equivalent bond length for zincblende structures is about 1.623 Å.

Although zincblende and wurtzite structures share the same tetrahedral coordination, the main difference between these two structures comes from the stacking sequence of close-packed diatomic planes. The stacking sequence for the wurtzite structure in the $\langle 0001 \rangle$ direction is AaBbAaBb taking Ga and N pairs as an example. In contrast, the close-packed (111) planes along the $\langle 111 \rangle$ direction in the zincblende structure have a 60° rotation that causes a stacking order of AaBbCcAaBbCc, where the small and large letters stand for the two different kinds of constituents. Because none of the three available structures for group III nitrides possess inversion symmetry, the crystal structure exhibits crystallographic polarity. The (0001) planes are terminated by group III (Al, Ga, or In) atoms and denoted as Ga polarity (c-plane), while $(000\bar{1})$ planes are terminated by nitrogen and denoted as N polarity, and these two planes are referred to as polar planes. Many material properties strongly depend on the polarity, thus it is critical to choose certain planes for desired device properties. For example, GaN-based heterojunction field effect transistors (HFETs) are predominantly based on c-plane GaN films due to the large polarization charge. While for the purpose of LED applications, nonpolar (i. e., $(10\bar{1}0)$ plane or m-plane, and $(11\bar{2}0)$ plane or a-plane) or semipolar $(11\bar{2}2)$ planes are preferred due to the reduced polarization induced internal electric field under these planes [31.3], on the condition that all else are equal, which is not the case because of technological disparity. Considering the cost and maturity, c-plane wurtzite nitrides are the most commonly used planes for device applications, although active research is underway for other secondary planes and directions.

31.2 Lattice Parameters of Nitrides

The lattice parameters of nitride-based semiconductors, as with other semiconductors [31.46, 47], depend on the following factors [31.48]:

1. Free electron concentration, which expands the lattice proportionally to the deformation potential of the conduction-band minimum
2. The concentration of impurities and intrinsic defects, and the difference between their ionic radii and the substituted matrix ions
3. External strains (for example, those induced by substrate or heterostructures)
4. Temperature.

High-resolution x-ray diffraction (HRXRD) is the most common tool to measure the lattice parameters of any crystalline material, and the results are usually obtained at a standard temperature of 21 °C [31.49] by using the Bond method [31.50] for a set of symmetrical and asymmetrical reflections. Because the lattice parameters of ternary compounds depend on the composition, the measured lattice parameters can also be used to determine the composition of the compounds, where the strain must be taken into consideration for precise determination of the composition. For nitrides, an accuracy of about 0.1% or less can be achieved in determining the composition, equivalently down to a mole fraction of about 1%, if the elastic parameters of all nitrides and lattice parameters of AlN and InN are taken into consideration. Considering that different growth techniques and/or substrates are used, which inevitably induce different strain states, defect densities and free-carrier concentrations, there is a wide dispersion in the reported values. Table 31.1 shows a comparison of measured and calculated lattice parameters reported by several groups for AlN, GaN, and InN crystallized in the wurtzite structure. The AlN crystal has a molar mass of 20.495 g/mol when it crystallizes in the hexagonal wurtzite structure. The measured lattice parameters for AlN in either bulk or epitaxial films range from 3.110–3.112 Å for the a parameter and from 4.980–4.982 Å for the c parameter, which gives a c/a ratio in the range of 1.600 and 1.602. The deviation from that of the ideal wurtzite crystal is most likely due to lattice stability, iconicity, and defects. The influence of carbon dopant concentration on the lattice parameters of AlN substrates grown by hydride vapor phase epitaxy using AlN substrates prepared by the physical vapor transport technique has been reported [31.51]. For samples with concentrations of carbon in the HVPE substrates from $< 2\times10^{17}$ to $< 1\times10^{19}\,\mathrm{cm^{-3}}$, while the concentrations of oxygen and silicon remained below $5\times10^{17}\,\mathrm{cm^{-3}}$ for all substrates, the HVPE-AlN

Table 31.1 Measured and calculated lattice constants of wurtzite AlN, GaN and InN

Compound	Sample	*a* (Å)	*c* (Å)	Reference
AlN	PVT seeded grown bulk	3.1117(5)	4.98180(2)	[31.52]
	Free standing HVPE-AlN grown on PVT-AlN substrate	3.1111	4.9808	[31.53]
	Epitaxial layer on SiC	3.110	4.980	[31.54]
	First-principle – LDA	3.0698	4.9101	[31.55]
	First-principle – CGA	3.1095	4.9938	[31.55]
GaN	Undoped Bulk Crystal ($n = 1\times10^{16}$) – HVPE	3.18914(5)	5.18508(3)	[31.56]
	O doped bulk crystal ($n = 3\times10^{18}$) – HVPE	3.18921(5)	5.18574(3)	[31.56]
	Si doped bulk crystal ($n = 1\times10^{18}$) – HVPE	3.18868(5)	5.18574(3)	[31.56]
	Fe doped bulk crystal ($n = 2\times10^{13}$) – HVPE	3.18841(5)	5.18570(3)	[31.56]
	Bulk crystal ($n = \text{low}10^{17}$) – HVPE	3.1880(20)	5.1868(15)	[31.57]
	Nonpolar (1100) bulk ($n = 10^{19}$) – ammonothermal	3.18908(10)	5.18517(10)	[31.58]
	m-Plan bulk crystal – Ammonothermal	3.1897	5.1861	[31.59]
	GaN substrate grown using a lateral epitaxial overgrowth (LEO) technique	3.1896(2)	5.1855(2)	[31.60]
	Homoepitaxial layers (low free-electron concentration)	3.1885	5.1850	[31.61]
	Homoepitaxial layers (high free-electron concentration)	3.189	5.1864	[31.48]
	Relaxed layer on sapphire	3.1892	5.1850	[31.62]
	Relaxed layer on sapphire	3.1878	5.1854	[31.46]
	Powder	3.1893	5.1851	[31.63]
	First-principle – LDA	3.193	5.2174	[31.64]
	First-principle – CGA	3.245	5.2958	[31.64]
InN	Powder	3.538	5.703	[31.65]
	First-principle– LDA	3.544	5.762	[31.64]
	First-principle– CGA	3.614	5.883	[31.64]

substrates did not show significant deviation in the lattice parameters. The average lattice parameters are $a = 3.1110$ Å and $c = 4.9809$ Å with $3\sigma = 0.0002$ Å. There are several reports on the lattice parameters of the cubic form of AlN with a lattice parameter of $a = 4.38$ Å [31.66], which is consistent with the theoretically estimated value [31.67]. However, the zincblende polytype AlN is in a metastable state. While for the rocksalt phase of AlN, which is pressure induced, a lattice parameter of 4.043–4.045 Å was obtained at room temperature [31.68, 69].

The wurtzite (WZ) crystal structure of GaN has a molecular weight of 83.7267 g/mol with four atoms per cell. Its lattice parameters depend on a variety of factors including free-electron concentration, impurities, and growth techniques. It has been reported that free charge is the dominant factor responsible for expanding the lattice [31.48]. The lattice parameters were found to be proportionally dependent on the deformation potential of the conduction-band minimum and inversely proportional to the carrier density and bulk modulus. Impurities, intrinsic point defects and extended defects, such as threading dislocations, are also important factors determining the lattice parameters of WZ-GaN, especially because bulk or epitaxial GaN is generally obtained on foreign substrates at high temperature, and thus suffers from both the lattice constant and thermal conductivity mismatch. Depending on the growth techniques, the defect density and impurity levels vary, which can have a direct influence on the lattice parameters. For example, solution growth at high pressure (15–20 kbar) and high temperature (in the range of 1600 K) can achieve high structural quality GaN material with a dislocation density as low as $100\,\text{cm}^{-2}$. However, the high level of background impurities, for example oxygen, can often result in free-carrier concentration exceeding levels of $10^{19}\,\text{cm}^{-3}$. The free-carrier density for undoped ammonothermally grown GaN substrates also reported a similar level of $10^{19}\,\text{cm}^{-3}$ [31.70–72] but can be as low as $2\times10^{18}\,\text{cm}^{-3}$ [31.73]. The lattice parameters from ammonothermally grown nonpolar and semipolar GaN bulk substrates are around $a = 3.1890$–3.1900 Å and $c = 5.185$–5.186 Å [31.58, 59]. It was found that doping has a strong effect on the lattice parameters for HVPE-grown WZ-GaN [31.74]. Undoped HVPE-grown GaN has a free-carrier density of $1\times10^{16}\,\text{cm}^{-3}$ and has $a = 3.18914$ Å, which increased to 3.18921 Å in oxygen-doped bulk GaN substrates with free-carrier concentrations of $3\times10^{18}\,\text{cm}^{-3}$. For Si- and Fe-doped bulk GaN substrates with free-carrier concentrations of $1\times10^{18}\,\text{cm}^{-3}$ and $2\times10^{13}\,\text{cm}^{-3}$ respectively, the a parameters decrease to 3.18868 and 3.18841 Å respectively. The trend for the change of lattice constant is generally consistent with the theoretical predictions based on the impurity size effect and deformation-potential effects as discussed in [31.75].

A precise analysis of the effect of doping on the lattice constant of GaN, however, requires a low-defect-density bulk material with controlled doping concentration. When and if the impurity levels can be controlled, attention then needs to be paid to the intrinsic defects. For zincblende GaN, the calculated lattice constant using the measured Ga–N bond distance in WZ-GaN is $a = 4.503$ Å. The measured lattice constant in epilayers ranges from 4.49–4.55 Å [31.42–44], where the fully relaxed lattice parameter was obtained to be 4.5036 ± 0.0004 Å [31.76]. The lattice parameter for freestanding cubic GaN grown by plasma-assisted molecular beam epitaxy on GaAs substrates, which subsequently is removed, demonstrated a lattice parameter of 4.510 ± 0.005 Å [31.77]. A high-pressure phase transition from the WZ to the rocksalt structure decreases the lattice constant down to $a_0 = 4.22$ Å in the rocksalt phase [31.78].

Due to the difficulties in the crystal growth of InN, reports on the physical properties of InN are limited. Nearly all the available data have been obtained from nonideal thin films. Indium nitride normally crystallizes in the wurtzite structure and has a molecular weight of 128.827 g/mol. The measured lattice parameters using a powder technique are in the range of $a =$ 3.530–3.548 Å and $c =$ 5.960–5.704 Å. By analyzing the strain in the InN film grown by MBE on sapphire substrates, the lattice parameters for strain-free InN are estimated to be in the range of $a = 3.535 \pm 0.005$ Å and $c = 5.699 \pm 0.004$ Å [31.37]. Zincblende (cubic) InN grown on sapphire (0001) using cubic indium oxide as a buffer layer generated an estimated lattice parameter of 4.9(8) Å [31.79], which is close to other reported values for epilayers grown on InAs (001) (5.04 Å) [31.80], on GaAs (001) (4.98 Å) [31.81], and on r-plane sapphire (4.986 Å) substrates [31.82].

31.3 Mechanical Properties of Nitrides

The mechanical properties of materials are usually characterized by parameters such as hardness, stiffness constant, Young's and bulk modulus and yield strength, and so on. For group III nitride semiconductor materials, the precise determination of the mechanical properties is hindered by various complexities, the most important of which is the lack of large size high-quality single crystals. Nevertheless, attempts have been made to estimate and measure the mechanical properties of both thin and thick epitaxial layers, and bulk crystals. The most precise technique to determine the elastic moduli of compound semiconductor materials is believed to be the ultrasonic measurement, which requires thick (about 1 cm-thick) single-crystalline samples to enable measurement of the timing of plane-wave acoustic pulses with sufficient resolution. Thus, this technique is almost inapplicable to the group III nitrides materials except wurtzite GaN where large size bulk substrates are commercially available. Brillouin scattering can determine the elastic constant and bulk moduli through the interaction of light with thermal excitation, in particular acoustic phonons, in the crystalline material. Various forms of x-ray diffraction, such as energy dispersive x-ray diffraction (EDX), angular dispersive x-ray diffraction (ADX) and x-ray absorption spectroscopy (XAS) can be used to determine the pressure dependence of the lattice parameters. By assuming that the bulk modulus has a linear dependence on the applied pressure to the crystal, it can be deduced as [31.83]

$$V = V_0 \left(1 + \frac{B'P}{B}\right)^{-\frac{1}{B'}} , \qquad (31.2)$$

where B and V_0 represent the bulk modulus and unit volume at ambient pressure respectively, and B' is the derivative of B with respect to pressure. X-ray diffraction can be used to determine the isothermal bulk modulus, and Brillouin scattering can determine the adiabatic bulk modulus. In the case of solids other than molecular solids, these two thermodynamic quantities bear no measurable difference. Predictive calculations of the structural and mechanical properties of group III nitrides can also be undertaken in addition to the above-mentioned experimental investigations. The most popular calculations are based on density functional theory within the local density approximation (LDA) using various types of exchange correlation functionals.

There are five independent elastic constants in hexagonal crystals, which are c_{11}, c_{33}, c_{12}, c_{13} and c_{44}. Among them, c_{11} and c_{33} correspond to longitudinal modes along the [1000] and [0001] directions respectively, while c_{44} and $c_{66} = (c_{11} - c_{12})/2$ can be determined from the speed of sound of the transverse modes propagating along the [0001] and [1000] directions respectively. c_{13} and the other four moduli relate to the velocity of the modes propagating in directions with lower symmetry, such as [0011]. The bulk modulus can be determined by the elastic constants through the following equation [31.84]

$$B = \frac{(c_{11} + c_{12})c_{33} - 2{c_{13}}^2}{c_{11} + c_{12} + 2c_{33} - 4c_{13}} .$$

If the material is isotropic, the Young's modulus E and shear modulus G can be evaluated by $E = 3B(1 - 2\upsilon)$

Table 31.2 Some mechanical properties of wurtzite AlN, GaN, and InN obtained by experimental measurements and theoretical calculations. The units are in GPa

Parameters	AlN (GPa)	GaN (GPa)	InN (GPa)
c_{11}	394 ± 1[a], 401.2 ± 0.5[b], 345[c], 396[d], 398[e]	296[r], 390[s], 377[t], 370[u], 373[an], 367[d], 396[e]	225 ± 7[ae], 223[d], 271[e]
c_{12}	134 ± 1[a], 135.0 ± 0.5[b], 125[c], 137[d], 140[e]	120[r], 145[s], 160[t], 145[u], 141[an], 135[d], 144[e]	109 ± 8[ae], 115[d], 124[e]
c_{13}	95 ± 1[a], 96.3 ± 22.1[b], 120[c], 108[d], 127[e]	158[r], 106[s], 114[t], 106[u], 80[an], 103[d], 100[e]	108 ± 8[ae], 92[d], 94[e]
c_{33}	402 ± 1[a], 368.2 ± 27.9[b], 395[c], 373[d], 382[e]	267[r], 398[s], 209[t], 398[u], 387[an], 405[d], 392[e]	265 ± 3[ae], 224[d], 200[e]
c_{44}	121 ± 1[a], 122.6 ± 0.2[b], 118[c], 116[d], 96[e]	24[r], 105[s], 81[t], 105[u], 94[an], 95[d], 91[e]	55 ± 3[ae], 48[d], 46[e]
Poisson's ratio v	0.19[f], 0.287[g], 0.216[g]	0.183 ± 0.003[p], 0.38[v], 0.372[r]	0.21 ± 0.05[ab]
Bulk modulus B	201[c], 210[h], 208[i], 160[j], 207[d], 218[e]	187 ± 7 and 319 ± 10[x], 195[r], 210[s], 245[am], 237[af], 188[ap], 202[d], 207[e]	152 ± 5[ae], 125[af], 141[d], 147[e]
dB/dP	5.2[j], 6.3[i], 5.7[al], 3.74[k], 3.77[l]	4[am], 4.3[af], 3.2[ap], 4.5[e], 2.9[ak]	12.7[af], 3.4[e]
Young's modulus E	308[j], 295[c], 374[m], 243.5[n]	325.3 ± 5.4[o], 320[q], 305 ± 11[w], 295[y]	149 ± 5[ac], 159[ad], 152.5 ± 3.9[ag]
Shear modulus	154[m], 131[j], 117[c]	157 ± 9.3[o], 152.6[z]	43[r]
Yield strength σ_y	0.3 at 1000 °C[m]	15[y], 0.1–0.2 at 900 °C[ao]	
Hardness	17.7[m], 18.0[m], 16.2[n],	28.5 ± 1.04[o], 19[aa], 18–20[y]	4.2 ± 0.1[ag], 8[ah], 3.6–9.1[ai], 11.2[aj]

[a] Brillouin scattering measurement on PVT grown bulk AlN [31.85]; [b] Measured by ultrasonic micro-spectroscopy (UMS) technique on PVT grown bulk AlN [31.86]; [c] Ultrasonic measurement on thin film [31.87]; [d] Calculated using pseudopotential LDA[31.88]; [e] Calculated using FP-LMTO LDA [31.89]; [f] AlN thin film grown on SiC substrate [31.90]; [g] *c*-plan and *r*-plane calculated [31.91]; [h] Brillouin scattering on single crystal [31.92]; [i] ADX on single-crystal AlN [31.93]; [j] Ultrasonic measurement on sintered, isotropic, polycrystalline AlN ceramic [31.94]; [k] Calculated using plane-wave pseudopotential [31.95]; [l] Calculated using Keating-Harrison model [31.96]; [m] Hardness measurement on bulk single-crystal AlN by micro-hardness and nano-hardness, respectively [31.97]; [n] nano-indentation measurement on AlN thin films on *c*-plane sapphire substrate [31.98]; [o] nano-indentation measurement on HVPE grown bulk GaN crystal [31.99]; [p] Determined by HR-XRD on MOCVD grown *c*-plane GaN film [31.100]; [q] Microbeam bending test on suspended GaN-on-patterned-silicon technique [31.101]; [r] Elastic constants calculated from temperature-dependent x-ray diffraction on polycrystalline GaN or InN. Poisson's ratio estimated from elastic constants [31.102]; [s] Brillouin spectroscopy on bulk GaN [31.84]; [t] Resonance ultrasound method on GaN plate [31.103]; [u] Surface-acoustic-wave measurement on GaN grown on sapphire [31.104]; [v] Determined by Bond's x-ray method on heteroepitaxially grown *c*-plane GaN [31.62]; [w] Obtained from nanowires with diameters ≈ 84 nm [31.105]; [x] Results obtained from high-pressure energy-dispersive x-ray diffraction on both bulk and nanocrystalline GaN, respectively [31.106]; [y] Nano-indentation on bulk GaN [31.107]; [z] Nano-indentation examination on *c*-plane bulk GaN [31.108]; [aa] Nano-indentation measurement on lateral overgrown epitaxial GaN films [31.109]; [ab] N-polar InN films grown on GaN template by plasma-assisted MBE [31.110]; [ac] Measured by AFM microbending test on single-crystalline wurtzite InN thin films [31.111]; [ad] First-principle calculations with the plane-wave pseudopotential density functional theory method [31.112]; [ae] Determined by grazing incidence inelastic x-ray scattering on InN thin films deposited on GaN template [31.113]; [af] X-ray diffraction on bulk GaN [31.41]; [ag] Nano-indentation measurement on InN films grown on GaN template [31.114]; [ah] Measured on *c*-plane wurtzite InN films [31.115]; [ai] Measured by nano-indentation technique on single-crystalline InN films on Si(111) substrates, where the hardness values depend on the growth temperatures [31.116]; [aj] Measured by nano-indentation technique on InN grown on sapphire [31.117]; [ak] Calculated using plane-wave pseudopotential [31.118]; [al] EDXD on polycrystalline AlN [31.68]; [am] X-ray absorption spectroscopy on GaN [31.40]; [an] Brillouin spectroscopy on GaN substrate grown by LEO [31.60]; [ao] Hardness on single-crystal GaN [31.119]; [ap] EDX on bulk GaN [31.39].

and $G = E/2(1+v)$ respectively, where the term v is the Poisson's ratio and is given by $v = c_{13}/(c_{11} + c_{12})$ [31.97].

The hardness of group III nitrides can be determined by micro- and nano-indentation methods over a wide range of size scales and temperatures. The measurements are usually conducted on the (0001) surface using a conventional pyramidal or spherical diamond tip, or alternatively, a sharp triangular indenter (Berhovich). Complete information on the hardness and pressure-induced phase transformation of semiconductor materials can be obtained via depth-sensing indentation measurements. Table 31.2 shows experimental as well as theoretical results of the mechanical parameters for wurtzite AlN, GaN and InN single crystals as well as polycrystallites reported by several groups.

Because the quality of the crystals varies, especially for InN, the experimental results are widely scattered

as demonstrated in Table 31.2. A clear example is the hardness data on InN, where the nanohardness of InN significantly depends on the growth temperature, which varies from 3.6 to 9.1 for an InN growth temperature from 440–500 °C [31.116]. The difference between the elastic moduli measured with the same technique (Brillouin scattering) for even GaN, which has a much better crystal quality than InN, is further evidence that the quality and nature (bulk single-crystal or epitaxial layer) of the samples is of significant importance. It has been demonstrated by *Moram* et al. [31.100] that the Poisson's ratio of GaN has a strong dependence on the strain state of the films. With the help of HR-XRD while inducing a series of different biaxial strain states in the same wafer, a Poisson's ratio of 0.183 ± 0.003 was estimated for a strain-free GaN film. Stress in GaN was also demonstrated to influence the Young's modulus. For high-quality suspended GaN microstructures fabricated from GaN-on-patterned-silicon techniques where the underlying silicon is removed, the stress in GaN decreases by 47%, which results in a 36% increase of the Young's modulus [31.101], nearly identical to the value deduced from the Brillouin scattering measurement on GaN films [31.120]. Except for InN, group III nitrides can be considered as hard and incompressible material family members with elastic and bulk moduli comparable to the magnitude of diamond. The hardness of a semiconductor relates to the bonding distance or shear modulus, which may explain why the InN is soft. InN has a smaller shear modulus and larger bonding distance (0.214 nm) compared to GaN (0.196 nm) and AlN (0.192 nm). Reports on the temperature dependence of the mechanical properties of group III nitrides are rare. It has been shown that the macroscopic dislocation motion and plastic deformation of GaN and AlN may start at around 1100 °C [31.121, 122]. The yield strength of bulk single-crystal GaN is found to be 100–300 MPa at 900 °C, while that for AlN was deduced to be $\approx$ 300 MPa at 1000 °C.

Many applications of group III nitrides utilize their high thermal conductivity, thus the precise knowledge of the vibrational modes in single crystals should be obtained in order to understand the fundamental thermal properties of nitrides. Infrared reflection and Raman spectroscopy are very useful techniques to derive zone-center and some zone-boundary phonon modes in nitrides. The A_1 and E_1 modes are each split into longitudinal optic (LO) and transverse optic (TO) components, giving a total of six Raman peaks. These A_1 and E_1 branches are both active for Raman and infrared techniques, while the E_2 branches are Raman-active only and B_1 branches are inactive. Table 31.3 gives a list of experimental as well as calculated values for the zone-center optical-phonon wave numbers of AlN, GaN, and InN.

The phonon dispersion spectrum of AlN has a total of twelve branches, including three acoustic and nine optical branches. The E_1 (LO), E_1 (TO), A_1 (TO), and E_2(high) peak positions were found to show a linear relationship with applied pressure up to 7 GPa [31.136]. Because the E_2 (high) peak position is reported to be sensitive to the in-plane strain due to its comparatively large strain coefficients, its stress-free values were obtained by linear fits to Raman frequencies of AlN layers under different biaxial strains and a stress-free value of $657.4 \pm 0.2\,\mathrm{cm^{-1}}$ is reported in AlN [31.146]. In contrast, the E_2 (low) phonon frequency is essentially constant under pressure, which indicates an approximate cancellation of the effects of central and noncentral forces on the pressure dependence of the phonon frequency [31.136]. The influence of impurities on E_2 (high) peak position showed controversial results. The E_2 (high) peak position showed no change for bulk AlN with carbon impurities up to $3 \times 10^{19}\,\mathrm{cm^{-3}}$. However, the principle Raman peaks are influenced by oxygen-related complexes [31.92], and the widths of principal Raman modes increase with increasing oxygen content, but at high oxygen concentrations ($\approx$ 5 at.%) the lowest values of these widths were obtained [31.103]. Through temperature-dependent Raman measurement, it was found out that both the lifetime of E_2 (high) and A_1 (LO) symmetry phonons of AlN are limited by two-phonon decay, where the E_2 (high) decays symmetrically while the A_1 (LO) asymmetrically decays into A_1 (TO) and LA phonons [31.125, 127].

The phonon frequencies in GaN also spread out due to different strain and defects states in different materials. Besides, the high phonon frequencies due to the strong bond in GaN and the light N atoms limit the range of observable impurity-related local vibrational modes to even lighter elements at higher frequencies. The E_1-TO and the E_2-(high) phonon modes in GaN possess comparatively large strain coefficients, thus their values are especially sensitive to the strain in the crystal. Therefore, care must be taken when measuring temperature-dependent phonon frequencies as different substrates have different thermal expansion coefficients and hence induce different strains at different temperatures [31.147]. Heretofore, few reports have appeared for the infrared and Raman modes of impurities, dopants, and hydrogen complexes [31.148, 149], and most of the reports focused on the hydrostatic pressure dependence of the zone-center phonon modes in bulk GaN [31.134, 136, 138, 150], and mode pressure coefficients up to a hydrostatic pressure of 6 GPa have been determined by Raman measurements [31.136].

Table 31.3 Optical phonon frequencies of wurtzite AlN, GaN, and InN at the center of the Brillouin zone in the units of cm^{-1}

Symmetry	AlN (cm^{-1})	GaN (cm^{-1})	InN (cm^{-1})
A_1-TO	613.64[b], 607.3[c], 609[e], 610[f], 609[g], 612[h], 601[i]	531.0[j], 531.4[l], 533.54[m], 531.2[n], 531.7[o], 540[p]	440[t], 446[u], 440 [31.123], 480[w], 445[x], 440[x]
E_1-TO	671.41[b], 666.5[c], 668[e], 669.6[f], 668[g] 679[h], 650[i]	558.0[j], 558.4[k], 559.99[m], 558.2[o], 568[p], 558.4[q]	477.9[v], 476[w], 472[x], 472[x]
A_1-LO	883.6[a], 891.80[b], 884.5[c], 891[d], 895[e], 888[f]	736.5[o], 748[p], 735 [31.124], 733[y], 737[r]	585.4[s], 592[t], 590[u], 590 [31.123], 580[w], 588[x]
E_1-LO	919.09[b], 911[e], 912.6[f], 911[g]	739.9[n], 742[o], 757[p], 743 [31.124], 740[y], 745[r]	570[w]
E_2-(low)/E_2^1	247.8[a], 249.57[b], 249[c], 246[e], 248[f], 246[g], 247[h], 228[i]	144.1[o], 142[p], 144 [31.124], 144[y], 146[i]	89[u], 88 [31.123], 87[w], 104[x]
E_2-(high)/E_2^2	653.6[a], 658.51[b], 653.6[c], 659[c], 655[e], 656.6[f], 655[g], 672[h], 638[i]	566.6[j], 567.6[k], 567.5[l], 568.28[m], 567.0[o], 576[p], 566.9[q]	490.1[s], 491[t], 491[u], 491.1[v], 490 [31.123], 488[w], 483[x]
B_1-(low)	636[h], 534[i]	337[p], 526[h], 335[i]	192[u], 200[w], 270[x]
B_1-(high)	645[h], 703[i]	713[p], 584[h], 697[i]	540[w], 530[x]

[a] Seeded grown of AlN boules on PVT-grown *c*-plane AlN [31.52]; [b] Bulk wurtzite AlN crystals grown by PVT method [31.125]; [c] 0.8 μm-thick AlN layer under a biaxial tensile stress of 0.6 GPa grown on Si(111) by MBE [31.126]; [d] Freestanding bulk AlN grown by sublimation sandwich technique on SiC seed [31.127]; [e] AlN bulk crystal grown by PVT technique [31.128]; [f] Self-nucleated AlN single crystal with facets [31.129]; [g] Bulk AlN grown by PVT technique [31.130]; [h] Calculated using first-principle total energy [31.131]; [i] Calculated using pseudopotential LDA [31.132]; [j] Nonpolar $(1\bar{1}00)$ bulk GaN grown by ammonothermal method [31.58]; [k] *c*-Plan bulk GaN grown by HVPE [31.57]; [l] *m*-Plane GaN substrate grown by HVPE [31.133]; [m] Nonpolar *a*-plane GaN grown on *r*-plane sapphire substrate [31.134]; [n] Strain-free frequencies in a high-quality bulk GaN [31.135]; [o] 50 μm thick hexagonal crystal of GaN grown on 6H-SiC by HVPE [31.136]; [p] Ab initio calculation using a pseudopotential-plane-wave method [31.137]; [q] Bulk-like GaN grown by HVPE and with removed substrate by laser liftoff [31.138]; [r] Raman study on high-quality freestanding GaN templates grown by HVPE [31.139]; [s] Strain-free values obtained by Raman measurements on a freestanding InN film grown by MBE [31.140]; [t] Raman measurements on wurtzite InN film deposited on sapphire substrate by MOVPE [31.141]; [u] Raman measurements on hexagonal InN thin films grown by MOVPE [31.142]; [v] Strain-free value obtained by Rama measurement on InN films grown on sapphire by MBE [31.143]; [w] Raman study on InN grown on sapphire and calculation based on the pairwise interatomic potentials and rigid-ion Coulomb interaction [31.144]; [x] Raman study on polycrystalline and faceted platelets of InN and calculation using FP-LMTO LDA [31.145]; [y] Brillouin spectroscopy on GaN substrate grown by LEO [31.60].

The E_2 (low) phonon mode in GaN exhibits a weak softening, which is qualitatively similar to that of the zone-boundary transverse acoustic modes of zincblende III–V semiconductors. An increase of the LO-TO splitting has been observed with hydrostatic pressure. Splitting of the GaN E_1 (TO), E_1 (LO), and E_2 phonons under anisotropic strain in the basal plane were also investigated, and their phonon deformation potentials were determined [31.135]. Phonon modes on virtually strain-free freestanding bulk GaN have been reported as well [31.138].

Strain-free Raman frequencies of the E_2 (high) and A_1 (LO) modes of hexagonal InN have been determined to be 490.1 ± 0.2 and $585.4 \pm 0.4\,cm^{-1}$ by Raman measurements on freestanding InN film grown by MBE [31.110]. The strain-free Raman frequencies were further verified by measuring biaxial strain-dependent Raman frequencies, where the strain-free values were extrapolated by a linear fit of the curve. The slope of the linear fit gave the Raman linear biaxial stress coefficients for the E_2 (high) and A_1 (LO) modes of InN to be 9.0 ± 0.8 and $8.4 \pm 0.8\,cm^{-1}\,GPa^{-1}$ respectively. Another set of pressure-dependent Raman frequencies demonstrated the phonon modes to be 440, 491, and $592\,cm^{-1}$ for A_1 (TO), E_2 (high), and A_1 (LO) respectively. Smaller stress coefficients of 5.81, 5.56, and $5.96\,cm^{-1}\,GPa^{-1}$ were also demonstrated for the above three phonon modes [31.151]. The wurtzite to rocksalt phase transition was also evidenced to be at a pressure of 13.5 ± 0.5 GPa as analyzed by means of Raman spectroscopy measurements conducted under high pressure (up to 50 GPa) [31.141]. Temperature-dependent Raman analysis of A_1 (LO) and E_2 phonon lifetimes from 80–700 K indicated that among the various possible decay channels, the A_1 (LO) phonon decays asymmetrically into a high energy and a low energy phonon, whereas the E_2 phonon predominantly decays into three phonons [31.152]. Possible decay channels of A_1 (LO) phonon may involve combinations of transverse optical and acoustic phonons.

31.4 Thermal Properties of Nitrides

31.4.1 Thermal Expansion Coefficients

The lattice parameters of semiconductors are temperature dependent, and the change of the lattice parameters are defined by thermal expansion coefficients (TEC), which are defined as $\Delta a/a$ or α_a and $\Delta c/c$ or α_c, for the *in* and *out of plane* orientations respectively. The importance of such parameters is owed to the expansion-caused strain during material growth, which is particularly important for group III nitrides as many applications of group III nitrides rely on successful growth of heterostructures, for example AlGaN/GaN HFETs and InGaN LEDs. What matters most is the lack of easily available substrates for group III nitride growth, thus the difference of TEC will cause strain and even cracking during the growth or cooling-down process for tensile strain, which is the case when grown for example on Si and SiC substrates. TEC is dependent on the stoichiometry and defects as well as the free-carrier concentration. A large scatter in the published data exists for TEC, partially due to the varying foreign substrates used for the growth.

The TEC was reported to be 4.03×10^{-6} in the temperature range of 298–473 K by assuming linear expansion in hot pressed aluminum nitride [31.155]. Ceramic AlN has been demonstrated to show a negative TEC at a temperature range of from 0 K to around 100 K [31.156]. Another TEC investigation on AlN powder showed that experimental data indicate no minimum for the a parameter and a possible shallow minimum for the c parameter, however, the magnitude of experimental errors does not allow confirmation of the existence/absence of negative thermal expansion without additional experimental efforts [31.157].

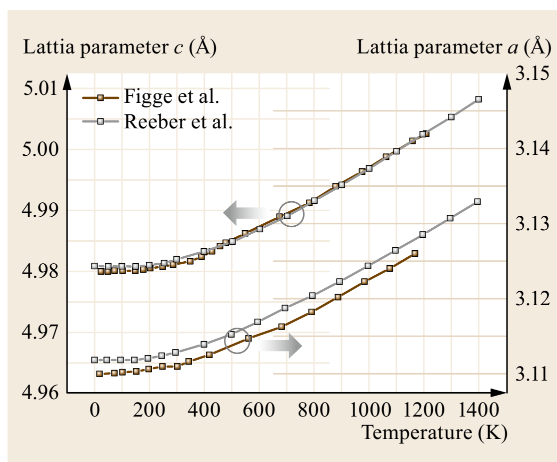

Fig. 31.1 Temperature-dependent lattice parameters of AlN in the c-direction and the a-direction. (After [31.153, 154])

Using x-ray techniques across a broad temperature range (77–1269 K), it has been noted that AlN demonstrated an isotropic thermal expansion with a room-temperature value of $2.56\times10^{-6}\,\mathrm{K}^{-1}$ [31.158]. Mean values of 4.20×10^{-6} and $5.30\times10^{-6}\,\mathrm{K}^{-1}$ were reported for $\Delta a/a$ and $\Delta c/c$, respectively, in the temperature range of 293–1073 K [31.159].

The thermal expansion coefficient of AlN bulk crystals were also investigated in the temperature range of 20–1300 K with the measured lattice parameters from both (002) and (006) reflections [31.153], and the lattice parameters were plotted at different temperature as shown in Fig. 31.1. In both lattice directions almost no thermal expansion is observed at low temperatures and an almost linear expansion at temperatures above 750 K, which is consistent with models based on the intrinsic phonon energy of a solid system. By fitting the experimental data to models based on Debye- and Einstein-like phonon dispersion, the lattice parameter c with its temperature dependence can be described as

$$c(T) = c(0\,\mathrm{K})\left[1 + \alpha_\infty\,\Theta f\left(\frac{\Theta}{T}\right)\right], \qquad (31.3)$$

where α_∞ is the lattice expansion coefficient in the high temperature limit, Θ is a characteristic temperature, and $f(x)$ is either the Debye or Einstein function defined as below

$$f_\mathrm{D}(x) = 3\int_0^1 \frac{t^3}{\mathrm{e}^{tx}-1}\,\mathrm{d}t$$
$$f_\mathrm{E}(x) = \frac{1}{\mathrm{e}^{x}-1}\,. \qquad (31.4)$$

The thermal expansion coefficients were reported to be 3.38×10^{-6} and $2.68\times10^{-6}\,\mathrm{K}^{-1}$ for $\Delta a/a$ and $\Delta c/c$ at room temperature, respectively.

Thermal expansion of single-crystal wurtzitic GaN has been investigated in the temperature range of 300–900 K [31.160], with a mean thermal expansion coefficient of $5.59\times10^{-6}\,\mathrm{K}^{-1}$ for $\Delta a/a$.

A superlinear dependence on temperature was also shown for the c parameter with mean thermal coefficients of 3.17×10^{-6} and $7.75\times10^{-6}\,\mathrm{K}^{-1}$, over the temperature ranges of 300–700 and 700–900 K respectively. Other values were also reported for α_a of 3.1×10^{-6} and $6.2\times10^{-6}\,\mathrm{K}^{-1}$ for the temperature ranges of 300–350 and 700–750 K respec-

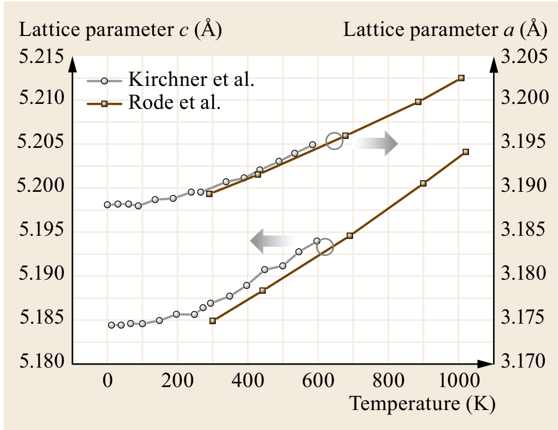

Fig. 31.2 Temperature-dependent lattice parameters of GaN in *c*-direction and *a*-directions. (After [31.162, 163])

tively [31.161]. The α_c values of 2.8×10^{-6} and $6.1\times10^{-6}\,K^{-1}$ were also reported in the same report. Thermal expansion coefficients should be obtained from freestanding bulk GaN substrates with minimal dislocations, defects and impurities, so that the influence by the substrate and defect states can be minimized. Thermal expansion coefficients for freestanding GaN bulk substrates with dislocation densities below $10^5\,cm^{-2}$ and room-temperature free-electron concentrations below $2\times10^{19}\,cm^{-3}$ were investigated in the temperature ranges of 0–600 K [31.162] and 300–1000 K [31.163] respectively. The temperature dependence of the lattice parameters are shown in Fig. 31.2. The thermal expansion coefficients at the very high temperature limits were reported to be $\alpha_c = 5.7\times10^{-6}\,K^{-1}$ and $\alpha_a = 6.2\times10^{-6}\,K^{-1}$, comparable to those proposed by *Reeber* and *Wang* [31.164]. The experimental results were also fitted to both Debye and Einstein models, and the results were demonstrated and compared with AlN as tabulated in Table 31.4. By comparing the lattice parameters of AlN and GaN at different temperatures, it was found that the maximum thermal mismatch between these two materials occurs at around 700 K [31.153]. Because the typical growth temperatures for AlN/GaN systems are much higher, the heterostructures suffer a larger strain during cooldown than during growth.

There is limited information available regarding the thermal expansion of InN. The first published experimental data in the temperature range of 190–560 K demonstrated that the TECs increase with temperature: α_a from 3.4×10^{-6} to $5.7\times10^{-6}\,K^{-1}$, α_c from 2.7×10^{-6} to $3.7\times10^{-6}\,K^{-1}$ [31.165]. More recent experimental data in the 100–673 K range based on diffraction data demonstrated average TECs of $\alpha_a = 3.6(2)\times10^{-6}\,K^{-1}$ and α_a from $\alpha_c = 2.6(3)\times10^{-6}\,K^{-1}$ [31.65]. However, due to the scatter of experimental data points obtained with the use of conventional equipment, there is lack of detectable TEC variation in the investigated temperature range. Lattice parameters and TECs were also calculated in the temperature range of 50–800 K based on a semi-empirical model [31.166]. More recently, results of Rietveld refinement for InN data collected in the temperature range of 105–295 K were published [31.167], wherein acicular microcrystals of InN were prepared by reaction liquid indium with nitrogen plasma and lattice parameters were measured by XRD. The TECs derived from linearly approximated lattice-parameter dependencies are $\alpha_a = 3.09(14)\times10^{-6}\,K^{-1}$ and $\alpha_c = 2.79(16)\times10^{-6}\,K^{-1}$. The temperature-dependent lattice parameters of InN are presented in Fig. 31.3a,b.

31.4.2 Thermal Conductivity

One key issue that enables group III nitrides to be useful for high-power/high-temperature electronic and optoelectronic devices is the high thermal conductivity (k), which is determined by the contributions from the vibrational, rotational, and electronic degrees of freedom, and as such is related to the mechanical properties of the material. The electronic thermal conductivity contribution is negligible for carrier concentrations $\leq 10^{19}\,cm^{-3}$. Heat transport is predominantly determined by phonon-phonon Umklapp scattering as well as phonon scattering by point and extended defects, such as vacancies, impurities, isotope fluctuations, grain boundaries, and dislocations. For the case when the effect of defects is trivial, phonon-phonon scattering, which is ideally proportional to T^{-1} above the Debye temperature, is the limiting process. However, due to the defective nature of group III nitride

Table 31.4 Thermal expansion parameters determined by XRD for AlN and GaN. (After [31.153] and [31.163] respectively)

Direction	Material	Debye model		Einstein model	
		α_∞ ($10^{-6}\,K^{-1}$)	Θ (K)	α_∞ ($10^{-6}\,K^{-1}$)	Θ (K)
out of plane	AlN	5.8 ± 0.1	1317 ± 25	5.6 ± 0.1	937 ± 25
	GaN	5.73 ± 0.44	898 ± 24	5.71 ± 0.43	662 ± 18
in-plane	AlN	7.1 ± 0.3	1455 ± 25	6.9 ± 0.3	1025 ± 25
	GaN	6.24 ± 0.41	868 ± 20	6.21 ± 0.35	636 ± 13

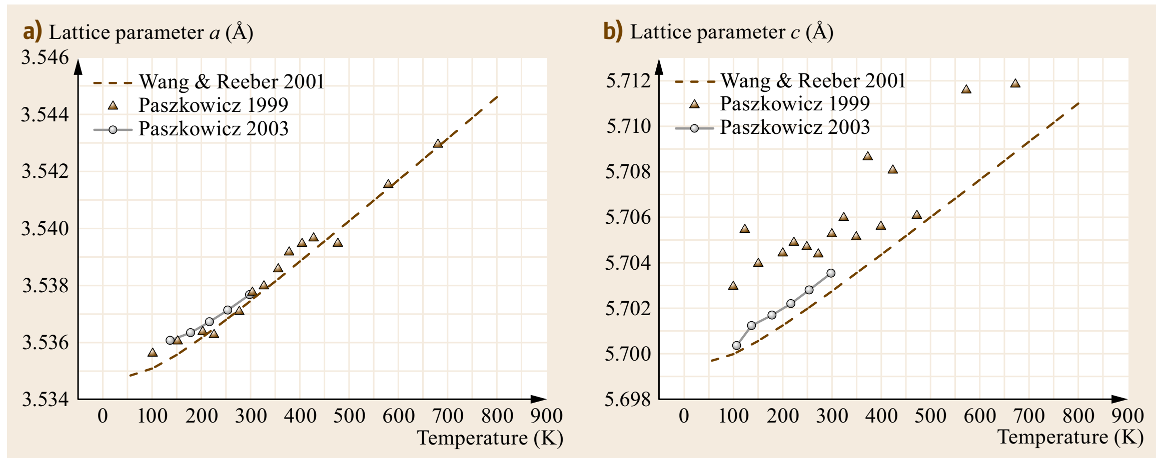

Fig. 31.3a,b Temperature dependence of lattice parameters of InN. (After [31.65, 166, 167])

materials, point defects play a significant role for single crystals during heat transport.

The thermal conductivity of AlN at room temperature was theoretically estimated to be $3.19\,W\,cm^{-1}\,K^{-1}$ for pure AlN single crystals [31.168], and experimental values of 2.5 [31.169] and $2.85\,W\,cm^{-1}\,K^{-1}$ [31.158] were reported at 300 K for AlN single crystals obtained by the sublimation technique. However, a more recent calculation predicted thermal conductivity of $5.4\,W\,cm^{-1}\,K^{-1}$ for a pure AlN single crystal, which is much larger than commonly reported experimental data [31.170]. One type of impurity that impacts the thermal conductivity of AlN is identified to be oxygen, and the thermal conductivities of AlN with various oxygen concentrations were demonstrated in Fig. 31.4. Although it was found that higher oxygen concentration reduced the thermal conductivity, it was believed that the reduction of the thermal conductivity was due to the oxygen-induced Al vacancies [31.171], which is supported by another report showing that AlN crystals with comparable oxygen vacancies ($\approx 1\times10^{19}\,cm^{-3}$) exhibited decreasing thermal conductivity with increasing Al vacancies [31.172]. As shown in Fig. 31.4, the reduction of thermal conductivity due to oxygen vacancies only occurs below room temperature. For high temperatures, the role of defects in affecting the thermal conductivity vanishes and the role of anharmonicity becomes dominant [31.173]. Recent AlN single-crystals have demonstrated higher room-temperature thermal conductivity values in the range of $3.0{-}3.3\,W\,cm^{-1}\,K^{-1}$ for freestanding [31.174] and $300{-}800\,\mu m$-thick AlN samples grown originally on Si (111) substrate by HVPE with a $10^8\,cm^{-2}$ dislocation density [31.175]. The thermal conductivity of polycrystalline or ceramic AlN has a much smaller value than that of single-

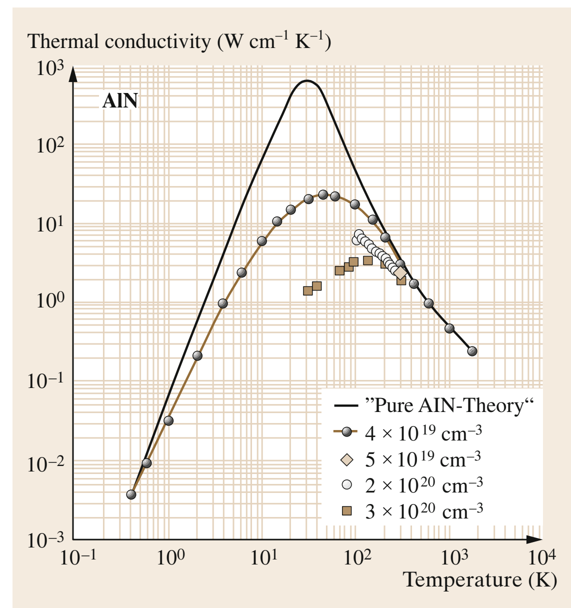

Fig. 31.4 Thermal conductivity of single-crystal AlN. The solid line represents the calculated data for pure AlN, while others represent AlN with various concentrations of oxygen impurities. (After [31.171])

crystalline AlN due to the larger amount of defects and grain boundaries [31.176], and the reported maximum value is $2.2\,W\,cm^{-1}\,K^{-1}$ [31.177].

Although a theoretical thermal conductivity of $k \approx 4.10\,W\,cm^{-1}\,K^{-1}$ at room temperature was predicted for pure GaN [31.170], experimental results yield much smaller values. The thermal conductivity of GaN layers grown on sapphire substrate by HVPE were measured as a function of temperature (25–60 K) using a heat-flow method, and a room-temperature thermal

Table 31.5 Thermal conductivity of high-quality GaN

Reference	Growth condition	Dislocation density (cm^{-2})	Impurity concentration (cm^{-3})	Carrier density (cm^{-3})	$k_{(300\,K)}$ ($W\,cm^{-1}\,K^{-1}$)	$k_{(max)}$ ($W\,cm^{-1}\,K^{-1}$)	Power n at 300 K
[31.178]	HVPE GaN boule	6×10^5	$\approx 6\times10^{16}$	1×10^{16}	2.94 ± 0.44		
[31.171]	HVPE		$\approx 2\times10^{16}$		2.27	20	-1.22
[31.179]	High-pressure-grown GaN		$\approx 10^{20}$	5×10^{19}	2.3	16	≈ -1.43
[31.180]	HVPE	$\approx 5\times10^6$	$\approx 2\times10^{17}$		2.53		
[31.181]	HVPE	$\approx 6.2\times10^6$	$\approx 3\times10^{16}$		2.25		≈ -1

conductivity of $\approx 1.3\,W\,cm^{-1}\,K^{-1}$ was recorded in the early days of GaN technology [31.182]. More recently, the room-temperature thermal conductivity of GaN was calculated to be $2.27\,W\,cm^{-1}\,K^{-1}$ assuming no isotope scattering [31.171]. This prediction is close to the generally reported value for high-quality bulk GaN as shown in Table 31.5. However, as also demonstrated in Table 31.5, the highest thermal conductivity is reported as $2.94\pm0.44\,W\,cm^{-1}\,K^{-1}$ for HVPE-grown GaN boule with very low dislocation density ($6\times10^5\,cm^{-2}$) and impurity concentrations $\approx 6\times10^{16}\,cm^{-2}$) [31.178], which in turn demands for more accurate predictions of thermal conductivity for high-quality GaN. From theoretical calculations, the highest possible thermal conductivity of bulk GaN can only be realized when point impurities such as oxygen and silicon are in small concentrations ($\approx 10^{16}\,cm^{-3}$ or less) and other defects are either absent or present in very small concentrations [31.183]. For GaN with relatively high quality, the measured thermal conductivity of GaN in the temperature range of 80–300 K has a $T^{-1.22}$ temperature dependence as demonstrated in Fig. 31.5, whose slope is typical of pure adamantine crystals below the Debye temperature, indicating acoustic phonon transport. Thus, the phonon-phonon scattering is a combination of acoustic–acoustic and acoustic–optic interactions, which means that thermal conductivity is mainly limited by the intrinsic phonon-phonon scattering instead of phonon-impurity scattering [31.171]. When the dislocation density (ρ_{TD}) exceeds $10^7\,cm^{-2}$, phonon-dislocation scattering will become nonnegligible compared to phonon-phonon scattering at room temperature [31.184], and an empirical relation indicated that thermal conductivity would be inversely proportional to $\rho_{TD}^{0.12}$ as ρ_{TD} goes to infinity. Another limiting factor of the thermal conductivity is the extent of dopants, and thermal conductivity decreased linearly with log n, where n is the electron concentration, the variation being about a factor of two decrease in k for every decade increase in n [31.185, 186].

Thermal conductivity measurements on InN are rare, partially due to the difficulty of growing high-quality InN films and single crystals. The first report of thermal conductivity was based on ceramic InN, which demonstrated a room-temperature value of $k = 0.45\,W\,cm^{-1}\,K^{-1}$ measured using the laser-flash method [31.187]. A more recent investigation is on single-crystalline InN films grown by MBE on c-sapphire substrate with a GaN buffer layer [31.188]. With background electron concentrations between 8×10^{17} and $3\times10^{18}\,cm^{-3}$ and mobilities between 1500 and $1045\,cm^2/Vs$, a room-temperature thermal conductivity of $1.2\,W\,cm^{-1}\,K^{-1}$ was obtained, which is closer to the theoretical thermal conductivity of $1.8\,W\,cm^{-1}\,K^{-1}$ estimated from $k_{theoretical} = C_\upsilon l\upsilon/3$, where c_υ is the molar specific heat, υ is the Debye-averaged acoustic phonon velocity, and $l = a/(\alpha_\upsilon \gamma T)$ is the phonon mean free path [31.188]. The effect of He^{2+} implantation on the thermal conductivity of InN

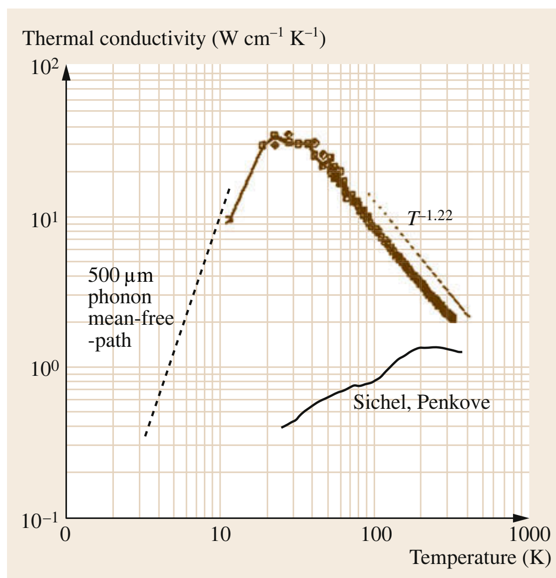

Fig. 31.5 Thermal conductivity of a 200 µm-thick free-standing GaN sample as a function of temperature. The *dashed line* indicates a calculation using the boundary scattering limit for a phonon mean free path of 500 µm. Also shown is the $T^{-1.22}$ dependence in the range of 80–300 K, and earlier results from [31.182] measured using a 400 µm HVPE sample. (After [31.171])

was also investigated, where the thermal conductivity reduced to around 0.1 W cm^{-1} K^{-1} when the implantation dose increased to 10^{16} cm^{-2}.

31.4.3 Specific Heat

The specific heat of a semiconductor can have various contributors, such as those by lattice vibrations, free carriers, point defects, and extended defects. For an ideal case where the semi-insulating crystals have good quality, the specific heat is only determined by the lattice vibrations. Due to the defective nature of group III nitrides, the specific heat is affected by contributions from free carriers and defects, especially at low temperatures. The temperature dependence of the specific heat can be expressed by the Debye expression as

$$C_\mathrm{p} = 18R\left(\frac{T}{\Theta_\mathrm{D}}\right)^3 \int_0^{x_\mathrm{D}} \frac{x^4 \mathrm{e}^x}{(\mathrm{e}^x-1)^2}\mathrm{d}x\,, \tag{31.5}$$

where $x_\mathrm{D} \equiv \Theta_\mathrm{D}/T$, and $R = 8.3144\,\mathrm{J/(molK)}$ is the molar gas constant. The coefficient in front of the term R has been multiplied by 2 to take into account the two constituents making up the group III nitrides. The Debye temperature Θ_D can be obtained by fitting the measured temperature-dependent capacity to the Debye expression.

The constant pressure specific heat C_p of AlN in the temperature range of 298–1800 K was approximated using the following expression [31.189]

$$C_\mathrm{p} = 45.94 + 3.347\times10^{-3}T - 14.98\times10^{-5}T^2\,\mathrm{J/(mol\,K)}\,. \tag{31.6}$$

By using the specific heat of $C_\mathrm{p} = 51.5\,\mathrm{J/mol\,K}$ at $T = 1800\,\mathrm{K}$ and the estimated value of $C_\mathrm{p} = 58.6\,\mathrm{(mol\,K)}$ at $T = 2700\,\mathrm{K}$, the specific heat at higher temperature range of 1800–2700 K, can be approximated as [31.190]

$$C_\mathrm{p} = 37.34 + 7.86\times10^{-3}T\,\mathrm{J/(mol\,K)}\,. \tag{31.7}$$

The above equations show the general and simplified trends for the specific heat of AlN. However, the exact values vary from sample to sample because the specific heat is a function of free electrons (very effective at low temperatures), impurities, defects (including point defects), and lattice vibrations.

The experimental temperature-dependent specific heat results are shown in Fig. 31.6. Also shown are the calculated specific heat results using the Debye equation for Debye temperature values of 800–1100 K with 50 K increments. The best fit between the experimental data and the Debye specific-heat expression reveals a Debye temperature of 1000 K, which is close to the value of 950 K reported in reference [31.191].

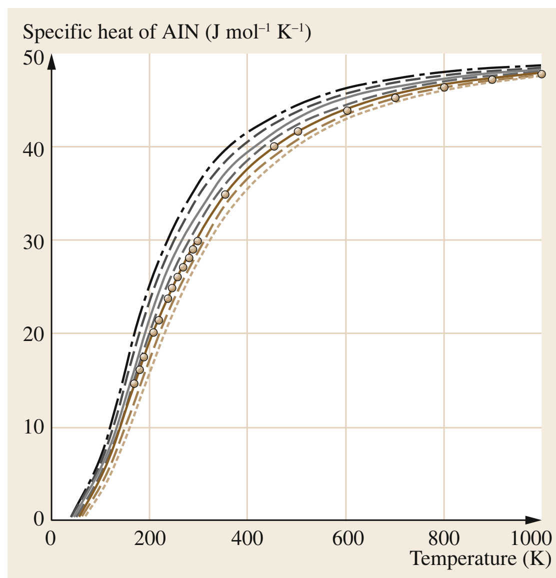

Fig. 31.6 Temperature-dependent molar specific heat of AlN at constant pressure C_p. *Brown dots* represent experimental data. The *lines* are for calculated data based on the Debye model for Debye temperature Θ_D in the range of 800–1100 K with 50 K increments. The best fit is obtained for a Debye temperature of 1000 K, which is close to the value of 950 K reported. (After [31.191])

The temperature-dependent specific heat for powdered GaN was obtained in a temperature range of 200–1400 K [31.192], which is in good agreement with the heat content data reported by *Itagaki* and *Yamaguchi* [31.193]. The combined data can be approximated by the following equation

$$C_\mathrm{p} = (49.552\pm2.279) + (5.440\pm2.936)\times10^{-3}\,T - (2.190\pm0.288)\times10^{6}\,T^{-2} + (2.460\pm0.459)\times10^{8}\,T^{-3}\,\mathrm{J/(mol\,K)}\,. \tag{31.8}$$

The specific heat for single-crystal GaN was also investigated in the temperature range of 20–1400 K by *Kremer* et al. [31.195] as demonstrated in Fig. 31.7, where the data below 300 K are in very good agreement with a later report by *Danilchenko* et al. [31.194]. Measured data in the range of 300–1400 K from *Kremer* can be best described with a Debye temperature of 863 K, which is consistent with the value calculated by *Nipko* et al. [31.196] from inelastic neutron scattering data. The dependence of the heat capacities of GaN, as a canonical binary material, on each of the Ga and N masses was also investigated, and it was shown that Ga

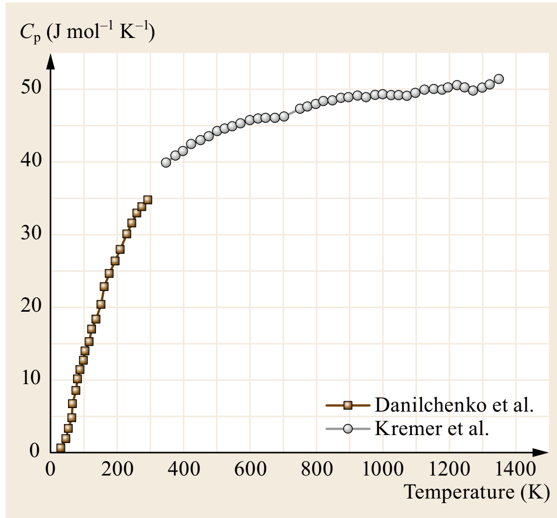

Fig. 31.7 Dependence of measured heat capacity on temperature measured in the range of 5–300 K [31.194] for single-crystal GaN, which overlaps with the data obtained from [31.195] in the same temperature range. The open circles represent measurement results by *Kremer* et al. in the temperature range of 300 to 1400 K

mass affects mainly the acoustic while N affects the optic phonons [31.195]. The temperature dependence of specific heat on bulk hexagonal GaN was also investigated [31.194], and it was shown that, for the studied specimens, the electron contribution to the C_p is negligible due to the fact that lattice C_p exhibits T^3 behavior and thus a C_p/T versus T^2 plot results in a straight line through the origin. From the measurement results in the temperature range of 20–300 K, a Debye temperature of 365 K was obtained.

A Debye temperature of 660 K was obtained for single-crystal InN based on fitting the measurement results in the temperature range of 150–300 K to the Debye expression [31.187]. However, due to the narrow temperature range of these measurements, it is difficult to compare these results to the Debye curve. The heat capacity and heat content of powdered InN were also measured by Calvet calorimetry (305–390 K) and by drop calorimetry (427–774 K), and the temperature dependence of heat capacity can be fitted as the following equation [31.197]

$$C_p = 43.886 + 8.194 \times 10^{-3} T - 1.007 \times 10^6 T^{-2} + 8.353 \times 10^7 T^{-3}\ \mathrm{J/(mol\,K)}\ . \quad (31.9)$$

Similar measurements were also conducted for powdered InN with 8.4% indium impurities in the temperature range of 314–978 K [31.198], and the temperature dependence of the heat capacity was presented in the following form

$$C_p = 41.400 + 0.499 \times 10^{-3}\, T - 1.355 \times 10^5\, T^{-2} - 2.617 \times 10^7\, T^{-3}\ \mathrm{J/(mol\,K)}\ . \quad (31.10)$$

For both cases, liquid droplets of pure indium were observed on the surface of InN after experiments at high temperature, thus a recalculation had to be conducted to determine only the heat capacity of indium nitride. Also due to the difficulty of growing high-quality pure InN crystals, the heat capacity of InN samples may have significant contributions from nonvibrational modes, which limits the credibility of the data presented above.

31.5 Electrical Properties of Nitrides

GaN and related nitrides, being direct and large bandgap materials, lend themselves to a variety of electronic and optoelectronic applications. Advantages associated with a large bandgap include relatively high breakdown voltages, the ability to sustain large electric fields, low noise generation, and high temperature and high power operation. Reasonable low-field mobility, large satellite energy separation, and high phonon frequency are among the other attributes. A high thermal conductivity, large electrical breakdown fields, and resistance to hostile environments also support the group III nitrides as true materials of choice for device applications. The electron transport in semiconductors, including nitrides, can be considered at low and high electric field conditions. At sufficiently low electric fields, the energy gained by the electrons from the applied electric field is small compared to the thermal energy of electrons, and therefore, the energy distribution of electrons is unaffected by such a low electric field. Since the scattering rates determining the electron mobility depend on the electron distribution function, electron mobility remains independent of the applied electric field, and Ohm's law is obeyed. When the electric field is increased to a point where the energy gained by electrons from the external field is no longer negligible compared to the thermal energy of the electron, the electron distribution function changes significantly from its equilibrium value. These electrons become hot electrons characterized by an electron temperature larger than the lattice temperature. Furthermore, as the

dimensions of the device are shrunk to the submicron regime, transient transport occurs where there is minimal or no energy loss to the lattice. The transient transport is characterized by the onset of ballistic or velocity overshoot phenomena, not that they have been demonstrated in the nitride semiconductor family. Since the transient electron drift velocity is higher than its steady-state value one can design a device operating at higher frequency, which is yet to be demonstrated for GaN based devices as of the time of this writing.

31.5.1 Low Field Transport

The Hall effect is the most widely used technique to measure the transport properties and assess the quality of epitaxial layers. For semiconductor materials, it yields the carrier concentration, its type, and carrier mobility. More specifically, temperature-dependent Hall measurements over a wide range (4.2–300 K) give information on impurities, imperfections, uniformity, scattering mechanism, and so on. The Hall coefficient and resistivity are experimentally determined and then related to the electrical parameters through $R_H = r_H/ne$ and $\mu_H = R_H/\rho$, where n is the free-carrier concentration, e is the unit of electrical charge, μ_H is the Hall mobility, and r_H is the Hall scattering factor. The drift mobility, μ, is the average velocity per unit electric field in the limit of zero electric field and is related to the Hall mobility through the Hall scattering factor by $\mu_H = r_H\mu$. The Hall scattering factor depends on the details of the scattering mechanisms in play, which limits the drift velocity. As the carriers travel through a semiconductor, they encounter various scattering mechanisms that govern the carrier mobility in the electronic system. The parameter for characterizing the various scattering mechanisms is the relaxation time τ, which determines the rate of change in electron momentum as it moves about in the semiconductor crystal. Mobility is related to the scattering time by

$$\mu = \frac{q\langle\tau\rangle}{m^*} , \quad (31.11)$$

where m^* is the electron effective mass, q is the electronic charge, and $\langle\tau\rangle$ is the relaxation time averaged over the energy distribution of electrons. The total relaxation time, τ_T, when various scattering mechanisms are operative is given by Matthiessen's rule

$$\frac{1}{\tau_T} = \sum_i \frac{1}{\tau_i} , \quad (31.12)$$

where i represents each scattering process. The major scattering mechanism that generally governs the electron transport in III-V semiconductors is also valid for group III nitrides. They are briefly listed as follows:

1. Ionized impurity scattering is due to deflection of free carriers by the long-range Coulomb potential of the charged centers caused by defects or dopants/impurities. This can be thought of as a local perturbation of the band edge, which affects the electron motion.
2. Polar longitudinal-optical (LO) phonon scattering is caused by the interaction of a moving charge with an electric field induced by electric polarization associated with lattice vibration due to the ionic nature of the bonds in polar semiconductors such as nitrides.
3. Acoustic phonon scattering through deformation potential arising from the energy change of the band edge induced by strain associated with acoustic phonons, where the scattering rate increases with the wave vector of the phonons.
4. Piezoelectric scattering arises from the electric fields that are produced by the strain associated with phonons in a crystal without inversion symmetry, such as wide bandgap nitrides.
5. Because of the high density of dislocations and native defects induced by nitrogen vacancies in GaN, dislocation scattering and scattering through nitrogen vacancies have also been considered as a possible scattering mechanism. Dislocation scattering is due to the fact that acceptor centers are introduced along the dislocation lines, which capture electrons from the conduction band in an n-type semiconductor. The dislocation lines become negatively charged and a space charge region is formed around them, which scatters electrons traveling across the dislocations, thus reducing the mobility.

Gallium Nitride

Electron mobility in GaN is one of the most important parameters associated with the material with great impact on devices. It has been the subject of intensive studies in recent years from both experimental and theoretical points of view. Experimental investigation of the temperature-dependent carrier mobility and concentration can be used to determine the fundamental material parameters and understand the carrier scattering mechanisms along with an accurate comparison with theory [31.200, 201]. Despite the many attributes of GaN, the lack of high-quality material, until very recently, prevented detailed investigations of carrier transport. The earlier transport investigations had to cope with poor crystal quality and low carrier mobility, well below predictions [31.202, 203]. Early MBE layers exhibited mobilities as high as 580 $cm^2/(Vs)$ on SiC

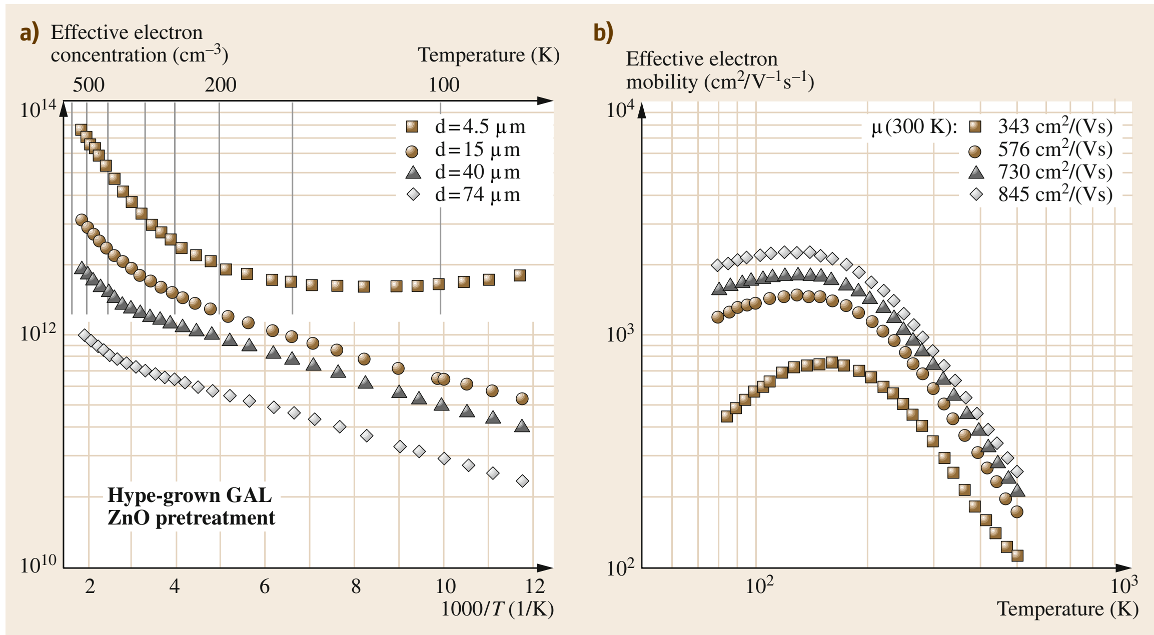

Fig. 31.8a,b Effective electron concentration versus reciprocal temperature in unintentionally doped n-type GaN films grown by HVPE on sapphire substrates **(a)** and effective electron mobility versus temperature **(b)** as determined from Hall-effect measurements under the assumption of uniform film properties. (After [31.199])

substrates, which at that time were not as commonly used as in recent times [31.204]. Typically however, the MBE-grown films produce much lower mobility values of $100-300\,\text{cm}^2/(\text{Vs})$ [31.205]. Different models were used to explain the observed low electron mobilities in GaN, especially at low temperatures. The scattering of electrons at charged dislocation lines [31.205–209] and scattering through elevated levels of point defects [31.210, 211], such as nitrogen vacancies [31.212, 213] were considered as possible mechanisms responsible for these observations. These scattering mechanisms were investigated by studying the temperature dependence of the carrier concentration and electron mobility. It has been argued that mobility is related to the dislocation density (N_{dis}) and free-carrier concentration (n) via a $\mu_{\text{dis}} \propto \sqrt{n}/N_{\text{dis}}$ relationship [31.207]. At low carrier concentrations ($< 5\times10^{17}\,\text{cm}^{-3}$), the mobility decreases due to charged dislocation scattering, while at higher carrier concentrations ionized impurity is the dominant mechanism determining the mobility. The temperature dependence of mobility for samples where dislocations play a dominant role shows that the mobility increases monotonically with temperature following a $T^{2/3}$ dependence. Moreover, electron mobility limited by nitrogen vacancy scattering was taken into account in n-type GaN grown by MOVPE by *Zhu* and *Sawaki*, [31.212] and *Chen* et al. [31.213]. A good fitting was obtained between the calculated and experimental results. The estimated mobility shows $T^{-1/2}$ temperature dependence and it was argued that the measured mobility is dominated by ionized impurity and dislocation scattering at low temperatures, but by polar optical phonon and nitrogen vacancy scattering at high temperatures.

Hall mobility and electron concentration in undoped GaN were investigated as a function of thickness of the buffer layers and epilayers. *Nakamura* [31.215] reported Hall effect data for undoped GaN layers grown by MOVPE on GaN buffer/sapphire substrates. As the thickness of the initial buffer layer increased from 100 Å, the mobility also increased up to a thickness of 200 Å. For larger thicknesses the mobility began to decrease. The value of the mobility was $600\,\text{cm}^2/(\text{V s})$ at room temperature for a 200 Å-thick initial buffer layer. The electron concentration was minimal at 520 nm buffer thickness and increased monotonically as buffer thickness increased. The mechanism responsible for this observation is not clearly established. *Götz* et al. [31.199] have studied the effect of the layer thickness on the Hall mobility and electron concentration in unintentionally doped n-type GaN films grown by HVPE on sapphire substrates, which were pretreated with either ZnO or GaCl. They found that the mobility increased and the carrier concentration decreased as the thickness of the epilayers increased as shown in Fig. 31.8.

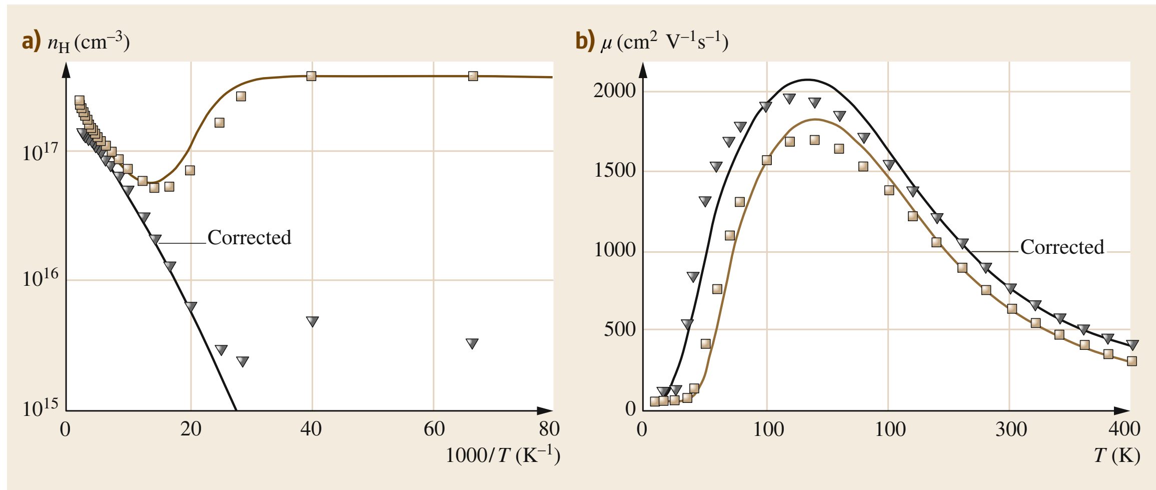

Fig. 31.9a,b GaN on sapphire: **(a)** Uncorrected Hall concentration data (*squares*) and fit (*solid line*), and corrected data (*triangles*) and fit (*dashed line*) versus inverse temperature. **(b)** Uncorrected Hall mobility data (*squares*) and fit (*solid line*), and corrected data (*triangles*) and fit (*dashed line*) versus temperature. (After [31.214])

Götz et al. related this variation to a nonuniform distribution of electrically active defects through the film thickness for both types of film. For GaCl-pretreated sapphire the presence of a highly conductive, 200 nm-thick, near-interface layer was assumed to account for the observed phenomena. For ZnO-pretreated sapphire, the Hall-effect data indicated a continuous reduction of the defect density with increasing film thickness. Since GaN layers are often grown on foreign substrates with very different properties, a degenerate layer forms at the interface caused by extended defects and impurities. Experiments show that, even for thick GaN grown by HVPE, the degenerate interfacial layer has an important contribution to the Hall conductivity.

Look and *Molnar* [31.214] investigated the Hall effect in the temperature range of 10–400 K in HVPE-grown layers on sapphire substrates by assuming a thin, degenerate n-type region at the GaN/sapphire interface. This degenerate interfacial region dominates the electrical properties below 30 K, but also significantly affects those properties even at 400 K, and can cause a second, deeper donor to falsely appear in the analysis. The mobility versus temperature curve is also affected in that the whole curve is shifted downward from the true, bulk curve. A model consisting of two layers was constructed to interpret these observations and the result is shown in Fig. 31.9.

The dependence of Hall mobilities on electron concentrations was also investigated in the electron concentration range of $\approx 10^{16}$–10^{19} cm^{-3} for undoped and intentionally doped (commonly used Si and Ge, which substitute for Ga, are shallow donors with almost identical binding energies) GaN layers grown by different growth techniques, and the results are displayed in Fig. 31.10. The most clearly observed trend is that the mobility shows no signs of leveling, down to the lowest carrier concentration reported, and the mobility values are practically the same irrespective of growth techniques and dopants used, which reflects transport properties inherent to GaN, not to extrinsic effects. Returning to the data of *Nakamura* et al. [31.218] the room-temperature mobility of 600 cm^2/(V s) for an electron concentration of $\approx 3\times10^{16}$ cm^{-3} decreased slowly with increas-

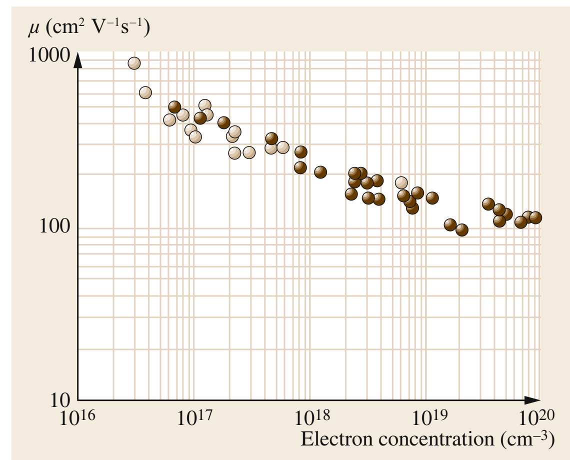

Fig. 31.10 The 300 K Hall mobility versus free-electron concentration for GaN from various groups using both MOVPE and MBE. The *open circles* are from unintentionally doped samples and the *solid circles* are for samples doped with either Si or Ge. (After [31.216])

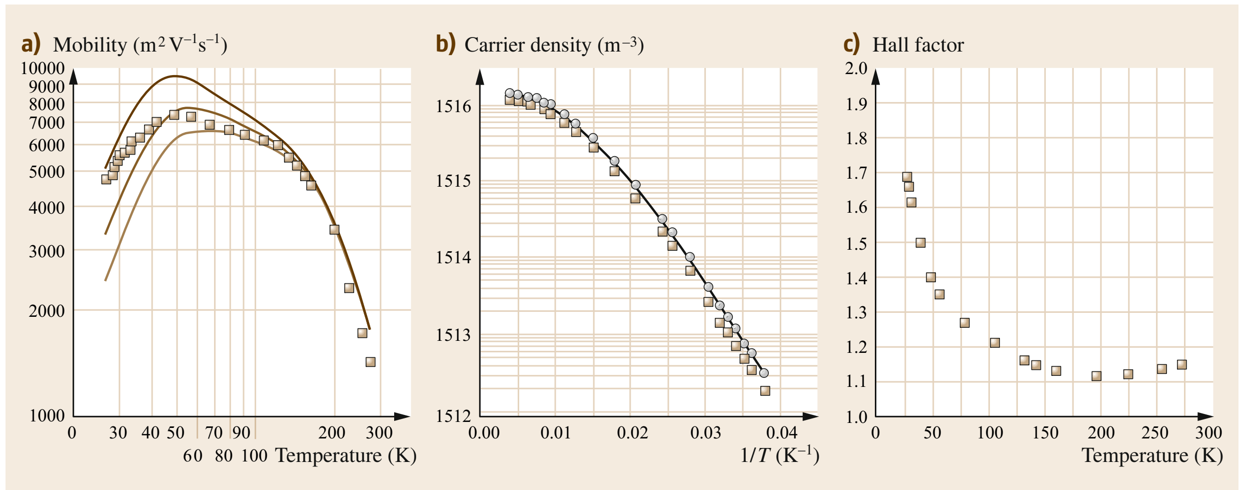

Fig. 31.11 (a) The measured Hall mobility data (*solid squares*) from the GaN template grown by HVPE as a function of temperature. The *solid line* is the calculated result using $N_a = 2.4\times10^{10}\,\text{cm}^{-3}$, representing the best fit to the measured results. The *upper* and *lower dotted lines* are the calculated results using $N_a = 1.4\times10^{15}$ and $3.4\times10^{15}\,\text{cm}^{-3}$. **(b)** The measured Hall densities n_H (*solid squares*) as a function of reciprocal temperature from the GaN template grown by HVPE. The *open circles* represent the carrier density corrected by the Hall factor, $n = n_H r_H$. The *solid line* is the fit to the theoretical expression of charge balance with hole and neutral acceptor densities neglected. **(c)** Temperature dependence of the calculated Hall factor, r_H. (After [31.217])

ing carrier concentration, dropping down to a value of about $100\,\text{cm}^2/(\text{V s})$ at a carrier concentration of $3\times10^{18}\,\text{cm}^{-3}$. For an electron concentration of $1\times10^{18}\,\text{cm}^{-3}$, the mobility was $250\,\text{cm}^2/(\text{V s})$. A higher room-temperature mobility of $845\,\text{cm}^2/(\text{V s})$ at an electron concentration of $\approx 6\times10^{16}\,\text{cm}^{-3}$ was achieved by *Götz* et al. [31.199]. In later publications, due to the advent of the high-quality samples grown by several growth techniques, there was a significant improvement in reported room-temperature mobility values. *Nakamura* et al. [31.219] and *Binari* and *Dietrich* [31.220] were able to obtain $900\,\text{cm}^2/(\text{V s})$ room-temperature mobility at an electron concentration of 3×10^{16} and $5\times10^{16}\,\text{cm}^{-3}$ respectively. Later on even higher electron mobilities of $1100\,\text{cm}^2/(\text{V s})$ at room temperature and $1425\,\text{cm}^2/(\text{V s})$ at 273 K were reported by *Yun* et al. [31.221] and *Huang* et al. [31.217] respectively, for a $200\,\mu\text{m}$ thick freestanding n-type GaN template grown by HVPE. This achievement was attributed to the excellent crystalline structure of the GaN sample with low levels of compensation and the defect-related scattering. A quantitative comparison with theoretical calculations demonstrated that the one-layer and one-donor conductance model is sufficient to account for the measured data in the entire temperature range without considering any dislocation scattering and any adjustable parameters other than the acceptor concentration. The measured temperature-dependent Hall mobility, carrier concentration, and Hall scattering factor are shown in Fig. 31.11 along with the best-fit theoretical calculation based on an iterative solution of the Boltzmann equation.

As shown, a quantitative agreement with the measured mobility in the entire temperature range was obtained to within about 30%. *Heying* et al. [31.222] investigated both the morphology and electrical properties of homoepitaxial GaN layers grown by MBE as a function of Ga/N ratio during growth. GaN films grown with higher Ga/N ratios (intermediate regime) showed fewer pits with areas of atomically flat surface, which gives the highest mobility $\approx 1191\,\text{cm}^2/(\text{V s})$ reported at the time at room temperature. *Koleske* et al. [31.223] investigated the effect of the AlN nucleation layer on transport properties of GaN films grown on 6H- and 4H-SiC substrates. Room-temperature electron mobilities of 876, 884, and $932\,\text{cm}^2/(\text{V s})$ were obtained on 6H-SiC, 4H-SiC, and 3.5° off-axis 6H-SiC substrates respectively. The authors attributed the observed high electron mobilities to the improved AlN morphology and reduction in screw dislocation density near the AlN/GaN interface.

The thermal activation energy of free carriers has also been extracted from the temperature-dependent Hall concentration and mobility measurements by fitting simple exponential dependence of the carrier concentration on inverse temperature, by a two-band model and by other theoretical fitting techniques. It was concluded that the activation energy of n-type GaN free carriers lies in the range 14–36 meV depending on the extent of screening [31.217, 218, 224–226]. In the di-

lute limit, the values are close to 30 meV. In order to analyze the mobility data, one must understand the scattering processes that dominates mobility at different temperatures. Monte Carlo simulations of the electron velocity in GaN as a function of electric field at different doping concentrations and temperatures predicted a peak drift velocity of 2×10^7 cm/s at an electric field of $\approx 1.4\times10^5$ V/cm for an electron concentration of 10^{17} cm^{-3} [31.227, 228]. These values show that an electron mobility as high as 900 cm^2/(V s) could be achieved in the case of uncompensated GaN at room temperature with $\approx 10^{17}$ cm^{-3} doping concentration. As discussed above, in the case of high-quality samples with very low compensation, a mobility of even more than 900 cm^2/(V s) at room temperature with a similar doping concentration has been reported.

Albrecht et al. [31.229] calculated the electron mobility for different concentrations of the ionized impurities and at different temperatures by using a Monte Carlo simulation technique based on empirical pseudopotential band structure calculations. For practical use they have also derived an analytical expression describing the dependence of the mobility on temperature and ionized impurity concentration as

$$\frac{1}{\mu_e} = a\left(\frac{N_1}{10^{17}\,\mathrm{cm}^{-3}}\right)\ln\left(1+\beta_{\mathrm{cw}}^2\right)\left(\frac{T}{300\,\mathrm{K}}\right)^{-1.5} + b\left(\frac{T}{300\,\mathrm{K}}\right)^{1.5} + c\frac{1}{\exp\left(\frac{\Theta}{T}\right)-1}\,, \tag{31.13}$$

where

$$\Theta = \frac{\hbar\omega_{\mathrm{LO}}}{k_\mathrm{B}} = 1065\,\mathrm{k}\,,$$

$$\beta_{\mathrm{WC}}^2 = 3.00\left(\frac{T}{300\,\mathrm{K}}\right)^2\left(\frac{N_1}{10^{17}\,\mathrm{cm}^{-3}}\right)\,,$$

$$N_1 = \frac{(1+k_\mathrm{c})}{N_\mathrm{D}}\,,$$

and

$$a = 2.61\times10^{-4}\,(\mathrm{V\,s})/\mathrm{cm}^2\,,$$

$$b = 2.90\times10^{-4}\,(\mathrm{V\,s}/\mathrm{cm}^2)\,,$$

$$c = 1.70\times10^{-2}\,(\mathrm{V\,s})/\mathrm{cm}^2\,.$$

Here N_D is the ionized donor concentration in cm^{-3} and $k_\mathrm{c} = N_\mathrm{A}/N_\mathrm{D}$ is the compensation ratio. Comparing the mobility calculated using this analytical expression and that calculated by Monte Carlo simulations, a reasonable agreement with a maximum error of 6% is realized between the temperature range of 300–600 K, and ionized donor concentration from 10^{16}–10^{18} cm^{-3}.

The calculation of low field electron mobility in GaN has also been carried out by using different techniques. *Chin* et al. [31.202] have used the variational principle to calculate low field electron mobilities as a function of temperature for carrier concentrations of 10^{16}, 10^{17} and 10^{18} cm^{-3} with the compensation ratio as a parameter. GaN exhibits maximum mobilities between 100 and 200 K, depending on the electron density and compensation ratio, with lower electron density peaking at lower temperature. This behavior is related to the interplay of piezoelectric acoustic phonon scattering at low carrier concentrations and ionized impurity scattering at higher carrier concentrations. The polar mode optical phonon scattering-limited maximum room-temperature mobility in GaN is found to be about 1000 cm^2/(V s). Although a degree of correlation is achieved with the experimental data, there is a disparity, which is attributed to the structural imperfections and an overestimated compensation ratio (compensation reduces electron mobility in GaN for a given electron concentration). Typical compensation ratios observed for MOCVD- and MBE-grown films are about 0.3, though a lower ratio of ≈ 0.24 was reported for HVPE-grown crystals.

Rode and *Gaskill* [31.203] have used an iterative technique, which takes into account all major scattering mechanisms for low field electron mobility in GaN, to investigate the dependence of mobility on electron concentration, but not on temperature. The result was applied to the Hall mobility data published by *Kim* et al. [31.231] and a good fitting between theory and experiment was demonstrated within 2.5% error for the lowest doped samples with free-electron concentrations of 7.24×10^{17} and 1.74×10^{17} cm^{-3}. However, there is a significant disagreement for the more heavily doped samples having much higher free-electron concentrations, where the Born approximation applied for the ionized impurity scattering might be the reason for poor fitting at high electron concentrations. By assuming uncompensated material and carrier freeze-out onto donors, the ionization energy was theoretically determined to be about 45 and 57 meV for the best-fitted samples with free-electron concentrations of 7.24×10^{17} and 1.74×10^{17} cm^{-3} respectively. Recent developments in major growth techniques such as HVPE, MOCVD, and MBE for GaN and other group III nitride semiconductors have led to the growth of high-quality epitaxial layers [31.232–234], which allowed the comparison of the Hall data with theory at a finer scale. *Dhar* and *Gosh* [31.230] have calculated the temperature and doping dependencies of the electron mobility using an iterative technique, in which the scattering mechanisms have been treated beyond the Born approximation. The compensation ratio was used

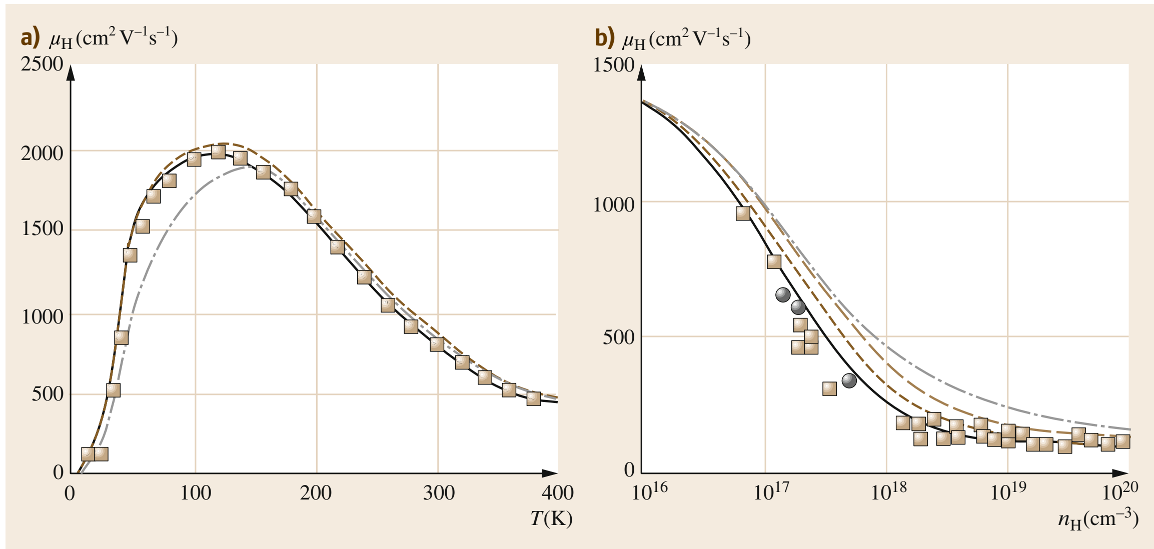

Fig. 31.12 **(a)** Temperature dependence of the calculated electron Hall mobility. The *dashed curve* shows the calculated mobility using the BH technique. The *dotted curve* shows the calculated mobility using phase-shift analysis with multi-ion screening correction. The *solid curves* show the calculated mobility using phase-shift analysis with multi-ion screening correction and electron-plasmon scattering. **(b)** Electron concentration dependence of the calculated electron Hall mobility for a compensation ratio $r = 0.2$. The *dashed curve* shows the calculated mobility using the BH technique. The *dashed-dotted curve* shows the calculated mobility using phase-shift analysis without multi-ion screening correction. The *dotted curve* shows the calculated mobility using phase-shift analysis with multi-ion screening correction. The solid curve shows the calculated mobility using phase-shift analysis with multi-ion screening correction and electron-plasmon scattering. Experimental data are taken from different references. (After [31.230])

as a parameter with a realistic charge neutrality condition. They tested their model with the experimental Hall data taken from literature [31.199, 202, 214, 218, 219, 225, 235]. Reasonable agreement was achieved between these data points and the calculation over a wide range of temperatures and electron concentrations, as shown in Fig. 31.12. They also investigated the effect of the degenerate layer at the GaN/substrate interface to extract reliable experimental values of the bulk electron mobility and concentration.

GaN samples from Kyma Technologies, Inc. (grown by hydride vapor phase epitaxy – HVPE) with a thickness of $40\,\mu$m were characterized by *Wang* et al. [31.236]. Undoped and Si-doped samples exhibited carrier densities of 4.58×10^{15} and $2.41\times10^{18}\,\mathrm{cm}^{-3}$ with mobilities of 1050 and $286\,\mathrm{cm}^2/(\mathrm{Vs})$ respectively. The decreased mobility in Si-doped GaN samples is, according to the authors, due to the increase of ionized impurity scattering. GaN grown by HVPE on an MOCVD-grown GaN/sapphire template with a photolithographically patterned Ti mask and ammonothermally grown GaN crystals (Am-GaN) was compared by *Sochacki* et al. [31.237]. Carrier concentration and carrier mobility were $2\times10^{16}\,\mathrm{cm}^{-3}$ and $1107\,\mathrm{cm}^2/(\mathrm{Vs})$, and $4\times10^{16}\,\mathrm{cm}^{-3}$ and $883\,\mathrm{cm}^2/(\mathrm{Vs})$ for GaN grown on MOCVD-GaN/sapphire and Am-GaN (at 800 mbar), respectively. The resistivity was in the range of $0.1{-}0.3\,\Omega\,\mathrm{cm}$ in both cases. Higher mobility and lower carrier concentration suggests that HVPE-GaN grown on MOCVD-GaN/sapphire templates incorporated fewer unintentional impurities, which was also consistent with the low-temperature PL spectra (not sown here). It is believed that the better electrical characteristic of HVPE-GaN grown on MOCVD-GaN/sapphire template is the result of a higher growth rate, which fosters a higher purity of the material.

Besides the numerical simulation techniques mentioned above, recently, *Mnatsakanov* et al. [31.238] derived a simple analytical approximation to describe the temperature and carrier concentration dependencies of the low-field mobility in wide temperature $50 \le T \le 1000\,\mathrm{K}$ and carrier concentration ($10^{14} \le N \le 10^{19}\,\mathrm{cm}^{-3}$ ranges. As the first step of this model, an adequate approximation of the doping level dependence of the mobility at room temperature is used on the basis of the Goughey–Thomas approximation [31.239]

$$\mu_i(N) = \mu_{\min,i} + \frac{\mu_{\max,i} - \mu_{\min,i}}{1 + \left(\frac{N}{N_{g,i}}\right)^{\gamma_i}}\,, \tag{31.14}$$

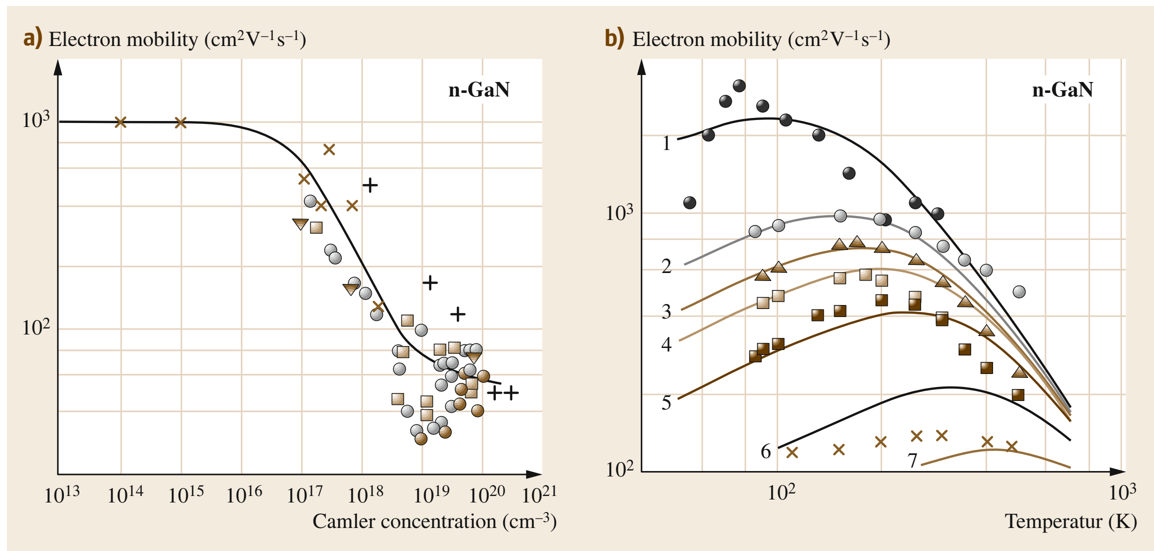

Fig. 31.13 **(a)** Low-field electron mobility as a function of doping concentration in GaN at room temperature. The *curve* represents the best approximate equation. The symbols (*crosses*, *open circles*, and *pluses*) are experimental data taken from different references for wurtzite GaN and zincblende. **(b)** Temperature dependencies of low-field electron mobility in wurtzite GaN at different values of doping concentration. Curves represent the best approximate equations. 1: $N = 3\times10^{16}\,\mathrm{cm^{-3}}$, 2: $N = 10^{17}\,\mathrm{cm^{-3}}$, 3: $N = 1.5\times10^{17}\,\mathrm{cm^{-3}}$, 4: $N = 2\times10^{17}\,\mathrm{cm^{-3}}$, 5: $N = 3.5\times10^{17}\,\mathrm{cm^{-3}}$, 6: $N = 10^{18}\,\mathrm{cm^{-3}}$, 7: $N = 3\times10^{18}\,\mathrm{cm^{-3}}$. (After [31.230])

where i= n, p for electrons and holes respectively, $\mu_{\mathrm{min},i}$, $\mu_{\mathrm{max},i}$, $N_{\mathrm{g},i}$ and γ_i are the model parameters dependent on the type of semiconductor materials, and N is the doping concentration. Figure 31.13a shows the comparison between the calculated low-field electron mobility as a function of doping level and some experimental data on the room-temperature electron mobility in GaN.

The proposed approximation provides a rather good agreement with the experimental data. For the temperature-dependent mobility calculation, the authors derived the following equation by taking into account the main scattering mechanisms

$$\mu_i(N,T) = \mu_{\mathrm{max},i}(T_0)\frac{B_i(N)\left(\frac{T}{T_0}\right)^{\beta_i}}{1 + B_i(N)\left(\frac{T}{T_0}\right)^{\alpha_i+\beta_i}}\,, \tag{31.15}$$

where

$$B_i(N) = \left.\left(\frac{\mu_{\mathrm{min},i} + \mu_{\mathrm{max},i}\left(\frac{N_{\mathrm{g},i}}{N}\right)^{\gamma_i}}{\mu_{\mathrm{max},i} - \mu_{\mathrm{min},i}}\right)\right|_{T=T_0}\,.$$

Figure 31.13b presents the calculated temperature-dependent electron mobility and experimental data reported in the literature and a good agreement is realized. Although ionized impurity scattering is the dominant mechanism at low temperatures, where the mobility increases with increasing temperature, at high temperatures mobility is limited by polar optical phonon scattering where mobility decreases with increasing temperature. Although a good agreement was achieved between theoretical calculations and experimental data, many material and physical parameters of GaN were not available for some of the previous simulations where those parameters were treated as adjustable parameters. This underscores the need for reliable parameters in the calculation of the electron mobility and in the interpretation of experimental results to gain more accuracy.

Aluminum Nitride

Due to the low intrinsic carrier concentration, and the deep native defect and impurity energy levels (owing to the wide bandgap of AlN $\approx 6.2\,\mathrm{eV}$ at $300\,\mathrm{K}$), the electrical transport properties of AlN have not been studied extensively and have usually been limited to resistivity measurements. Resistivities in the range of $\rho = 10^7-10^{13}\,\Omega\,\mathrm{cm}$ have been reported for unintentionally doped AlN single crystals [31.240, 241], a value consistent with other reports [31.242–244]. The conductivity exhibited an Arrhenius behavior for all crystals and the activation energies were reported to be 1.4 eV for temperatures between 300 and 400 K and 0.5 eV between 300 and 330 K. Intentional doping of AlN has resulted

in both n- and p-type AlN by introducing Hg and Se respectively (caution is warranted here). *Gorbatov* and *Kamyshon* [31.245] obtained n-type conductivity of polycrystalline AlN with the incorporation of Si. Unintentionally doped n-AlN films grown by a modified physical transport technique by *Rutz* [31.246] had a resistivity as low as 400 Ω cm. Although the source of the electrons has not been determined, *Rutz* et al. [31.247] observed an interesting transition in their AlN films in which the resistivity abruptly decreased by two orders of magnitude with an increase in the applied bias. This observation found applications to switchable resistive memory elements that are operated at 20 MHz. Based on an ab initio density functional calculation, *Fara* et al. [31.248] concluded that energy levels are deep for acceptors, donors, and native defects in AlN, due to the semi-insulating characteristic of AlN. For example, acceptors are deeper (Be ≈ 0.25, Mg ≈ 0.45) and less soluble in AlN than that in GaN, and both the extrinsic donors Si_{Al} and C_{Al}, and the native donor V_N are found to be deep (about 1 to 3 eV below the conduction band). Consequently, doped AlN may in general turn out to be semi-insulating, when attained using Al-rich conditions, in agreement with the known doping difficulties of high Al-content AlGaN alloys.

As far as the mobility of AlN is concerned, in early studies, *Edwards* et al. [31.240] and *Kawabe* et al. [31.241] carried out Hall measurements in p-type AlN, which produced a very rough estimate of the hole mobility; $\mu_p = 14\,cm^2/(V\,s)$ at 290 K. Later work on carbon-doped materials has resulted in highly conductive p-type AlN with hole mobilities in the range of $60\,cm^2/(V\,s)$ for carbon doping of $10^{18}\,cm^{-3}$ (*Wongchotigul* et al. [31.249] – again caution should be exercised here). The theoretical calculations have only been made to estimate the mobility in AlN by *Chin* et al. [31.202]. Since AlN is a semi-insulator with extremely low carrier concentration, only phonon-limited scattering processes were considered in the calculation of the temperature-dependent mobility as shown in Fig. 31.14. The mobility was found to decline rapidly at high temperatures, with a value of about $2000\,cm^2/(V\,s)$ at 77 K and dropping to $300\,cm^2/(V\,s)$ at 300 K for optical phonon-limited mobility.

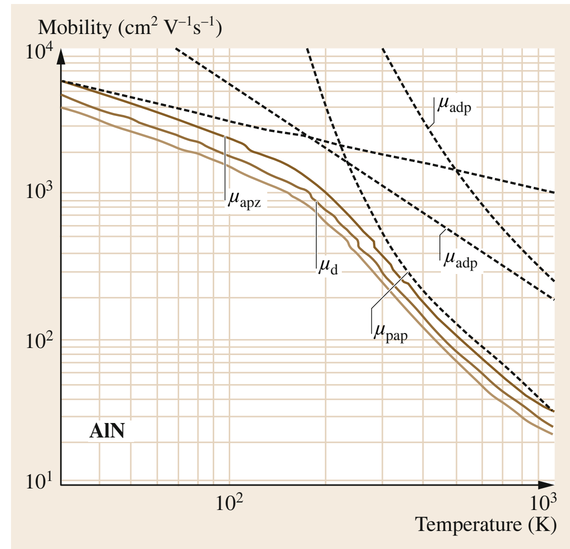

Fig. 31.14 The phonon-limited electron drift mobility in AlN plotted as a function of temperature for $m^* = 0.48$. The *upper* and *lower solid curves* are for the phonon-limited electron drift mobility calculated using $m^* = 0.42$ and 0.52 respectively. (After [31.202])

Indium Nitride

InN suffers from the lack of a suitable substrate material as well, causing a high concentration of extended defects in the films. A sapphire substrate is usually used for InN growth, but the difference in lattice constants between InN and sapphire is as large as 25% and even more than 19% with the other nitrides. A large disparity of the atomic radii of In and N is an additional contributing factor to the difficulty of obtaining InN of good quality. Because of all these factors, the electron mobilities obtained from various films have varied significantly. Electrical properties also vary substantially depending on the growth techniques. A range of film deposition techniques, such as reactive ion sputtering, reactive RF magneton sputtering, metal organic vapor phase epitaxy and MBE, have been used. Table 31.6 gives values of electron mobility and concentration in InN films grown by various growth techniques.

The transport properties reported in the literature are mostly based on Hall effect measurements, assuming the Hall scattering factor to be unity. In the majority of the samples, electron mobilities often remain relatively poor, despite predicted values as high as $3000\,cm^2/(V\,s)$ at room temperature for InN [31.268]. It is widely believed that nitrogen vacancies lead to large background electron concentrations, which are responsible for the observed low electron mobility. An empirical linear relationship between the electron mobility and electron concentration can be deduced from Table 31.6 for a series of InN films, although not all films exhibit this type of behavior. A systematic study carried out by *Tansley* et al. indicates that the electron concentration decreases as the nitrogen density is increased in the plasma in reactive ion sputtering. Although the reported time is relatively old, the maximum mobility of $2700\,cm^2/(V\,s)$ at an electron concentration of $5\times10^{16}\,cm^{-3}$ was reported for RF reactive ion sputtered growth of InN. Early studies of the electron

Table 31.6 A compilation of electron mobilities obtained n wide-bandgap InN on different substrates and for various deposition conditions in InN

Growth method	Carrier concentration (cm^{-3})	Electron mobility ($cm^2 V^{-1} s^{-1}$)	Reference
Reactive ion sputtering	7.0×10^{18}	250	[31.250]
Reactive ion sputtering	2.1×10^{17}	470	[31.251]
Reactive ion sputtering	8.0×10^{16}	1300	[31.251]
Reactive ion sputtering	5.5×10^{16}	2700	[31.251]
Reactive ion sputtering	2.0×10^{20}	9	[31.252]
RF magnetron sputtering	–	44	[31.253]
Reactive ion sputter	$\approx 10^{20}$	60	[31.254]
Plasma assisted MBE	$\approx 10^{20}$	229	[31.255]
ECR-assisted MOMBE	2.0×10^{20}	100	[31.256]
ECR-assisted reactive ion sputtering	–	80	[31.257]
Reactive sputter	6.0×10^{18}	363	[31.258]
MOVPE	5.0×10^{19}	700	[31.233]
Migration-enhanced epitaxy	3.0×10^{18}	542	[31.259]
RF MBE	3.0×10^{19}	760	[31.260]
MOMBE	8.8×10^{18}	500	[31.261]
MBE	$2–3 \times 10^{18}$	800	[31.262]
Reactive ion sputtering	$\approx 10^{19}$	306	[31.263]
RF MBE	1.0×10^{19}	830	[31.264]
Plasma-assisted MBE	1.6×10^{18}	1180	[31.265]
MBE	4×10^{17}	2100	[31.266]
Plasma-assisted MBE	1.4×10^{18}	1420	[31.267]

mobility of InN as a function of the growth temperature indicate that the mobility of ultrahigh vacuum-electron cyclotron resonance-radio-frequency magnetron sputtering (UHV-ECR-RMS)-grown InN can be as much as four times the mobility of conventionally grown (vacuum deposition) InN [31.257]. However, more recent work indicates a progressive improvement in electrical properties of InN films grown by MBE and MOVPE. The value of electron mobility as high as $1420\,cm^2/(V\,s)$ at an electron concentration of $1.4 \times 10^{18}\,cm^{-3}$ was reported for the InN layers grown by plasma-assisted MBE using a low-temperature-grown GaN intermediate layer and a low-temperature-grown InN buffer layer. Hall measurements in InN films grown on AlN buffer layers, which are in turn grown on sapphire, indicated an electron mobility to be $2100\,cm^2/(V\,s)$ with a relatively low electron concentration ($4 \times 10^{17}\,cm^{-3}$) at room temperature in material grown by MBE. Very high inadvertent donor concentrations, $> 10^{18}\,cm^{-3}$, seem to be one of the major problems for further progress of device applications of InN. O_N and Si_{In} and possible interstitial H have been proposed to be the likely dominant defects responsible for high electron concentration in the state-of-the-art MBE-grown InN due to their low formation energies [31.269, 270].

Electron mobility in InN has been calculated using the variational principle for a range of temperatures, carrier concentrations, and compensation ratios [31.202]. Figure 31.15 shows the theoretical results with experimental mobility values taken from [31.251]. The calculated peak mobilities are found to be 25 000, 12 000, and $8000\,cm^2/(V\,s)$ for carrier concentrations of 10^{16}, 10^{17} and $10^{18}\,cm^{-3}$ respectively, at different temperatures (between 100–200 K) depending on the electron density and compensation ratio. This is due to the interplay of piezoelectric acoustic phonon scattering at low concentrations and ionized impurity scattering at high temperatures. These two mechanisms are the dominant scattering mechanisms below 200 K, while polar-mode optical phonon scattering is the most significant process above this temperature. The low-concentration limit for room-temperature mobility in uncompensated InN is estimated to be $4400\,cm^2/(V\,s)$.

31.5.2 High Field Transport

Ensemble Monte Carlo simulations have been the popular tool to theoretically investigate the steady-state electron transport in nitrides. In particular, the steady-state velocity-field characteristics have been determined for AlN [31.271, 272], GaN [31.229, 271, 273–276], and InN [31.277, 278]. These reports show that the drift velocity initially increases with the applied electric field to reach a maximum and decreases with further increase in the field strength. The intervalley electron

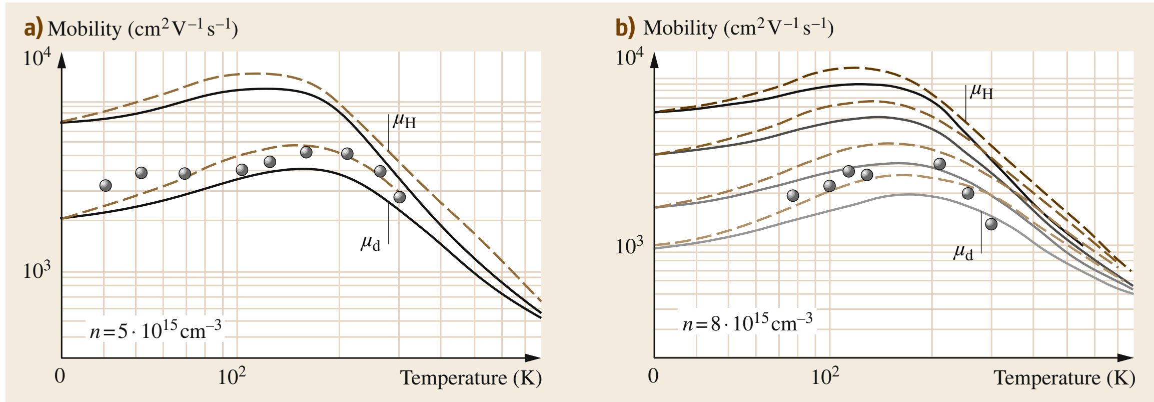

Fig. 31.15a,b The electron drift and Hall mobilities in InN as a function of temperature for **(a)** $n = 5 \times 10^{16}$ cm^{-3} for compensation ratios of 0.00 and 0.60; and **(b)** 8×10^{16} cm^{-3} for compensation ratios of 0.00, 0.30, 0.60, and 0.75. (After [31.202])

transfer plays a dominant role at high electric fields leading to a strongly inverted electron distribution and to a large negative differential resistance (NDR). Note that credible experimental confirmation of intervalley scattering is still pending. The reduction in the drift velocities was attributed to transfer of electrons from the high-mobility Γ-valley to the low-mobility satellite X-valley. The onset electric field and peak drift velocities, however, show some disparity among the reported calculations due to the variety of the degree of approximation and used physical constants of the materials. A typical velocity-field characteristic for bulk group III nitrides at room temperature is shown in Fig. 31.16 along with the well-studied GaAs data used to test the author's Monte Carlo model. For the doping concentration set to 10^{17} cm^{-3}, InN has the highest steady-state peak drift velocity; 4.2×10^7 cm/s at an electric field of 65 kV/cm. In the case of GaN and AlN, steady-state peak drift velocities are rather low and occur at larger electric fields; 2.9×10^7 cm/s at 140 kV/cm for GaN and 1.7×10^7 cm/s at 450 kV/cm for AlN.

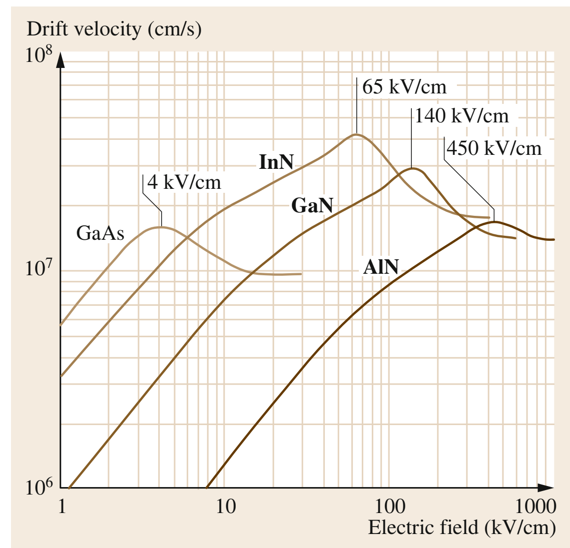

Fig. 31.16 The velocity-field characteristics associated with wurtzite GaN, InN, AlN, and zincblende GaAs. In all cases, the temperature was set to 300 K and the doping concentration was set to 10^{17} cm^{-3}. The critical fields at which the peak drift velocity is achieved for each velocity-field characteristic are clearly marked: 140 kV/cm for GaN, 65 kV/cm for InN, 450 kV/cm for AlN, and 4 kV/cm for GaAs. (After [31.279])

Another interesting aspect of electron transport is its transient behavior, which is relevant to short channel devices with dimensions smaller than 0.2 µm where a significant overshoot is expected to occur in the electron velocity over the steady-state drift velocity. Transient electron transport and velocity overshoot in both wurtzite and zincblende GaN, InN, and AlN have been studied theoretically by a number of groups. *Foutz* et al. [31.279] employed both Monte Carlo simulations and one-dimensional energy-momentum balance techniques. They used a three-valley model for the conduction band by taking the main scattering mechanisms, such as ionized impurity, polar optical phonon, acoustic phonon through deformation potential and piezoelectric, and intervalley scatterings, into account. In particular, they examined how electrons, initially in equilibrium, respond to the instant application of a constant electric field. Figure 31.17 shows the average velocity of the electrons in AlN, GaN, and InN as a function of distance.

According to their calculation, electron velocity overshoot only occurs when the electric field exceeds

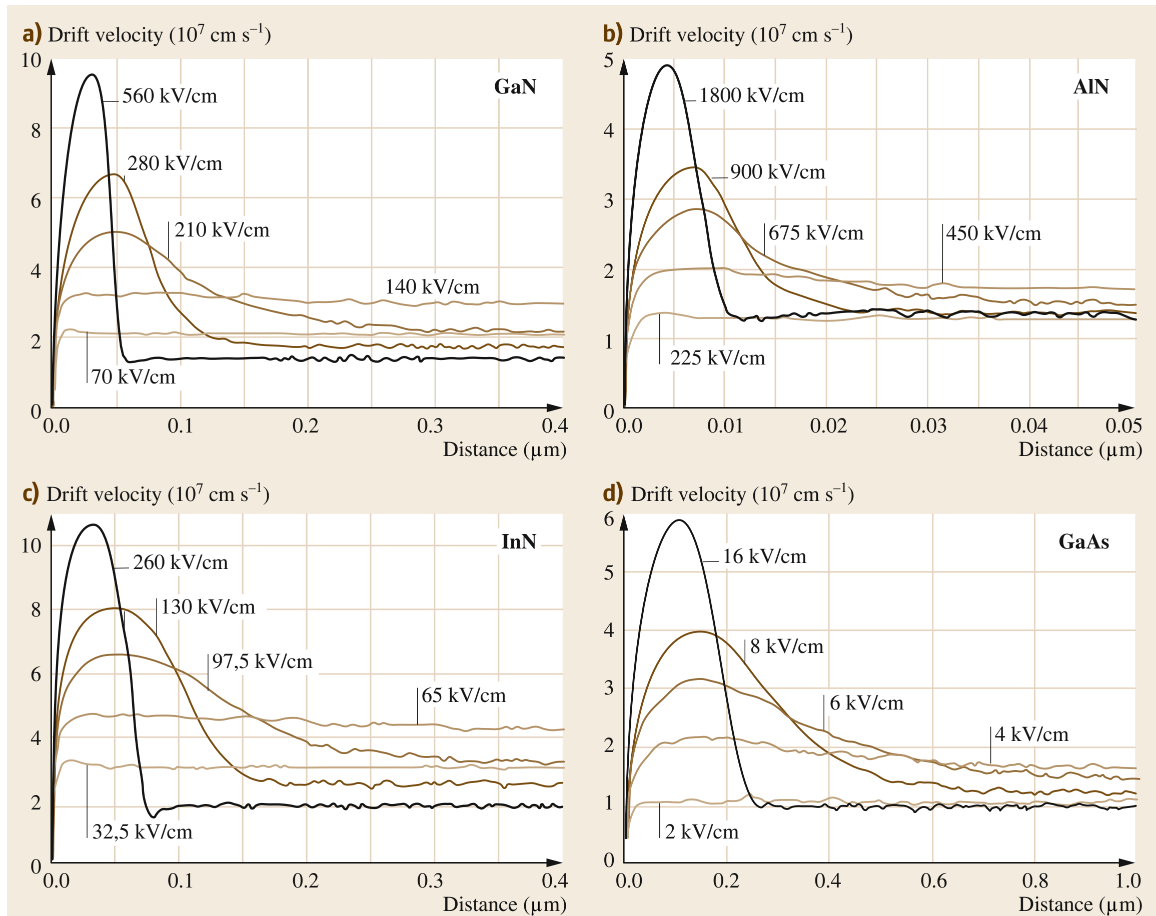

Fig. 31.17a–d The average electron velocity as a function of the displacement for various applied fields for the cases of **(a)** GaN, **(b)** InN, **(c)** AlN, and **(d)** GaAs. In all cases, we have assumed an initial zero-field electron distribution, a crystal temperature of 300 K, and a doping concentration of 10^{17} cm^{-3}. (After [31.279])

a certain critical value unique to each material and it lasts over a certain distance dependent on applied field. These critical fields are points where the highest steady-state peak drift velocities are achieved and being reported as 65, 140, and 450 kV/cm with corresponding peak velocities of 2.9×10^7, 1.7×10^7, and 1.6×10^7 cm/s for InN, GaN, and AlN respectively. Among them, InN exhibits the highest peak overshoot velocity on the order of 10^8 cm/s at 260 kV/cm and the longest overshoot relaxation distance on the order of 0.8 µm at 65 kV/cm. The variation of the velocity with respect to the field, not just the peak velocity, must be considered in our attempts to minimize the transit time. The upper bound for the cutoff frequency of InN- and GaN-based HFETs benefits from larger applied fields and accompanying large velocity overshoot when the gate length is less than 0.3 µm in GaN- and 0.6 µm in InN-based devices. However, all measured cutoff frequencies are gate-length-dependent and well below these expectations, indicating that devices operate in the steady-state regime and other effects, such as real-space transfer, should also be considered. On the other hand, there is some controversy in the reports related to the onset of velocity overshoot in nitride semiconductors. For example, *Rodrigues* et al. [31.280] reported overshoot onsets at 10 kV/cm in InN, 20 kV/cm in GaN, and 60 kV/cm in AlN by using a theoretical model based on a nonlinear quantum kinetic theory, which compares the relation between the carriers' relaxation rate of momentum and energy. Experimental investigations of the transient transport in group III nitrides are very limited and only a few results are reported by using different techniques. *Wraback* et al. [31.281] employed a femtosecond time-resolved electroabsorption technique to study the transient electron velocity overshoot for trans-

port in the AlGaN/GaN heterojunction p-i-n photodiode structures. It has been reported that electron velocity overshoot can be observable at electric fields as low as 105 kV/cm. The velocity overshoot increases with electric fields up to ≈ 320 kV/cm with a peak velocity of 7.25×10^7 cm/s relaxing within the first 0.2 ps after photoexcitation. The increase in electron transit time across the device and the decrease in peak velocity overshoot with increasing field beyond 320 kV/cm is attributed to a negative differential resistivity region of the steady-state velocity-field characteristic in this high field range. *Collazo* et al. [31.282] used another experimental technique based on the measurement of the energy distribution of electrons, which were extracted into a vacuum through a semitransparent Au electrode, after their transport through intrinsic AlN heteroepitaxial films using an electron spectrometer. They observed electron velocity overshoot as high as five times the saturation velocity and a transient length of less than 80 nm at the field of 510 kV/cm. In order to design an electronic device that is expected to operate at high power and high frequency, one could consider harnessing velocity overshoot in group III nitride semiconductor heterojunctions. However, the strong coupling between hot electrons and LO phonons appear to limit the velocity attainable by electrons, being dependent on the LO phonon decay time. A systematic investigation of InN, GaN, AlN and their alloys as a function of various parameters in dynamics mode would be very beneficial for the development of higher performance, next generation electronic and optoelectronic devices.

31.6 Optical Properties of Nitrides

The optical properties of a semiconductor have vital importance due to the wide range of useful information that can be obtained in our attempts to understand the semiconductor properties, especially the direct bandgap material for optoelectronic applications. For ideal defect-free semiconductors, the optical transitions occur between conduction band and valence band, including excitonic effects due to the Coulomb interaction, where excitons can be classified into free and bound varieties. For high-quality samples with low defect concentrations, the free excitons can also exhibit excited states in addition to their ground state. Bound excitons are those that are bound to dopants or defects, which usually create a discrete energy below the bandgap energy, and therefore influence the optical behavior of the excitons as well as optical absorption and emission. Excitons could be bound to neutral or charged donors and acceptors. It is generally assumed that the dominant coupling is of the like particles for principal bound exciton (BEs) states associating with neutral donors and acceptors [31.283]. For the case of shallow neutral donor-bound excitons (DBEs), the two electrons in the BE state are assumed to pair off into a two-electron state with zero spin, where the additional hole is assumed to be weakly bound in the net hole-attractive Coulomb potential set up by this bound two-electron aggregate. A similar scenario applies to acceptor-bound excitons (ABEs). The DBEs and ABEs are by far the most important cases for bound excitons in direct-bandgap materials, and thus attract intensive investigation. Various techniques can be used to investigate the optical properties of group III nitrides, and the most commonly used ones are optical absorption, transmission, photoreflection, photoluminescence, time-resolved photoluminescence, cathodeluminescence, calorimetric spectroscopy, pump-probe spectroscopy, and so on. This section will only summarize some important optical properties of group III nitride materials.

31.6.1 Gallium Nitride

Free Exciton in GaN

The conduction band (Γ_7^c) of wurtzite GaN is mainly constructed from the s state of gallium, while the valence band is mainly constructed from the p state of nitrogen. Due to the crystal-field and spin-orbit interactions, the valence band splits into three bands, namely the highest Γ_9^ν (heavy hole), upper Γ_7^ν (light hole), and lower Γ_7^ν (crystal-field split band). The optical transitions between the conduction and valence bands are usually denoted as $\mathrm{A} \equiv \Gamma_7^c \leftrightarrow \Gamma_9^\nu$, $\mathrm{B} \equiv \Gamma_7^c \leftrightarrow \Gamma_7^\nu$ (the upper one), and $\mathrm{C} \equiv \Gamma_7^c \leftrightarrow \Gamma_7^\nu$ (the lower one), which have almost the same binding energy of around 25–26 meV [31.284]. For optical one-phonon processes, these three excitons of the wurtzite structure obey the following selection rules: for σ polarization ($E \| c$ and $k \perp c$ axis), C all excitons are allowed although C exciton is quite weak. For π polarization ($E \| c$ and $k \perp c$ axis), C exciton is strongly allowed and B exciton is weakly observable while A exciton is forbidden in this geometry. In the α polarization ($E \perp c$ and $k \| c$), all three transitions are clearly observable [31.285]. The A exciton consists of a two-fold degenerate spin-singlet state with Γ_5 symmetry and a two-fold degenerate spin-triplet state with Γ_6 symmetry. Both the B and C

excitons consist of a two-fold degenerate spin-singlet state with Γ_5 symmetry, a spin-triplet state with Γ_2 symmetry, and a mixed singlet-triplet state with Γ_1 symmetry. Among all the exciton states, only those with Γ_5 and Γ_1 symmetry are dipole-allowed and can be seen in reflectance or photoluminescence spectra, where the Γ_5 states are allowed for $E \perp c$ polarization while the Γ_1 states are allowed for $E \parallel c$ polarization. In order to reveal the fine structure of the exciton states, which have splitting on the order of 1–2 meV [31.286], the spectroscopic line width in optical spectra (such as photoluminescence) needs to be a fraction of an meV. The line width is determined by microscopic electric field and strain fields, which in practice requires single crystals with a low residual doping ($< 10^{16}\,\mathrm{cm}^{-3}$) and a low structural defect density ($\leq 10^{6}\,\mathrm{cm}^{-2}$). These requirements can only be achieved for nominally undoped freestanding GaN with a thickness of at least several hundred µm, which is not possible for most commonly available GaN grown on foreign substrates, such as sapphire, SiC or silicon. The commonly employed techniques for investigating the exciton properties are photoluminescence (PL), absorption, and/or derivative techniques like photoreflectance (PR) and calorimetric absorption and reflection techniques [31.287, 288], which are powerful techniques to determine the exciton binding energy, exciton Bohr radii, dielectric constant, and spin-orbit and crystal-field parameters with the aid of the quasicubic model.

There have been intensive studies on the emission properties of GaN during the last decade. The energy position, relative intensities, and linewidth of the emission peaks have been found to strongly depend on the residual strain, crystal line defects, and impurity incorporation, thus making the interpretation of the spectra in heteroepitaxial GaN layers rather difficult and even leading to confusing conclusions. With the availability of high-quality freestanding and homoepitaxial GaN layers, correct identifications of the emission peaks becomes possible. There are reports in the literature on the reflectance study for thick GaN epilayers [31.289–293] as well as homoepitaxial layers [31.294–298] and bulk GaN [31.58, 294, 299–303]. Studies by Monemar et al. on thin and thick GaN layers on various substrates, including homoepitaxial layers on GaN substrates, concludes that the A, B, and C excitons in GaN, with an accuracy of ±2 meV, are at 3.478, 3.484, and 3.502 eV respectively, at 2 K. These values are consistent with results obtained from freestanding or bulk GaN samples published in the literature as demonstrated in Table 31.7. An example of a reflectance spectrum obtained in the α polarization for a 2 µm-thick GaN epilayer on sapphire is displayed in Fig. 31.18, where the corresponding excitonic transition energies were evaluated using a classical damped-oscillator transition model [31.304].

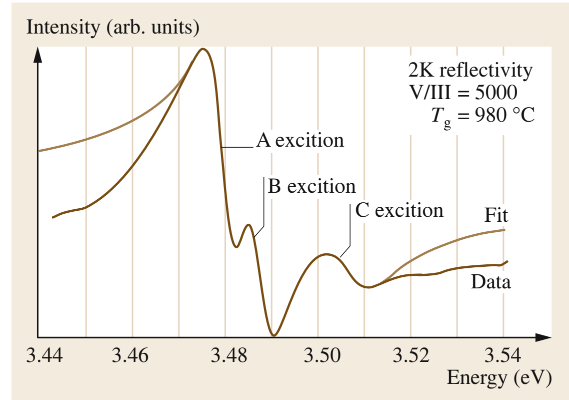

Fig. 31.18 Reflectance spectrum taken at 2 K for a 2 µm-thick GaN film grown on a sapphire substrate. The experimental data was fitted using a damped-oscillator theoretical model. (After [31.304])

Another powerful technique for studying the exciton structure is photoluminescence (PL), and Fig. 31.19 displays a typical PL spectrum taken at 2 K, which is dominated by donor-bound excitons, for an almost strain-free thick GaN epilayer grown on sapphire by HVPE. The free excitons appear at relatively higher energies, at their ground states as well as the $n = 2$ excited states of the A exciton [31.307]. The splitting between the A, B, and C exciton ground states, Δ_{AB} and Δ_{AC}, are (5.5 ± 0.1) and (22.0 ± 0.1) meV, which are close to recently reported values for quasibulk GaN samples grown by HVPE [31.303]. Based on the exciton energies, the crystal-field splitting and spin-orbit splitting of the top three valance bands were estimated to be $\Delta_{cr} = 20 \pm 2$ meV and $\Delta_{so} = 10 \pm 2$ meV respectively [31.288]. Other reported values are $\Delta_{cr} \approx \Delta_{so} \approx 16 \pm 2$ meV [31.240], and $\Delta_{cr} \approx 12.3 \pm 0.1$ meV and $\Delta_{so} \approx 18.5 \pm 0.1$ meV.

Another interesting feature of exciton lines is the fine structure near the band edge of GaN due to various splitting mechanisms. As mentioned earlier, the A, B, and C excitons have spin-related degenerate states. Based on experimental results as well as theoretical calculation, the following splittings have been reported [31.314]: $\Gamma_5(A) - \Gamma_6(A) = 0.53$ meV, $\Gamma_5(B) - \Gamma_2(B) = 0.4$ meV, $\Gamma_1(B) - \Gamma_2(B) = 0.41$ meV, $\Gamma_5(C) - \Gamma_2(C) = 0.23$ meV and $\Gamma_1(C) - \Gamma_2(C) = 0.75$ meV, where we can find out that the Γ_1 and Γ_1 states of the B exciton are almost degenerate with only 0.1 meV difference. For wavevector $k \perp c$, the long-range exchange interaction splits the spin-singlet states Γ_5 into a transverse and a longitudinal state. The longitudinal-transverse splitting of $\Gamma_5(A)$,

Table 31.7 Reported free-exciton (FX) energies in GaN using different experimental techniques

FX (A)	FX (B)	FX (C)	Orientation	Substrate	Strain	Growth	Technique	Reference
3.4776	3.4827	3.5015	*m*-Plane	Bulk GaN	Unstrained	Ammonothermal	PL	[31.294]
3.4786	3.4834		*c*-Plane	Free standing	Unstrained	HVPE	PL	[31.301]
3.4779	3.4831		*c*-Plane	Bulk GaN	Unstrained	Ammonothermal	PL	[31.295]
3.477	3.494	3.511	*a*-Plane	Sapphire	Compressive	ELO	Reflectivity	[31.305]
3.478	3.483	3.501	*c*-Plane	GaN template	N/A	PA-MBE	Reflectivity	[31.306]
3.4760	3.4817	3.4991	*c*-Plane	Bulk GaN	Unstrained	MOCVD	PR	[31.296]
3.483	3.491	3.512	*c*-Plane	Sapphire	Compressive	MOCVD	PR	[31.296]
3.474	3.481	3.501	*c*-Plane	Sapphire	Compressive	VPE	Reflectance	[31.283]
3.480	3.486	3.503	*c*-Plane	Sapphire	Compressive	HVPE	PL	[31.307]
3.485	3.493	3.518	*c*-Plane	Sapphire	Compressive	MOCVD	Reflectance	[31.308]
3.4903	3.4996	3.525	*c*-Plane	Sapphire	Compressive	MBE	Reflectance	[31.293]
3.476	3.489	3.511	*c*-Plane	ZnO	Compressive	RAMBE	Reflectance	[31.309]
3.470	3.474	3.491	*c*-Plane	6H-SiC	Tensile	MOCVD	Reflectance	[31.310]
3.478	3.484	3.502	*c*-Plane	GaN	Unstrained	MOCVD	Reflectance	[31.311]
3.4772	3.4830	3.4998	*c*-Plane	Bulk GaN	Unstrained	Na-Ga melt	Reflectance	[31.299]
3.490	3.500	3.520	*c*-Plane	Freestanding	Unstrained	HVPE	Contactless electroreflectance	[31.312]

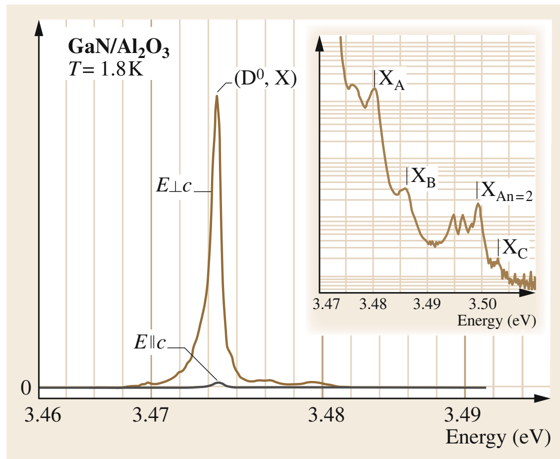

Fig. 31.19 Photoluminescence spectra at 1.8 K for a 400 μm-thick GaN grown on a sapphire substrate, where the spectrum is dominated by the donor-bound exciton transition. The intrinsic exciton states are resolvable after magnification as demonstrated in the *inset*. (After [31.313])

Γ_5(B) and Γ_5(C) states has been found to be 1.02, 0.85 and 0.34 meV respectively, in a homoepitaxial GaN layer [31.298].

Discrepancies on the reported results of free-exciton energies can be noted as indicated in Table 31.7, most of which is due to the in-plane strains induced by the foreign substrates. For most of the earlier studies of free excitons in GaN, the substrates used were either sapphire or SiC, thus inducing compressive or tensile strains respectively. When the strain is isotropic the crystal symmetry and correspondingly the symmetry of the exciton states are not changed. Instead, the strain will mix the states with different symmetry, modifying their energies and oscillator strengths [31.303]. For compressive strains, caused by for example sapphire, the bandgap, the three free-exciton energies, and the splittings, are blueshifted compared to that of unstrained GaN layers. The A and B free-exciton energies have been found to increase by as much as 20 meV at 2 K, while the C free-exciton energy increased about 50 meV [31.291]. An opposite trend was observed for tensile-strained GaN, which decreases the bandgap, overall exciton energies, and the splittings among the three exciton energies. The dependence of the free-exciton energies on the in-plane strains of GaN films is displayed in Fig. 31.20. A frequently cited set of free-exciton energies is 3.4776, 3.4827, and 3.5015 eV for the A, B, and C excitons respectively, as measured on ammonothermally grown bulk GaN [31.294].

The temperature dependence of free-exciton energies was also found to be dependent on the particular sample and strain as demonstrated in Fig. 31.21, where comparisons of temperature dependence were based on three samples: relaxed (bulk GaN), compressed (grown on sapphire), and under tension (grown on SiC). The temperature dependence of the excitonic resonance, in the absence of localization, can be described by the Varshni empirical relation

$$E(T) = E_0(0) - \frac{\alpha T^2}{(\beta + T)} , \quad (31.16)$$

where $E_0(0)$ is the transition energy at 0 K, and α and β are the temperature coefficients.

Similar to other direct-bandgap semiconductors, the dipole-allowed exciton states in GaN encounter strong coupling with photons, which results in formation of a mixed-mode state (so called exciton-polariton) with

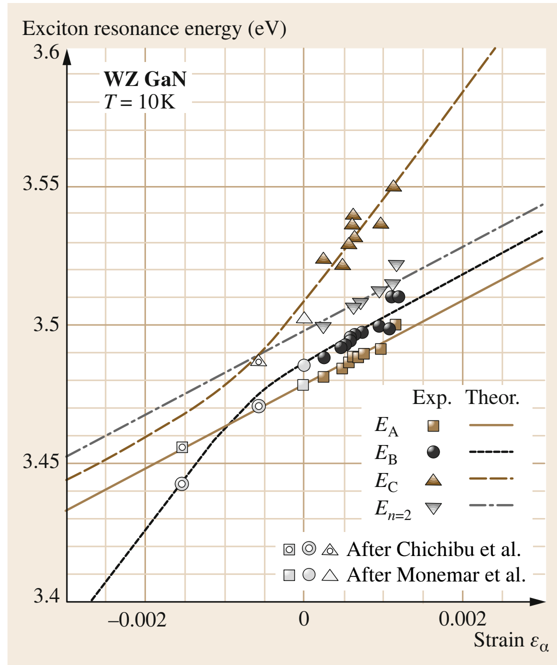

Fig. 31.20 Dependence of free-exciton energies on strain in wurtzite GaN grown on a sapphire substrate, where the strain values were obtained from measured lattice parameters. Also shown is the theoretical modeling of the strain dependence of exciton energies. (After [31.315])

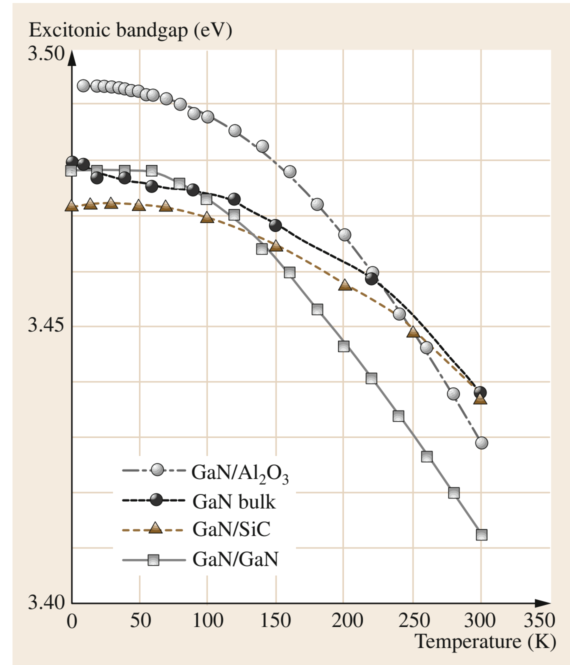

Fig. 31.21 Temperature dependence of the A free exciton energy in samples grown on different substrates. (After [31.297, 316])

a two-branch dispersion curve in the energy region near the intersection of the original exciton and photon dispersion curves [31.317]. The existence of the exciton-polariton has a profound effect on the optical emission in GaN, making the exciton recombination a propagation of polariton waves to the crystal surface and subsequent transmission to the outside as photons instead of transition from the exciton state to the photon state and subsequent photon propagation [31.318]. Thus, the emission line width does not reflect the inherent lifetime broadening of the free excitons. Instead, the emission peaks are usually quite broad and their line shapes are not exactly symmetric and are determined by the spectral dependence of the density of states, group velocity, and transmission coefficient of the different polariton branches [31.301]. Although it is difficult to study the emission of exciton-polaritons, the experimentally observed exciton-polariton spectrum is usually a doublet peak with a dip around the energy of the longitudinal exciton as demonstrated in heteroepitaxial [31.319], homoepitaxial [31.320], and freestanding GaN layers [31.321], where the doublet peaks were interpreted as an emission from the lower and upper polariton branches. An example of excitonic spectra taken at 4.2 K for homoepitaxial GaN layers is illustrated in Fig. 31.22, where the A exciton line splits into two components about 2 meV apart with the lowest component at about 3.477 eV.

Free-exciton transitions in wide-bandgap materials have a characteristic of coupling to phonons, which results in homogeneous broadening of the free-exciton states. At low temperatures, the coupling is dominated by exciton-acoustic phonon scattering, while at high temperatures the longitudinal-optical (LO) phonon Fröhlich scattering is dominant. The exciton line width is composed of three parts as [31.322]

$$\Gamma(T) = \Gamma_0 + \gamma_{\mathrm{ph}} T + \frac{\Gamma_{\mathrm{LO}}}{\left[\exp\left(\frac{E_{\mathrm{LO}}}{k_{\mathrm{B}} T}\right) - 1\right]} ,$$

where Γ_0 is the inhomogeneous line width due to the scattering by defects and impurities, and exciton-exciton interaction, γ_{ph} is the exciton-acoustic-phonon coupling strength, Γ_{LO} is the exciton-LO-phonon coupling strength, and E_{LO} is the energy of the LO-phonons involved in the scattering event (≈ 92 meV for GaN [31.323]). The temperature dependence of the line width has been investigated by many groups with various methods including absorption, PL, reflectance, spectroscopy ellipsometry, and four-wave mixing; however, the reported values have a large spread (varies between 10 and 25 meV) as summarized by *Zhang*

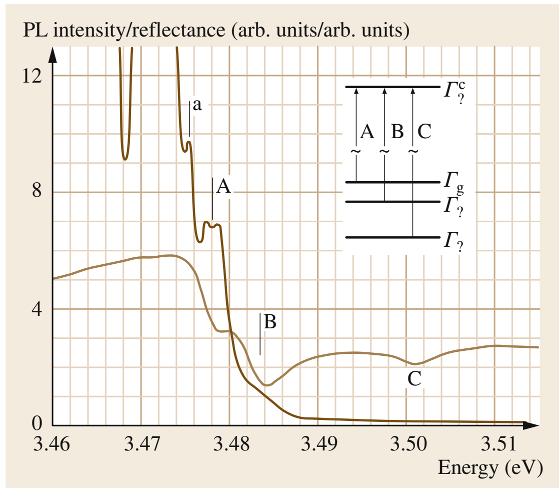

Fig. 31.22 Doublet structure of the A exciton as measured by photoluminescence (*darker line*) at 4.2 K for a homoepitaxial GaN layer. Also shown is the corresponding reflectance spectrum for the same sample (*lighter line*). (After [31.311])

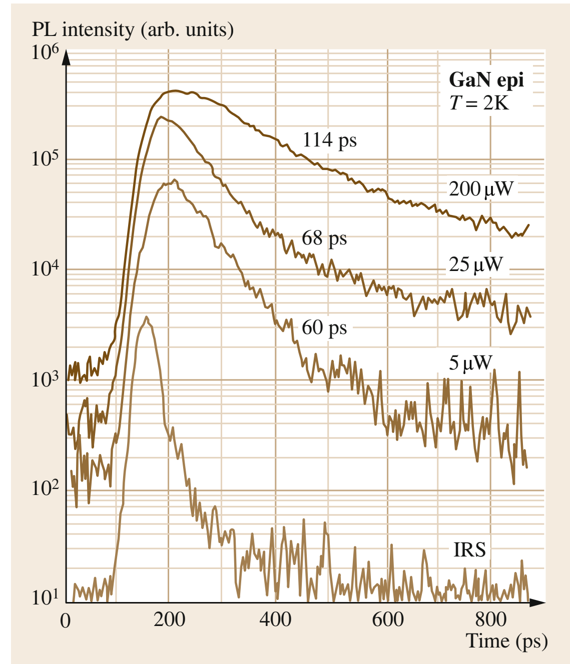

Fig. 31.23 Photoluminescence transients at 2 K for a GaN epilayer grown on sapphire, measured at different excitation power intensities. IRS denotes the instrumental response in the experiment. (After [31.288])

et al. [31.324]. The exciton-LO-phonon coupling is strongest for the first two replicas, and the 3-LO and 4-LO replicas are also clearly observable. As predicted by theory, the LO-phonon replicas are linearly proportional to the temperature, and this behavior is experimentally confirmed for the A exciton for temperatures below 100 K [31.325]. The line shape of the 1-LO and 2-LO replicas can be fitted to a good accuracy with $\approx E^{3/2}\exp(-E/k_{B}T)$ and $\approx E^{1/2}\exp(-E/k_{B}T)$ respectively, where E is the exciton kinetic energy and the exponential terms represent the equilibrium Maxwell distribution [31.326, p. 177].

The binding energies of the excitons determine the bandgap of the materials, which also denote the thermal stability of the excitons. There is large discrepancy on the binding energies of excitons in GaN, ranging from 18 to 26 meV as reviewed by [31.316], which was explained due to the strain in the studied layers or misinterpretations of some features in the optical spectra. The exciton binding energies can be obtained indirectly using temperature dependence of the free-exciton transition in PL [31.327] or the position of the excited states if the positions of the excited states of the excitons are known [31.328–330]. The temperature dependence of the excitons energies showed a monotonic shift to lower energies, which can be satisfactorily fitted by Varshni or Bose–Einstein formulas [31.331]. If exciton energies shift to higher energies, it is indicative of the transition from free-exciton to a band-to-band recombination. The survival of the free excitons at room temperature in GaN is supported by the exciton binding energies of around ≈ 25 meV for the A, B, and C excitons [31.298, 332]. This value is comparable to the thermal energy at room temperature ($k_{B}T = 25.8$ meV). Another fact that supports the presence of excitons at room temperature is that the exciton Bohr radius is very small (≈ 3.5 nm) and a high carrier density ($< 10^{18}\,\mathrm{cm}^{-3}$) is needed to screen the Coulomb interaction [31.303].

The transient behavior of free-exciton recombination in GaN can be investigated by time-resolved PL spectroscopy, while noting that PL transient of the free excitons is very complicated, partially due to the presence of exciton polaritons (EPs). The intrinsic lifetime of this EP was estimated to be about 300 ps (based on acoustic phonon scattering only) [31.333]. The much shorter lifetimes observed in experiments are most likely due to the nonradiative recombination in GaN. Typical transients are shown in Fig. 31.23, which were obtained for different excitation intensities for a GaN epilayer grown on sapphire. The decay time at 2 K was found to vary between 60 and 115 ps, which strongly indicates a contribution from defect-related nonradiative processes. Thus, the decay in luminescence is described by a combination of fast processes followed by a slower processes with a decay time of about 300 ps, although the free-exciton lifetime was estimated to be about 2 ns at low temperatures, deduced from the free-exciton

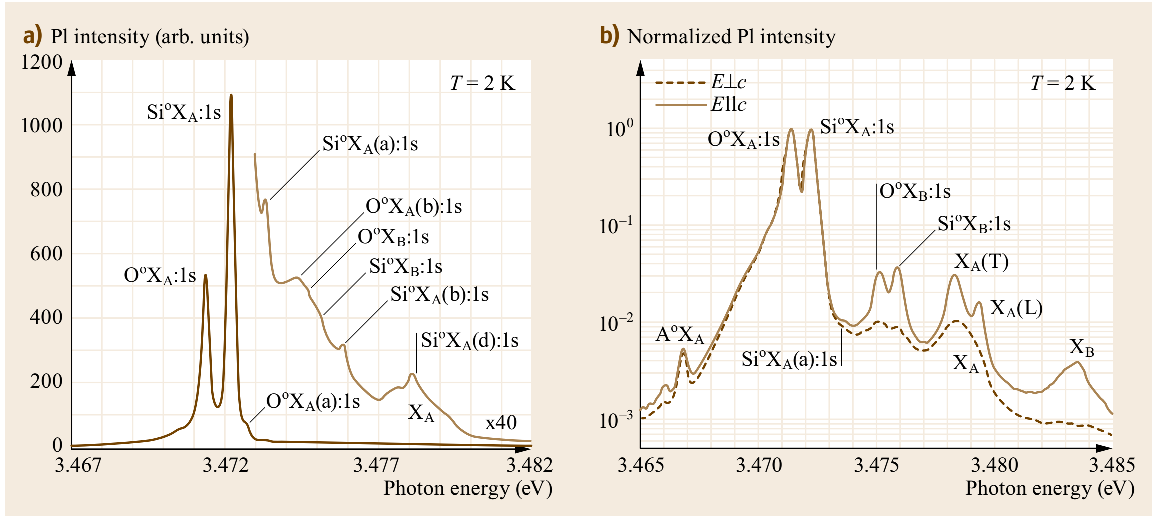

Fig. 31.24a,b PL spectra measured at 2 K for Ga-face bulk GaN for the following configurations: **(a)** α polarization $(k\|c, E\perp c)$; **(b)** $\sigma(k\perp c, E\perp c)$ and $\pi(k\perp c, E\|c)$ polarizations. (After [31.303], courtesy of Dr. B. Monemar)

lifetime with two-photo spectroscopy on freestanding HVPE samples [31.334].

Bound Excitons in GaN

Due to the abundance of impurities in GaN, the neutral shallow donor-bound exciton is often dominant in optical spectra. For samples containing acceptors, the acceptor-bound exciton is also observable. Each donor, acceptor, or neutral defect typically is associated with a bound exciton. The recombination of bound excitons typically gives rise to sharp lines, and can easily be identified for each BE. The neutral donor BE is a four-particle complex with two electrons and one hole located around the positive impurity ion. For excited BEs, an electron will be excited into a series of exciton states, where the first excited state shifts away from the ground state by about three-quarters of the donor binding energy. If the hole in the neutral DBE is excited instead of an electron, this state is called a rotational states, which is quite weak in PL spectra, and is difficult to resolve unless selective excitation is used [31.335]. Oxygen and silicon are the two most dominant residual shallow donors in GaN, thus induce a series of oxygen- and silicon-related DBE states in PL spectra. An example of PL spectra for a bulk GaN sample featuring oxygen and silicon-related DBE states is displayed in Fig. 31.24.

The two dominant PL lines at 3.4714 and 3.4723 eV presented in Fig. 31.24 are believed to be due to the principal recombination of an A exciton bound to a neutral O donor on the N site and a neutral Si donor on the Ga site respectively [31.303]. Emission peaks at very similar energies of 3.4718 and 3.4755 eV were also reported in a high-quality MBE-grown GaN layer on a GaN substrate, where the two peaks are also believed to be associated with Si- and O-related shallow donor states [31.336]. Weak excited rotational states of the O and Si DBEs were observed as well at 3.4727 eV (O^0X_A(a):1s) and 3.4735 eV (Si^0X_A(a):1s) respectively. The energy separation between these lines and the correspondingly principal DBE lines are found to be consistent with previously reported values [31.335, 337]. For even the higher energy DBE region, the DBEs related to the B valence band come into the picture, where the major peaks at 3.4755 eV [31.336] or 3.4751 and 3.4759 eV [31.303, 335] were observed. The peaks at 3.4751 and 3.4759 eV were believed to correspond to O^0X_B:1s and Si^0X_B:1s respectively. These two peaks are more pronounced in the PL spectra measured in π $(k\perp c, E\|c)$ polarization as demonstrated in Fig. 31.24. For a complete review of the commonly observed and reported peak positions and localization energies of DBE in GaN grown by various growth techniques on different substrates, readers can refer to *Viswanath*'s review [31.338, p. 63]. In addition to the emission lines discussed above, there also exist the so-called two-electron transitions (TETs) of the shallow DBEs in the PL spectra with energies ranging from 3.43 to 3.46 eV [31.303]. The origin of these PL lines is attributed to the neutral donor in the final state of the DBE recombination that remains in an excited donor state [31.339]. Strong O- and Si-related TETs pave the way for determining the associated donor binding energies, which are 33.2 ± 0.4 and 30.4 ± 0.4 meV for O and Si donors respectively. These values are quite close to results reported by *Reshchikov* et al. with binding energies of 32.6 and 28.8 meV for O and Si

donors respectively, as measured in MBE-grown GaN on a freestanding GaN template [31.340]. Similar values were also reported by *Moore* et al. [31.341].

Similar to the transient behavior of free excitons, the transient behavior of DBEs also showed a variety of surprising properties. The radiative decay time τ can be estimated from the so-called giant oscillator strength F_{DBE} as $\tau \approx 1/F_{DBE}$ [31.342]. Experimentally, the radiative lifetime can be measured from the low-temperature decay rate associated with the DBE PL lines. For a thick HVPE-grown ($\approx 100\,\mu m$) GaN layer on sapphire with dislocation density of $10^7\,cm^{-2}$, a low-intensity decay time of about 200 ps was observed at 2 K as demonstrated in Fig. 31.25, which is believed to be a typical radiative lifetime for DBEs associated with shallow neutral donors [31.343]. For a thinner layer with higher defect density, a shorter lifetime was observed [31.344, 345], probably due to the excitation transfer to defect states. For a homoepitaxial GaN layer, a fast DBE decay was also observed, due to excitation transfer to point defects [31.288]. Recently, PL decay of a DBE no-phonon line for an HVPE-grown thick GaN layer at low temperatures showed a nonexponential behavior with a fast initial slope (a decay time of about 300 ps), and a much slower tail towards longer times (a decay time of about 1000 ps or higher) [31.303]. It is believed that the initial fast decay time may not be the true decay time of DBEs. Instead, it may be due to other processes, such as surface recombination or optical dispersion in the semiconductor medium with exciton resonances accompanied by resonant light scattering at the neutral donors [31.346]. In order to eliminate the contribution from such processes, the DBE decay time was derived from the transient behavior of the LO replicas of DBE, which should reflect the actual density of BE states. Since the two LO phonon replicas of the O- and Si-related donors are not spectrally resolved, average decay times of about 1.3−1.4 ns were observed for the DBE LO replicas in a 1 mm-thick freestanding HVEP sample with a relatively low donor concentration of $\approx 8\times10^{15}\,cm^{-3}$, which may represent a close approximation to the radiative decay time of the DBEs [31.303]. For a 300 μm-thick freestanding sample with a donor concentration of $\approx 5\times10^{16}\,cm^{-3}$, a shorter decay time of ≈ 600 ps was recorded. Since two-electron transitions (TETs) also rely on the population of DBE states, the transient behavior of TETs was also used to estimate the decay time of DBEs, and a similar decay time was observed as compared to the decay time extracted from the transient behavior of LO replicas of the DBEs. An example of the transient behavior is presented in Fig. 31.26.

Acceptor-bound excitons in GaN are not as well understood as DBEs, and a major ABE1 line at 3.466 eV

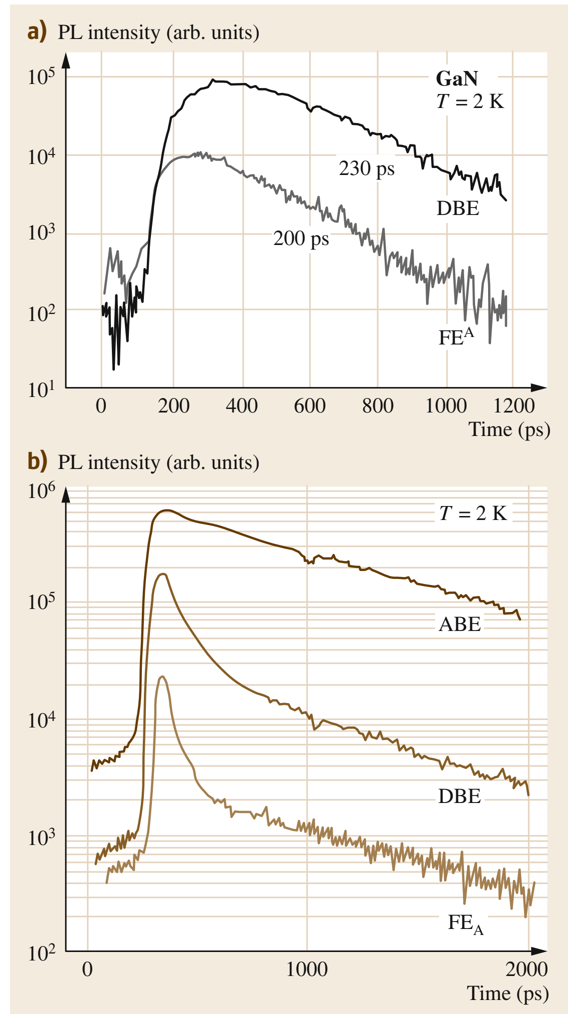

Fig. 31.25 Transient PL **(a)** for a 400 μm-thick GaN layer and **(b)** for a thin strained layer, of which both were grown on a sapphire substrate. (After [31.343])

was observed in strain-free GaN at 2 K [31.347–351], as demonstrated in Fig. 31.27. This peak has been found to be dominant in slightly Mg-doped GaN samples, thus a common assignment of this peak is Mg_{Ga}. This ABE spectrum is stable for n-type or high resistivity materials. However, for p-type (Mg-doped) GaN the emission is clearly unstable and is quenched in a matter of minutes upon photoexcitation, indicating that the acceptor itself may not be stable under these conditions [31.352]. Contradictory evidence comes from the fact that this ABE line disappears in the cathodoluminescence (CL) spectrum under electron irradiation at low temperatures [31.352, 353]. However, one should keep in mind that electron irradiation has been proven to activate the Mg acceptor. Other proposed assignment

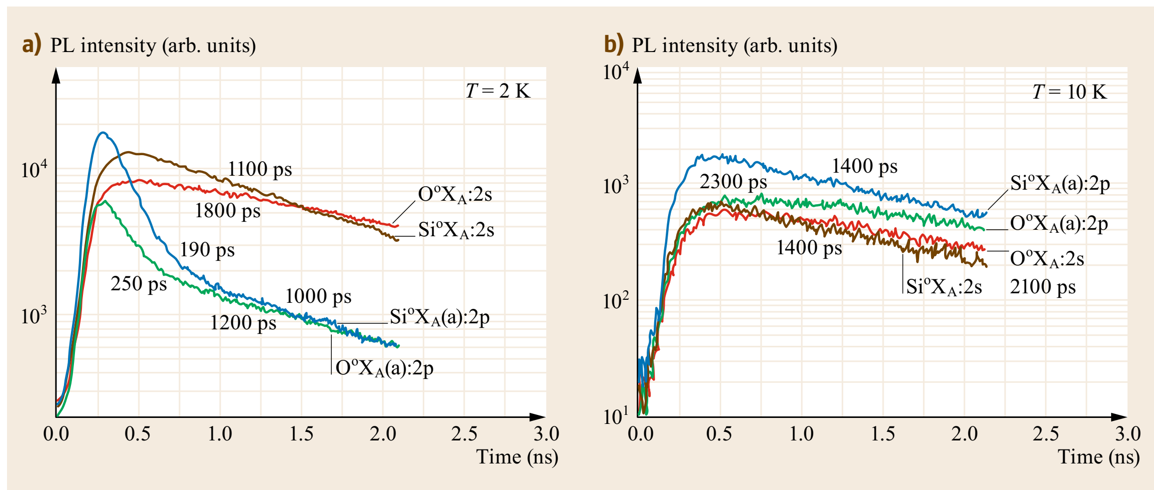

Fig. 31.26a,b Transient PL of TET (two electron transition) related to Si and O donors at **(a)** 2 K and **(b)** 10 K. (After [31.303], courtesy of Dr. B. Monemar)

are: a different acceptor from the substitutional Mg_{Ga}, such as C_N [31.354], and charged donor-bound excitons [31.355–358]. Another broader peak at 3.455 eV (ABE2) has been attributed to Zn based on the fact that this line is close to the position of the dominant ABE observed in Zn-doped samples, if strain-induced shifts are considered [31.359]. However, this still needs further justification. Another tentative assignment for this peak is Mg_{Ga} acceptor due to the fact that the intensity of this broad ABE peak increases with Mg doping [31.360]. This naturally assumes that Mg doping does not facilitate any other process. Recently, both ABE1 and ABE2 lines were proposed to be caused by the Mg doping [31.361], with the ABE2 only observed in highly doped GaN:Mg, which suggest a possible correlation with structural defects, such as basal stacking faults (BSFs), induced by high-Mg doping [31.362]. It was proposed that the A1 acceptor (responsible for the ABE1 emission) will be perturbed by the nearby BSF potential and give rise to the A2 acceptor and its characteristic ABE2 spectrum [31.361]. Decay curves demonstrated the spectral shift of the PL signal from the ABE1 position to ABE2 position, mostly during the first 100 ps, which was interpreted as exciton transfer.

The broader peak at 3.44 eV is probably due to a low-energy acoustic-phonon wing connected to the main peak at 3.455 eV, which is a characteristic for ABEs [31.363, 364]. The decay curves for ABEs in GaN usually show a clean exponential shape as demonstrated in Fig. 31.25b. The radiative lifetime is about 0.7 ns for the shallowest ABE peaked at 3.466 eV, as compared to the much longer decay time of 3.6 ns for the deeper acceptors with an ABE peak in the range of 3.455–3.46 eV [31.348]. The decay time for

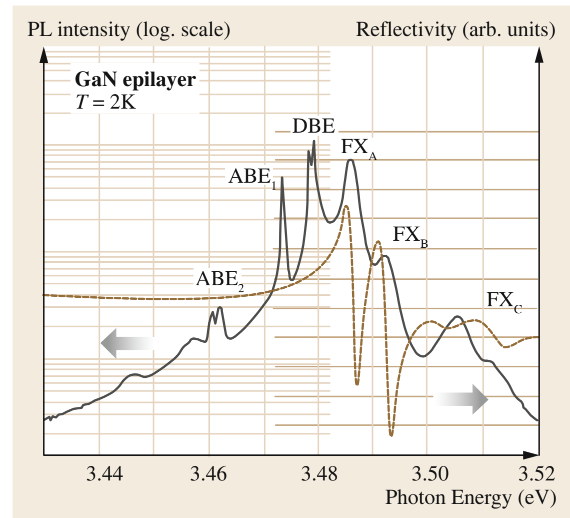

Fig. 31.27 Low-temperature PL spectrum (*solid line*) of a HVPE GaN layer shown on a semilog scale. The reflectivity spectrum (*dashed line*) of the same sample taken at normal incidence geometry is plotted on a linear scale. (After [31.343])

the 3.466 eV ABE peak varies for different samples, presumably due to a nonradiative contribution from excitation transfer effects [31.303].

Donor–Acceptor Transitions in GaN

Due to the various impurities and intrinsic defects, donors and acceptors usually coexist in the same semiconductor material. The electrons bound in the donor states can radiatively recombine with holes bound in the acceptor states, a process termed donor-acceptor

pair (DAP) transition. A commonly observed DAP peak in GaN is located at 3.27 eV, and well-resolved LO-phonon replicas at lower energies were also observed [31.285, 365, 366]. The emission peak is temperature dependent, which is indicative of the change from a DAP signature at low temperatures to a free-to-bound conduction-band-to-acceptor transition at higher temperatures (120 K). This is due to thermal ionization of the shallow donors ($E_D \approx 29$ meV), where an acceptor binding energy of 230 meV was obtained from the temperature-dependent measurements [31.340]. The acceptor responsible for this 3.27 eV DAP is generally believed to be due to the Mg_{Ga} acceptor. There are other interpretations, however, such as an Mg-H complex [31.367], but this interpretation implies that this peak will only be observable in p-type GaN, which is in conflict with the fact that this 3.27 DAP is also prominent in n-type GaN. Another DAP also exists in the blue PL band peaking at about 2.9 eV, which is strong only in MOCVD-grown GaN with high Mg doping. For the same material grown with MBE or HVPE, this blue PL peak does not appear, even though a similar concentration of Mg_{Ga} acceptor would be present. The identity of this blue PL peak is not clear yet, but suggestively it may be related to an H-related deep donor (binding energy 0.37 eV) and the shallow Mg acceptor [31.368, 369].

An interesting feature regarding the ABE as well as 3.27 eV DAP spectra is the long-term instability during prolonged excitation with above bandgap UV light, which was proposed to be due to the instability of the acceptor responsible for the ABE1 and 3.27 eV emission line [31.370]. Additional data suggest that the unstable acceptor might be the Mg-related acceptor as discussed above [31.361]. Short-term instability was also observed, which features a rapid degradation of the PL efficiency in the entire near-bandgap region, indicating a rapid nonradiative process induced by UV excitation. A downshift in energy of the 3.27 eV DAP peak was observed after long-term excitation, which means that the hole occupation of the Mg acceptor decreased [31.371, 372]. This can be explained as that the quasi-Fermi level is raised in the bandgap during the long-term excitation, which can be due to another deeper (nonradiative) defect level. During the recombination process, this deeper defect level is active and can capture photoexcited holes to a metastable state, which decreases the hole occupation in the Mg acceptor [31.361].

Defect-Related Transitions in GaN

Yellow Luminescence (YL). A broad PL band peaking at 2.2 ± 0.1 eV, the so-called yellow emission, has caused enormous debate regarding the nature of this peak for almost 30 years. This PL emission has been systematically observed in undoped or n-GaN [31.373, 374]. The activation energy (thermodynamic transition level) of the YL band was experimentally demonstrated to be 850 meV by fitting the temperature dependence of the YL intensity [31.375]. As studied extensively by *Ogino* and *Aoki* [31.376–379] there seems to be an agreement that this YL can be attributed to transitions from the conduction band or a shallow donor to a deep acceptor. Transition from a deep donor to a shallow acceptor was also proposed to explain the results of magnetic-resonance experiments [31.374]. Early works attributed the YL band to the V_{Ga}-C_{Ga} complex [31.376]. Theoretical calculation from density functional theory suggested that Ga vacancies, both isolated and bound into a complex with oxygen donors, are responsible for the observed YL [31.378, 379], which was supported by positron annihilation experiments, where the YL intensity was found to increase with the concentration of Ga vacancies. Other experimental findings indicated that lattice defects alone do not cause YL, rather its origin should be attributed to some impurities, possibly bound into complexes [31.380]. *Shalish* et al. [31.381] invoked a broad distribution of acceptor-like surface states to account for the YL band. The YL band was also found to shift to lower energies with decreasing energy of the below-gap excitation, which also indicates that the broadening of the YL band may be due to emission from several closely spaced traps [31.382]. More recently, carbon substituting for nitrogen C_N [31.383] and C_N-O_N [31.375] complexes were proposed to be responsible for the YL band by two different groups.

The transient behavior of the YL band has been investigated by several investigators, and a rather long and nonexponential decay in the range of $0.1-100\,\mu s$ at low temperature has been reported by *Hofmann* et al. [31.384] and *Korotkov* et al. [31.385] by using the Thomas–Hopfield model [31.371] of the donor-acceptor pair recombination. Similar work was also demonstrated by *Reshchikov* et al. [31.386] on freestanding high-quality GaN templates grown by HVPE, which concluded that, at temperatures below 40 K, the time decay of the yellow peak is nonexponential and can be explained in the framework of the Thomas–Hopfield model for DAP-type recombination involving shallow donors. For elevated temperatures, the decay becomes exponential with two components, suggesting transitions from the conduction band to two deep acceptors.

31.6.2 Aluminum Nitride

The optical properties of AlN have been investigated in many forms of it, including powders, sintered ce-

ramics, polycrystals, and single-crystal samples. Owing to the availability of large-size single-crystal bulk AlN in recent years, intensive studies on optical properties have been conducted. Because the AlN lattice has a very large affinity to oxygen dissolution, oxygen contamination is difficult to eliminate in AlN. AlN samples contaminated with 1–6% oxygen were found to have two broad emission peaks centered near 3.0 and 4.2 eV [31.387]. *Youngman* and *Harris* [31.388] and *Harris* et al. [31.389] found broad peaks centered at 2.7 and 3.8 eV in large single-crystal AlN with oxygen content of 380 ppm. However, *Strasburg* et al. [31.130] argued that oxygen alone is not able to generate such emission bands by comparing the obtained PL spectra with elemental analysis data obtained from glow discharge mass spectrometry (GDMS), where the emission intensities did not show a direct correlation to the oxygen concentration. GDMS analysis also revealed that in addition to O, Si and C were also present at concentrations that may have a significant influence on the luminescence properties of AlN. An absorption band around 265 nm ($\approx$ 4.7 eV) was found to be more pronounced with the increase of the carbon concentration [31.51], and one possible origin of this absorption band is reported to be due to the substitution of C impurities on the nitrogen site (C_N), which becomes a deep acceptor in AlN [31.390]. Room-temperature PL spectra also showed that a peak at 3.9 eV only becomes prominent as long as the C concentration is much higher than the concentration of other impurities. This suggests a change in the compensation mechanism once the amount of C is not sufficient to act as the main acceptor [31.390], which is consistent with the assignment of C_N to a deep acceptor. However, in another report, the intensity ratios of deep CL bands at 4.6, 3.1 and 3.8 eV to the near-band-edge emission at 11 K were found to increase with V_{Al} concentration, where the V_{Al} concentration was detected from positron annihilation spectroscopy [31.391]. Another proposed origin for the 3.9 eV in the PL spectrum is due to a complex of an aluminum vacancy (V_{Al}) and an oxygen impurity on the N site (V_{Al}-O_N) [31.392]. Another 2.8 eV luminescence peak, whose intensity also increases with increasing carbon doping concentration, was observed even in HVPE-grown samples with relatively low concentrations of O and Si impurities, which reduces the concentration of V_{Al} by increasing the formation energy of V_{Al} [31.379]. One can then conclude that the deep emission around 2.8 eV may be either directly or indirectly related to C impurities [31.51].

The investigation of free-exciton energies has expanded considerably due to the availability of high-quality single-crystalline AlN layers, especially AlN bulk material. The majority of reported free-exciton energies of A are between 6.0–6.05 eV, depending on the strain state of the AlN material, while the free-exciton energies of B and C are difficult to fully resolve, but which would be in the range of 6.2–6.3 eV. A survey of the free-exciton energies is presented in Table 31.8. The free-exciton energy is strongly dependent on the biaxial strain of the AlN lattice, where the free-exciton energy is blueshifted in AlN/sapphire due to compressive strain and redshifted in AlN/SiC and AlN/Si due to tensile strain. A linear relationship between the free-exciton transition energy peak position and in-plane stress was obtained [31.393] with a linearity coefficient of 45 meV/GaP, which is about 88% higher than that in GaN (24 meV/GPa) [31.394]. The dependence of the free-exciton energies on the strain is demonstrated in Fig. 31.28 with four data points, including AlN/sapphire, AlN/AlN bulk, AlN/SiC, and AlN/Si. Based on the free-exciton energy of A and its first excited state, the AlN bandgap can be determined, and the reported values are 6.077 eV [31.395], 6.093(8) eV [31.396], 6.094 eV [31.397, 398], and 6.096 eV for unstrained bulk AlN at low temperatures [31.399]. The binding energy of free excitons can also be determined from the same technique, with reported values of 57 meV [31.400], 48 meV [31.395], 63 meV [31.401], 52.4 meV [31.397], 55 meV [31.402] and 51 meV [31.403] for FX(A). These reported binding energies are much larger than the thermal energy at room temperature, thus enabling one to clearly observe free-exciton luminescence at room temperature [31.404]. Based on a quasicubic model developed for the wurtzite crystal as well as other reported exper-

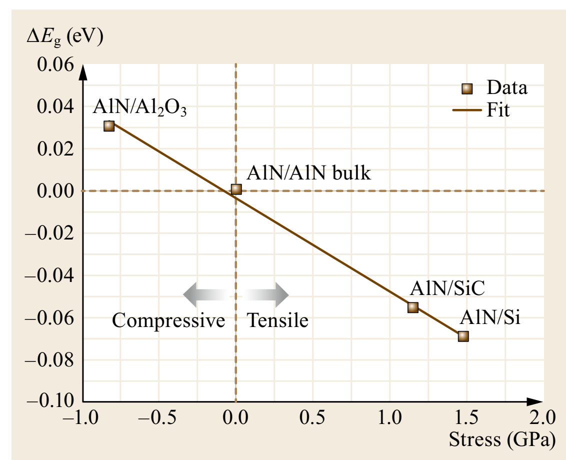

Fig. 31.28 Stress-induced shift of free-exciton energy in AlN epilayers as a function of the in-plane strain. The *solid line* is the least-square linear fit to the experimental data, where a value of 45 meV/GPa is obtained for the linear coefficient of stress-induced bandgap shift. (After [31.393])

imental exciton energy values, the AlN spin-orbit splitting and the crystal-field splitting were estimated to be $\delta = 36$ meV and $\Delta = 225$ meV respectively [31.395]. The obtained value for the crystal-field splitting is close to the value of 230 meV in unstrained AlN as reported earlier [31.399].

Due to the large free-exciton binding energy and strong oscillator strength, the excitons can stably exist at high excitation densities, enabling the study of the interaction between two or more excitons. This unique property can be characterized by the formation of biexcitons (excitonic molecules) and the inelastic scattering of excitons. Exciton-exciton scattering processes occur when, at high enough exciton densities, inelastic collisions of excitons occur. Following scattering, one exciton is scattered into a higher excited state while another decays with equal-energy loss. Excitons can not only be scattered into $n = 2$ state but also scattered to $n = 3 \ldots \infty$, where the number n is usually given as an index to distinguish the different scattering events therefore leading to P_2 to P_∞ bands. Note that under high excitation densities at room temperature, the electron-hole plasma (EHP) has been found to be the dominant recombination process in AlN [31.402]. Biexciton emission (also called the M band) has been observed in ELO-grown *a*-plane AlN epitaxial layers with an energy separation between free-exciton luminescence and biexciton luminescence of 19 meV, which is also the binding energy of biexcitons [31.400]. The PL plots of exciton and biexciton emissions at 7 K at different excitation densities are displayed in Fig. 31.29. By integrating the PL intensities of both the free-exciton line and the biexciton line for different excitation power densities, it was found out that the free-exciton line intensity grows almost linearly with the excitation power density (a power factor of 1) while the biexciton line intensity grows superlinearly with a power factor of around 1.5. This indicates that the biexciton density does not vary as the squares of the free-exciton density, which may be due to a relatively short recombination time of excitons and biexcitons in direct-bandgap semiconductors [31.405]. In the instant case, it may imply that the biexcitons have a shorter radiative lifetime than that of free excitons. Biexciton emission was also observed at a different energy, some 27 meV below the free-exciton emission in AlN layers grown on SiC and sapphire substrates [31.406]. In addition, another band was identified at 36 meV below the free A-exciton transition and was ascribed to the exciton-exciton scattering (P_2 band), which showed a power factor of 1.66 instead of 1.54 for the biexciton emission in the same report [31.406].

A few DBE emission lines have been reported as shown in Fig. 31.30, with D^0X occurring at 9.8, 13.3, 19.0, 22.5, and 28.5 meV below the free exciton X_A [31.396] in AlN layers grown homoepitaxially on AlN substrates, which were in turn grown by physi-

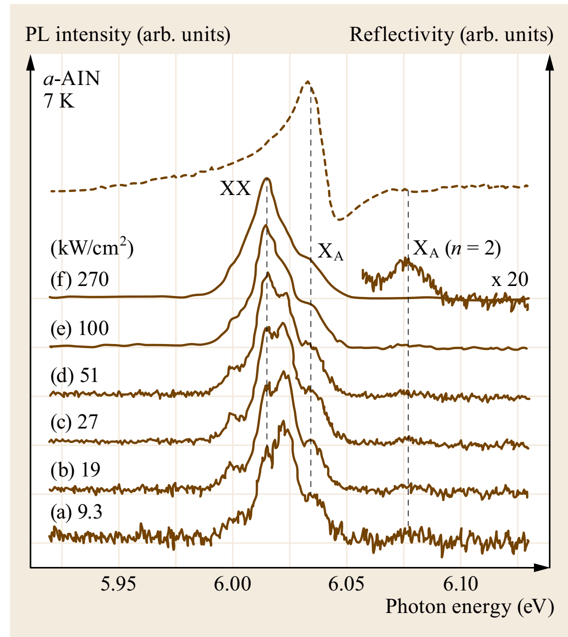

Fig. 31.29 Excitonic photoluminescence spectra (*solid lines*) at 7 K taken from an *a*-plane AlN epitaxial layer under different excitation-power densities ranging from 9.3 to 270 kW/cm^2. Each spectrum is normalized at the peak height. An optical reflectance spectrum is also demonstrated in the upper part by the *dashed line*. The symbol XX represents the biexciton. (After [31.400], courtesy of Yamada))

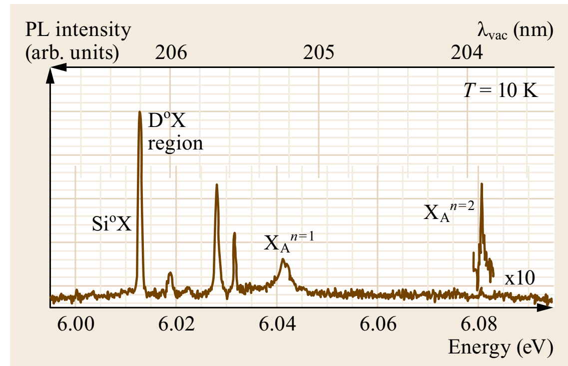

Fig. 31.30 PL emission lines of a nominally undoped AlN homoepitaxial layer with a few donor-bound exciton lines (D^0X) besides the free-exciton emission (X_A) and its first excited state with $n = 2$. The *leftmost line* is ascribed to the excitons bound to silicon (Si^0X) found at 28.5 meV below the X_A emission. (After [31.396])

Table 31.8 Reported free-exciton (FX) energies in AlN

FX(A)	FX(B)	FX(C)	Orientation	Substrate	Strain	Growth	Technique	Reference
6.0430			*c*-plane	AlN	Homoepitaxial	MOVPE	PL	[31.407]
6.041			*c*-plane	AlN	Homoepitaxial	PVT	PL	[31.396]
6.0414			*c*-plane	AlN	Homoepitaxial	MOCVD	PL	[31.397]
5.958	6.216	6.229	*c*-plane	Silicon	Tensile	MOCVD	PL	[31.408]
6.074	6.273	6.283	*c*-plane	Sapphire	Compressive	MOCVD	PL	[31.408]
6.109	6.285	6.295	*c*-plane	SiC	Compressive	PA-MBE	PL	[31.408]
6.0414			*c*-plane	AlN	Homoepitaxial	MOCVD	PL	[31.409]
6.025	6.243	6.257	*c*-plane	AlN	Homoepitaxial	MOCVD	Reflectance	[31.399]
6.1383	6.277	6.304	*c*-plane	Sapphire	Compressive	LP-MOVPE	CL	[31.403]
6.0346			*a*-plane	AlN template	ELO	MOVPE	PL	[31.400]
6.060			*c*-plane	Sapphire	Compressive	MOCVD	PL	[31.393]
5.974			*c*-plane	SiC	Tensile	MOCVD	PL	[31.393]
5.960			*c*-plane	Silicon	Tensile	MOCVD	PL	[31.393]
6.029	6.243	6.268	*c*-plane	Sapphire	Compressive	LP-MOVPE	Reflectance	[31.403]
6.023	6.243	6.268	*a*-plane	Bulk AlN	Bulk	Sublimation	Reflectance	[31.395]
6.023	6.036		*c*-plane	Bulk AlN	Homoepitaxial	OMVPE	CL	[31.401]
6.025	6.243	6.257	*m*-plane	Bulk AlN	Bulk	Sublimation	Reflectance	[31.399]

cal vapor transport. The tentative assignment of these emission lines to DBEs is based on the agreement with earlier reports, the temperature-dependent behavior of the emission bands, and their very narrow line widths (500 μV for the dominant line of 6.0125 eV in Fig. 31.30). The assignment to ABEs was discounted because, in analogy to GaN, the binding energies of common acceptors [31.366] are expected to be larger than those of donors [31.341]. With increasing silicon doping concentration from 1×10^{17} to $1\times10^{19}\,\mathrm{cm}^{-3}$, a clear increase in the intensity was observed for one single D^0X band with 28.5 meV exciton localization energy (located at 6.0125 eV) relative to the intensity of the free-exciton emission [31.396]. This assignment is in agreement with the available data for silicon in AlN, where the localization energy has been reported to be 24 meV [31.410], 22–29 meV [31.411], and 26 meV [31.412]. Based on the PL spectra, the donor binding energy of silicon in AlN was estimated to be 133 meV. The line width of this Si^0X line was broadened due to the increased Si doping, possibly due to the band filling as proposed earlier by *Yoshikawa* et al. [31.413] for silicon-doped GaN, and local potential fluctuations according to $\mathrm{FWHM} = E_0 + a\sqrt{N_{Si}}$ as reported by *Nam* et al. [31.412]. Additionally, Si doping also gave rise to a blue luminescence band at around 400 nm, which may be due to secondary defect creation processes or charge transfer due to higher silicon doping [31.396]. However, another report ascribed the DBE line with localization energy of 22.4 meV to the Si^0X line, most prominent in the sample having the highest silicon concentration, while other DBE lines remained unidentified and may be due to oxygen donors or intrinsic donors [31.397]. An ABE emission line due to an Mg acceptor was claimed to be observed in Mg-doped AlN epilayers at 6.02 eV at 10 K, which is about 40 meV below the free-exciton transition in undoped AlN epilayers [31.414]. The intensity of this ABE line is rather weak, which is about 40 times smaller than that of the free-exciton transition in undoped AlN epilayers.

Time-resolved PL measurement in 1 μm-thick AlN epilayers grown by MOCVD on sapphire substrates revealed that the recombination lifetimes were around 80 ps for DBE and 50 ps for free excitons [31.415]. For Mg-related ABE, the decay kinetics can be described by a single exponential with a decay lifetime constant of about 130 ps at 10 K [31.414]. In another report, time-resolved PL and CL were used to investigate the decay properties in AlN, and the excitonic radiative lifetime (τ_R) at 7 K was measured to be 10 ps, which increased up to 530 ps with increasing amount of impurities and V_{Al} concentrations, irrespective of the dislocation density [31.416]. It was found that radiative lifetime of excitons bound to neutral donors and *e-h* pairs bound in impurity-induced band-tails is much longer than for the intrinsic free excitons.

The temperature dependence of the optical bandgap of AlN has been investigated by a few groups with consistent results. As reported by *Guo* and *Yoshida* [31.417], the bandgap energy increases linearly from room temperature down to about 150 K with a temperature coefficient of 0.55 meV/K. Similar temperature behavior was reported by *Kuokstis* et al. [31.418] for single-crystal *c*-plane AlN with a temperature coefficient of 0.53 meV/K between 150 and 300 K. These two reports are close to each other and also close to the value of 0.51 meV/K reported by *Tang* et al. [31.419]. For temperatures below 150 K, it

was found that for all the measurements a new structure starts to form, where the bandgap does not change linearly with temperature and has a very small temperature coefficient, which is unusual for semiconductors.

31.6.3 Indium Nitride

InN is not as well understood compared to other group III nitrides. Due to the large background electron concentration as well as the relatively low crystalline quality, the excitonic features, neither in the absorption spectra nor in the band-edge photoluminescence spectra, have been observed. Many early efforts determined the bandgap to be in the range of 1.7–2.07 eV [31.421–423]. One widely cited bandgap value for InN was 1.89 eV obtained by *Transley* and *Foley* [31.424]. This value was also often used as an end-point value to interpret experimentally measured composition dependence of the bandgap of InN alloys [31.425]. With improved growth techniques for InN, a strong luminescence transition at energies around 1 eV appeared [31.426–428], which led to a sudden revision of the bandgap down to about 0.7 eV [31.429]. The sudden revision for the bandgap of InN came from the observation of an absorption edge at about 0.7 eV at low temperatures for moderately n-type samples (about $10^{18}\,\mathrm{cm}^{-3}$) [31.430, 431] and the value blueshifts for higher doping [31.427, 432, 433]. *Thakur* et al. [31.434] investigated the optical-absorption spectra of InN thin films with electron densities varying from $\approx 10^{17}$ to $\approx 10^{21}\,\mathrm{cm}^{-3}$. The optical-absorption edge was found to increase from 0.61 to 1.90 eV as the electron density of the film is increased from low to high density. Shifting of the optical-absorption edge is due to a corresponding up-shift of the Fermi level in the conduction band (the so-called Burstein–Moss shift). By subtracting the influence of self-energies and chemical potential from the optical-absorption edge energy, the intrinsic bandgap values were estimated to be ≈ 0.59 eV for the film with lowest carrier density, and ≈ 0.60 to ≈ 0.68 eV for the film with highest carrier density, where the dispersion was attributed to the variation in the electron effective mass and static dielectric constant. However, care must be taken to interpret the carrier density values obtained from the Hall measurements due to the presence of surface electron accumulation for InN [31.435–437] and due to a gradient in defect properties across the film [31.438].

Due to the fact that, in many highly doped samples, the main absorption edge occurs at much higher energies while the PL peak remains at about 0.7–0.8 eV [31.432, 439, 440], an alternative model of this absorption edge as being of extrinsic origin has been suggested in the literature [31.440–442], which ascribed the absorption edge to a deep level to conduction band transition. The value of the absorption coefficient at about 0.5 eV above the absorption edge was measured experimentally to be about $3\times10^{4}\,\mathrm{cm}^{-1}$ (within a factor of two) [31.443], which is a typical value for a direct band-to-band transition. In order for the deep level model to be consistent with the large absorption coefficient measured, the deep donor concentration was estimated to be close to $10^{20}\,\mathrm{cm}^{-3}$ [31.443]. In addition, this concentration has to be the same within

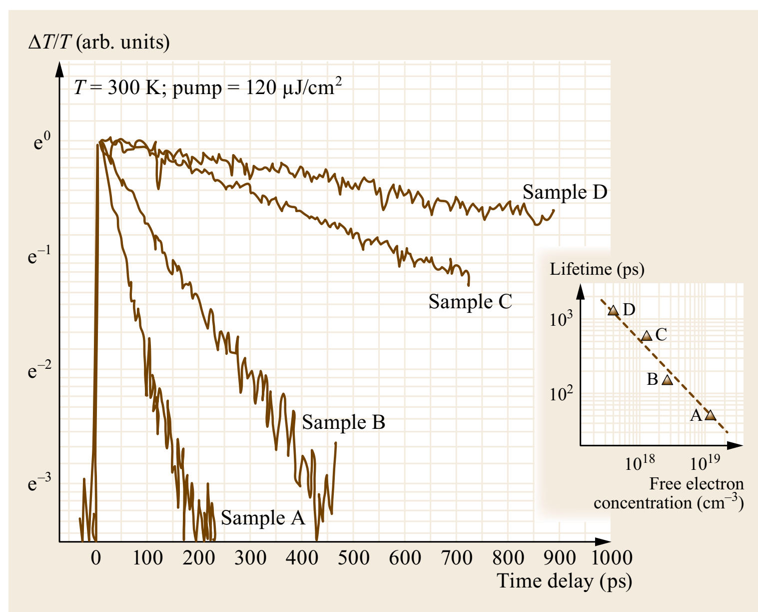

Fig. 31.31 Strength of the differential transmission signal versus time delay under a pump fluence of $120\,\mu\mathrm{J/cm}^2$ at room temperature. The *inset* shows the carrier lifetime as a function of free-electron concentration. (After [31.420], courtesy of Dr. A.N. Cartwright)

a factor of two in all samples studied, which appears implausible and no such deep level could be identified from SIMS data in the highest quality samples studied [31.270, 444]. Besides the optical measurement of absorption edge and direct band nature, the PL signal was found to depend linearly on the excitation laser intensity over a wide intensity range from 10 to 200 mW, indicating that the observed nonsaturable PL peak is due to the emission associated with the direct band-to-band recombination rather than the band-to-defect (or impurity) deep emission [31.445].

Ultrafast differential transmission measurements have been conducted on a series of InN epilayers to determine the carrier lifetimes [31.420], where a fast initial hot carrier cooling followed by a slow recombination process after pulse excitation was observed. The carrier lifetime was measured to be ranging from 48 ps to 1.3 ns, and an inverse proportionality between the carrier lifetime and the free-electron concentration was observed as demonstrated in Fig. 31.31. The ultrafast recombination was assigned to be due to nonradiative recombination related to defects or impurities, which was confirmed by the fact that the defect-related nonradiative lifetime, depending on the defect density, is independent of photogenerated carrier density. The carrier lifetimes were measured as a function of photogenerated carrier density by varying the pump fluence from 60 to 480 $\mu J/cm^2$, the decay curve was observed to remain as a single exponential and there was no observable change in the carrier lifetime.

The temperature dependence of the bandgap of InN has been studied by a few groups [31.421, 446], where a bandgap temperature coefficient of $1.3-1.8 \times 10^{-4}$ eV/K was demonstrated near room temperature by using E_g (300 K) = 1.89 eV. For more recent InN samples with a ≈ 0.7 eV bandgap, a small blueshift (nearly linear at 0.1 meV/K) was observed with increasing temperature in the peak energy position [31.430]; although redshift of the peak energy position was also observed with increasing temperature [31.447]. The PL peak broadened with increasing temperature, which may indicate that longitudinal-acoustic phonon scattering dominates the emission broadening process in the InN samples studied [31.447].

31.7 Properties of Nitride Alloys

Many important applications of GaN-based devices require alloying GaN with other group III nitride materials to form, for example, AlGaN, InGaN, AlInN, and even AlInGaN. Ternary alloys of wurtzite polytypes of GaN, AlN, and InN have been obtained continuously whose direct bandgap ranges from ≈ 0.7 eV for InN to 6 eV for AlN. Many material as well as device properties, such as bandgap, effective mass of electrons and holes, and the dielectric constant, depend on the alloy composition. The lattice constants $a(x)$ and $c(x)$ of the wurtzite group III nitride alloys $A_xB_{1-x}N$ ($Al_xGa_{1-x}N$, $In_xGa_{1-x}N$ and $Al_xIn_{1-x}N$) are predicted to follow composition-weighted averages between the end-binary compounds AN and BN (Vegard's law) [31.55], which was confirmed within 2% error over the whole range of possible compositions between theoretical calculations and experimental measurements by a combination of techniques, such as HRXRD, Rutherford and elastic recoil detection analysis [31.63, 448, 449]. However, for pseudomorphic Al-rich $Al_xIn_{1-x}N$ films, the large present strain in the film was found to cause the dispersion between the In contents determined by XRD and RBS, suggesting a strain-driven deviation of the lattice parameters from the Vegard's rule in this case [31.450]. In fact, many materials' properties have been shown to deviate from Vegard's rule, such as the direct bandgap, polarization charge, and so on. The optical bandgap of ternary alloys can be predicted by the following empirical expression

$$E_g(A_xB_{1-x}N) = xE_g(AN) + (1-x)E_g(BN) - x(1-x)b\,, \tag{31.17}$$

where $E_g(AN)$ and $E_g(BN)$ are the optical bandgaps of material AN and BN respectively, and x and b are the AN molar fraction and bowing parameter respectively. For the case of $Al_xGa_{1-x}N$, this empirical equation has been determined to be [31.451]

$$E^g_{AlGaN}(x) = [6.0\,x + 3.42\,(1-x) - 1.0\,x(1-x)]\ \mathrm{eV}\,. \tag{31.18}$$

The above equation can be obtained by simultaneously determining the bandgap and alloy composition precisely. The alloy composition can be obtained from XRD or Rutherford back-scattering (RBS) or both. The bandgap can be determined by optical reflectance and absorption measurements. A plot of the bandgap versus the Al composition is given in Fig. 31.32, where a bowing parameter of 1.0 eV was obtained with a least-square fitting of the data to (31.17). The XRD peak positions as well as the peaks in optical measurement

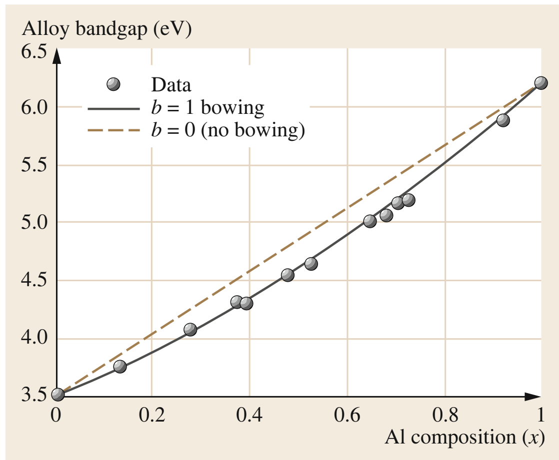

Fig. 31.32 Experimental data for the energy bandgap of AlGaN plotted as a function of Al composition in the whole Al composition range (*solid circle*). The *solid line* is a least-square fit, which gives a bowing parameter of $b = 1.0$ eV. The *dashed line* represents the case of zero bowing parameter. (After [31.451])

techniques can be significantly affected by the material crystalline quality and purity, and thus can potentially influence the bowing parameter obtained. Temperature- and composition-dependent bandgaps of $Al_xGa_{1-x}N$ alloys were investigated in the temperature range between 10 and 800 K, where the temperature dependence of the bandgaps at each different composition can be fitted to the Varshini equation yielding the Varshini coefficients [31.452].

The optical properties of Ga-rich $Al_xGa_{1-x}N$ ($x = 0.019$, 0.038, 0.057, 0.077, and 0.092) alloys in the form of epilayers have been investigated by temperature-dependent PL and time-resolved PL spectroscopy [31.453]. Thermal quenching was observed with two activation energies, which were attributed to the delocalization of excitons and thermal dissociation of excitons. The localization energy increased as the 1.7th power of the PL line width, which reflected a broadening of the density of localized exciton states. Additionally, the luminescence decay of the localized excitons for the five epilayers studied became longer with decreasing emission energy, indicating that the decay of excitons is caused not only by radiative recombination, but also by transfer to lower energy states.

As far as the electrical and doping properties are concerned, there exist several reports of n-type doping of AlGaN with various Al compositions. Hall measurement for n-$Al_{0.09}Ga_{0.91}N$ demonstrated a carrier concentration of $5\times10^{18}\,cm^{-3}$ and a mobility of $35\,cm^2/(V\,s)$ at room temperature [31.454]. A 1.8 μm-thick Si-doped $Al_{0.3}Ga_{0.7}N$ was grown on sapphire by using a superlattice buffer layer that demonstrated a mobility of $80\,cm^2/(V\,s)$ and a carrier concentration of $3\times10^{18}\,cm^{-3}$ at room temperature [31.455]. Crack-free $Al_{0.75}Ga_{0.25}N$ layers with electron concentrations as high as $1\times10^{18}\,cm^{-3}$ were also demonstrated with Hall mobility of about $50\,cm^2/(V\,s)$ at room temperature [31.456]. Highly conductive n-type $Al_xGa_{1-x}N$ ($x = 0.7$) films have been achieved with resistivity as low as 8 mΩ cm (electron concentration $n = 2.6\times10^{19}\,cm^{-3}$ and mobility $\mu = 30\,cm^2/(V\,s)$) for a Si-doping concentration of $3.5\times10^{19}\,cm^{-3}$ [31.457]. The resistivity was found to increase by one order of magnitude when the Al composition increased by 8%, which is due to the deepening of the Si donor energy level with increasing Al composition, and possibly increasing electron trap density. The Si donor activation energy was estimated to vary from 23 to 180 meV as Al composition was increased from 0.7 to 1.0 [31.457]. A similar trend was also observed that demonstrated that the activation energy of the Si donor increases linearly from 0.02 eV in GaN to 0.32 eV in AlN [31.458]. It should be noted that 23 meV is smaller than the well-established binding energy for dilute GaN, which means that the above-mentioned values represent somewhat screened figures. p-Type doping of the AlGaN alloy was achieved by Mg doping as in the case of GaN. The hole mobility in Mg-doped p-$Al_{0.08}Ga_{0.92}N$ was found to decrease with increasing temperature, reaching a value of about $9\,cm^2/(V\,s)$ for a doping density of $1.48\times10^{19}\,cm^{-3}$, where the low mobility was ascribed to a high carrier concentration and the intergrain scattering present in the samples [31.459]. The Mg doping and resistivity correlation in AlGaN was also investigated [31.460]. In this particular study, the undoped AlGaN layer is highly resistive with resistivity of larger than $10^7\,\Omega\,cm$, which decreased to $10^3\,\Omega\,cm$ after doping to a Mg chemical concentration of $2\times10^{19}\,cm^{-3}$. When the Mg level reached $3.5\times10^{19}\,cm^{-3}$, the resistivity reduced to $10\,\Omega\,cm$ with corresponding hole concentration of $2.2\times10^{17}\,cm^{-3}$ and mobility of $2.7\,cm^2/(V\,s)$. Resistivity values increased by several orders of magnitude for Mg concentrations beyond mid-$10^{19}\,cm^{-3}$ due to generation of structural defects, such as inversion domains and stacking faults, caused by Mg in the lattice. These issues will certainly influence the performance of devices, such as lasers, which depend critically on the overall device series resistance including the p-type AlGaN material. Another issue that needs to be considered for optimum device performance is the thermal conductivity of the $Al_xGa_{1-x}N$ alloy, which demonstrated strong reduction of the thermal conductivity due to even a small portion of alien atoms in host materials [31.461]. The thermal conductivity decreases with increasing Al composition and reaches the minimum

at $x = 0.5$; however, the largest reduction of the thermal conductivity took place when either the Al or Ga composition fell in the band from $x = 1.0$ to 0.9, indicating that profound phonon scattering was induced by even a small portion of alien atoms in host materials. The reduction was observed over a wide temperature range from about 10 to 800 K, but was more sensitive at temperatures higher than 200 K, suggesting that the point-defect and phonon-phonon scattering are the dominant phonon relaxation processes.

The InGaN alloy is used mostly for quantum wells in the active regions of LEDs and lasers, which can emit in the violet or blue wavelength range but can be extended to green. Although high efficiency blue and green LEDs utilizing InGaN active layers are commercially available, this technology might suffer from the phase segregation and other inhomogeneities due to the large disparity between Ga and In, making the determination of the bandgap of InGaN versus composition difficult. Extensive theoretical and experimental studies have been carried out to determine the value of the bowing parameter, which requires the precise information of strain, phase separation and inhomogeneities in InGaN grown by various techniques and on various substrates. Bowing parameter values ranging from 1 to 6 eV have been reported, a summary of which can be found in [31.462]. Considering using either ≈ 1.9 or ≈ 0.8 eV bandgap for InN to fit the experimental results, two bowing factors can be obtained as demonstrated in Fig. 31.33 with bowing parameter of $b = 1.43$ eV for the 0.77 eV bandgap for InN and $b = 2.63$ eV for the 1.9 eV bandgap for InN.

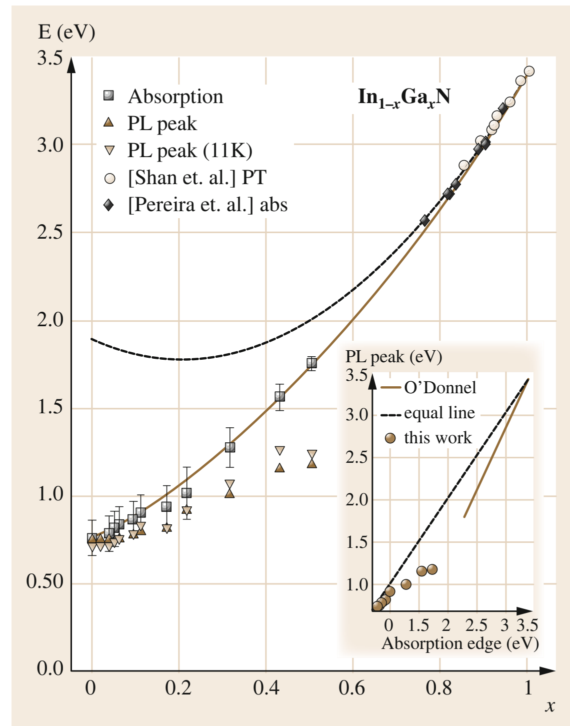

Fig. 31.33 PL peak energy and bandgap determined by optical absorption as a function of composition, including the previously reported data for the Ga-rich end of the ternary, which is not affected by the large InN bandgap previously used. The *solid curve* shows the fit to the bandgap energies using an InN bandgap of 0.77 eV and a bowing parameter of $b = 1.43$ eV. The *dashed line* is the fit to the bandgap energies on the Ga-rich side assuming a bandgap of 1.9 eV for InN. The *inset* shows the PL peak energy plotted against absorption edge energy, where the *solid line* is a least-square fit to experimental data on the Ga-rich side and the *dashed straight line* shows the relationship when the Stokes shift is zero. (After [31.428])

The incorporation of indium in growing InGaN alloys was found to increase with decreasing temperature [31.463–465]. For samples grown at high temperature ($T \geq 750\,°C$), prominent near-band-edge emission was observed, while for samples grown at low temperatures ($T \geq 700\,°C$), a deep level or impurity transition was found to be dominant [31.465], which can significantly deteriorate the quality of the InGaN material. *Kumakura* et al. [31.466] investigated the electrical properties of Mg-doped InGaN grown by MOCVD with an indium composition smaller than 0.2. The activation energy E_A of the Mg acceptors in InGaN was found to decrease with the increase of the indium content, leading to higher hole concentration at room temperature for higher indium composition within the studied mole fraction range ($x > 0.2$). This phenomenon is consistent with other group III nitride semiconductors, which demonstrated that activation energy increases with energy gap [31.459, 467]. Another report also investigated the p-type doping in $In_xGa_{1-x}N$ alloys grown by MOCVD on semi-insulating *c*-GaN/sapphire templates [31.468]. p-Type layers were achieved for indium composition up to 0.35. The hole concentration was found to continuously increase from 2×10^{17} cm^{-3} for $x = 0$ (GaN) to 5×10^{18} cm^{-3} for $x = 0.22$, while the hole mobility was found to decrease from 15 to 1.8 cm^2/(V s) as x increased from 0 to 0.35. The reduction in hole concentration in p-type $In_xGa_{1-x}N$ with $x > 0.22$ was attributed to the effect of hole compensation by background electrons, which may be due to the defects generated during low-temperature growth, a condition necessary for growing higher indium composition InGaN. The presence of high background electron concentration, most likely due to the low growth temperature, is suggested as the main obstacle for obtaining p-type conductivity in InGaN with indium composition larger than 0.35. The Mg-acceptor level was estimated

to be about 43 meV for Mg-doped $In_{0.35}Ga_{0.65}N$ alloys, which is roughly four times smaller than that in Mg-doped GaN [31.468]. A room-temperature resistivity as low as 0.4 Ω cm was obtained with a hole concentration of $\approx 5\times10^{18}\,cm^{-3}$ and hole mobility of $\approx 3\,cm^2/(V\,s)$ in Mg-doped $In_{0.22}Ga_{0.78}N$. The PL intensity associated with the Mg-related emission line was found to decrease exponentially with indium composition, which may be related to the incorporation of impurities. As stated above, higher temperature is preferred for growing high-quality InGaN while lower growth temperature is required for growing higher indium composition InGaN; thus it may be concluded that the major challenge for obtaining high-quality InGaN is to find a compromise value for the growth temperature.

The $In_{1-x}Al_xN$ alloy is also an important compound that can be grown lattice-matched to GaN, low-fraction AlGaN and InGaN. Due to their large spontaneous polarization, lattice-matched InAlN/GaN-based HFETs achieve significantly larger two-dimensional electrogas (2DEG) densities and consequently large current densities [31.469]. Owing to the high-index-contrast as well as possible lattice-matching between AlInN and GaN, high-quality AlInN/GaN multipair distributed Bragg reflectors have been achieved [31.470]. The bandgap of AlInN versus the Al composition has been investigated intensively; however, no consensus has been achieved for the bowing parameter due to complexities associated with the precise determination of the composition in AlInN alloys. By adopting a bandgap of ≈ 1.95 eV for InN, which is widely believed to be incorrect, a bowing parameter of 5.4 eV was obtained [31.471]. As mentioned earlier, precise information on the bandgap and alloy composition should be obtained for a fit to determine the bowing parameter. By considering the complications of the band structure of In-rich InAlN, including the Burstein–Moss shift, the nonparabolic conduction band, and the softening of the absorption edge, bandgaps of $In_{1-x}Al_xN$ with $x = 0.017–0.60$ were extracted from optical absorption data [31.472]. As demonstrated in Fig. 31.34, with 0.7 eV for the bandgap of InN, the bowing parameter was calculated to be 4.7 eV, which is reasonably close to the value of 4.96 eV obtained in [31.473]. Also noted is that the value of the bowing parameter is found to be sensitive to the bandgap used for AlN as well as whether the composition is determined from RBS or XRD measurements as a divergence was found between these two measurement techniques [31.450].

Similar to the case of InGaN, the indium incorporation in AlInN strongly depends on the growth temperature [31.474]. In-rich InAlN requires lower growth temperatures; however, lower growth temperatures reduce the AlInN crystalline quality and de-

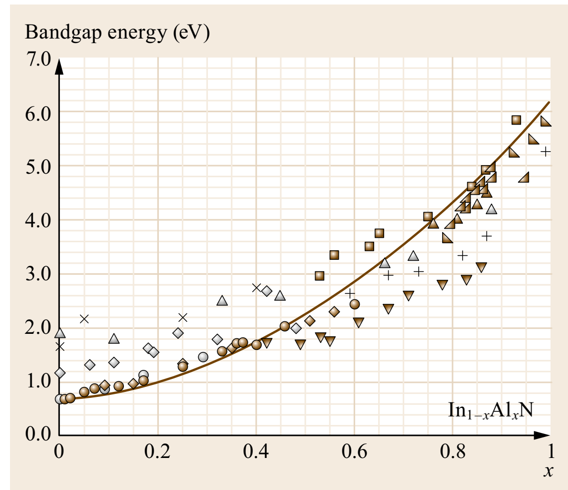

Fig. 31.34 Bandgap energies reported in the literature. A bowing parameter of 4.7 eV was obtained from the fitted *solid curve* with data. (After [31.472], courtesy of Dr. W. Walukiewicz)

teriorate the surface morphology. Transport data for InAlN are extremely scarce. The carrier concentration and the mobility of $In_{1-x}Al_xN$ for $x = 0.04$ were reported as $2\times10^{20}\,cm^{-3}$ and $35\,cm^2/(V\,s)$ respectively, and $8\times10^{19}\,cm^{-3}$ and $2\,cm^2/(V\,s)$ for $x = 0.25$ respectively [31.475]. Room-temperature resistivity and Hall measurements were conducted on In-rich and Al-rich AlInN layers respectively [31.476]. For In-rich AlInN with indium composition of 0.55 and 0.67, the electron concentration n is around 2×10^{19} and $1\times10^{20}\,cm^{-3}$ with associated mobilities around 5 and $7\,cm^2/(V\,s)$ respectively. The Al-rich films showed much higher resistivity, namely $\rho \approx 10^4$ and 10^8 Ω cm for Al composition of 0.66 and 0.72 respectively. These results are consistent with the trend that the mobility decreases substantially with an increasing Al mole fraction and increases with increasing In mole fraction, a close analogy to the parent compounds AlN and InN.

By alloying InN with GaN and AlN, the bandgap of the resulting alloy(s) can be expand from the bandgap of InN to that of AlN, which is from 1.9 eV (or ≈ 0.7 eV if we use the recently determined InN bandgap) to a value of 6.0 eV. The benefits of utilizing this quaternary alloy are that: (i) the bandgap of this quaternary can be changed while keeping the lattice constant matched to GaN [31.477, 478]; (ii) an independent control over interface polarization charges and bandgaps is possible, which can result in more uniform carrier distribution among quantum wells while maintaining sufficient electron confinement [31.479, 480]. The InGaN/GaN-based multiquantum wells have been extensively utilized for LED lighting; however, due to the

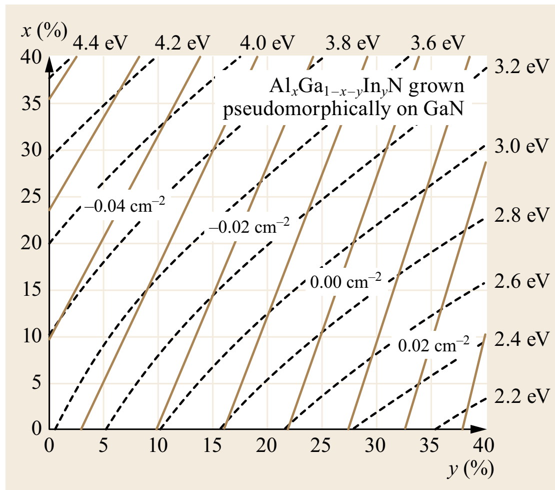

Fig. 31.35 Ga-face polarization charge (*brown*) and bandgap (*black dashed*) contours of quaternary $Al_xGa_{1-x-y}In_yN$ grown pseudomorphically on GaN substrates. (After [31.450], courtesy of Dr. E. Fred Schubert)

polarization charges at the InGaN/GaN interface, the electrons and holes in the quantum wells are separated at two ends of each quantum well due to the polarization charge (mainly of piezoelectric origin) induced electric field, which results in reduced electron-hole overlap and thus radiative recombination. Thus, the radiative recombination would depend on the quantum well width since different well widths result in different electric fields inside the well if all other parameters are fixed, which is the case for InGaN/GaN quantum well structures [31.481]. By utilizing unstrained quantum well layers with quaternary barriers, no emission energy dependence on width was observed due to the elimination of the piezoelectric field. By growing polarization-matched AlGaInN/InGaN LEDs, significant improvements have been achieved in terms of reduced forward voltage, reduced efficiency droop, and improved light-output power at large currents compared to conventional InGaN/GaN LEDs [31.480].

The bandgap and polarization charge versus the In and Al compositions have been calculated for AlGaInN as shown in Fig. 31.35, which clearly demonstrate independent control over the polarization charge and bandgap. However, among other difficulties brought about by the four-component systems, the optimal growth temperature is important to optimize and control, as Al-based compounds generally require higher growth temperatures, while In-based compounds require lower temperatures. Hence, the growth temperature will therefore govern the limits of In and Al incorporation into the AlGaInN quaternary alloy [31.478]. *Ryu* et al. [31.482] reported on optical emission in this quaternary system and AlInGaN/AlInGaN multiple quantum wells grown by pulsed metalorganic chemical-vapor deposition. A strong blueshift with excitation intensity was observed in both the quaternary layers and quantum wells, which was attributed to localization. This would imply that the structures are of inhomogeneous nature and/or presence of band-tail states indicative or early stages of material development and/or serious technological problems.

31.8 Doped GaN

Controlled doping in a broad range of concentrations in wide-bandgap semiconductors is very challenging for p-type varieties, as has been pointed out, for example, by *Walukiewicz* [31.483]. Simple substitution of elements such as C, Si, and Ge on the Ga sites and O, S, and Se on the N sites can potentially form shallow donors in GaN. Simple substitution of elements, such as Be, Mg, Ca, Zn, and Cd on the Ga sites and C, Si, and Ge on the N sites have the potential of forming relatively shallow acceptors in GaN. In practice, however, GaN n-type is achieved by using Si, Ge, and Se, the latter being not that common. On the other hand for p-type GaN only Mg has been successful but the level of hole concentration that can be achieved hit a ceiling of about $10^{18}\,cm^{-3}$.

Electronic and optoelectronic applications require n-type and p-type semiconductors. Even for high-quality GaN, grown by the many different processes (MBE, CVD, and HVPE), is unintentionally n-type doped, a phenomenon that is attributed to native defects (i.e., points defects, dislocation, stacking fault, V_N, antisites) and impurities (i.e., C, O, H) in GaN. Many potential p-type dopants attempted for incorporation into GaN cannot effectively compensate electrons in GaN and lead to p-type GaN. Hence, formation of p-type GaN is not straightforward. On the other hand, n-type doping of GaN is accomplished without major complications. This means that GaN p-type doping is the bottleneck to taking full advantage of the potential of GaN, especially in applications where both n-type GaN and p-type GaN are required, such as in optoelectronics.

The precursors, carrier gas, growth conditions, substrate material, among others, define the incorporation of impurities and imperfections in the crystal that result in the generation of defect-induced free carriers. De-

spite many decades of improvements in GaN technology, the residual electron concentration hovers around $1\times10^{16}\,cm^{-3}$. Unintentional impurities imply lack of control, which is undesirable. In the following subsections a succinct description of GaN n-type and p-type doping is presented. A detailed treatment of the topic can be found in [31.1].

31.8.1 n-Type Doping

In unintentional GaN samples with a low n-type background, n-type doped GaN with Si is a very well-founded practice for both MBE and MOCVD techniques [31.484]. Controllability of electron concentration $\approx 10^{17}$ to $2\times10^{19}\,cm^{-3}$ by varying the SiH_4 flow rate in MOCVD growth is possible [31.455]. With GeH_4 an order of magnitude higher electron concentration beyond what is feasible by Si is possible [31.485]. The Si ionization energy level in GaN is about 30 meV (dilution limit) and decreases as the doping level increases due to screening (see, e.g., [31.2, Chap. 5] for details). PL measurements in average-quality GaN yield a binding energy value of 22 meV [31.224]. Measurements on high-quality GaN layers grown on freestanding GaN wafers indicate (as determined by magneto-optical studies [31.486] and detailed analysis of the two-electron satellite transitions [31.487]) a binding energy of 30.18 meV.

Owing to the high solubility of Si ($10^{20}\,cm^{-3}$) in GaN, Si is suitable for group III nitride doping and it is the most frequently used. Carrier concentrations in Si-doped GaN in the range 10^{17}–$10^{19}\,cm^{-3}$ were observed, when silane (SiH_4) (used as an Si precursor) molar flow was varied 100 times. Also, Ge doping is well behaved. Ge solubility in GaN is in the range of 10^{17} to $10^{19}\,cm^{-3}$ when germane (GeH_4) (used as Ge precursor) molar flow was varied 100 times in MOCVD growth. Ge doping has produced materials with electron concentrations of 7×10^{16}–$10^{19}\,cm^{-3}$. More recently, *Wieneke* et al. [31.488] reported electron concentrations above $10^{20}\,cm^{-3}$ in nonpolar *a*-plane GaN epilayers grown by MOVPE on *r*-plane sapphire substrates using isobutylgermane (IBGe) as a Ge precursor. A linear electron concentration versus molar flow relationship for both SiH_4 and GeH_4 precursors was observed [31.218, 489]. However, Ge incorporation is less efficient (by one order of magnitude) than Si incorporation.

31.8.2 p-Type Doping

As noted above, p-type doping in wide bandgap semiconductors is challenging and elusive, and nitrides are no exception. p-Type GaN, for the fabrication of p-n junction LEDs, was first achieved by *Akasaki* and *Amano* [31.490] in MOVPE-grown Mg-doped GaN. Doping activation was attained on Mg-doped GaN via low-energy electron-beam irradiation (LEEBI) treatment. The Hall measurement data showed a hole concentration of $\approx 2\times10^{16}\,cm^{-3}$ with a mobility of $\approx 8\,cm^2/(V\,s)$ and a resistivity of $\approx 35\,\Omega\,cm$ at room temperature. *Nakamura* et al., with the same process that Amano used, obtained a hole concentration of $3\times10^{18}\,cm^3$, a mobility of $9\,cm^2/(V\,s)$, and a resistivity of $0.2\,\Omega\,cm$ at room temperature [31.491]. Soon thereafter, *Nakamura* et al. [31.492] developed a doping activation technique based on N_2-ambient thermal annealing at temperatures above 700 °C. After the thermal treatment, the resistivity of Mg-doped GaN films dropped from 1×10^6 to $2\,\Omega\,cm$ and the hole concentration and mobility were $3\times10^{17}\,cm^{-3}$ and $10\,cm^2/(V\,s)$ [31.492]. Nowadays, thermal activation is one of the most widely used techniques to active Mg in GaN. The thermal process is reversible with the GaN reverting to an insulating compensated state when annealed under NH_3, where the decomposed hydrogen from NH_3 was thus considered as the critical compensating agent during the annealing process under the NH_3 atmosphere.

A great deal of effort has been addressed to p-dope GaN and its ternaries by incorporating group II and group IV elements. So far, no other dopant has been as successful as Mg in converting GaN, AlGaN, and InGaN, with low Al and In mole fractions, to p-type materials. Needless to say, p-type doping in GaN and its ternaries remains a topic of interest both in terms of technological aspects and also at the fundamental level. In the case of the chemical vapor phase epitaxy technique [31.493], CCp_2Mg and MCp_2Mg are utilized for the source of Mg. Experimental results indicate CCp_2Mg is less volatile and its incorporation in GaN is more efficient at high temperatures, where a better GaN quality compared with the quality of GaN grown at lower temperatures is attained. Mg concentrations in p-type GaN films may be extremely high: $\approx 1\%$ of the host species. When substitutionally incorporated, only about 1% of the Mg atoms are ionized in GaN.

In Mg-doped GaN grown by MOCVD, the concentration of free holes at room temperature reaches its maximum value of about $10^{18}\,cm^{-3}$ for a Mg chemical concentration of about $3\times10^{19}\,cm^{-3}$, and it decreases with further increase of Mg concentration [31.494]. The activation energy of Mg acceptors in GaN and $Al_xGa_{1-x}N$ is in the range of 160–200 meV, which is larger than k_BT at 300 K and increases with Al fraction [31.495–499]. As a result, low conductivity of holes in p-type GaN and p-type $Al_xGa_{1-x}N$ is observed, degrading the performance of light emitters.

Because of the relevance of GaN-based optoelectronic devices, studies conducted to better understand the process and realize highly conductive p-type GaN and AlGaN are in demand, especially for the case of high Al-composition p-type AlGaN. Results on Mg-doped p-type $Al_xGa_{1-x}N$ with low Al content $0 < x < 0.27$ are available in [31.459, 500–502]. An activation energy as high as 310 meV was reported in [31.502] for $x = 0.27$. Demonstration of p-type conductivity in Mg-doped $Al_xGa_{1-x}N$ ($x = 0.35$) epilayers was reported by *Yu* et al. [31.503]. The influence of growth conditions on p-type conductivity was also investigated. The authors found that a proper V/III ratio and a relatively high growth rate were needed to improve the electrical characteristics of the p-type AlGaN epilayers. As a result of optimized growth conditions, a p-type resistivity of $3.5\,\Omega\,cm$ and a hole concentration of $> 5\times10^{17}\,cm^{-3}$ were attained.

Unlike layers grown by MOCVD, MBE-grown p-type GaN layers do not require postgrowth annealing, neither employing activated nitrogen nor employing ammonia as the nitrogen source [31.504]. Mg-doped GaN layers grown by RMBE with ammonia as the nitrogen source exhibit p-type conductivity without any postgrowth treatment [31.496], which is very advantageous. In the case of GaN growth by MBE, Mg incorporation depends on the stoichiometry, the polarity of the growing surface [31.505, 506], the substrate temperature, and the growth rate [31.507–509].

Codoping for Improving p-Type Conductivity

As mentioned above, p-type GaN is challenging and low resistivity is difficult to achieve. One of the reasons is the compensation effect due to the low solubility and the low activation rate owing to the deep energy level of the acceptor. The acceptor energy level is very deep (about a few hundred meV) relative to room temperature ($\approx$ 25 meV), for instance, GaN:Mg (200 meV) and AlN:C (500 meV). A 500 meV-deep acceptor if activated would yield one hole for every 10^6 acceptors at room temperature. To attain low-resistivity in wide bandgap semiconductors, the solubility of dopants should be increased while their compensation avoided. Also, the activation rate of the carriers and their mobility should be increased by reducing the energy level of the acceptors and the scattering rate of the carriers. As a response to mitigate the aforementioned concerns an interesting and promising method called codoping was proposed [31.510]. The codoping method is based on the idea that both n and p-type dopants are provided simultaneously under thermal nonequilibrium crystal growth conditions during MBE or MOCVD. The theoretical foundation of the codoping method was provided by *Reiss* et al. [31.511] [31.512] during the early stages of Si and Ge development using solution theory. Codoping can result in an enhancement of equilibrium solubility of the dopants (problematic for p-type impurities in GaN), low ionization energies, and also might affect the carrier mobility. All the above-mentioned benefits are relevant to GaN. Experimental results on codoping in GaN and in AlGaN are reported in [31.513–517] and [31.513, 518] respectively.

The hole concentration was observed to be enhanced in p-type GaN:Mg codoped with oxygen donors wherein the hole concentration increased linearly from 8×10^{16} to $2\times10^{18}\,cm^{-3}$ with increasing oxygen dopant partial pressure. An increment of 3–5 times in the hole concentration resulted for a fixed oxygen partial pressure during growth of p-type GaN:Mg. Unlike the theoretical predictions, for reduced formation energy/increased solubility, when Si was codoped with GaN:Mg, the hole concentration remained constant [31.510].

Use of Superlattices for Improving p-Type Conductivity

Another promising method to get higher acceptor activation and lower resistivity is by using $Al_xGa_{1-x}N$/GaN doped superlattices [31.519–521]. The idea of using AlGaN/GaN heterojunctions for enhancement of p-type doping has been proposed as a technique to increase the average hole concentration [31.521–523]. Increased hole concentrations at room temperature through the use of AlGaN/GaN superlattices have been reported in the literature [31.524–526]. The mechanism for hole enhancement is the periodic oscillation of the valence band edge. Acceptors are ionized where the band edge is far below the Fermi energy and the resulting holes accumulate where the band edge is close to the Fermi level, forming a confined sheet of carriers. Although the free carriers are separated into parallel sheets, their spatially averaged density will be much higher than in a simple bulk film. High electric fields due to both spontaneous and piezoelectric polarization within the strained AlGaN layers strongly impact the band bending within the superlattice. The fields created by the superlattice/carriers exhibit sawtooth variation in the band diagram. The hole concentration expected from an AlGaN/GaN superlattice was calculated in [31.523].

The spatially averaged measured hole concentration and mobility for the Mg-doped $Al_{0.2}Ga_{0.8}N$/GaN superlattices with equal thickness, L, of the GaN and AlGaN layers (superlattice period $2L$) exhibit approximately constant mobility of $10\,cm^2/(V\,s)$ for $2\,nm < L < 14\,nm$ and an average hole concentration which peaks at $2\times10^{18}\,cm^{-3}$ for $L \approx 8\,nm$. Further improvements of the p-type conductivity of the lattice were obtained by minimizing the ionized and neutral impurity scattering mechanisms via doping that maximize the separation of

the dopants (ionized scattering centers) from the multiple two-dimensional hole gas (2DHG) sheets.

Samples incorporating modulation-doped (MD) and shifted-modulation-doped (SMD) superlattices have been shown to have superior electrical properties compared to uniformly doped (UD) samples, especially at low temperatures [31.525].

After all the efforts invested to achieve high-p-type doping levels in GaN and AlGaN, the maximum attainable doping level is still a limitation for optoelectronic devices, particularly for shorter wavelength devices such as solar-blind (≈ 290 nm) detectors, UV LEDs, LDs and even visible LEDs, which need p-type AlGaN with high-Al composition and large hole concentration for efficiency retention. For example, a UV LED using an AlGaN p-n junction with an emission wavelength shorter than 290 nm can only give submilliwatt or milliwatt power [31.527].

31.9 Defects in GaN

Regardless of the degree of perfection of the material, defects are always present in semiconductors, particularly during the early stages of development. In fact, defects in complex semiconductors may never be fully solved [31.528]. By having to be grown on nonnative substrates due to the prohibitively expensive bulk material, GaN layers exhibit a wide variety of defects. Extended defects, such as threading dislocations and staking faults, and intrinsic defects, such as point defects and vacancies, among many others (for an in-depth discussion on defects the reader is encouraged to read [31.2]), may coexist in GaN eptaxial layers. In order to improve the quality of the layers a good deal of effort still is devoted to attaining material perfection via heteroepitaxy. However, after decades of research and investigations, both extended and intrinsic defects are still present to varying degrees. Nevertheless, defect densities have been reduced to a level where the realization of commercial devices based on GaN is feasible.

In what follows we center our discussion on two different kinds of defects. Because of their importance in the determination of electrical properties, we address the intrinsic point defects followed by staking fault defects, which is particularly important in nonpolar GaN for optoelectronic applications.

31.9.1 Points Defects

The importance of intrinsic point defects in nitrides is due to their role in determining the electrical and optical properties of the material, as well as their influence on the material behavior in various processing steps such as ion implantation and thermal annealing. Point defects are created in semiconductor materials during growth, where their formation is governed by thermodynamics and growth kinetics. Because GaN is unintentionally n-type, it is assumed that an acceptor-like defect is ionized and negatively charged as the Fermi level is close to the conduction band. Then, the important question is what is the source of these negative charges? To answer this question we need to take into account two factors in our analysis, namely the effect of incorporated impurities and charged defects. Both entities may behave like n or p donors. In GaN, point defects are identified as nitrogen vacancy (V_N), gallium vacancy (V_{Ga}) and Ga interstitial. A large variety of analysis tools have been used to study point defects and their impact on GaN physical properties. Some of the utilized techniques are photoluminescence (introduced already in Sect. 31.6), deep-level transient spectroscopy, minority carrier lifetime measurements, positron annihilation, electron paramagnetic resonance (EPR), and optically detected magnetic resonance (ODMR).

Deep-level transient spectroscopy (DLTS) [31.529, 530] is a popular method to get insight into electrical characteristics of point defects; both donor- or acceptor-like traps. The drawback of DLTS is its incapability to give local information or the chemical nature of the defect centers. These shortcomings can be alleviated to some extent if DLTS studies are realized in conjunction with systematic studies, such as irradiation damage and measurements in a pressure cell. Even though DTLS is a mature method, the characteristics of defects as analyzed by DLTS for GaN are widely scattered. A large dispersion in the basic reported parameters of the defects in GaN hide their genesis and nature. As many as eight point defects active in DLTS, some of which may be the same due to the aforementioned dispersion, have been reported in n-type GaN, and only one in p-type GaN.

GaN samples prepared by OMVPE on sapphire substrates have been investigated by DLTS by several groups [31.531–533]. Typical defect states are termed as E1, E2, E3, E4, and E5 with energy level in the range of 0.14–0.27, 0.49–0.598, 0.62–0.67, 0.81–0.85, and 1.07–1.44 eV respectively. The concentration of the same defects are in the ranges of 1.6×10^{13}–7.7×10^{14}, 2×10^{13}–1.2×10^{15}, 1.6×10^{14}–3.8×10^{14}, 1.5×10^{14}–2×10^{15}, and 2.4×10^{14}–3.34×10^{15} cm^{-3} for E1, E2, E3, E4, and E5 traps respectively. An illustration of various defect states detected in DLTS and photoemission tran-

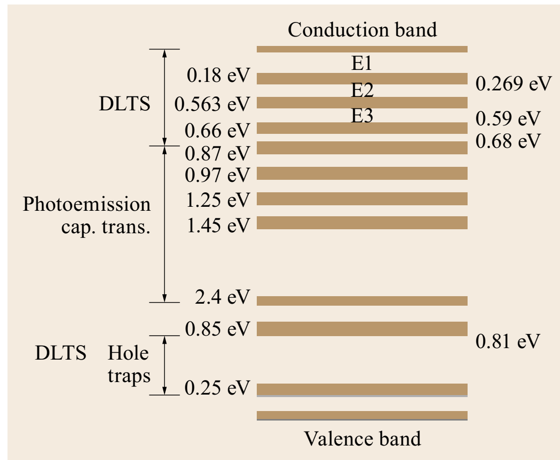

Fig. 31.36 Various deep levels within the gap energy of GaN grown by OMVPE, as observed by DLTS and photoemission transient spectroscopy. The two hole trap energies are with respect to the valence band maximum. (After [31.1])

sient capacitance methods are schematically shown in Fig. 31.36.

Minority carriers are widely trapped by defects, easily reducing their lifetime and diffusion length in the material. Minority carrier lifetime measurements are of importance in the evaluation of device performance and assessment of the material quality. Minority carrier lifetimes, τ, can be estimated using diffusion length L and measured mobility μ, through the expression $L = \sqrt{D\tau}$, where the diffusivity, D, and τ are related via the Einstein relation. The minority hole diffusion length can be derived from the line-scan electron beam-induced current (EBIC) measurements [31.534, 535]. The measurements are carried out at a distance from the material/substrate interface i. e., the GaN/sapphire interface [31.536]. In this kind of measurements the electron beam (positioned perpendicular to the sample edge) is moved from the vertical wall of the Au/n-GaN Schottky barrier toward another Au contact. The diffusion length L, can be obtained from the EBIC current decay versus distance from the edge of the Schottky contact (for distances $> 2L$). The methodology for diffusion length extraction can be found elsewhere [31.534, 535]. TEM and DLTS results clearly indicate that the defect density is reduced away from the GaN/sapphire interface. Then it is reasonable to evaluate the minority carrier lifetime as a function of distance away from the interface. Comparing the depth dependence of the dislocation density with that of the diffusion length, it is observed that the decrease in minority carrier diffusion length toward the GaN/sapphire interface is correlated with an increase in the dislocation density. The minority carrier diffusion length at a certain distance from the interface agrees well with the spacing between two adjacent dislocations, provided that the sample thickness is four times the minority carrier diffusion length. In which case, no sample thickness correction is needed because the sample can be construed as bulk [31.514].

Certain intrinsic defects (point defects/vacancies) can be studied with nondestructive positron annihilation spectroscopy (PAS) [31.537–558], which together with theoretical calculations provides a means to deduce both the nature and the concentration of the vacancies in the material. Parametric measurements with varying temperature provide information on the charge states of the detected vacancies. Positrons impingent onto a sample can get trapped in and localize neutral and negative vacancies due to the missing positive ion core. This positron lifetime and the momentum distribution of the annihilating positron-electron pair (Doppler broadening) represent the observable changes that the method relies on. Positron studies have been performed in nitride semiconductors for decades after the pioneering work of *Saarinen* et al. [31.559], which resulted in the identification of Ga vacancies in bulk GaN crystals. Many others studies were carried out [31.545, 547–549, 551–553, 555, 558]. The following is the most relevant data, regarding vacancies in GaN, InN, and AlN [31.540].

Vacancies in GaN

Most of the average positron lifetimes (τ_{ave}) measured in a variety of thick bulk or quasibulk GaN samples are above the bulk lifetime of 160 ps [31.560] for temperatures below 240 K indicating that positrons are annihilated as they get trapped at vacancy defects. The defects are identified as Ga vacancies by the second lifetime component $\tau_2 = 235 \pm 10$ ps deconvolved (separated) from the lifetime spectra [31.559, 561] as demonstrated in Fig. 31.37 [31.562].

The temperature dependence of τ_{ave} in O-doped and undoped GaN samples grown by HVPE at low temperatures points to an enhanced positron trapping at Ga vacancies, indicating that Ga vacancies are negatively charged. The lifetime, $\tau_{ave,}$ in GaN grown by the high nitrogen pressure (HNP) method indicates that nonopen volume defects, identified as MgGa-acceptors [31.559, 560], act as shallow traps competing with Ga vacancies in positron trapping at low temperatures.

No evidence of, or very low levels of, shallow traps in undoped and O-doped GaN grown by HVPE [31.561, 563, 564] set Ga vacancies as the dominant intrinsic acceptor defects in n-type GaN [31.565] (Fig. 31.37). The above-mentioned assessment is supported by a very good agreement between the vacancy and total acceptor densities, acquired by combining PAS and temperature-

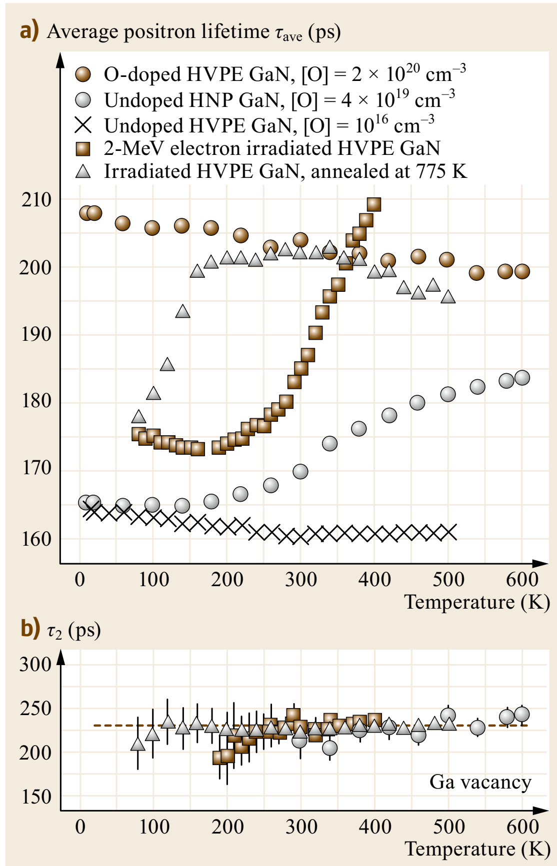

Fig. 31.37 (a) Average positron lifetime as a function of temperature. Vacancies are present when the average positron lifetime is above the bulk lifetime of $\tau_B \approx 160$ ps. The temperature dependence of the average positron lifetime evidences the different effects of negative charge of both the vacancies and acceptor-type impurities. **(b)** The second lifetime component extracted from the lifetime spectra, $\tau_2 \approx 235$ ps. This component is attributed to Ga vacancies or Ga-O complexes. (After [31.562], courtesy of Dr. F. Tuomisto)

dependent Hall measurements [31.564]. Experimental data show the Ga vacancy as being the most important compensating acceptor (over four orders of magnitude of the intentional oxygen doping) [31.563]. Ga vacancies in as-grown and highly O-doped GaN were identified as V_{Ga}–O_N pairs [31.563, 566], while isolated Ga vacancies are generated in electron irradiation experiments [31.561, 567]. Second lifetime components (Fig. 31.37b) are similar in grown O-complexed (V_{Ga}–O_N) and in isolated Ga vacancies, in good agreement with theory [31.563].

The τ_{ave} in as-irradiated (2 meV at room temperature) samples exhibit the coexistence of a high-Ga vacancy concentration and irradiation-induced negative ions. Annealed at 775 K, irradiated samples display a change in threshold temperature at which positrons can escape from negative ions (Fig. 31.37a). This can be interpreted as a change of positron-defects binding energy, i. e., change in the charge state of negatives ions, from 2^- to 1^-. Results from electron irradiation experiments [31.561, 567] showed a migration barrier $E_M = 1.8 \pm 0.2$ eV for isolated Ga vacancies. On the other hand, in HVPE GaN samples annealed at high temperatures and high nitrogen pressure, a redistribution of the V_{Ga}-O_N pairs [31.566–569] was observed, giving a way to calculate the binding energy of the pair as $E_B = 1.6 \pm 0.2$ eV, which is in good agreement with theoretical results [31.378, 379]. Studies on the effect of polarity (N-polar, Ga-polar, and nonpolar in both homo- and heteroepitaxy by HVPE) on Ga vacancies provided further understanding of the V_{Ga}–O_N pair formation [31.560, 570–572]. Experimental results indicate that Ga vacancies are created thermally as isolated defects in GaN growth at high temperatures in both HVPE and HNP methods and that the formation of V_{Ga}–O_N complexes is determined by the fraction of Ga vacancies that remain after the cool-down process.

O incorporation and subsequent vacancy depends on GaN growth polarity, owing to the different surface sticking coefficients of oxygen on different polarities. This effect is not observed in Si doping as the binding energy between Si donors and Ga vacancies is weaker, due to a larger distance between a Ga vacancy (acceptor) and substitutional Si (donor) [31.573].The above-mentioned results show that Ga vacancies act as dominant compensating centers in n-type GaN. In p-type GaN, because of its acceptor nature, Ga vacancy formation is energetically unfavorable. Studies of N vacancies (V_N) by PAS are useless owing to the small open volume generated by N vacancies. However, evidence of V_N-Mg_{Ga} complexes was obtained by PAS in Mg-doped (p-type) GaN grown by MOCVD [31.574, 575]. In [31.561] it is reported that N vacancies in p-type GaN samples that are electron irradiated (0.5 meV) behave like isolated neutral vacancies. Vacancies in both n-type and p-type GaN are a few percent of the doping densities. In n-type GaN, vacancies are dominantly compensating centers. On the other hand, in p-type GaN, other defects and impurities, such as hydrogen, play a more relevant role from the point of view of compensating centers.

The effect of growth conditions in thin-film (MBE, MOCVD), and bulk or quasibulk (HVPE)-grown samples were also studied by slow positron beam. Showing that stoichiometry has a very strong impact on Ga vacancy formation, the richer the growth in N and the higher the growth temperature, the higher the Ga va-

cancy concentration. This indicates that Ga vacancy is ruled by the thermodynamics of the reaction, but not necessarily by the growth method. The latter statement is supported by the results obtained from samples grown with various polarities [31.560, 570, 572, 576], where it is observed that the sticking coefficient and density of O on different growing surfaces determine the formation of Ga vacancies.

Vacancies in InN

InN layers of different thicknesses grown on sapphire by MBE [31.577, 578] have also been studied by PSA. The low electron-momentum parameter S and the high electron-momentum parameter W were calculated at room temperature to evaluate the positron annihilation with the valence electrons and the annihilation contribution from the core electrons, respectively [31.579]. In the context of the S parameter, the larger the value the higher the vacancy density in the layer. Regardless of the sample thickness, a value of $S = 0.48$ is registered for all samples for positron implantation energies in the range of (E) 0–1 keV (0–5 nm) (Fig. 31.38). For higher values of E and up to 30 keV, S remains constant. The S value and the extent of E values for which S remains constant is a characteristic of each sample. Note that for thinner InN layers, S decreases when the layer thickness increases. This is an indication of improvement in the quality of InN layer growth. Close to the InN-sapphire interface, the parameter S starts to decrease, approaching a value of 0.41, due to the increasing fraction of positrons annihilating.

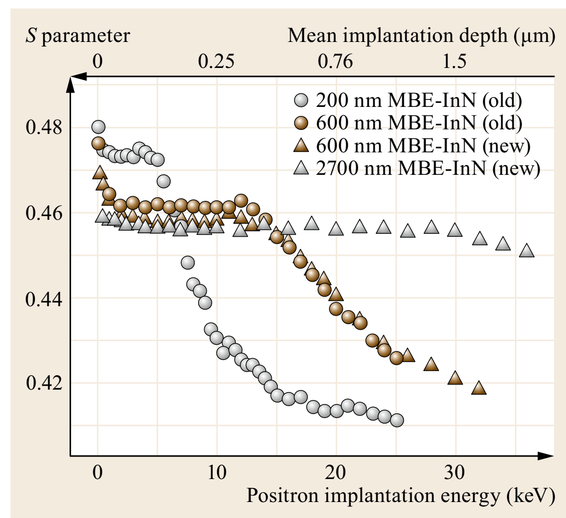

Fig. 31.38 The S parameter measured as a function of positron implantation energy in selected MBE-grown InN layers. *Old* from [31.577], *new* from [31.578]. (After [31.562], courtesy of Dr. F. Tuomisto)

Indium vacancy concentration is typically not sufficient to compensate electron conductivity in n-type InN. Indium vacancies are, as evaluated by electron mobility, effective scattering centers in InN. Improved electron mobility for thicker layers (up to 1 μm) suggest that In vacancy concentration is dramatically reduced [31.577]. An interesting point is that In vacancy formation does not seem to be promoted by the growth stoichiometry in MOVCD grown InN [31.580] and the same has been suggested to hold for MBE growth as well [31.581].

Vacancies in AlN

Average positron lifetime as a function of the temperature was measured in bulk AlN [31.582] grown by physical vapor transport (PVT) [31.172] and in thin layers grown heteropitaxily on various substrates by MBE [31.391] and MOCVD [31.583]. Qualitatively, the temperature dependence of τ_{ave} in AlN is similar to that on GaN. Any deviation in τ_{ave} as function of temperature in GaN and AlN can be interpreted as a competition between the negative ion type defects (shallow traps with no open volume) and vacancy defects for trapping positrons.

Taking an Al vacancy trapping coefficient of $3 \times 10^{15}\,cm^3\,s^{-1}$ at 300 K and its temperature dependency, a lower limit for Al vacancy concentration is estimated as $1 \times 10^{17}\,cm^{-3}$ at 600 K. On the other hand, negative ion concentration is $4 \times 10^{18}\,cm^{-3}$ from data taken below 300 K, which indicates that negative ions are the dominant acceptor centers in AlN. A comparison between impurity and negative ion concentrations suggests that negative ions are related to oxygen incorporation and not to carbon impurity as is usually the case. In contrast with the case in GaN, O in AlN is predicted to behave as a negative charge.

In thin AlN films PAS results are similar to those acquired in GaN and InN thin films. Larger AlN-substrate mismatch and higher growth temperatures lead to higher Al vacancy concentrations. Also the growth stoichiometry effect is more notorious at very high V/III ratios. Measurements as a function of temperature provide valuable information on the charge states of the detected defects. Briefly, group III sublattice vacancies are common defects in all the group III nitrides. They compensate donors either by forming vacancy-impurity complexes or by providing deep states for electrons. Additionally, the presence of N vacancies was observed.

31.9.2 Extended Defects

As mentioned in Sect. 31.7 GaN-based LEDs and lasers rely for their functionality on QWs, which are formed,

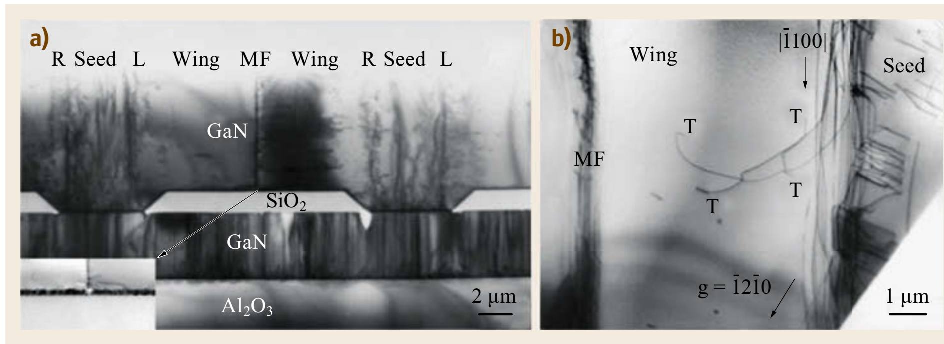

Fig. 31.39 **(a)** Cross-sectional TEM image showing defect distribution in a LEO layer. The seeds, left (L) and right (R) wings, meeting fronts (MF) of two wings, dielectric (SiO_2) layer and original GaN deposited on the Al_2O_3 (seed layer) are indicated. The *inset* shows a formation of a small void where two wings originally meet each other; **(b)** Plan view of the laterally overgrown area showing a meeting front of the two wings (MF) and one wing with a small part of the seed on the *right-hand side* of the image. The indicated threading parts of the dislocation, which originate either at the interface with the substrate or at some obstacles in the seed, are indicated as T. (After [31.584], courtesy of Dr. Zuzanna Liliental-Weber)

basically, by sandwiching a semiconductor material layer (GaN-based active region) with layers of semiconductor material with larger bandgap. On the other hand, because of economical, practical and functional reasons, the material for GaN-based optoelectronic devices is usually grown on SiC (for high-intensity LEDs) and sapphire substrates (note that the improved quality of GaN grown on Si substrates paved the way for high-brightness LEDs, which already made it into the marketplace); the latter is of low cost and light-transparent (from UV to IR). The lattice mismatch between the epitaxial layer and the substrate result in high-strain fields, which in turn lead to a high density of extended defects, i. e., threading dislocations (TD) and staking faults (SFs). Residual strain is also present in epitaxial layers upon cool-down due to the difference in temperature expansion coefficients. In fact the tensile strain when grown on SiC and Si leads to cracking, which must be addressed by strain engineering during growth.

Extended defects do affect device performance. TDs can act as both scattering centers and nonradiative recombination centers lowering either or both carrier mobility [31.585] and quantum efficiency [31.586]. The SFs are linked to high leakage current [31.587]. In short, extended defect density needs to be decreased in order to attain better device performance. A well-known method to decrease the defect density, for GaN growth on *c*-plane, is the epitaxial lateral overgrowth method (ELO) [31.588–590] (Fig. 31.39), which has been developed [31.591–593]. This approach yields a much lower density of defects (SF $\approx 1\times10^4\,\mathrm{cm}^{-1}$), especially those that propagate along the growth direction. The ELO technique is also used to grow GaN along the semipolar and nonpolar directions.

When group III nitride samples grown on *c*-plane sapphire are heavily doped to produce n-type GaN, structural defect formation occurs. High-resolution transmission electron microscopy (HRTEM) investigation has revealed that these defects are small dislocation loops (in the range of few nanometers) associated with extrinsic SFs. This problem can be mitigated with the use of Ge doping instead of Si, as discussed below. The demonstrated superiority of Ge doping compared to Si, on GaN layers on *c*-plane sapphire, in terms of achievable free-carrier concentrations (up to $2.9\times10^{20}\,\mathrm{cm}^{-3}$), surface smoothness, and reduced layer stress, has been reported in [31.485]. The authors observed a reduction in tensile stress for any Ge doping level, which could lead to a reduction of crystal defect density at high doping levels. On the other hand and in contrast with the structural defects formation in GaN heavily doped with Si, TEM investigations on Si-doped and undoped GaN samples grown by MOVCD on the (11−20) plane of sapphire revealed an improvement of the GaN layer quality with Si doping. For a Si concentration of $3\times10^{18}\,\mathrm{cm}^{-3}$ dislocation density decreased from $5\times10^{9}\,\mathrm{cm}^{-2}$ (undoped sample) to $7\times10^{8}\,\mathrm{cm}^{-2}$ [31.594]. Also, a correlation between the Mg doping level and SF concentration in highly Mg-doped *c*-plane homoepitaxial GaN layers was found. As the Mg concentration increased from 2×10^{18} to $5\times10^{19}\,\mathrm{cm}^{-3}$, the density of small, 3−10 nm-sized, SFs increased [31.595].

A scheme, which overcomes ELO limitations to a great extent, is the nanoheteroepitaxy (NHE) as shown schematically in Fig. 31.40. NHE has the potential

to eliminate defects more efficiently than conventional ELO. In the NHE technique coalescence would occur at a nanodimension scale reducing subsequent overall strain for minimal defect propagations. The NHE growth process begins with the definition of a two-dimensional array of e.g., 10–300 nm-sized nucleation islands on a substrate. It is then followed by a selectively grown epitaxial material vertically on the islands (in the case of AlN/SiC template, AlN array is generated with lithography followed by etching). What follows is the lateral overgrowth to achieve coalescence as indicated in Fig. 31.40. In contrast to the millimeter scale of patterns in ELO, patterning is in the nanometer scale in NHE, which allows for stress in the NHE sample to decay exponentially away from the heterointerface. The characteristic decay length is proportional to the diameter of the island. According to the NHE theory, a mismatch dislocation formation can be eliminated from materials systems with a lattice mismatch in the range of 0–4%. For a higher mismatch, defects are probably unavoidable, such as the case for GaN on Si (20% lattice mismatch); however, NHE may still result in a significant reduction in the local defect density.

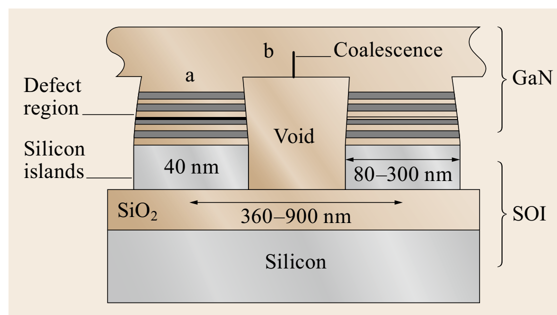

Fig. 31.40 Patterned silicon-on-insulator (SOI) substrate with islands created in the upper Si layer. The selective growth of GaN is also illustrated. A defected region is located at the heterointerface. *Point* a corresponds to selective growth of islands on a patterned substrate. *Point* b corresponds to the case where lateral epitaxy has been performed already. (After [31.596])

31.10 GaN-Based Nanostructures

At the nanometer scale, semiconductor structures exhibit novel electronic and optical properties, primarily owing to the dimensions that are comparable to the length of intrinsic processes (Fig. 31.41). The aforementioned novel properties are observed in GaN devices based on quantum wells [31.597–601], nanowires [31.601–605], or nanodots [31.606, 607]. In addition to the common issues related to conventional semiconductors such as band discontinuity, and dopant and carrier redistribution, polarization effects have to be taken into account in GaN devices. Polarization field effects may be in some cases desirable as in HFETs. But intense polarization fields foster an undesirable effect, the stark effect, which reduces the internal quantum efficiency in quantum confined structures. To mitigate the polarization effect, a quaternary alloy, InGaAlN, is used to neutralize the strain-induced component of the polarization field. Spontaneous polarization can be avoided by growing the heterostructure on $(1\bar{1}00)$ (*m*-plane) or $(1\bar{2}20)$ (*a*-plane), which represent the nonpolar planes.

31.10.1 Quantum Wells

As already discussed, the polarization-induced fields can drastically reduce the oscillator strength (Sect. 31.6.1, *Free Exciton in GaN* and Sect. 31.6.2, *Bound Exciton in GaN* for details on oscillator strength concept) for the ground-state optical transition [31.609–611]. The observed Stokes shift in two-dimensional (2-D) systems such as QWs [31.612, 613] is partly due to polarization effects. In this subsection we focus on the impacts of the piezoelectric effect and how to minimize them by manipulating well size and the crystal orientation. In multiple quantum wells

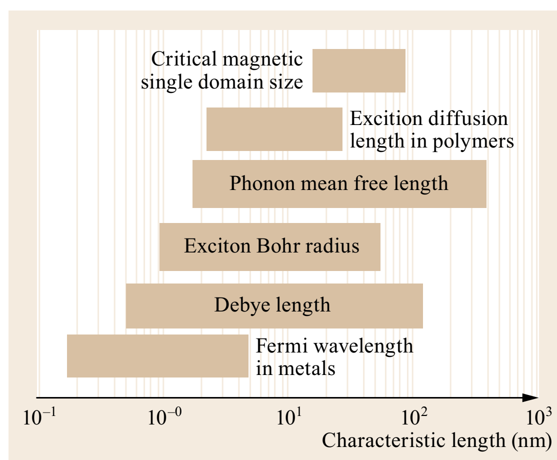

Fig. 31.41 Some of the well-known processes taking place in a semiconductor. Indicated characteristic lengths at 300 K go from tens of nanometers to hundreds of nanometers. The exciton Bohr radius is the most critical parameter in optical processes. (After [31.1])

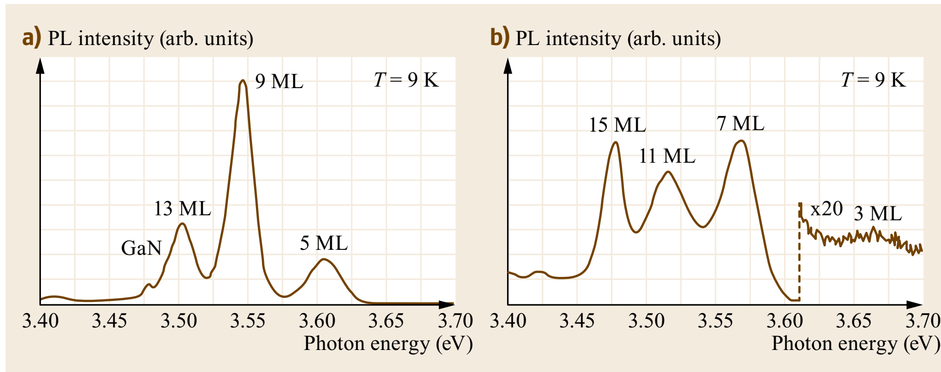

Fig. 31.42a,b Photoluminescence spectra at 9 K of GaN/$Al_{0.11}Ga_{0.89}N$ single QW. **(a)** corresponds to series A, **(b)** corresponds to series B. Note that in **(a)** the GaN buffer layer emission at 3.478 eV. (After [31.608], courtesy of Dr. N. Grandjean)

(MQWs), polarization effects manifest themselves as a redshift excitonic transition peak position [31.614, 615]. The effect can be compensated (blueshifting) by making the well size small enough to induce quantum confinement. The balance between redshift and blueshift is attained at a well thickness of 2 nm or less ($\approx$ 10 monolayers – MLs). The effect of QW thickness on the low-temperature photoluminescence spectra was studied by *Grandjean* et al. [31.608]. A single QW with 50 Å-thick $Al_{0.11}Ga_{0.89}N$ barrier layers grown by ammonia MBE were used. The data were from two samples: sample A consisting of 5, 9, and 13 ML well width, and sample B consisting of 3, 7, 11, and 15 ML width. PL spectra at 9 K are shown in Fig. 31.42.

It is evident from Fig. 31.42b, for the samples therein in particular, that the balance between the blueshift due to the confinement and the redshift, a consequence of the polarization effect, takes place at a QW thickness of 15 ML ($\approx$ 4 nm). The latter is wider than the values reported by other studies where a barrier layer with higher Al content was used. It is not necessarily a discrepancy and it may be because at a higher Al content the polarization effect is larger, which means the larger redshift needs to be compensated by a larger blueshift afforded by thinner QWs. Similar studies on AlGaN/GaN quantum wells grown by MOCVD but with high Al content (50%) in the barrier layer have been reported [31.616]. PL transition energies (not shown here) display a clear dominant transition from a redshift of 100 meV for a 4 nm QW width to a blueshift of 300 and 600 meV for QW widths of 2 and 1 nm respectively. The difference among the QW widths reported for the redshift-blueshift crossover, is mainly due to a larger than expected Al mole fraction in the PL reference samples and the growth technique, which may limit to some extent the heterostructure quality, particularly in terms of different degrees of localizing potentials. In the GaN system, the barrier thickness redistributes the polarization difference between wells and barriers, and thinner barrier layers were found to lead to larger blueshifts [31.600]. A point worth noting is that the trend of the electric field dependence on the barrier layer thickness can be found by using simple electrostatic calculations. However, not only piezoelectric-induced polarization, but also spontaneous polarization should be taken into account.

Nitrides are usually grown heteropitaxially on the basal plane of sapphire and SiC as well as Si substrates. Under normal growth conditions, nitrides assume wurtzite crystal structures, which have a hexagonal symmetry and a polar axis, c-axis [0001], along which both piezoelectric and spontaneous polarization are manifested. For optoelectronics, the ideal situation could be to grow nitride layers on nonpolar planes, i. e., $[1\bar{1}00]$ (m) and $[11\bar{2}0]$ (a) planes, in which case the polarization-induced shift would be eliminated, or at least the effect of the polarization-induced field associated with Stark shift could be suppressed. However, the inconvenience with nonpolar nitrides has to do with their film quality, which is lower than for those grown on c-planes. The most intensively investigated nonpolar directions are the $[1\bar{1}00]$ m-plane [31.617, 618] and the $[11\bar{2}0]$ a-plane [31.619, 620], which are free of polarization-induced internal electric fields along the growth direction.

At the present time, a-plane GaN is routinely grown on $(1\bar{1}02)$ or $(10\bar{1}2)$ r-plane sapphire by both MBE [31.619, 621] and MOCVD [31.618, 622–624]. However, heterostructures grown on a-plane, as well as the other nonpolar orientations, such as the m-plane, suffer from large stacking fault densities due to the low formation energy, making the radiative recombination at the desired wavelength relatively weak (this correction is a matter of style). Effects of systematic variation of well width on GaN/$Al_{0.16}Ga_{0.84}N$ quantum wells with a fixed 10 nm-thick barrier layer and 10-period a- or c-plane MQWs regrown by MBE on MOCVD-grown GaN/r-plane sapphire templates was investigated. Because of the absence of a polarization-

induced field, *a*-plane MQWs showed enhanced recombination efficiency as compared with *c*-plane wells, even though the *a*-plane variety presented a higher dislocation density [31.625]. It should be pointed out that this limited comparison does not necessarily hold in general.

31.10.2 Quantum Dots

In semiconductor quantum dots (QDs) electronic states are spatially localized and the energy is fully quantizied for all three directions. The atomic-like density of states near the bandgap is higher than in three-dimensional (3-D) and 2-D systems, leading to relatively high efficiency optical transitions. The latter is of great interest in terms of its potential in light emitting applications and optical sensors. The caveat of course is the carrier transport, which is impeded as well. Another interesting characteristic of the QDs is they are less sensitive to thermal perturbations, due to confinement, which is important for thermal stability of devices. Also, because the carriers are strongly localized their migration toward nonradiative centers such as dislocations outside of the dot region is somewhat inhibited [31.626].

Assuming good uniformity and control over the shape, quantum dots present some advantages as compared with QWs. Among them are a sharp energy level transition leading to reduced lasing thresholds, tunable bandgaps, and additionally reduced defects in nitrides. As in quantum wells, the optical properties of group III nitride QDs are assessed via photoluminescence. There is not an established consensus on the spectra emitted by GaN-based QDs. Published data indicate PL peak energies from 2.15 to 3.9 eV, depending on sample and temperature. QDs exhibit strong, albeit broad, PL intensity peaks with energies ranging from 2.6 to 3.9 eV (Fig. 31.43). The spread in the spectrum is most likely due to the divergence in dot size and shape.

As mentioned already, quantum confinement shifts the effective bandgap to higher energies. The amount of energy shift depends on the size and shape of the QDs, as well as the material optical properties of both the QD and its surrounding matrix. For small dots (disk, cubic, or sphere-like shape) of few nanometers in size, confinement energy is very sensitive to the dot size, becoming lower and less sensitive to the dot size for large-size quantum dots. Depending on the dot shape, confinement energy may change from 20 meV to 1 V for dot size from 2–10 nm [31.627].

Because of the relevance of strain-induced effects on group III nitrides, it should also be taken into account in QDs. In GaN QDs grown on $Al_xGa_{1-x}N$ and $In_xGa_{1-x}N$, which in turn is grown on GaN, strain is compressive, leading to a blueshift in the bandgap. For

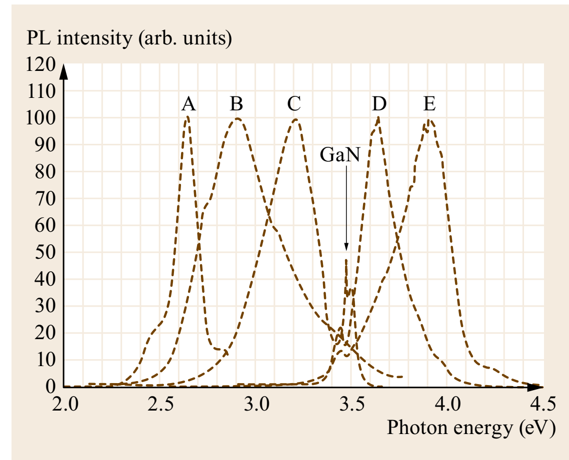

Fig. 31.43 PL spectra of GaN/AlN QD samples grown by MBE on different substrates and under different conditions. Samples A and B were grown on Si substrates; C, D, and E on sapphire substrates. Spectra were taken at 15 K under Ti-sapphire laser excitation (photon energy 5.06 eV). Intensity is normalized with respect to QD maximum signal. Also, for comparison, GaN bulk PL spectrum is displayed at 3.45 eV. (After [31.2])

example, for a fully strained GaN on $Al_xGa_{1-x}N$, assuming the validity of Vergad's law, the bandgap energy shift is of 0.04 x eV, where x is the Al composition. On the other hand, as in the case of QWs, the polarization effect induces a redshift in the bandgap. Both spontaneous and piezoelectic (strain-induced) polarization induce very strong electric fields in nitride-based QDs, affecting significantly their optical properties. It should also be noted that the small dimensions associated with dots reduce the extent of the energy shift induced by polarization effects.

31.10.3 Vertical Cavities

In terrestrial long-range and high-data-density communication systems based on fiber optics, where data transfer speed is as high as 100 G/s on 10 Tb/s [31.628], zero dispersion at a wavelength 1.3 μm [31.598, 599, 629–644], and lowest attenuation at 1.5 μm [31.597, 645–648] are possible. Then, it is desirable to count with powerful lasers emitting at the mentioned fiber-optic transmission windows. Vertical cavity surface emitting lasers (VCSELs) based on more recently developed dilute nitrides (GaAsN), are touted to satisfy the mentioned requirements (8 W at 1300 nm [31.649] and 12 W at 1120 nm [31.650]), but the quality requirements have not yet been met. A schematic cross-section description of a particular VCSEL design is presented in Fig. 31.44.

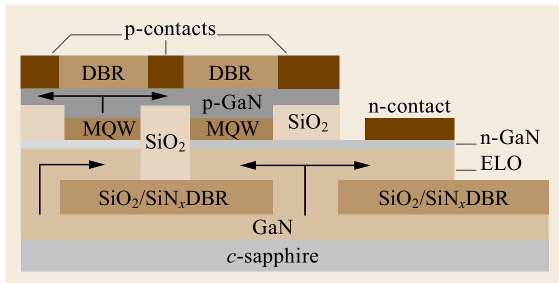

Fig. 31.44 Cross-sectional schematic of VCU's (Virginia Commonwealth University) VCSEL design. The design is meant for current injection. Lateral epitaxial overgrowth allows the implementation of distributed Bragg reflectors (DBR). The ELO growth technique allows all-dielectric DBR implementation. The design exhibits a SiO_2-defined current aperture. Current is injected and distributed via n and p GaN layers (after [31.651])

Aspects fostering the development of VCSELs are its small size ($\approx 10\,\mu m$ diameter), easier packaging and testing, possible fabrication and integration of 2-D arrays, and manufacturability. The smallest lasers available commercially today are vertical-cavity surface-emitting lasers [31.652]. The core part of VCSELs is the microcavity (MC). The constituting parts of a MC are top- and bottom-distributed Bragg reflectors (DBRs), which consist of $\lambda/4$-thick (where λ is the designed wavelength) alternating semiconductor or dielectric layers with low and high refractive index. Located between the DBRs is the active region of the VCSEL formed by multiple quantum wells (MQWs). The higher the refractive index dissimilarity, the contrast, between the alternating layers forming the dielectric stack, the fewer the number of stack pairs needed to attain DBRs with high reflectivity, which should be as close as possible to 100% for low-threshold current density. The cavity thickness should be an integer number of $\lambda/2$ times the length of the active region.

Difficulties arise when we shift from the 850 nm wavelength, either to shorter wavelengths (toward UV) or to longer wavelengths (toward infrared). In the case of short wavelengths, the number of quarter-wavelength DBR mirror pairs required increases considerably, which lowers the thermal conductivity and also increases the electrical contact's resistance. As a result, the heat dissipation problem increases substantially, which limits the VCSEL's thermal operating range.

Reflectors are commonly composed of either heterostructures or dielectric stacks and thus cleaved and/or etched facets are not applicable for vertical cavities. In the case of reflectors based on heterostructures, layers are made of materials with similar crystal structures but with different reflection indices; the larger the difference between their reflection indices the fewer the number of layers and the wider the blocking wavelength band. Due to the epitaxial growth of the active region of the VCSEL, bottom reflector stacks are commonly made of compounds compatible with the active region. Thanks to the development of the epitaxial lateral overgrowth technique (Sect. 31.10.2) for the GaN material system, it is possible to use dielectric stacks (SiN/SiO_2) as reflectors. Dielectrics constituting the stacks offer large reflection index contrast, which is beneficial to obtain a wider blocking band as well as a high reflection coefficient. On the other hand, top reflectors can be made of either semiconductors or dielectrics. Due to the short length of the active region in a vertical cavity, the gain is low. A minimum reflective coefficient for top and bottom DBR of 90% or higher is required, in order to have optical efficiency for lasing. The ideal case could be a reflection of 100% for the bottom DBR while the value for the top one should be slightly lower to allow light extraction, the extent of which depends on the desired output power.

Also in VCSELs based on GaN, AlN/GaN DBRs have been investigated. The main interest in such stacks stems from the fact that they possess the highest refractive index contrast among all the III–V compounds, so that a fewer number of stacks is required to obtain high reflectivity and relatively wide stop bands. But owing to the lattice mismatch between the AlN and GaN, which leads to crack formation (promoted by tensile strained GaN on AlN, and causing generation and propagation of defects), stack thickness is somehow limited. A way to mitigate the mentioned issues is by using AlGaN/GaN DBRs with Al concentration lower than 40% [31.653–657], and also introducing a digital equivalent of lower index materials as opposed to constant composition.

Figure 31.45 shows a stop-band-wide comparison between a 10-pair SiO_2/Si_3N_4 quarter wavelength DBR and a 30-pair $Al_{0.5}Ga_{0.5}N/GaN$ quarter wavelength DBR, both designed for a central frequency of 380 nm. The relevant point here is that even though few stacks were used, dielectric DBR achieves a higher reflectivity and a wider stop band compared with those obtained with semiconductor DBRs. GaN-based VCSELs with semiconductor-dielectric and all-dielectric reflectors were compared by *Okur* et al. [31.651]. The active region of VCSELs was formed by 6× $In_{0.01}Ga_{0.99}N$ (12 nm)/$In_{0.15}Ga_{0.85}N$ (2 nm) QWs. Sample 1 had semiconductor-dielectric DBRs, the top one being composed of 13.5 pairs of SiO_2/SiN_x while the bottom DBR was formed by 29 AlN/GaN pairs on top of a freestanding GaN (*c*-plane) substrate. Sample 2

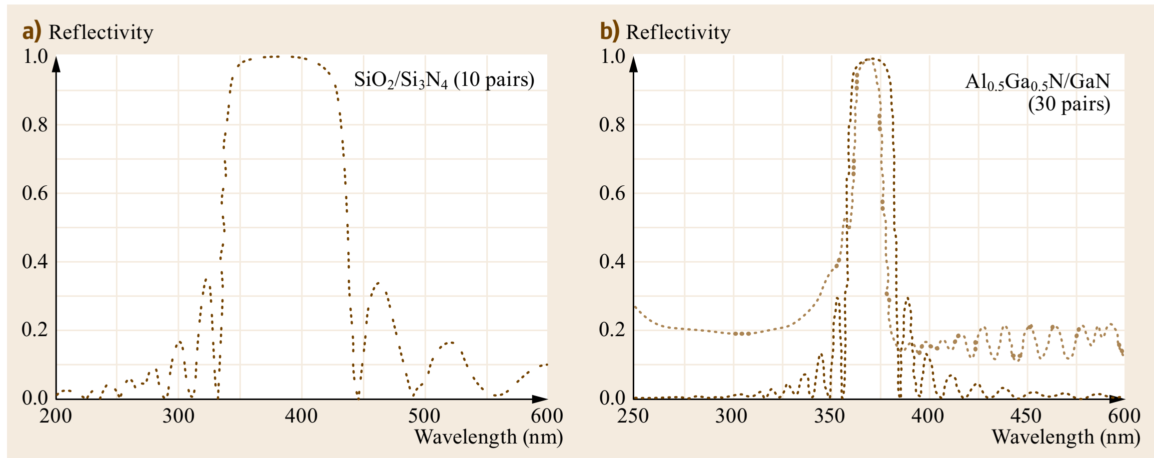

Fig. 31.45a,b Calculated reflection spectra. **(a)** for a 10-pair SiO_2/Si_3N_4 quarter wavelength DBR **(b)** for a 30-pair $Al_{0.5}Ga_{0.5}N/GaN$ quarter wavelength DBR. The *dotted line* is the calculated reflection spectra. Note that even though fewer pair stacks were used, dielectric DRBs exhibit a better reflectivity and wider stop band. (After [31.3])

consisted of all dielectric reflectors, where the top and bottom DBRs consisted of 13.5 pairs of SiO_2/SiN_x. In the latter case the entire structure was grown on a 3 µm GaN layer prepared by the ELO technique on top of a *c*-plane sapphire. Sample 2 exhibited a quality factor of 1200 at high excitation against a quality factor of 800 for sample 1, both at a wavelength of 403 nm. Also, sample 1 demonstrated one order of magnitude lower stimulated emission density ($\approx 5\,\mu J/cm^2$). On the other hand, *Butté* et al. [31.658] reported on VCSELs formed by a $5\lambda/2$ GaN cavity containing three $In_{0.15}Ga_{0.85}N/GaN$ QWs composed of a bottom 50-pair $Al_{0.83}In_{0.17}N/GaN$ DBR and a top 20-pair SiO_2/Si_3N_4 DBR with a quality factor as high as 6400 as determined from PL spectra at a wavelength of 421.1 nm.

Even though VCSELs are advantageous in many respects, some technological aspects delayed the GaN-based VCSEL development. One of those aspects is related to the fabrication of high-Q optical resonators. Another issue is the electrical current injection, which should incorporate lateral current spreading, because of the low conductivity of the p-GaN and its alloys used in the construction of some DBRs. Also, smooth dielectric and semiconductor interfaces are required of VCSELs to a greater extent due to the relatively short wavelengths involved. A roughness of smaller than 2–3 nm for areas of several hundred square micrometers is required. VCSELs based on nonpolar GaN have also been demonstrated by *Holder* et al. [31.659]. Vertical cavities were implemented on *m*-plane freestanding GaN substrates grown by HVPE. The active region, grown by MOCVD, consisted of five $In_{0.1}Ga_{0.9}N$ QWs (7 nm-thick) separated by 5 nm GaN barriers. DBRs were formed by 10-pair SiO_2/Ta_2O_5 (bottom) and 13-pair SiO_2/Ta_2O_5 (top).

Kasahara et al. [31.660] demonstrated current injection stimulated lasing at room temperature in GaN-based VCSELs on GaN substrates. CW operation for blue (8 µm aperture) and under pulsed (pulse width: 1.0 µs; pulse period: 500 µs) current operation (10 µm aperture) was reported. Devices were formed by InGaN/GaN quantum wells in conjunction with dielectric DBRs and a vertical current injection configuration. Blue CW lasing at 451 nm had a threshold current and voltage of 1.5 mA and 3.3 V respectively. Pulsed green lasing (503 nm) was attained at a threshold current of 22 mA and a threshold voltage of 6.3 V. Maximum output power for blue emission was 0.7 mW, while for green light it was 0.8 mW. The authors suggest that the difference in the threshold current, from blue to green emission, is caused by the quantum confinement Stark effect caused by the piezoelectric polarization-induced field, the genesis of which is the strain due to the mismatch between GaN and InGaN and which increases for higher In content. Electrically injected stimulated emission at a wavelength of 411.9 nm and a maximum power output of 19.5 µW in these devices was observed. However, high threshold current and very low forward voltage suggests high leakage current. Laser emission was polarized-locked with an optical electric field oriented parallel to the *a*-plane, in contrast to that which occurs in *c*-plane VCSELs, where the emitted light is randomly polarized. This can be a key characteristic of VCSELs built on m-plane orientations for applications where high-intensity polarized light is desired.

31.10.4 Nitride Nanorods

Nanorods, also known as nanowires (NWs) and whiskers, can be synthesized with a 5–500 nm diameters, and be dozens of micrometers long given the opportunity, as mentioned in the introduction of this section, to explore the realm of the mesoscopic phenomena. Some of the potential and interesting applications are nanowire light-emitting diodes (NW LEDs) in all visible spectra [31.606, 661–664], white light generation [31.11], nanowire lasers (NW lasers) [31.665–668] with emission wavelengths from the deep ultraviolet (UV) [31.669] to the near-infrared [31.670–672] spectral range, and photodetectors [31.673–676]. However, for successful insertion of nitride nanowires into the actual market, electrical injection, ultralow-threshold, and continuous wave (CW) operation at room temperature are crucial. In this vein some obstacles need to be overcome first, such as the carrier loss to defect-related nonradiative and surface recombination processes [31.602], electron overflow [31.677, 678], and poor hole transport [31.679]. In order to enhance group III nitride NW performance, thermal management in NW lasers, which plays a principal role, also needs to be addressed.

Because of the reduced diameter of the NWs, thermal conductivity is also lower compared with that of the bulk. Thermal conductivity of single-GaN NWs for different diameters has been reported [31.680–682]. Thermal conductivities as low as 0.13–0.19 $\mathrm{W cm^{-1} K^{-1}}$ at 300 K (while for bulk Si, GaN and 4HSiC is 1.5, 2.3, 4.5 $\mathrm{W cm^{-1} K^{-1}}$ respectively) were reported. NW doping, for both n and p-type materials, still remains a challenging problem, especially the p-type variety, which makes electrical injection difficult to attain. n-ype NWs doped with Si have been demonstrated [31.683, 684], while p-type doping, as in the case of planar structures, is a main concern, especially for InGaN and InAlN with high Al and In compositions. Generally, lasing in NW lasers is demonstrated via optical pumping, while electrical injection in group III nitride NW lasers remains elusive. At this time there is no report on electrically pumped group III nitride NW lasers.

One-dimensional nanostructures are usually grown by a variety of techniques. Among them are vapor phase, laser ablation, chemical vapor deposition [31.685, 686], chemical vapor transport methods, molecular beam epitaxy [31.687], sputtering [31.688–692], vapor-liquid-solid (VLS) [31.693–697], inclusive of self-catalytic and vapor phase varieties, vapor-solid (VS) growth [31.698, 699], confined chemical reaction [31.700–702] such as that utilized for carbon nanotube preparation, and anodized Al membrane confined reactions [31.703, 704]. No matter what growth techniques is used, it must have attributes such as reproducibility, uniformity, scalability, cost-effectiveness, and a well understood growth process. Nanorods are typically grown by patterning techniques as an integral part of the growth process. For instance, high-quality InGaN NWs have been grown by many methods including CVD [31.603, 705], MBE [31.603, 705–708], and hydride vapor phase epitaxy [31.709, 710] to produce a diverse class of heterostructures: core-shell [31.604, 705], core-multishell [31.604], well/disk-in-a-wire [31.711, 712], and dot-in-a-wire [31.606, 706]. Also, InN nanostructures have been grown in many different shapes: nanocrystals [31.713], nanocolumns [31.714], nanorods [31.715], NWs [31.684], nanotubes [31.716], and nanobelts [31.602, 717]. For more details on group III nitride nanorods, the reader may wish to see reviews [31.667, 718–723].

As in the case of layers grown by heteroepitaxy, the material perfection is highly coveted, and in order to master the growth process, an in-depth understanding of the kinetics and thermodynamics of reactions applied to a wide variety of material systems is necessary [31.724]. Note that for group III nitride nanowires there are no affordable lattice-matched substrates available. The small base area, however, together with the large surface/volume ratio leads to relaxed nanowires without extended defects on nonnative substrates. As a result, nearly structural defect-free nanorods are possible to attain. A relaxed material is beneficial in terms of minimization of the strain-induced polarization effects in the polar direction, which is advantageous for heterojunction systems, such as green LDs based on InGaN in a GaN matrix.

For optoelectronic applications, sapphire and Si are of most interest. The optical window of sapphire is consistent with UV, visible, and near-infrared applications. Even though the Si transmission window begins at the far-deep-infrared spectrum, the main interest in Si wafers lies in their relatively low cost and possibility to integrate light emitters with electronics in cases where the performance of the emitter does not rely on substrate transparency i. e., VCSELs, NWs Fabry–Pérot cavities and longitudinal heterostructures. The cost issue alone has been driving the LED industry to migrate to Si substrates along with processes that are already in place for substrate removal.

As noted already, nanowire growth in a variety of cross-sectional shapes (hexagonal, triangular, circular, and rectangular) has been achieved. The triangular cross-section is to some extent related to the growth method and growth conditions employed. Hexagonal or triangular cross-section NWs are attained commonly by MOCVD [31.605, 725]. Nearly extended defect-free wurtzite single-crystal GaN nanocolumns grown

by plasma-assisted molecular beam epitaxy with a diameter in the range of 20–40 nm were grown along the [0001] c-direction on Si substrates with (001) and (111) surfaces [31.726]. This represents another piece of evidence that, when not bounded by the substrate, the wurzite phase is the preferential polytype with dominant growth parallel to the polar direction. Vertically aligned [0001] GaN nanorods on sapphire were grown by MBE using an RF source for reactive nitrogen [31.687]. Nanorod growth that took place under GaN growth conditions deviated from that used for standard growth (planar growth). In other words, the growth takes place at relatively high temperatures (> 800 °C), some 200 °C higher than that used to obtain uniform layers under Ga-rich conditions, and under very high nitrogen fluxes. This approach exploits the very high sticking coefficient of nitrogen and the high evaporation rate of Ga at high temperatures.

Because high-quality devices based on heterostructures are commonly produced by MOCVD and to a lesser extent by MBE, these methods could facilitate a smooth integration of nanowire growth with compositional and doping modulation in the growth direction. In practical applications, more precisely those based on electrical injection, a p-type semiconductor is crucial. The p-type doping in GaN systems for functional device structures was reported in [31.727]. The authors used a chemical vapor transport vapor-solid process to introduce Cp_2Mg to accomplish p-type doping. In another report [31.601], the authors used the vapor-liquid-solid (VLS) method to grow nanowires. The tuned incorporation of Mg during synthesis resulted in 35 nm-diameter nanowires with rectifying p-n junction properties. GaN nanowires synthesized by a catalytic chemical vapor deposition, with hexagonal single-crystalline structure and diameters of 10–50 nm and lengths of tens of micrometers, exhibited UV bands at 3.481 and 3.285 eV in low-temperature PL measurements associated with donor-bound excitons and donor-acceptor pairs respectively [31.728]. The observed blueshift of UV bands was attributed to quantum confinement effects in thin GaN nanowires with diameters of about 11 nm. The turn-on field emission of nanowires was $8.5\,V\,mm^{-1}$ and the current density was about $0.2\,mA\,cm^{-2}$ at $17.5\,V\,mm^{-1}$, which is sufficient for field emission display applications and vacuum microelectronic devices. Also, GaN nanowires formed via the VLS mechanism with gold, iron, or nickel as catalysts, exhibited orientations predominantly along directions [001] and [101]. The NWs with growth orientation [210] featured a triangular cross-section with an n-type character and a mobility of $65\,cm^2\,V^{-1}s^{-1}$ [31.729].

In an attempt to accomplish highly efficiency light emission, *Qian* et al. [31.604] prepared core multishell nanowire (CMS) radial heterostructures by MOVPE having triangular cross-sections, which allowed synthetically tunable multicolor light emitting diodes. Structures consisted of n-GaN cores surrounded by $In_xGa_{(1-x)}N$/GaN/p-AlGaN/p-GaN shells. Electrical carrier injection was achieved by forming metal contacts on the p-type outer shell and n-type cores at the ends of individual nanowires. I–V curves exhibited p-n diode characteristics with a knee voltage of around 3.5 V. CMS nanowires display electroluminescence spectra with emission peaks at 367, 412, 459, 510, and 577 nm, consistent with $In_xGa_{1-x}N$ band edge emissions for In compositions of 1, 10, 20, 25, and 35%, respectively. Estimation of quantum efficiencies (QEs) for these CMS nanowire LEDs gave a value of 5.8% at 440 nm and 3.9% at 540 nm, both of which are several times better than the QEs reported for nanoscale LEDs and approach InGaN-based SQW thin-film LEDs at similar emission wavelengths. InGaN/GaN multiple quantum disk (MQD) nanocolumn LEDs are fabricated on n-type Si(111) substrates [31.730] as well. The columnar growth was preceded by the deposition of GaN dots. The latter was obtained by exposing the surface of the wafer to a Ga beam and RF plasma excited nitrogen at 530 °C. In order to attain p-type GaN, growth conditions were changed to those suitable for GaN-Mg doping. Resulting nanocolumn LEDs exhibited diode I–V characteristics with a typical turn-on voltage of 2.5–3 V at room temperature [31.711]. With this process, functional LEDs emitting in the entire visible spectrum were demonstrated.

Regardless of the growth direction of the NWs, the junction area between InGaN and GaN is reduced. Therefore, strain along the direction perpendicular to the growth is relaxed. Then a lower density of defects and weaker piezoelectric polarization-induced fields are expected, which is an advantage in comparison with InGaN-GaN quantum wells in planar structures where strain degrades the internal quantum efficiency (IQE) of the LED. In contrast, and in addition to a higher extraction efficiency (because of the NW aspect ratio), NWs exhibit an improved IQE. By way of background, white LEDs are commonly achieved by blue LED pumping a yellow phosphor-dye and leaking through it [31.731], a technique where a blue LED chip is packaged with a precise phosphor arrangement. As a result, blue light is converted to white light. *Nguyen* et al. [31.606, 732] obtained phosphor-free nanowire white light LEDs by the incorporation of different In content levels in stacked InGaN/GaN QWs and the use of an p-doped AlGaN electron blocking layer between the active region and the uppermost NW layer, the p-GaN layer. The authors attained stable white light emission, which was attributed to the large variation of QW In composition,

uniform carrier distribution in the LED active region, and reduced quantum confinement stark effect [31.733]. Also, the authors claim a negligible degradation up to $\approx 2200\,\mathrm{A/cm^2}$.

Lasers have also been attained in NWs, albeit with optical pumping at this stage. The possibility to grow NWs on Si wafers paves the way for their integration with very-large-scale integration circuits (VLSIs) if suitable applications can be visualized. Along these lines, recent investigations have focused on making NW lasers compatible with VLSI circuits. The integration of optics and digital electronics in the same chip is of great interest in high-speed communication systems, fiber optic communication, and in all the relevant potential applications where optoelectronic at the nanometer scale is required. The reduction of laser dimensions is associated with some beneficial features, such as low-threshold, high efficiency, and low power consumption, all of which are difficult to achieve with VCSELs. It should be noted that group III nitride NW lasers under electrical injection at room temperature and continuous wave face considerable challenges. Carrier loss mechanisms (nonradiative centers), electron overflow, poor hole transport, thermal management, and poor ohmic contact to the p-GaN layer all need to be overcome in order to fully exploit the potential of group III nitride NW lasers.

Among the studied micro- and nanocavities are Fabry–Pérot [31.665, 669, 717, 734–738], nanoplasmonics [31.739, 740], photonic crystals [31.741], micro stadium lasers [31.666], and ring cavities [31.742]. The Fabry–Pérot (FP) cavity, the simplest one, has been very widely investigated. The NW lasers based on FP cavities consist of two crystalline facets at the ends of the NWs. The optical field propagates along the longitudinal direction of the NW, being amplified and absorbed inside the active region and reflected back by the crystalline facets. Lasing threshold conditions in NWs result from the balance of the round-trip losses and the round-trip gains in the cavity. For details on NW Fabry–Pérot lasers see [31.668].

Optoelectronic devices based on nitrides, such as LEDs and lasers, although commercially available, are still far from being fully exploited from the viewpoint of what GaN has to offer. This is mainly because the material quality, in spite of continual improvement, is still far from being nearly defect-free. In addition, limitations imposed by p-type doping make it difficult to obtain good contacts and provide a sufficient number of holes to match that of electrons in optical devices. As a result, electrical carrier injection is limited. Optically pumped nanolasers have been demonstrated by many groups around the world. However, electrical carrier injection in group III nitride NW lasers is still lacking. To succeed in practice, nitride-based NW lasers need to be electrically driven, and therefore they should feature good electric contacts. Also their manipulation should be well controlled.

31.11 Summary and Conclusions

Group III nitride semiconductors continue to attract a good deal of interest due to their numerous industrial applications. To begin with, AlN exhibits many useful mechanical, electronic, and thermal properties, for example, hardness, resistance to high temperature and caustic chemicals, and high thermal conductivity in crystalline shape, and so on. The wide bandgap is also the reason AlN is touted as an insulating material in semiconductor device applications, for example, AlN has been attempted as surface passivation layer in AlGaN/GaN-based heterojunction field effect transistors (HFETs) with the benefit of better heat dissipation compared to other common passivation materials. Piezoelectric properties also make AlN suitable for surface-acoustic-wave devices and sensor applications. However, the majority of interest in this semiconductor, in the context of electronic and optoelectronic devices, stems from its ability to form alloys with GaN and InN to tune the bandgap, polarization charge, and lattice constant. A few usages of AlGaN alloy are as a barrier layer in AlGaN/GaN HFETs, as an electron blocking layer in InGaN-based LEDs, as buffer layers in AlGaN/GaN HFETs to reduce the buffer leakages, and in deep UV LEDs, and so on. AlN also forms a crucial component of the nitride-based AlInGaN quaternary, which allows tuning of the bandgap independently of the composition over a reasonably wide range of bandgaps. Currently, AlN crystals up to 2 in in diameter are available; however, many challenges still remain that need to be addressed to further exploit its usage in electronic and optoelectronic applications.

Although GaN has been studied far more extensively than the other group III nitrides, there is still a great need for further investigations to approach the level of understanding of technologically important materials such as Si and GaAs. GaN growth still suffers from the insufficient control of impurity levels, defects and dislocations. Although native substrates are commercially available, which can alleviate the above-mentioned challenges to a certain extent, these issues

may remain for a fairly long time when foreign substrates such as sapphire and silicon are used for cost reduction as well as other considerations. These, together with the difficulties in obtaining high-quality p-type doping layers, will certainly slow down the process of further improvements in the performance of GaN-based electronic and optoelectronic devices.

Oddly enough, InN received much of the early attention compared to the other nitride binaries. However it is still difficult to grow high-quality crystalline InN layers. Although InN can be alloyed with GaN, which enables the tuning of the bandgap from ≈ 0.7 to $\approx 3.4\,\mathrm{eV}$, the high-In composition InGaN has to be grown at low temperatures, rendering rather low-quality layers. Thus, small-bandgap InN does not escape competition by the existing alternatives: well-characterized/developed semiconductors such as AlGaAs and In (Ga, Al)AsP. Consequently, practical applications of InN may be restricted to its alloys with GaN and AlN, especially low-indium composition alloys, in addition to tandem solar cells, which are very unlikely to be successful. The growth of high-quality InN/high-indium-composition alloys and the enumeration of their fundamental physical properties remain, for the present, a scientific enterprise.

References

31.1 H. Morkoç: *Handbook of Nitride Semiconductors and Devices*, Vol. 1 (Wiley, Weinheim 2008)

31.2 H. Morkoç: *Handbook of Nitride Semiconductors and Devices*, Vol. 2 (Wiley, Weinheim 2008)

31.3 H. Morkoç: *Handbook of Nitride Semiconductors and Devices*, Vol. 3 (Wiley, Weinheim 2008)

31.4 L. Sang, M. Liao, M. Sumiya: A comprehensive review of semiconductor ultraviolet photodetectors: From thin film to one-dimensional nanostructures, Sens. Switz. **13**(8), 10482 (2013)

31.5 M. de la Mata, X. Zhou, F. Furtmayr, J. Teubert, S. Gradecak, M. Eickhoff, A. Fontcuberta i Morral, J. Arbiol: A review of MBE grown 0-D, 1-D and 2-D quantum structures in a nanowire, J. Mater. Chem. C **1**(28), 4300 (2013)

31.6 M.P. Ulmer: A review of UV detectors for astrophysics: Past, present, and future, Proc. SPIE–Int. Soc. Opt. Eng. **7222**, 722210 (2009)

31.7 M. Meneghini, A. Tazzoli, G. Mura, G. Meneghesso, E. Zanoni: A review on the physical mechanisms that limit the reliability of GaN-based LEDs, IEEE Trans. Electron Devices **57**(1), 108 (2010)

31.8 N. Trivellin, M. Meneghini, E. Zanoni, K. Orita, M. Yuri, T. Tanaka, D. Ueda, G. Meneghesso: A review on the reliability of GaN-based laser diodes, Proc. 2010 IEEE Int. Reliab. Phys. Symp. (IRPS 2010), Piscataway (2010) p. 6

31.9 M. Meneghini, L.-R. Trevisanello, G. Meneghesso, E. Zanoni: A review on the reliability of GaN-based LEDs, IEEE Trans. Device Mater. Reliab. **8**(2), 323 (2008)

31.10 T. Hashimoto, E. Letts, S. Hoff: Current status and future prospects ammonothermal bulk GaN growth, Sens. Mater. Jpn. **25**(3), 155 (2013)

31.11 E. Okahisa, S. Masui, T. Yanamoto, S. Nagahama: Current status and issues of blue laser diodes, Rev. Laser Eng. Jpn. **41**(4), 230 (2013)

31.12 D.F. Feezell, M.C. Schmidt, S.P. DenBaars, S. Nakamura: Development of nonpolar and semipolar InGaN/GaN visible light-emitting diodes, MRS Bull. **34**(5), 318 (2009)

31.13 E. Zanoni, M. Meneghini, N. Trivellin, M. Dal Lago, G. Meneghesso: GaN-based LEDs: State of the art and reliability-limiting mechanisms, Proc. 2014 15th Int. Conf. Thermal, Mech. Multi-Physics Simulation and Experiments in Microelectronics and Microsystems (EuroSimE), Piscataway (2014) p. 5

31.14 Z.J. Liu, W.C. Chong, K.M. Wong, K.M. Lau: GaN based light-emitting diode on silicon (LEDoS) micro-displays for BLU-free full-color projector application, Proc. 2013 IEEE Photonics Conf. (IPC), Piscataway (2013) p. 171

31.15 T. Paskova, D.A. Hanser, K.R. Evans: GaN substrates for III-nitride devices, Proc. IEEE **98**(7), 1324 (2010)

31.16 V. Avrutin, D.J. Silversmith, Y. Mori, F. Kawamura, Y. Kitaoka, H. Morkoc: Growth of bulk GaN and AlN: Progress and challenges, Proc. IEEE **98**(7), 1302 (2010)

31.17 J. Piprek: III-nitride LED efficiency droop models: A critical status review, Proc. 2013 13th Int. Conf. on Numerical Simulation of Optoelectronic Devices (NUSOD), Piscataway (2013) p. 107

31.18 M. Beeler, E. Trichas, E. Monroy: III-nitride semiconductors for intersubband optoelectronics: A review, Semicond. Sci. Technol. **28**(7), 074022 (2013)

31.19 M. Razeghi: III-Nitride optoelectronic devices: From ultraviolet toward terahertz, IEEE Photonics. J. **3**(2), 263 (2011)

31.20 R. Paiella, K. Driscoll, Y. Li, Y. Liao, A. Bhattacharyya, C. Thomidis, L. Zhou, D.J. Smith, T.D. Moustakas: Intersubband transitions in GaN-based quantum wells: A new materials platform for infrared device applications, Proc. SPIE Int. Soc. Opt. Eng. **7808**, 780807 (2010)

31.21 S.P. Najda, P. Perlin, T. Suski, L. Marona, M. Bockowski, M. Leszczynski, P. Wisniewski, R. Czernecki, R. Kucharski, G. Targowski: Latest developments in AlGaInN laser diode technology, Proc. SPIE Int. Soc. Opt. Eng. **8625**, 862517 (2013)

31.22 R. Kucharski, M. Zajac, R. Doradzinski, M. Rudzinski, R. Kudrawiec, R. Dwilinski: Non-polar

and semi-polar ammonothermal GaN substrates, Semicond. Sci. Technol. **27**(2), 024007 (2012)
31.23 H.T. Grahn: Nonpolar-oriented GaN films for polarization-sensitive and narrow-band photodetectors, MRS Bulletin **34**(5), 341 (2009)
31.24 H. Ohta, K. Okamoto: Nonpolar/semipolar GaN technology for violet, blue, and green laser diodes, MRS Bulletin **34**(5), 324 (2009)
31.25 S. Albert, A. Bengoechea-Encabo, M.A. Sanchez-Garcia, F. Barbagini, E. Calleja, E. Luna, A. Trampert, U. Jahn, P. Lefebvre, L.L. Lopez, S. Estrade, J.M. Rebled, F. Peiro, G. Nataf, P. De Mierry, J. Zuniga-Perez: Ordered GaN/InGaN nanorods arrays grown by molecular beam epitaxy for phosphor-free white light emission, Frontiers in Electronics. Selected Papers from the Workshop on Frontiers in Electronics 2011 (WOFE-11), Singapore (2013) p. 109
31.26 D. Zhu, D.J. Wallis, C.J. Humphreys: Prospects of III-nitride optoelectronics grown on Si, Rep. Prog. Phys. **76**(10), 106501 (2013)
31.27 M. Tchernycheva, F.H. Julien, E. Monroy: Review of nitride infrared intersubband devices, Proc. SPIE–Int. Soc. Opt. Eng. **7602**, 76021A (2010)
31.28 S.J. Pearton, R. Deist, F. Ren, L. Liu, A.Y. Polyakov, J. Kim: Review of radiation damage in GaN-based materials and devices, J. Vac. Sci. Technol. A: Vac. Surf. Films **31**(5), 050801 (2013)
31.29 V. Consonni: Self-induced growth of GaN nanowires by molecular beam epitaxy: A critical review of the formation mechanisms, Phys. Status Solidi RRL Rapid Res. Lett. Ger. **7**(10), 699 (2013)
31.30 F. Scholz: Semipolar GaN grown on foreign substrates: A review, Semicond. Sci. Technol. **27**(2), 024002 (2012)
31.31 H. Amano: Progress and prospect of the growth of wide-band-gap group III nitrides: Development of the growth method for single-crystal bulk GaN, Jpn. J. Appl. Phys. **52**(5), 050001 (2013)
31.32 W.A. Harrison: *Electronic Structure and the Properties of Solids: The Physics of the Chemical Bond* (Dover, New York 1989)
31.33 C.-Y. Yeh, Z. Lu, S. Froyen, A. Zunger: Zinc-blende–wurtzite polytypism in semiconductors, Phys. Rev. B **46**(16), 10086 (1992)
31.34 G.A. Jeffrey, G.S. Parry, R.L. Mozzi: Study of the Wurtzite-Type Binary Compounds. I. Structures of Aluminum Nitride and Beryllium Oxide, J. Chem. Phys. **25**(5), 1024 (1956)
31.35 H. Schulz, K.H. Thiemann: Crystal structure refinement of AlN and GaN, Solid State Commun. **23**(11), 815 (1977)
31.36 A. Zubrilov: *Properties of Advanced Semiconductor Materials: GaN, AlN, InN, BN, SiC, SiGe* (Wiley, New York 2001)
31.37 E. Dimakis, E. Iliopoulos, K. Tsagaraki, A. Adikimenakis, A. Georgakilas: Biaxial strain and lattice constants of InN (0001) films grown by plasma-assisted molecular beam epitaxy, Appl. Phys. Lett. **88**(19), 191918 (2006)
31.38 M.F. Wu, S.Q. Zhou, A. Vantomme, Y. Huang, H. Wang, H. Yang: High-precision determination of lattice constants and structural characterization of InN thin films, J. Vac. Sci. Technol. A: Vac. Surf. Films **24**(2), 275 (2006)
31.39 Q. Xia, H. Xia, A.L. Ruoff: Pressure-induced rock-salt phase of aluminum nitride: A metastable structure at ambient condition, J. Appl. Phys. **73**(12), 8198 (1993)
31.40 P. Perlin, C. Jauberthie-Carillon, J. Itie, A. San Miguel, I. Grzegory, A. Polian: Raman scattering and x-ray-absorption spectroscopy in gallium nitride under high pressure, Phys. Rev. B **45**(1), 83 (1992)
31.41 M. Ueno, M. Yoshida, A. Onodera, O. Shimomura, K. Takemura: Stability of the wurtzite-type structure under high pressure: GaN and InN, Phys. Rev. B **49**(1), 14 (1994)
31.42 M.J. Paisley: Growth of cubic phase gallium nitride by modified molecular-beam epitaxy, J. Vac. Sci. Technol. Vac. Surf. Films **7**(3), 701 (1989)
31.43 T. Lei, M. Fanciulli, R.J. Molnar, T.D. Moustakas, R.J. Graham, J. Scanlon: Epitaxial growth of zinc blende and wurtzitic gallium nitride thin films on (001) silicon, Appl. Phys. Lett. **59**(8), 944 (1991)
31.44 R.C. Powell, N.-E. Lee, Y.-W. Kim, J.E. Greene: Heteroepitaxial wurtzite and zinc-blende structure GaN grown by reactive-ion molecular-beam epitaxy: Growth kinetics, microstructure, and properties, J. Appl. Phys. **73**(1), 189 (1993)
31.45 M. Mizuta, S. Fujieda, Y. Matsumoto, T. Kawamura: Low Temperature Growth of GaN and AlN on GaAs Utilizing Metalorganics and Hydrazine, Jpn. J. Appl. Phys. **25**(12), L945 (1986)
31.46 M. Leszczynski, J. Bak-Misiuk, J. Domagala, J. Muszalski, M. Kaniewska, J. Marczewski: Lattice dilation by free electrons in heavily doped GaAs:Si, Appl. Phys. Lett. **67**(4), 539 (1995)
31.47 G. Cargill, A. Segmüller, T. Kuech, T. Theis: Lattice strain from DX centers and persistent photocarriers in Sn-doped and Si-doped $Ga_{1-x}Al_xAs$, Phys. Rev. B **46**(16), 10078 (1992)
31.48 M. Leszczynski, H. Teisseyre, T. Suski, I. Grzegory, M. Bockowski, J. Jun, S. Porowski, K. Pakula, J.M. Baranowski, C.T. Foxon, T.S. Cheng: Lattice parameters of gallium nitride, Appl. Phys. Lett. **69**(1), 73 (1996)
31.49 J. Härtwig, S. Grosswig: Measurement of x-ray diffraction angles of perfect monocrystals with high accuracy using a single crystal diffractometer, Phys. Status Solidi A **115**(2), 369 (1989)
31.50 W.L. Bond: Precision lattice constant determination, Acta Crystallogr. **13**(10), 814 (1960)
31.51 T. Nagashima, Y. Kubota, T. Kinoshita, Y. Kumagai, J. Xie, R. Collazo, H. Murakami, H. Okamoto, A. Koukitu, Z. Sitar: Structural and optical properties of carbon-doped AlN substrates grown by hydride vapor phase epitaxy using AlN substrates prepared by physical vapor transport, Appl. Phys. Express **5**(12), 125501 (2012)
31.52 P. Lu, R. Collazo, R.F. Dalmau, G. Durkaya, N. Dietz, B. Raghothamachar, M. Dudley, Z. Sitar: Seeded growth of AlN bulk crystals in *m*- and *c*-orientation, J. Cryst. Growth **312**(1), 58 (2009)

31.53 Y. Kumagai, Y. Kubota, T. Nagashima, T. Kinoshita, R. Dalmau, R. Schlesser, B. Moody, J. Xie, H. Murakami, A. Koukitu, Z. Sitar: Preparation of a freestanding AlN substrate from a thick AlN layer grown by hydride vapor phase epitaxy on a bulk AlN substrate prepared by physical vapor transport, Appl. Phys. Express **5**(5), 055504 (2012)

31.54 J. Domagala, M. Leszczynski, P. Prystawko, T. Suski, R. Langer, A. Barski, M. Bremser: Strain relaxation of $Al_xGa_{1-x}N$ epitaxial layers on GaN and SiC substrates, J. Alloys Compd. **286**(1/2), 284 (1999)

31.55 A. Zoroddu, F. Bernardini, P. Ruggerone, V. Fiorentini: First-principles prediction of structure, energetics, formation enthalpy, elastic constants, polarization, and piezoelectric constants of AlN, GaN, and InN: Comparison of local and gradient-corrected density-functional theory, Phys. Rev. B **64**(4), 045208 (2001)

31.56 T. Paskova, E.A. Preble, A.D. Hanser, K.R. Evans, R. Kröger, P.P. Paskov, A.J. Cheng, M. Park, J.A. Grenko, M.A.L. Johnson: Polar and nonpolar HVPE GaN substrates: Impact of doping on the structural, electrical and optical characteristics, Phys. Status Solidi C **6**(S2), S344 (2009)

31.57 D. Gogova, D. Siche, A. Kwasniewski, M. Schmidbauer, R. Fornari, C. Hemmingsson, R. Yakimova, B. Monemar: HVPE GaN substrates: Growth and characterization, Phys. Status Solidi C **7**(7/8), 1756 (2010)

31.58 D. Gogova, P.P. Petrov, M. Buegler, M.R. Wagner, C. Nenstiel, G. Callsen, M. Schmidbauer, R. Kucharski, M. Zajac, R. Dwilinski, M.R. Phillips, A. Hoffmann, R. Fornari: Structural and optical investigation of non-polar (1–100) GaN grown by the ammonothermal method, J. Appl. Phys. **113**(20), 203513 (2013)

31.59 R. Kucharski, M. Zajac, R. Doradziński, M. Rudziński, R. Kudrawiec, R. Dwiliński: Non-polar and semi-polar ammonothermal GaN substrates, Semicond. Sci. Technol. **27**(2), 024007 (2012)

31.60 T. Deguchi, D. Ichiryu, K. Toshikawa, K. Sekiguchi, T. Sota, R. Matsuo, T. Azuhata, M. Yamaguchi, T. Yagi, S. Chichibu, S. Nakamura: Structural and vibrational properties of GaN, J. Appl. Phys. **86**(4), 1860 (1999)

31.61 M. Leszczynski, P. Prystawko, T. Suski, B. Lucznik, J. Domagala, J. Bak-Misiuk, A. Stonert, A. Turos, R. Langer, A. Barski: Lattice parameters of GaN single crystals, homoepitaxial layers and heteroepitaxial layers on sapphire, J. Alloys Compd. **286**(1/2), 271 (1999)

31.62 T. Detchprohm, K. Hiramatsu, K. Itoh, I. Akasaki: Relaxation process of the thermal strain in the GaN/α-Al_2O_3 heterostructure and determination of the intrinsic lattice constants of GaN free from the strain, Jpn. J. Appl. Phys. **31**(10B), L1454 (1992)

31.63 H. Angerer, D. Brunner, F. Freudenberg, O. Ambacher, M. Stutzmann, R. Höpler, T. Metzger, E. Born, G. Dollinger, A. Bergmaier, S. Karsch, H.-J. Körner: Determination of the Al mole fraction and the band gap bowing of epitaxial $Al_xGa_{1-x}N$ films, Appl. Phys. Lett. **71**(11), 1504 (1997)

31.64 C. Stampfl, C. Van de Walle: Density-functional calculations for III–V nitrides using the local-density approximation and the generalized gradient approximation, Phys. Rev. B **59**(8), 5521 (1999)

31.65 W. Paszkowicz, J. Adamczyk, S. Krukowski, M. Leszczyński, S. Porowski, J.A. Sokolowski, M. Michalec, W. Łasocha: Lattice parameters, density and thermal expansion of InN microcrystals grown by the reaction of nitrogen plasma with liquid indium, Philos. Mag. A **79**(5), 1145 (1999)

31.66 I. Petrov, E. Mojab, R.C. Powell, J.E. Greene, L. Hultman, J.-E. Sundgren: Synthesis of metastable epitaxial zinc-blende-structure AlN by solid-state reaction, Appl. Phys. Lett. **60**(20), 2491 (1992)

31.67 M.E. Sherwin, T.J. Drummond: Predicted elastic constants and critical layer thicknesses for cubic phase AlN, GaN, and InN on β-SiC, J. Appl. Phys. **69**(12), 8423 (1991)

31.68 H. Xia, Q. Xia, A. Ruoff: High-pressure structure of gallium nitride: Wurtzite-to-rocksalt phase transition, Phys. Rev. B **47**(19), 12925 (1993)

31.69 H. Vollstädt, E. Ito, M. Akaishi, S. Akimoto, O. Fukunaga: High pressure synthesis of rocksalt type of AlN, Proc. Jpn. Acad. Ser. B Phys. Biol. Sci. **66**(1), 7 (1990)

31.70 R. Dwiliński, R. Doradziński, J. Garczyński, L. Sierzputowski, J. Baranowski, M. Kamińska: AMMONO method of GaN and AlN production, Diam. Relat. Mater. **7**(9), 1348 (1998)

31.71 T. Hashimoto, K. Fujito, F. Wu, B.A. Haskell, P.T. Fini, J.S. Speck, S. Nakamura: Structural characterization of thick GaN films grown on free-standing GaN seeds by the ammonothermal method using basic ammonia, Jpn. J. Appl. Phys. **44**(25), L797 (2005)

31.72 B. Wang, M.J. Callahan: Transport growth of GaN crystals by the ammonothermal technique using various nutrients, J. Cryst. Growth **291**(2), 455 (2006)

31.73 R. Dwiliński, R. Doradziński, J. Garczyński, L.P. Sierzputowski, A. Puchalski, Y. Kanbara, K. Yagi, H. Minakuchi, H. Hayashi: Excellent crystallinity of truly bulk ammonothermal GaN, J. Cryst. Growth **310**(17), 3911 (2008)

31.74 T. Paskova, K.R. Evans: GaN substrates – Progress, status, and prospects, IEEE J. Sel. Top. Quantum Electron. **15**(4), 1041 (2009)

31.75 C. van de Walle: Effects of impurities on the lattice parameters of GaN, Phys. Rev. B **68**(16), 165209 (2003)

31.76 X.H. Zheng, Y.T. Wang, Z.H. Feng, H. Yang, H. Chen, J.M. Zhou, J.W. Liang: Method for measurement of lattice parameter of cubic GaN layers on GaAs (001), J. Cryst. Growth **250**(3/4), 345 (2003)

31.77 S.V. Novikov, N. Zainal, A.V. Akimov, C.R. Staddon, A.J. Kent, C.T. Foxon: Molecular beam epitaxy as a method for the growth of freestanding zinc-blende (cubic) GaN layers and substrates, J. Vac.

Sci. Technol. B **28**(3), C3B1 (2010)
31.78 A. Muoz, K. Kunc: High-pressure phase of gallium nitride, Phys. Rev. B **44**(18), 10372 (1991)
31.79 J.G. Lozano, F.M. Morales, R. García, D. González, V. Lebedev, C.Y. Wang, V. Cimalla, O. Ambacher: Cubic InN growth on sapphire (0001) using cubic indium oxide as buffer layer, Appl. Phys. Lett. **90**(9), 091901 (2007)
31.80 A. Lima, A. Tabata, J. Leite, S. Kaiser, D. Schikora, B. Schöttker, T. Frey, D. As, K. Lischka: Growth of cubic InN on InAs (001) by plasma-assisted molecular beam epitaxy, J. Cryst. Growth **201/202**, 396 (1999)
31.81 D. Chandrasekhar, D.J. Smith, S. Strite, M.E. Lin, H. Morkoç: Characterization of Group III-nitride semiconductors by high-resolution electron microscopy, J. Cryst. Growth **152**(3), 135 (1995)
31.82 V. Cimalla, J. Pezoldt, G. Ecke, R. Kosiba, O. Ambacher, L. Spieß, G. Teichert, H. Lu, W.J. Schaff: Growth of cubic InN on *r*-plane sapphire, Appl. Phys. Lett. **83**(17), 3468 (2003)
31.83 F.D. Murnaghan: The compressibility of media under extreme pressures, Proc. Natl. Acad. Sci. **30**(9), 244 (1944)
31.84 A. Polian, M. Grimsditch, I. Grzegory: Elastic constants of gallium nitride, J. Appl. Phys. **79**(6), 3343 (1996)
31.85 M. Kazan, E. Moussaed, R. Nader, P. Masri: Elastic constants of aluminum nitride, Phys. Status Solidi C **4**(1), 204 (2007)
31.86 Y. Ohashi, M. Arakawa, J. Kushibiki, B.M. Epelbaum, A. Winnacker: Ultrasonic microspectroscopy characterization of AlN single crystals, Appl. Phys. Express **1**, 077004 (2008)
31.87 K. Tsubouchi, K. Sugai, N. Mikoshiba: AlN material constants evaluation and SAW properties on AlN/Al203 and AlN/Si, IEEE 1981 Ultrasonics Symp. (1981) p. 375
31.88 A.F. Wright: Elastic properties of zinc-blende and wurtzite AlN, GaN, and InN, J. Appl. Phys. **82**(6), 2833 (1997)
31.89 K. Kim, W. Lambrecht, B. Segall: Elastic constants and related properties of tetrahedrally bonded BN, AlN, GaN, and InN, Phys. Rev. B **53**(24), 16310 (1996)
31.90 Y. Taniyasu, M. Kasu, T. Makimoto: Threading dislocations in heteroepitaxial AlN layer grown by MOVPE on SiC (0001) substrate, J. Cryst. Growth **298**, 310 (2007)
31.91 R. Thokala, J. Chaudhuri: Calculated elastic constants of wide band gap semiconductor thin films with a hexagonal crystal structure for stress problems, Thin Solid Films **266**(2), 189 (1995)
31.92 L.E. McNeil, M. Grimsditch, R.H. French: Vibrational spectroscopy of Aluminum Nitride, J. Am. Ceram. Soc. **76**(5), 1132 (1993)
31.93 M. Ueno, A. Onodera, O. Shimomura, K. Takemura: X-ray observation of the structural phase transition of aluminum nitride under high pressure, Phys. Rev. B **45**(17), 10123 (1992)
31.94 D. Gerlich, S.L. Dole, G.A. Slack: Elastic properties of aluminum nitride, J. Phys. Chem. Solids **47**(5), 437 (1986)
31.95 P. Van Camp, V. Van Doren, J. Devreese: High-pressure properties of wurtzite- and rocksalt-type aluminum nitride, Phys. Rev. B **44**(16), 9056 (1991)
31.96 E. Ruiz, S. Alvarez, P. Alemany: Electronic structure and properties of AlN, Phys. Rev. B **49**(11), 7115 (1994)
31.97 I. Yonenaga, T. Shima, M.H.F. Sluiter: Nano-indentation hardness and elastic moduli of bulk single-crystal AlN, Jpn. J. Appl. Phys. **41**(7A), 4620 (2002)
31.98 S.-R. Jian, J.-Y. Juang: Indentation-induced mechanical deformation behaviors of AlN thin films deposited on *c*-plane sapphire, J. Nanomater. **2012**, 1 (2012)
31.99 M. Fujikane, M. Leszczyński, S. Nagao, T. Nakayama, S. Yamanaka, K. Niihara, R. Nowak: Elastic–plastic transition during nanoindentation in bulk GaN crystal, J. Alloys Compd. **450**(1/2), 405 (2008)
31.100 M.A. Moram, Z.H. Barber, C.J. Humphreys: Accurate experimental determination of the Poisson's ratio of GaN using high-resolution x-ray diffraction, J. Appl. Phys. **102**, 023505 (2007)
31.101 Z. Yang, R.N. Wang, S. Jia, D. Wang, B.S. Zhang, K.M. Lau, K.J. Chen: Mechanical characterization of suspended GaN microstructures fabricated by GaN-on-patterned-silicon technique, Appl. Phys. Lett. **88**(4), 041913 (2006)
31.102 V.A. Savastenko, A.U. Sheleg: Study of the elastic properties of gallium nitride, Phys. Status Solidi A **48**(2), K135 (1978)
31.103 R.B. Schwarz, K. Khachaturyan, E.R. Weber: Elastic moduli of gallium nitride, Appl. Phys. Lett. **70**(9), 1122 (1997)
31.104 C. Deger, E. Born, H. Angerer, O. Ambacher, M. Stutzmann, J. Hornsteiner, E. Riha, G. Fischerauer: Sound velocity of $Al_xGa_{1-x}N$ thin films obtained by surface acoustic-wave measurements, Appl. Phys. Lett. **72**(19), 2400 (1998)
31.105 C.-Y. Nam, P. Jaroenapibal, D. Tham, D.E. Luzzi, S. Evoy, J.E. Fischer: Diameter-dependent electromechanical properties of GaN nanowires, Nano Lett. **6**(2), 153 (2006)
31.106 J.-E. Jørgensen, J.M. Jakobsen, J.Z. Jiang, L. Gerward, J.S. Olsen: High-pressure x-ray diffraction study of bulk- and nanocrystalline GaN, J. Appl. Crystallogr. **36**(3), 920 (2003)
31.107 R. Nowak, M. Pessa, M. Suganuma, M. Leszczynski, I. Grzegory, S. Porowski, F. Yoshida: Elastic and plastic properties of GaN determined by nano-indentation of bulk crystal, Appl. Phys. Lett. **75**(14), 2070 (1999)
31.108 M. Fujikane, T. Yokogawa, S. Nagao, R. Nowak: Yield shear stress dependence on nanoindentation strain rate in bulk GaN crystal, Phys. Status Solidi C **8**(2), 429 (2011)
31.109 M. Martyniuk, G. Parish, H. Marchand, P.T. Fini, S.P. DenBaars, L. Faraone: Nanoindentation of laterally overgrown epitaxial gallium nitride, Electron. Mater. Lett. **8**(2), 111 (2012)

31.110 X. Wang, S.-B. Che, Y. Ishitani, A. Yoshikawa: Effect of epitaxial temperature on N-polar InN films grown by molecular beam epitaxy, J. Appl. Phys. **99**(7), 073512 (2006)

31.111 Y.-S. Lu, C.-H. Hsieh, S. Gwo, M.T. Hou, J.-S. Yao, J.A. Yeh: An investigation of the Young's modulus of single-crystalline wurtzite indium nitride using an atomic force microscopy based micromechanical bending test, Appl. Phys. Lett. **101**(22), 221906 (2012)

31.112 F. Peng, Y. Han, H. Fu, X. Yang: First-principles calculations on structure and elasticity of wurtzite-type indium nitride under pressure, J. Alloys Compd. **475**(1/2), 885 (2009)

31.113 J. Serrano, A. Bosak, M. Krisch, F.J. Manjón, A.H. Romero, N. Garro, X. Wang, A. Yoshikawa, M. Kuball: In N thin film lattice dynamics by grazing incidence inelastic x-ray scattering, Phys. Rev. Lett. **106**(20), 205501 (2011)

31.114 S.-R. Jian, C.-Y. Huang, W.-C. Ke: Nanoindentation responses of InN thin films, J. Alloys Compd. **609**, 125 (2014)

31.115 S. Kataria, T.-W. Liu, C.-L. Hsiao, S. Dhara, L.-C. Chen, K.-H. Chen, S. Dash, A.K. Tyagi: Growth orientation dependent hardness for epitaxial Wurtzite in N films, J. Nanosci. Nanotechnol. **10**(8), 5170 (2010)

31.116 C.-H. Tsai: Nanoindention study of indium nitride thin films grown using RF plasma-assisted molecular beam epitaxy, Vacuum **86**(9), 1328 (2012)

31.117 J.H. Edgar, C.H. Wei, D.T. Smith, T.J. Kistenmacher, W.A. Bryden: Hardness, elastic modulus and structure of indium nitride thin films on AlN-nucleated sapphire substrates, J. Mater. Sci. Mater. Electron. **8**(5), 307 (1997)

31.118 P.E. Van Camp, V.E. Van Doren, J.T. Devreese: High pressure structural phase transformation in gallium nitride, Solid State Commun. **81**(1), 23 (1992)

31.119 I. Yonenaga, K. Motoki: Yield strength and dislocation mobility in plastically deformed bulk single-crystal GaN, J. Appl. Phys. **90**(12), 6539 (2001)

31.120 M. Yamaguchi, T. Yagi, T. Azuhata, T. Sota, K. Suzuki, S. Chichibu, S. Nakamura: Brillouin scattering study of gallium nitride: Elastic stiffness constants, J. Phys. Condens. Matter **9**(1), 241 (1997)

31.121 I. Yonenaga: High-temperature strength of III–V nitride crystals, J. Phys. Condens. Matter **14**(48), 12947 (2002)

31.122 I. Yonenaga: High-temperature strength of bulk single crystals of III–V nitrides, J. Mater. Sci. Mater. Electron. **14**(5–7), 279 (2003)

31.123 G. Kaczmarczyk, A. Kaschner, S. Reich, A. Hoffmann, C. Thomsen, D.J. As, A.P. Lima, D. Schikora, K. Lischka, R. Averbeck, H. Riechert: Lattice dynamics of hexagonal and cubic InN: Raman-scattering experiments and calculations, Appl. Phys. Lett. **76**(15), 2122 (2000)

31.124 T. Azuhata, T. Sota, K. Suzuki, S. Nakamura: Polarized Raman spectra in GaN, J. Phys. Condens. Matter **7**(10), L129 (1995)

31.125 M. Kazan, C. Zgheib, E. Moussaed, P. Masri: Temperature dependence of Raman-active modes in AlN, Diam. Relat. Mater. **15**(4–8), 1169 (2006)

31.126 A. Link, K. Bitzer, W. Limmer, R. Sauer, C. Kirchner, V. Schwegler, M. Kamp, D.G. Ebling, K.W. Benz: Temperature dependence of the E_2 and A_1(LO) phonons in GaN and AlN, J. Appl. Phys. **86**(11), 6256 (1999)

31.127 D.Y. Song, M. Holtz, A. Chandolu, S.A. Nikishin, E.N. Mokhov, Y. Makarov, H. Helava: Optical phonon decay in bulk aluminum nitride, Appl. Phys. Lett. **89**(2), 021901 (2006)

31.128 J. Senawiratne, M. Strassburg, N. Dietz, U. Haboeck, A. Hoffmann, V. Noveski, R. Dalmau, R. Schlesser, Z. Sitar: Raman, photoluminescence and absorption studies on high quality AlN single crystals, Phys. Status Solidi C **2**(7), 2774 (2005)

31.129 M. Bickermann, B.M. Epelbaum, P. Heimann, Z.G. Herro, A. Winnacker: Orientation-dependent phonon observation in single-crystalline aluminum nitride, Appl. Phys. Lett. **86**(13), 131904 (2005)

31.130 M. Strassburg, J. Senawiratne, N. Dietz, U. Haboeck, A. Hoffmann, V. Noveski, R. Dalmau, R. Schlesser, Z. Sitar: The growth and optical properties of large, high-quality AlN single crystals, J. Appl. Phys. **96**(10), 5870 (2004)

31.131 K. Shimada, T. Sota, K. Suzuki: First-principles study on electronic and elastic properties of BN, AlN, and GaN, J. Appl. Phys. **84**(9), 4951 (1998)

31.132 K. Miwa, A. Fukumoto: First-principles calculation of the structural, electronic, and vibrational properties of gallium nitride and aluminum nitride, Phys. Rev. B **48**(11), 7897 (1993)

31.133 K. Fujito, K. Kiyomi, T. Mochizuki, H. Oota, H. Namita, S. Nagao, I. Fujimura: High-quality nonpolar m-plane GaN substrates grown by HVPE, Phys. Status Solidi A **205**(5), 1056 (2008)

31.134 H. Gao, F. Yan, H. Zhang, J. Li, J. Wang, J. Yan: First and second order Raman scattering spectroscopy of nonpolar *a*-plane GaN, J. Appl. Phys. **101**(10), 103533 (2007)

31.135 V. Darakchieva, T. Paskova, M. Schubert, H. Arwin, P.P. Paskov, B. Monemar, D. Hommel, M. Heuken, J. Off, F. Scholz, B.A. Haskell, P.T. Fini, J.S. Speck, S. Nakamura: Anisotropic strain and phonon deformation potentials in GaN, Phys. Rev. B **75**(19), 195217 (2007)

31.136 A. Goñi, H. Siegle, K. Syassen, C. Thomsen, J.-M. Wagner: Effect of pressure on optical phonon modes and transverse effective charges in GaN and AlN, Phys. Rev. B **64**(3), 035205 (2001)

31.137 J.-M. Wagner, F. Bechstedt: Properties of strained wurtzite GaN and AlN: Ab initio studies, Phys. Rev. B **66**(11), 115202 (2002)

31.138 D. Gogova, A. Kasic, H. Larsson, B. Pécz, R. Yakimova, B. Magnusson, B. Monemar, F. Tuomisto, K. Saarinen, C. Miskys, M. Stutzmann, C. Bundesmann, M. Schubert: Optical and structural characteristics of virtually unstrained bulk-like GaN, Jpn. J. Appl. Phys. **43**(4A), 1264 (2004)

31.139 D. Huang, F. Yun, M.A. Reshchikov, D. Wang, H. Morkoç, D.L. Rode, L.A. Farina, Ç. Kurdak, K.T. Tsen, S.S. Park, K.Y. Lee: Hall mobility and carrier concentration in free-standing high quality GaN templates grown by hydride vapor phase epitaxy, Solid-State Electron. **45**(5), 711 (2001)
31.140 X. Wang, S.-B. Che, Y. Ishitani, A. Yoshikawa: Experimental determination of strain-free Raman frequencies and deformation potentials for the E2 high and A1(LO) modes in hexagonal InN, Appl. Phys. Lett. **89**(17), 171907 (2006)
31.141 C. Pinquier, F. Demangeot, J. Frandon, J.-C. Chervin, A. Polian, B. Couzinet, P. Munsch, O. Briot, S. Ruffenach, B. Gil, B. Maleyre: Raman scattering study of wurtzite and rocksalt InN under high pressure, Phys. Rev. B **73**(11), 115211 (2006)
31.142 X.D. Pu, J. Chen, W.Z. Shen, H. Ogawa, Q.X. Guo: Temperature dependence of Raman scattering in hexagonal indium nitride films, J. Appl. Phys. **98**(3), 033527 (2005)
31.143 V. Darakchieva, P.P. Paskov, E. Valcheva, T. Paskova, B. Monemar, M. Schubert, H. Lu, W.J. Schaff: Deformation potentials of the E_1(TO) and E_2 modes of InN, Appl. Phys. Lett. **84**(18), 3636 (2004)
31.144 V.Y. Davydov, V.V. Emtsev, I.N. Goncharuk, A.N. Smirnov, V.D. Petrikov, V.V. Mamutin, V.A. Vekshin, S.V. Ivanov, M.B. Smirnov, T. Inushima: Experimental and theoretical studies of phonons in hexagonal InN, Appl. Phys. Lett. **75**(21), 3297 (1999)
31.145 J.S. Dyck, K. Kim, S. Limpijumnong, W.R.L. Lambrecht, K. Kash, J.C. Angus: Identification of Raman-active phonon modes in oriented platelets of InN and polycrystalline InN, Solid State Commun. **114**(7), 355 (2000)
31.146 T. Prokofyeva, M. Seon, J. Vanbuskirk, M. Holtz, S. Nikishin, N. Faleev, H. Temkin, S. Zollner: Vibrational properties of AlN grown on (111)-oriented silicon, Phys. Rev. B **63**(12), 125313 (2001)
31.147 D.G. Zhao, S.J. Xu, M.H. Xie, S.Y. Tong, H. Yang: Stress and its effect on optical properties of GaN epilayers grown on Si(111), 6H-SiC(0001), and *c*-plane sapphire, Appl. Phys. Lett. **83**(4), 677 (2003)
31.148 W. Götz, N.M. Johnson, D.P. Bour, M.D. McCluskey, E.E. Haller: Local vibrational modes of the Mg–H acceptor complex in GaN, Appl. Phys. Lett. **69**(24), 3725 (1996)
31.149 C. Van de Walle: Interactions of hydrogen with native defects in GaN, Phys. Rev. B **56**(16), R10020 (1997)
31.150 D. Gogova, A. Kasic, H. Larsson, C. Hemmingsson, B. Monemar, F. Tuomisto, K. Saarinen, L. Dobos, B. Pécz, P. Gibart, B. Beaumont: Strain-free bulk-like GaN grown by hydride-vapor-phase-epitaxy on two-step epitaxial lateral overgrown GaN template, J. Appl. Phys. **96**(1), 799 (2004)
31.151 C. Pinquier, F. Demangeot, J. Frandon, J.W. Pomeroy, M. Kuball, H. Hubel, N.W.A. van Uden, D.J. Dunstan, O. Briot, B. Maleyre, S. Ruffenach, B. Gil: Raman scattering in hexagonal InN under high pressure, Phys. Rev. B **70**(11), 113202 (2004)
31.152 J.W. Pomeroy, M. Kuball, H. Lu, W.J. Schaff, X. Wang, A. Yoshikawa: Phonon lifetimes and phonon decay in InN, Appl. Phys. Lett. **86**(22), 223501 (2005)
31.153 S. Figge, H. Kröncke, D. Hommel, B.M. Epelbaum: Temperature dependence of the thermal expansion of AlN, Appl. Phys. Lett. **94**(10), 101915 (2009)
31.154 K. Wang, R.R. Reeber: Thermal expansion Of GaN and AlN, MRS Proc. **482**, 863 (1997)
31.155 K.M. Taylor, C. Lenie: Some properties of Aluminum Nitride, J. Electrochem. Soc. **107**(4), 308 (1960)
31.156 S.N. Ivanov, P.A. Popov, G.V. Egorov, A.A. Sidorov, B.I. Kornev, L.M. Zhukova, V.P. Ryabov: Thermophysical properties of aluminum nitride ceramic, Phys. Solid State **39**(1), 81 (1997)
31.157 W. Paszkowicz, M. Knapp, S. Podsiadlo, G. Kamler, J.B. Pelka: Lattice parameters of aluminium nitride in the range 10–291 K, Acta Phys. Pol. A **101**(5), 781 (2002)
31.158 G.A. Slack, S.F. Bartram: Thermal expansion of some diamondlike crystals, J. Appl. Phys. **46**(1), 89 (1975)
31.159 W.M. Yim, R.J. Paff: Thermal expansion of AlN, sapphire, and silicon, J. Appl. Phys. **45**(3), 1456 (1974)
31.160 H.P. Maruska: The preparation and properties of vapor-deposited single-crystal-line GaN, Appl. Phys. Lett. **15**(10), 327 (1969)
31.161 M. Leszczynski, T. Suski, H. Teisseyre, P. Perlin, I. Grzegory, J. Jun, S. Porowski, T.D. Moustakas: Thermal expansion of gallium nitride, J. Appl. Phys. **76**(8), 4909 (1994)
31.162 V. Kirchner, H. Heinke, D. Hommel, J.Z. Domagala, M. Leszczynski: Thermal expansion of bulk and homoepitaxial GaN, Appl. Phys. Lett. **77**(10), 1434 (2000)
31.163 C. Roder, S. Einfeldt, S. Figge, D. Hommel: Temperature dependence of the thermal expansion of GaN, Phys. Rev. B **72**(8), 085218 (2005)
31.164 R.R. Reeber, K. Wang: Lattice parameters and thermal expansion of GaN, J. Mater. Res. **15**(1), 40 (2000)
31.165 A.U. Sheleg, V.A. Sevastenko: Investigation of thermal expansion of indium and gallium nitrides, Vestsi Akad Navuk BSSR **3**, 126 (1976)
31.166 K. Wang, R.R. Reeber: Thermal expansion and elastic properties of InN, Appl. Phys. Lett. **79**(11), 1602 (2001)
31.167 W. Paszkowicz, R. Černý, S. Krukowski: Rietveld refinement for indium nitride in the 105–295 K range, Powder Diffr. **18**(2), 114 (2003)
31.168 G.A. Slack: Nonmetallic crystals with high thermal conductivity, J. Phys. Chem. Solids **34**(2), 321 (1973)
31.169 G.A. Slack, T.F. McNelly: Ain single crystals, J. Cryst. Growth **42**, 560 (1977)
31.170 A. Witek: Some aspects of thermal conductivity of isotopically pure diamond – A comparison with nitrides, Diam. Relat. Mater. **7**(7), 962 (1998)
31.171 G.A. Slack, L.J. Schowalter, D. Morelli, J.A. Freitas: Some effects of oxygen impurities on AlN and GaN,

J. Cryst. Growth **246**(3/4), 287 (2002)
31.172 M. Bickermann, B.M. Epelbaum, A. Winnacker: Characterization of bulk AlN with low oxygen content, J. Cryst. Growth **269**(2–4), 432 (2004)
31.173 A. AlShaikhi, G.P. Srivastava: Thermal conductivity of single crystal and ceramic AlN, J. Appl. Phys. **103**(8), 083554 (2008)
31.174 A. Nikolaev, I. Nikitina, A. Zubrilov, M. Mynbaeva, Y. Melnik, V. Dmitriev: AlN wafers fabricated by hydride vapor phase epitaxy, MRS Proc. **595**, 6.5 (1999)
31.175 D.I. Florescu, V.M. Asnin, F.H. Pollak: Thermal conductivity measurements of GaN and AlN, Compd. Semicond. **7**(2), 62 (2001)
31.176 L. Qiao, H. Zhou, C. Li: Microstructure and thermal conductivity of spark plasma sintering AlN ceramics, Mater. Sci. Eng. B **99**(1–3), 102 (2003)
31.177 K. Watari, K. Ishizaki, F. Tsuchiya: Phonon scattering and thermal conduction mechanisms of sintered aluminium nitride ceramics, J. Mater. Sci. **28**(14), 3709 (1993)
31.178 E. Richter, M. Gründer, B. Schineller, F. Brunner, U. Zeimer, C. Netzel, M. Weyers, G. Tränkle: GaN boules grown by high rate HVPE, Phys. Status Solidi C **8**(5), 1450 (2011)
31.179 A. Jeżowski, P. Stachowiak, T. Plackowski, T. Suski, S. Krukowski, M. Boćkowski, I. Grzegory, B. Danilchenko, T. Paszkiewicz: Thermal conductivity of GaN crystals grown by high pressure method, Phys. Status Solidi B **240**(2), 447 (2003)
31.180 H. Shibata, Y. Waseda, H. Ohta, K. Kiyomi, K. Shimoyama, K. Fujito, H. Nagaoka, Y. Kagamitani, R. Simura, T. Fukuda: High thermal conductivity of gallium nitride (GaN) crystals grown by HVPE process, Mater. Trans. **48**(10), 2782 (2007)
31.181 W. Liu, A.A. Balandin, C. Lee, H.-Y. Lee: Increased thermal conductivity of free-standing low-dislocation-density GaN films, Phys. Status Solidi A **202**(12), R135 (2005)
31.182 E.K. Sichel, J.I. Pankove: Thermal conductivity of GaN, 25–360 K, J. Phys. Chem. Solids **38**(3), 330 (1977)
31.183 A. AlShaikhi, S. Barman, G.P. Srivastava: Theory of the lattice thermal conductivity in bulk and films of GaN, Phys. Rev. B **81**(19), 195320 (2010)
31.184 C. Mion, J.F. Muth, E.A. Preble, D. Hanser: Accurate dependence of gallium nitride thermal conductivity on dislocation density, Appl. Phys. Lett. **89**(9), 092123 (2006)
31.185 D.I. Florescu, V.A. Asnin, L.G. Mourokh, F.H. Pollak, R.J. Molnar: Doping dependence of the thermal conductivity of hydride vapor phase epitaxy grown n-GaN/Sapphire(0001) using a scanning thermal microscope, MRS Proc. **595**, F99W3.89 (1999)
31.186 D.I. Florescu, V.M. Asnin, F.H. Pollak, R.J. Molnar, C.E.C. Wood: High spatial resolution thermal conductivity and Raman spectroscopy investigation of hydride vapor phase epitaxy grown n-GaN/Sapphire(0001): Doping dependence, J. Appl. Phys. **88**(6), 3295 (2000)
31.187 S. Krukowski, A. Witek, J. Adamczyk, J. Jun, M. Bockowski, I. Grzegory, B. Lucznik, G. Nowak, M. Wróblewski, A. Presz, S. Gierlotka, S. Stelmach, B. Palosz, S. Porowski, P. Zinn: Thermal properties of indium nitride, J. Phys. Chem. Solids **59**(3), 289 (1998)
31.188 A.X. Levander, T. Tong, K.M. Yu, J. Suh, D. Fu, R. Zhang, H. Lu, W.J. Schaff, O. Dubon, W. Walukiewicz, D.G. Cahill, J. Wu: Effects of point defects on thermal and thermoelectric properties of InN, Appl. Phys. Lett. **98**(1), 012108 (2011)
31.189 A.D. Mah, W.W. Weller, A.U. Christensen: Thermodynamic Properties of Aluminum Nitride, Report of Investigation (US Bureau of Mines), Vol. RI-5716 (1961) p. 78
31.190 V.P. Glushko, L.V. Gurevich, G.A. Bergman, I.V. Weitz, V.A. Medvedev, G.A. Chachkurov, V.S. Yungman: *Thermodinamicheskiie Swoistwa Indiwidualnych Weshchestw (the old USSR)*, Vol. 1 (Nauka, Moscow 1979) p. 164
31.191 G.A. Slack, R.A. Tanzilli, R.O. Pohl, J.W. Vandersande: The intrinsic thermal conductivity of AlN, J. Phys. Chem. Solids **48**(7), 641 (1987)
31.192 J. Leitner, A. Strejc, D. Sedmidubský, K. Røužička: High temperature enthalpy and heat capacity of GaN, Thermochim. Acta **401**(2), 169 (2003)
31.193 K. Itagaki, K. Yamaguchi: High temperature heat contents of III–V semiconductor systems, Thermochim. Acta **163**, 1 (1990)
31.194 B.A. Danilchenko, T. Paszkiewicz, S. Wolski, A. Jeżowski, T. Plackowski: Heat capacity and phonon mean free path of wurtzite GaN, Appl. Phys. Lett. **89**(6), 061901 (2006)
31.195 R. Kremer, M. Cardona, E. Schmitt, J. Blumm, S. Estreicher, M. Sanati, M. Bockowski, I. Grzegory, T. Suski, A. Jezowski: Heat capacity of α-GaN: Isotope effects, Phys. Rev. B **72**(7), 075209 (2005)
31.196 J.C. Nipko, C.-K. Loong, C.M. Balkas, R.F. Davis: Phonon density of states of bulk gallium nitride, Appl. Phys. Lett. **73**(1), 34 (1998)
31.197 J. Leitner, P. Maršík, D. Sedmidubský, K. Røužička: High temperature enthalpy, heat capacity and other thermodynamic functions of solid InN, J. Phys. Chem. Solids **65**(6), 1127 (2004)
31.198 I. Zięborak-Tomaszkiewicz, R. Świerzewski, P. Gierycz: Heat capacity of indium nitride, J. Therm. Anal. Calorim. **91**(2), 649 (2008)
31.199 W. Götz, L.T. Romano, J. Walker, N.M. Johnson, R.J. Molnar: Hall-effect analysis of GaN films grown by hydride vapor phase epitaxy, Appl. Phys. Lett. **72**(10), 1214 (1998)
31.200 D.L. Rode, R.K. Willardson, A.C. Beer: *Semiconductors and Semimetals*, Vol. 10 (Academic, New York 1975)
31.201 K. Seeger: *Semiconductor Physics*, 2nd edn. (Springer, Berlin, Heidelberg 1982)
31.202 V.W.L. Chin, T.L. Tansley, T. Osotchan: Electron mobilities in gallium, indium, and aluminum nitrides, J. Appl. Phys. **75**(11), 7365 (1994)
31.203 D.L. Rode, D.K. Gaskill: Electron Hall mobility of n-GaN, Appl. Phys. Lett. **66**(15), 1972 (1995)

31.204 M.E. Lin, B. Sverdlov, G.L. Zhou, H. Morkoc: A comparative study of GaN epilayers grown on sapphire and SiC substrates by plasma-assisted molecular-beam epitaxy, Appl. Phys. Lett. **62**(26), 3479 (1993)
31.205 H.M. Ng, D. Doppalapudi, T.D. Moustakas, N.G. Weimann, L.F. Eastman: The role of dislocation scattering in n-type GaN films, Appl. Phys. Lett. **73**(6), 821 (1998)
31.206 D.C. Look, J.R. Sizelove: Dislocation scattering in GaN, Phys. Rev. Lett. **82**(6), 1237 (1999)
31.207 H.W. Choi, J. Zhang, S.J. Chua: Dislocation scattering in n-GaN, Proc. ICMAT 2001 Symp. Mater. for Optoelectron. High Freq. Electron. Appl (2001) p. 567
31.208 J.Y. Shi, L.P. Yu, Y.Z. Wang, G.Y. Zhang, H. Zhang: Influence of different types of threading dislocations on the carrier mobility and photoluminescence in epitaxial GaN, Appl. Phys. Lett. **80**(13), 2293 (2002)
31.209 N.G. Weimann, L.F. Eastman, D. Doppalapudi, H.M. Ng, T.D. Moustakas: Scattering of electrons at threading dislocations in GaN, J. Appl. Phys. **83**(7), 3656 (1998)
31.210 Z.-Q. Fang, D.C. Look, W. Kim, Z. Fan, A. Botchkarev, H. Morkoc: Deep centers in n-GaN grown by reactive molecular beam epitaxy, Appl. Phys. Lett. **72**(18), 2277 (1998)
31.211 W. Kim, A.E. Botohkarev, H. Morkoc, Z.-Q. Fang, D.C. Look, D.J. Smith: Effect of ammonia flow rate on impurity incorporation and material properties of Si-doped GaN epitaxial films grown by reactive molecular beam epitaxy, J. Appl. Phys. **84**(12), 6680 (1998)
31.212 Q.-S. Zhu, N. Sawaki: Nitrogen vacancy scattering in n-GaN grown by metal-organic vapor phase epitaxy, Appl. Phys. Lett. **76**(12), 1594 (2000)
31.213 Z. Chen, H. Yuan, D.-C. Lu, X. Sun, S. Wan, X. Liu, P. Han, X. Wang, Q. Zhu, Z. Wang: Nitrogen vacancy scattering in GaN grown by metal-organic vapor phase epitaxy, Solid-State Electron. **46**(12), 2069 (2002)
31.214 D.C. Look, R.J. Molnar: Degenerate layer at GaN/Sapphire interface: Influence on Hall-effect measurements, Appl. Phys. Lett. **70**(25), 3377 (1997)
31.215 S. Nakamura: GaN growth using GaN buffer layer, Jpn. J. Appl. Phys. Part 2 **30**(10A), 1705 (1991)
31.216 S. Nakamura, T. Mukai: High-quality InGaN films grown on GaN films, Jpn. J. Appl. Phys. Part 2 **31**(10B), 1457 (1992)
31.217 D. Huang, F. Yun, M.A. Reshchikov, D. Wang, H. Morkoc, D.L. Rode, L.A. Farina, C. Kurdak, K.T. Tsen, S.S. Park, K.Y. Lee: Hall mobility and carrier concentration in free-standing high quality GaN templates grown by hydride vapor phase epitaxy, Solid-State Electron. **45**(5), 711 (2001)
31.218 S. Nakamura, T. Mukai, M. Senoh: Si- and Ge-doped GaN films grown with GaN buffer layers, Jpn. J. Appl. Phys. **31**, 2883 (1992)
31.219 S. Nakamura, T. Mukai, M. Senoh: In situ monitoring and hall measurements of GaN grown with GaN buffer layers, J. Appl. Phys. **71**(11), 5543 (1992)
31.220 S.C. Binari, H.C. Dietrich: III-V Nitride electronic devices. In: *GaN and Related Materials*, ed. by S.J. Pearson (Gordon Breach, New York 1997) pp. 509–534
31.221 F. Yun, M.A. Reshchikov, K. Jones, P. Visconti, H. Morkoc, S.S. Park, K.Y. Lee: Electrical, structural, and optical characterization of free-standing GaN template grown by hydride vapor phase epitaxy, Solid-State Electron. **44**(12), 2225 (2000)
31.222 B. Heying, I. Smorchkova, C. Poblenz, C. Elsass, P. Fini, S. Den Baars, U. Mishra, J.S. Speck: Optimization of the surface morphologies and electron mobilities in GaN grown by plasma-assisted molecular beam epitaxy, Appl. Phys. Lett. **77**(18), 2885 (2000)
31.223 D.D. Koleske, R.L. Henry, M.E. Twigg, J.C. Culbertson, S.C. Binari, A.E. Wickenden, M. Fatemi: Influence of AlN nucleation layer temperature on GaN electronic properties grown on SiC, Appl. Phys. Lett. **80**(23), 4372 (2002)
31.224 W. Gotz, N.M. Johnson, C. Chen, H. Liu, C. Kuo, W. Imler: Activation energies of Si donors in GaN, Appl. Phys. Lett. **68**(22), 3144 (1996)
31.225 D.C. Look, D.C. Reynolds, J.W. Hemsky, J.R. Sizelove, R.L. Jones, R.J. Molnar: Defect donor and acceptor in GaN, Phys. Rev. Lett. **79**(12), 2273 (1997)
31.226 M. Ilegems, H.C. Montgomery: Electrical properties of n-type vapor-grown gallium nitride, J. Phys. Chem. Solids **35**(5), 885 (1973)
31.227 M.A. Littlejohn, J.R. Hauser, T.H. Glisson: Monte Carlo calculation of the velocity-field relationship for gallium nitride, Appl. Phys. Lett. **26**(11), 625 (1975)
31.228 U.V. Bhapkar, M.S. Shur: Monte Carlo calculation of velocity-field characteristics of wurtzite GaN, J. Appl. Phys. **82**(4), 1649 (1997)
31.229 J.D. Albrecht, R.P. Wang, P.P. Ruden, M. Farahmand, K.F. Brennan: Monte Carlo calculation of electron transport properties of bulk AlN, J. Appl. Phys. **83**(3), 1446 (1998)
31.230 S. Dhar, S. Ghosh: Low field electron mobility in GaN, J. Appl. Phys. **86**(5), 2668 (1999)
31.231 J.G. Kim, A.C. Frenkel, T. Liu, R.M. Park: Growth by molecular beam epitaxy and electrical characterization of Si-doped zinc blende GaN films deposited on -SiC coated(001) Si substrates, Appl. Phys. Lett. **65**(1), 91 (1994)
31.232 R.J. Molnar, W. Götz, L.T. Romano, N.M. Johnson: Growth of gallium nitride by hydride vapor-phase epitaxy, J. Cryst. Growth **178**(1/2), 147 (1997)
31.233 S. Yamaguchi, M. Kariya, S. Nitta, T. Takeuchi, C. Wetzel, H. Amano, I. Akasaki: Structural properties of InN on GaN grown by metalorganic vapor-phase epitaxy, J. Appl. Phys. **85**(11), 7682 (1999)
31.234 H. Morkoc: Wurtzite GaN-based heterostructures by molecular beam epitaxy, IEEE J. Sel. Top. Quantum Electron. **4**(3), 537 (1998)
31.235 S. Keller, B.P. Keller, Y.-F. Wu, B. Heying, D. Kapolnek, J.S. Speck, U.K. Mishra, S.P. DenBaars: Influence of sapphire nitridation on properties of gallium nitride grown by metalorganic chemical

vapor deposition, Appl. Phys. Lett. **68**(11), 1525 (1996)

31.236 B. Wang, P. Yu, B. Kucukgok, A.G. Melton, N. Lu, I.T. Ferguson: Characterization of undoped and Si-doped bulk GaN fabricated by hydride vapor phase epitaxy, Phys. Status Solidi C Curr. Top, Solid State Phys. **11**(3/4), 573 (2014)

31.237 T. Sochacki, Z. Bryan, M. Amilusik, M. Bobea, M. Fijalkowski, I. Bryan, B. Lucznik, R. Collazo, J.L. Weyher, R. Kucharski, I. Grzegory, M. Bockowski, Z. Sitar: HVPE-GaN grown on MOCVD-GaN/sapphire template and ammonothermal GaN seeds: Comparison of structural, optical, and electrical properties, J. Cryst. Growth **394**(0), 55 (2014)

31.238 T.T. Mnatsakanov, M.E. Levinshtein, L.I. Pomortseva, S.N. Yurkov, G.S. Simin, M.A. Khan: Carrier mobility model for GaN, Solid-State Electron. **47**(1), 111 (2003)

31.239 D.M. Caughey, R.E. Thomas: Carrier mobilities in silicon empirically related to doping and field, Proceeding IEEE **55**(12), 2192 (1967)

31.240 J. Edwards, K. Kawabe, G. Stevens, R.H. Tredgold: Space charge conduction and electrical behaviour of aluminium nitride single crystals, Solid State Commun. **3**(5), 99 (1965)

31.241 K. Kawabe, R.H. Tredgold, Y. Inuishi: Electrical and optical properties of AlN – A thermostable semiconductor, Electr. Eng. Jpn. **87**(1), 62 (1967)

31.242 G.A. Cox, D.O. Cummins, K. Kawabe, R.H. Tredgold: On the preparation, optical properties and electrical behaviour of aluminium nitride, J. Phys. Chem. Solids **28**(4), 543 (1967)

31.243 W.M. Yim, E.J. Stofko, P.J. Zanzucchi, J.I. Pankove, M. Ettenberg, S.L. Gilbert: Epitaxially grown AlN and its optical band gap, J. Appl. Phys. **44**(1), 292 (1973)

31.244 S. Yoshida, S. Misawa, Y. Fujii, S. Takada, H. Hayakawa, S. Gonda, A. Itoh: Reactive molecular beam epitaxy of aluminium nitride, J. Vac. Sci. Technol. **16**(4), 990 (1979)

31.245 A.G. Gorbatov, V.M. Kamyshoc: Sov. Powder Metall. Met. Ceram. **9**, 917 (1970)

31.246 R.F. Rutz: Ultraviolet electroluminescence in AlN, Appl. Phys. Lett. **28**(7), 379 (1976)

31.247 R.F. Rutz, E.P. Harris, J.J. Cuomo: IBM J. Res. Dev. **17**, 61 (1973)

31.248 A. Fara, F. Bernardini, V. Fiorentini: Theoretical evidence for the semi-insulating character of AlN, J. Appl. Phys. **85**(3), 2001 (1999)

31.249 K. Wongchotigul, N. Chen, D.P. Zhang, X. Tang, M.G. Spencer: Low resistivity aluminum nitride: Carbon (AlN:C) films grown by metal organic chemical vapor deposition, Mater. Lett. **26**(4/5), 223 (1996)

31.250 H.J. Hovel, J.J. Cuomo: Electrical and optical properties or rf-sputtered GaN and InN, Appl. Phys. Lett. **20**(2), 71 (1972)

31.251 T.L. Tansley, C.P. Foley: Electron mobility in indium nitride, Electron. Lett. **20**(25/26), 1066 (1984)

31.252 K.L. Westra, M.J. Brett: Near IR optical properties of sputtered InN films, Thin Solid Films **192**(2), 227 (1990)

31.253 J.S. Morgan, T.J. Kistenmacher, W.A. Bryden, S.A. Ecelberger: Sputter deposition of indium nitride on the (111) face of elemental and compound semiconductors, Proc. Evolution of Thin-Film and Surface Microstructure Symp (1991) p. 383

31.254 T.J. Kistenmacher, W.A. Bryden: Overgrowth of indium nitride thin films on aluminum nitride nucleated (00.1) sapphire by reactive magnetron sputtering, Appl. Phys. Lett. **59**(15), 1844 (1991)

31.255 S. Strite, D. Chandrasekhar, D.J. Smith, J. Sariel, H. Chen, N. Teraguchi, H. Morkoç: Structural properties of InN films grown on GaAs substrates: Observation of the zincblende polytype, J. Cryst. Growth **127**(1–4), 204 (1993)

31.256 C.R. Abernathy, S.J. Pearton, F. Ren, P.W. Wisk: Growth of InN for ohmic contact formation by electron cyclotron resonance metalorganic molecular-beam epitaxy, J. Vac. Sci. Technol. B **11**(2), 179 (1993)

31.257 W.A. Bryden, S.A. Ecelberger, M.E. Hawley, T.J. Kistenmacher: ECR-assisted reactive magnetron sputtering of InN, Proc. 1994 MRS Spring Meet (1994) p. 497

31.258 T. Maruyama, T. Morishita: Indium nitride thin films prepared by radio-frequency reactive sputtering, J. Appl. Phys. **76**(10), 5809 (1994)

31.259 H. Lu, W.J. Schaff, J. Hwang, H. Wu, W. Yeo, A. Pharkya, L.F. Eastman: Improvement on epitaxial grown of InN by migration enhanced epitaxy, Appl. Phys. Lett. **77**(16), 2548 (2000)

31.260 Y. Saito, N. Teraguchi, A. Suzuki, T. Araki, Y. Nanishi: Growth of high-electron-mobility InN by RF molecular beam epitaxy, Jpn. J. Appl. Phys. Part 2 Lett. **40**(2A), 91 (2001)

31.261 J. Aderhold, V.Y. Davydov, F. Fedler, H. Klausing, D. Mistele, T. Rotter, O. Semchinova, J. Stemmer, J. Graul: InN thin films grown by metalorganic molecular beam epitaxy on sapphire substrates, J. Cryst. Growth **222**(4), 701 (2001)

31.262 H. Lu, W.J. Schaff, J. Hwang, H. Wu, G. Koley, L.F. Eastman: Effect of an AlN buffer layer on the epitaxial growth of InN by molecular-beam epitaxy, Appl. Phys. Lett. **79**(10), 1489 (2001)

31.263 E. Motlan, M. Goldys, T.L. Tansley: Optical and electrical properties of InN grown by radio-frequency reactive sputtering, J. Cryst. Growth **241**(1/2), 165 (2002)

31.264 Y. Saito, T. Yamaguchi, H. Kanazawa, K. Kano, T. Araki, Y. Nanishi, N. Teraguchi, A. Suzuki: Growth of high-quality InN using low-temperature intermediate layers by RF-MBE, Proc. Thirteen. Int. Conf. Cryst. Growth Conj. Unction Elev. Int. Conf. Vap. Growth Epitaxy (2002) p. 1017

31.265 M. Higashiwaki, T. Matsui: High-quality InN film grown on a low-temperature-grown GaN intermediate layer by plasma-assisted molecular-beam epitaxy, Jpn. J. Appl. Phys. Part 2 Lett. **41**(5B), 540 (2002)

31.266 H.W. Lu, J. Schaff, L.F. Eastman, J. Wu, W. Walukiewicz, K.M. Yu, J.W. Auger III, E.E. Haller, O. Ambacher: Conf. Digest of the 44th Electron.

Mat. Conf., Santa Barbara (2002) p. 2
31.267 M. Higashiwaki, T. Matsui: Epitaxial growth of high-quality InN films on sapphire substrates by plasma-assisted molecular-beam epitaxy, J. Cryst. Growth **252**(1–3), 128 (2003)
31.268 T.L. Tansley, C.P. Foley: Proc. 3rd Inter. Conf. Semi-Insulating III-V-Materials, Warm Springs, 1984, ed. by J. Blakemore (Shiva, London 1985) pp. 497–500
31.269 C. Stampfl, C.G. Van de Walle, D. Vogel, P. Kruger, J. Pollmann, D. Vogel: Native defects and impurities in InN: First-principles studies using the local-density approximation and self-interaction and relaxation-corrected pseudopotentials, Phys. Rev. B Condens. Matter **61**(12), 7846 (2000)
31.270 D.C. Look, H. Lu, W.J. Schaff, J. Jasinski, Z. Liliental-Weber: Donor and acceptor concentrations in degenerate InN, Appl. Phys. Lett. **80**(2), 258 (2002)
31.271 J.D. Albrecht, R.P. Wang, P.P. Ruden, M. Farahmand, K.F. Brennan: Electron transport characteristics of GaN for high temperature device modeling, J. Appl. Phys. **83**(9), 4777 (1998)
31.272 S.K. O'Leary, B.E. Foutz, M.S. Shur, U.V. Bhapkar, L.F. Eastman: Monte Carlo simulation of electron transport in wurtzite aluminum nitride, Solid State Commun. **105**(10), 621 (1998)
31.273 B. Gelmont, K. Kim, M. Shur: Monte Carlo simulation of electron transport in gallium nitride, J. Appl. Phys. **74**(3), 1818 (1993)
31.274 N.S. Mansour, K.W. Kim, M.A. Littlejohn: Theoretical study of electron transport in gallium nitride, J. Appl. Phys. **77**(6), 2834 (1995)
31.275 J. Kolník, İ.H. Oğuzman, K.F. Brennan, R. Wang, P.P. Ruden, Y. Wang: Electronic transport studies of bulk zincblende and wurtzite phases of GaN based on an ensemble Monte Carlo calculation including a full zone band structure, J. Appl. Phys. **78**(2), 1033 (1995)
31.276 M. Shur, B. Gelmont, M.A. Khan: Electron mobility in two-dimensional electron gas in AlGaN/GaN heterostructures and in bulk GaN, Proc. 37th Electronic Materials Conf. III–V Nitrides and Silicon Carbide, 1995 (1996) p. 777
31.277 S.K. O'Leary, B.E. Foutz, M.S. Shur, U.V. Bhapkar, L.F. Eastman: Electron transport in wurtzite indium nitride, J. Appl. Phys. **83**(2), 826 (1998)
31.278 E. Bellotti, B.K. Doshi, K.F. Brennan, J.D. Albrecht, P.P. Ruden: Ensemble Monte Carlo study of electron transport in wurtzite InN, J. Appl. Phys. **85**(2), 916 (1999)
31.279 B.E. Foutz, S.K. O'Leary, M.S. Shur, L.F. Eastman: Transient electron transport in wurtzite GaN, InN, and AlN, J. Appl. Phys. **85**(11), 7727 (1999)
31.280 C.G. Rodrigues, V.N. Freire, A.R. Vasconcellos, R. Luzzi: Velocity overshoot onset in nitride semiconductors, Appl. Phys. Lett. **76**(14), 1893 (2000)
31.281 M. Wraback, H. Shen, S. Rudin, E. Bellotti: Experimental and theoretical studies of transient electron velocity overshoot in GaN, Phys. Status Solidi B **234**(3), 810 (2002)
31.282 R. Collazo, R. Schlesser, Z. Sitar: Experimental observation of electron velocity overshoot in AlN, Appl. Phys. Lett. **81**(27), 5189 (2002)
31.283 B. Monemar, U. Lindefelt, W.M. Chen: Electronic structure of bound excitons in semiconductors, Phys. B Condens. Matter **146**(1), 2–256 (1987)
31.284 A. Rodina, M. Dietrich, A. Göldner, L. Eckey, A. Hoffmann, A. Efros, M. Rosen, B. Meyer: Free excitons in wurtzite GaN, Phys. Rev. B **64**(11), 115204 (2001)
31.285 R. Dingle, M. Ilegems: Donor-acceptor pair recombination in GaN, Solid State Commun. **9**(3), 175 (1971)
31.286 E.L. Ivchenko: *Excitons* (North-Holland, Amsterdam 1982)
31.287 J.J. Song, W. Shan: *Group III Nitride Semiconductor Compounds: Physics and Applications* (Oxford Univ. Press, Clarendon, New York 1998)
31.288 B. Monemar, J.P. Bergman, I.A. Buyanova: Optical characterization of GaN and related material. In: *GaN and Related Material*, ed. by S.J. Pearton (Golden Breach, Amsterdam 1997) p. 85
31.289 R. Dingle, D. Sell, S. Stokowski, M. Ilegems: Absorption, reflectance, and luminescence of GaN epitaxial layers, Phys. Rev. B **4**(4), 1211 (1971)
31.290 B. Monemar: Fundamental energy gap of GaN from photoluminescence excitation spectra, Phys. Rev. B **10**(2), 676 (1974)
31.291 B. Gil, O. Briot, R.-L. Aulombard: Valence-band physics and the optical properties of GaN epilayers grown onto sapphire with wurtzite symmetry, Phys. Rev. B **52**(24), R17028 (1995)
31.292 W. Shan, B. Little, A. Fischer, J. Song, B. Goldenberg, W. Perry, M. Bremser, R. Davis: Binding energy for the intrinsic excitons in wurtzite GaN, Phys. Rev. B **54**(23), 16369 (1996)
31.293 M. Smith, G.D. Chen, J.Z. Li, J.Y. Lin, H.X. Jiang, A. Salvador, W.K. Kim, O. Aktas, A. Botchkarev, H. Morkoç: Excitonic recombination in GaN grown by molecular beam epitaxy, Appl. Phys. Lett. **67**(23), 3387 (1995)
31.294 R. Kucharski, M. Rudziński, M. Zajac, R. Doradziński, J. Garczyński, L. Sierzputowski, R. Kudrawiec, J. Serafińczuk, W. Strupiński, R. Dwiliński: Nonpolar GaN substrates grown by ammonothermal method, Appl. Phys. Lett. **95**(13), 131119 (2009)
31.295 R. Dwilinski, R. Doradzinski, J. Garczynski, L.P. Sierzputowski, M. Zajac, M. Rudzinski: Homoepitaxy on bulk ammonothermal GaN, J. Cryst. Growth **311**(10), 3058 (2009)
31.296 R. Kudrawiec, M. Rudziński, J. Serafinczuk, M. Zajac, J. Misiewicz: Photoreflectance study of exciton energies and linewidths for homoepitaxial and heteroepitaxial GaN layers, J. Appl. Phys. **105**(9), 093541 (2009)
31.297 K.P. Korona, A. Wysmołek, K. Pakuła, R. Stępniewski, J.M. Baranowski, I. Grzegory, B. Łucznik, M. Wróblewski, S. Porowski: Exciton region reflectance of homoepitaxial GaN layers, Appl. Phys. Lett. **69**(6), 788 (1996)
31.298 K. Kornitzer, T. Ebner, M. Grehl, K. Thonke, R. Sauer, C. Kirchner, V. Schwegler, M. Kamp, M. Leszczynski, I. Grzegory, S. Porowski: High-resolution photoluminescence and reflectance spec-

tra of homoepitaxial GaN layers, Phys. Status Solidi B **216**(1), 5 (1999)
31.299 B.J. Skromme, K.C. Palle, C.D. Poweleit, H. Yamane, M. Aoki, F.J. DiSalvo: Optical spectroscopy of bulk GaN crystals grown from a Na–Ga melt, Appl. Phys. Lett. **81**(20), 3765 (2002)
31.300 R. Kucharski, M. Zajac, R. Doradzinski, J. Garczynski, L. Sierzputowski, R. Kudrawiec, J. Serafinczuk, J. Misiewicz, R. Dwilinski: Structural and optical properties of semipolar GaN substrates obtained by ammonothermal method, Appl. Phys. Express **3**(10), 101001 (2010)
31.301 P. Paskov, T. Paskova, P. Holtz, B. Monemar: Polarized photoluminescence study of free and bound excitons in free-standing GaN, Phys. Rev. B **70**(3), 035210 (2004)
31.302 O. Aoudé, P. Disseix, J. Leymarie, A. Vasson, M. Leroux, E. Aujol, B. Beaumont, A. Trassoudaine, Y. André: Continuous-wave and ultrafast coherent reflectivity studies of excitons in bulk GaN, Phys. Rev. B **77**(4), 045206 (2008)
31.303 B. Monemar, P.P. Paskov, J.P. Bergman, A.A. Toropov, T.V. Shubina, T. Malinauskas, A. Usui: Recombination of free and bound excitons in GaN, Phys. Status Solidi B **245**(9), 1723 (2008)
31.304 M. Tchounkeu, O. Briot, B. Gil, J.P. Alexis, R.-L. Aulombard: Optical properties of GaN epilayers on sapphire, J. Appl. Phys. **80**(9), 5352 (1996)
31.305 T. Gühne, Z. Bougrioua, S. Laügt, M. Nemoz, P. Vennéguès, B. Vinter, M. Leroux: Band-edge photoluminescence and reflectivity of nonpolar $(11\bar{2}0)$ and semipolar $(11\bar{2}2)$ GaN formed by epitaxial lateral overgrowth on sapphire, Phys. Rev. B **77**(7), 075308 (2008)
31.306 P. Misra, U. Behn, O. Brandt, H.T. Grahn, B. Imer, S. Nakamura, S.P. DenBaars, J.S. Speck: Polarization anisotropy in GaN films for different nonpolar orientations studied by polarized photoreflectance spectroscopy, Appl. Phys. Lett. **88**(16), 161920 (2006)
31.307 A.V. Rodina, M. Dietrich, A. Göldner, L. Eckey, A.L. Efros, M. Rosen, A. Hoffmann, B.K. Meyer: Exciton energy structure in Wurtzite GaN, Phys. Status Solidi B **216**(1), 21 (1999)
31.308 W. Shan, T.J. Schmidt, X.H. Yang, S.J. Hwang, J.J. Song, B. Goldenberg: Temperature dependence of interband transitions in GaN grown by metalorganic chemical vapor deposition, Appl. Phys. Lett. **66**(8), 985 (1995)
31.309 F. Hamdani, A. Botchkarev, W. Kim, H. Morkoç, M. Yeadon, J.M. Gibson, S.-C.Y. Tsen, D.J. Smith, D.C. Reynolds, D.C. Look, K. Evans, C.W. Litton, W.C. Mitchel, P. Hemenger: Optical properties of GaN grown on ZnO by reactive molecular beam epitaxy, Appl. Phys. Lett. **70**(4), 467 (1997)
31.310 W. Shan, A.J. Fischer, J.J. Song, G.E. Bulman, H.S. Kong, M.T. Leonard, W.G. Perry, M.D. Bremser, R.F. Davis: Optical studies of GaN and GaN/AlGaN heterostructures on SiC substrates, Appl. Phys. Lett. **69**(6), 740 (1996)
31.311 K. Pakuła, A. Wysmołek, K.P. Korona, J.M. Baranowski, R. Stępniewski, I. Grzegory, M. Boćkowski, J. Jun, S. Krukowski, M. Wróblewski, S. Porowski: Luminescence and reflectivity in the exciton region of homoepitaxial GaN layers grown on GaN substrates, Solid State Commun. **97**(11), 919 (1996)
31.312 Y.S. Huang, F.H. Pollak, S.S. Park, K.Y. Lee, H. Morkoç: Contactless electroreflectance, in the range of 20–300 K, of freestanding wurtzite GaN prepared by hydride-vapor-phase epitaxy, J. Appl. Phys. **94**(2), 899 (2003)
31.313 L. Eckey, L. Podlowski, A. Goldner, A. Hoffmann, I. Broser, B.K. Meyer, D. Volm, T. Streibl, K. Hiramatsu, T. Detchprohm: Excitonic structure of GaN epitaxial films grown by hydride-vapor-phase epitaxy, Inst. Phys. Conf. Ser. **142**, 943 (1996)
31.314 P. Paskov, T. Paskova, P. Holtz, B. Monemar: Spin-exchange splitting of excitons in GaN, Phys. Rev. B **64**(11), 115201 (2001)
31.315 A. Shikanai, T. Azuhata, T. Sota, S. Chichibu, A. Kuramata, K. Horino, S. Nakamura: Biaxial strain dependence of exciton resonance energies in wurtzite GaN, J. Appl. Phys. **81**(1), 417 (1997)
31.316 B. Monemar, J.P. Bergman, I.A. Buyanova, H. Amano, I. Akasaki, T. Detchprohm, K. Hiramatsu, N. Sawaki: The excitonic bandgap of GaN: Dependence on substrate, Solid-State Electron. **41**(2), 239 (1997)
31.317 J. Hopfield: Theory of the contribution of excitons to the complex dielectric constant of crystals, Phys. Rev. **112**(5), 1555 (1958)
31.318 T. Steiner, M. Thewalt, E. Koteles, J. Salerno: Effect of neutral donor scattering on the time-dependent exciton-polariton photoluminescence line shape in GaAs, Phys. Rev. B **34**(2), 1006 (1986)
31.319 B. Gil, S. Clur, O. Briot: The exciton-polariton effect on the photoluminescence of GaN on sapphire, Solid State Commun. **104**(5), 267 (1997)
31.320 R. Stępniewski, K. Korona, A. Wysmołek, J. Baranowski, K. Pakuła, M. Potemski, G. Martinez, I. Grzegory, S. Porowski: Polariton effects in reflectance and emission spectra of homoepitaxial GaN, Phys. Rev. B **56**(23), 15151 (1997)
31.321 K. Torii, T. Deguchi, T. Sota, K. Suzuki, S. Chichibu, S. Nakamura: Reflectance and emission spectra of excitonic polaritons in GaN, Phys. Rev. B **60**(7), 4723 (1999)
31.322 S. Rudin, T. Reinecke, B. Segall: Temperature-dependent exciton linewidths in semiconductors, Phys. Rev. B **42**(17), 11218 (1990)
31.323 A.J. Fischer, W. Shan, J.J. Song, Y.C. Chang, R. Horning, B. Goldenberg: Temperature-dependent absorption measurements of excitons in GaN epilayers, Appl. Phys. Lett. **71**(14), 1981 (1997)
31.324 X.B. Zhang, T. Taliercio, S. Kolliakos, P. Lefebvre: Influence of electron-phonon interaction on the optical properties of III nitride semiconductors, J. Phys. Condens. Matter **13**(32), 7053 (2001)
31.325 I.A. Buyanova, J.P. Bergman, B. Monemar, H. Amano, I. Akasaki: Intrinsic optical properties of GaN epilayers grown on SiC substrates: Effect

of the built-in strain, Appl. Phys. Lett. **69**(9), 1255 (1996)
31.326 S. Permogorov: *Excitons* (North-Holland, Amsterdam 1982)
31.327 A. Viswanath, J. Lee, D. Kim, C. Lee, J. Leem: Exciton-phonon interactions, exciton binding energy, and their importance in the realization of room-temperature semiconductor lasers based on GaN, Phys. Rev. B **58**(24), 16333 (1998)
31.328 M. Smith, G.D. Chen, J.Y. Lin, H.X. Jiang, M.A. Khan, C.J. Sun, Q. Chen, J.W. Yang: Free excitonic transitions in GaN, grown by metal-organic chemical-vapor deposition, J. Appl. Phys. **79**(9), 7001 (1996)
31.329 M. Smith, G.D. Chen, J.Y. Lin, H.X. Jiang, A. Salvador, B.N. Sverdlov, A. Botchkarev, H. Morkoç: Dynamics of a band-edge transition in GaN grown by molecular beam epitaxy, Appl. Phys. Lett. **66**(25), 3474 (1995)
31.330 D.C. Reynolds, D.C. Look, W. Kim, O. Aktas, A. Botchkarev, A. Salvador, H. Morkoç, D.N. Talwar: Ground and excited state exciton spectra from GaN grown by molecular-beam epitaxy, J. Appl. Phys. **80**(1), 594 (1996)
31.331 R. Pässler: Dispersion-related assessments of temperature dependences for the fundamental band gap of hexagonal GaN, J. Appl. Phys. **90**(8), 3956 (2001)
31.332 R. Stępniewski, M. Potemski, A. Wysmołek, K. Pakuła, J. Baranowski, J. Łusakowski, I. Grzegory, S. Porowski, G. Martinez, P. Wyder: Symmetry of excitons in GaN, Phys. Rev. B **60**(7), 4438 (1999)
31.333 S. Hess, F. Walraet, R. Taylor, J. Ryan, B. Beaumont, P. Gibart: Dynamics of resonantly excited excitons in GaN, Phys. Rev. B **58**(24), R15973 (1998)
31.334 Y. Zhong, K.S. Wong, W. Zhang, D.C. Look: Radiative recombination and ultralong exciton photoluminescence lifetime in GaN freestanding film via two-photon excitation, Appl. Phys. Lett. **89**(2), 022108 (2006)
31.335 G. Neu, M. Teisseire, P. Lemasson, H. Lahreche, N. Grandjean, F. Semond, B. Beaumont, I. Grzegory, S. Porowski, R. Triboulet: Selective photoluminescence spectroscopy of shallow levels in wide band gap semiconductors, Phys. B Condens. Matter **302/303**, 39 (2001)
31.336 J.M. Baranowski, Z. Liliental-Weber, K. Korona, K. Pakuła, R. Stępniewski, A. Wysmołek, I. Grzegory, G. Nowak, S. Porowski, B. Monemar, P. Bergman: Structural and optical properties of homoepitaxial GaN layers, MRS Proc. **449**, 393 (1996)
31.337 J. Freitas, W. Moore, B. Shanabrook, G. Braga, S. Lee, S. Park, J. Han: Donor-related recombination processes in hydride-vapor-phase epitaxial GaN, Phys. Rev. B **66**(23), 233311 (2002)
31.338 A.K. Viswanath: Growth and optical properties of GaN. In: *Semiconductors and Semimetals*, Vol. 73, ed. by R. Willardson, H.S. Nalwa (Academic, San Diego 2001) p. 63
31.339 P. Dean, J. Haynes, W. Flood: New radiative recombination processes involving neutral donors and acceptors in silicon and germanium, Phys. Rev. **161**(3), 711 (1967)
31.340 M.A. Reshchikov, D. Huang, F. Yun, L. He, H. Morkoç, D.C. Reynolds, S.S. Park, K.Y. Lee: Photoluminescence of GaN grown by molecular-beam epitaxy on a freestanding GaN template, Appl. Phys. Lett. **79**(23), 3779 (2001)
31.341 W.J. Moore, J.A. Freitas, G.C.B. Braga, R.J. Molnar, S.K. Lee, K.Y. Lee, I.J. Song: Identification of Si and O donors in hydride-vapor-phase epitaxial GaN, Appl. Phys. Lett. **79**(16), 2570 (2001)
31.342 E.I. Rashba, G.E. Gurgenishvili: Edge absorption theory in semiconductors, Sov. Phys. Solid State **4**(4), 759 (1962)
31.343 B. Monemar, P. Paskov, T. Paskova, J. Bergman, G. Pozina, W. Chen, P. Hai, I. Buyanova, H. Amano, I. Akasaki: Optical characterization of III-nitrides, Mater. Sci. Eng. B **93**(1–3), 112 (2002)
31.344 G. Pozina, N.V. Edwards, J.P. Bergman, T. Paskova, B. Monemar, M.D. Bremser, R.F. Davis: Time-resolved spectroscopy of strained GaN/AlN/6H-SiC heterostructures grown by metalorganic chemical vapor deposition, Appl. Phys. Lett. **78**(8), 1062 (2001)
31.345 S. Pau, J. Kuhl, M. Khan, C. Sun: Application of femtosecond-excitation correlation to the study of emission dynamics in hexagonal GaN, Phys. Rev. B **58**(19), 12916 (1998)
31.346 T. Shubina, M. Glazov, A. Toropov, N. Gippius, A. Vasson, J. Leymarie, A. Kavokin, A. Usui, J. Bergman, G. Pozina, B. Monemar: Resonant light delay in GaN with ballistic and diffusive propagation, Phys. Rev. Lett. **100**(8), 087402 (2008)
31.347 K. Kornitzer, T. Ebner, K. Thonke, R. Sauer, C. Kirchner, V. Schwegler, M. Kamp, M. Leszczynski, I. Grzegory, S. Porowski: Photoluminescence and reflectance spectroscopy of excitonic transitions in high-quality homoepitaxial GaN films, Phys. Rev. B **60**(3), 1471 (1999)
31.348 G. Pozina, J.P. Bergman, T. Paskova, B. Monemar: Bound exciton dynamics in GaN grown by hydride vapor-phase epitaxy, Appl. Phys. Lett. **75**(26), 4124 (1999)
31.349 K.P. Korona, R. Doradziński, M. Palczewska, M. Pietras, M. Kamińska, J. Kuhl: Properties of zinc acceptor and exciton bound to zinc in ammonothermal GaN, Phys. Status Solidi B **235**(1), 40 (2003)
31.350 M. Leroux, B. Beaumont, N. Grandjean, P. Lorenzini, S. Haffouz, P. Vennéguès, J. Massies, P. Gibart: Luminescence and reflectivity studies of undoped, n- and p-doped GaN on (0001) sapphire, Mater. Sci. Eng. B **50**(1–3), 97 (1997)
31.351 M. Leroux, N. Grandjean, B. Beaumont, G. Nataf, F. Semond, J. Massies, P. Gibart: Temperature quenching of photoluminescence intensities in undoped and doped GaN, J. Appl. Phys. **86**(7), 3721 (1999)

31.352 G. Pozina, B. Monemar, P.P. Paskov, C. Hemmingsson, L. Hultman, H. Amano, I. Akasaki, T. Paskova, S. Figge, D. Hommel, A. Usui: Metastability of the UV luminescence in Mg-doped GaN layers grown by MOVPE on quasi-bulk GaN templates, Phys. B Condens. Matter **401/402**, 302 (2007)
31.353 O. Gelhausen, M. Phillips, E. Goldys, T. Paskova, B. Monemar, M. Strassburg, A. Hoffmann: Dissociation of H-related defect complexes in Mg-doped GaN, Phys. Rev. B **69**(12), 125210 (2004)
31.354 T.A.G. Eberlein, R. Jones, S. Öberg, P.R. Briddon: Shallow acceptors in GaN, Appl. Phys. Lett. **91**(13), 132105 (2007)
31.355 D.C. Reynolds, D.C. Look, B. Jogai, V.M. Phanse, R.P. Vaudo: Identification of an ionized-donor-bound-exciton transition in GaN, Solid State Commun. **103**(9), 533 (1997)
31.356 B. Šantic, C. Merz, U. Kaufmann, R. Niebuhr, H. Obloh, K. Bachem: Ionized donor bound excitons in GaN, Appl. Phys. Lett. **71**(13), 1837 (1997)
31.357 A.K. Viswanath, J.I. Lee, S. Yu, D. Kim, Y. Choi, C. Hong: Photoluminescence studies of excitonic transitions in GaN epitaxial layers, J. Appl. Phys. **84**(7), 3848 (1998)
31.358 R.A. Mair, J. Li, S.K. Duan, J.Y. Lin, H.X. Jiang: Time-resolved photoluminescence studies of an ionized donor-bound exciton in GaN, Appl. Phys. Lett. **74**(4), 513 (1999)
31.359 C. Merz, M. Kunzer, U. Kaufmann, I. Akasaki, H. Amano: Free and bound excitons in thin wurtzite GaN layers on sapphire, Semicond. Sci. Technol. **11**(5), 712 (1996)
31.360 B. Monemar, P.P. Paskov, J.P. Bergman, T. Paskova, S. Figge, J. Dennemarck, D. Hommel: The dominant shallow 0.225 eV acceptor in GaN, Phys. Status Solidi B **243**(7), 1604 (2006)
31.361 B. Monemar, P.P. Paskov, G. Pozina, C. Hemmingsson, J.P. Bergman, S. Khromov, V.N. Izyumskaya, V. Avrutin, X. Li, H. Morkoç, H. Amano, M. Iwaya, I. Akasaki: Properties of the main Mg-related acceptors in GaN from optical and structural studies, J. Appl. Phys. **115**(5), 053507 (2014)
31.362 S. Khromov, C.G. Hemmingsson, H. Amano, B. Monemar, L. Hultman, G. Pozina: Luminescence related to high density of Mg-induced stacking faults in homoepitaxially grown GaN, Phys. Rev. B **84**(7), 075324 (2011)
31.363 D. Thomas, J. Hopfield: Optical properties of bound exciton complexes in cadmium sulfide, Phys. Rev. **128**(5), 2135 (1962)
31.364 H. Saito, S. Shionoya, E. Hanamura: New luminescence line associated with the inelastic collision of excitonic molecules in CdS and CdSe, Solid State Commun. **12**(3), 227 (1973)
31.365 O. Lagerstedt: Luminescence in epitaxial GaN:Cd, J. Appl. Phys. **45**(5), 2266 (1974)
31.366 S. Fischer, C. Wetzel, E.E. Haller, B.K. Meyer: On p-type doping in GaN-acceptor binding energies, Appl. Phys. Lett. **67**(9), 1298 (1995)
31.367 J.L. Lyons, A. Janotti, C.G. van de Walle: Shallow versus deep nature of Mg acceptors in nitride semiconductors, Phys. Rev. Lett. **108**(15), 156403 (2012)
31.368 Y. Kamiura, M. Kaneshiro, J. Tamura, T. Ishiyama, Y. Yamashita, T. Mitani, T. Mukai: Enhancement of blue emission from Mg-doped GaN using remote plasma containing atomic hydrogen, Jpn. J. Appl. Phys. **44**(29), L926 (2005)
31.369 M. Reshchikov, G.-C. Yi, B. Wessels: Behavior of 2.8 and 3.2 eV photoluminescence bands in Mg-doped GaN at different temperatures and excitation densities, Phys. Rev. B **59**(20), 13176 (1999)
31.370 B. Monemar, P. Paskov, G. Pozina, C. Hemmingsson, J. Bergman, T. Kawashima, H. Amano, I. Akasaki, T. Paskova, S. Figge, D. Hommel, A. Usui: Evidence for two Mg related acceptors in GaN, Phys. Rev. Lett. **102**(23), 235501 (2009)
31.371 D. Thomas, J. Hopfield, W. Augustyniak: Kinetics of radiative recombination at randomly distributed donors and acceptors, Phys. Rev. **140**(1A), A202 (1965)
31.372 B. Monemar, S. Khromov, G. Pozina, P. Paskov, P. Bergman, C. Hemmingsson, L. Hultman, H. Amano, V. Avrutin, X. Li, H. Morkoç: Luminescence of acceptors in Mg-doped GaN, Jpn. J. Appl. Phys. **52**(8S), 08JJ03 (2013)
31.373 M.A. Reshchikov, H. Morkoç: Luminescence properties of defects in GaN, J. Appl. Phys. **97**(6), 061301 (2005)
31.374 E. Glaser, T. Kennedy, K. Doverspike, L. Rowland, D. Gaskill, J. Freitas, M. Asif Khan, D. Olson, J. Kuznia, D. Wickenden: Optically detected magnetic resonance of GaN films grown by organometallic chemical-vapor deposition, Phys. Rev. B **51**(19), 13326 (1995)
31.375 D. Demchenko, I. Diallo, M. Reshchikov: Yellow luminescence of gallium nitride generated by carbon defect complexes, Phys. Rev. Lett. **110**(8), 087404 (2013)
31.376 T. Ogino, M. Aoki: Mechanism of yellow luminescence in GaN, Jpn. J. Appl. Phys. **19**(12), 2395 (1980)
31.377 K. Saarinen, T. Laine, S. Kuisma, J. Nissilä, P. Hautojärvi, L. Dobrzynski, J. Baranowski, K. Pakula, R. Stepniewski, M. Wojdak, A. Wysmolek, T. Suski, M. Leszczynski, I. Grzegory, S. Porowski: Observation of native Ga vacancies in GaN by positron annihilation, Phys. Rev. Lett. **79**(16), 3030 (1997)
31.378 J. Neugebauer, C.G. Van de Walle: Gallium vacancies and the yellow luminescence in GaN, Appl. Phys. Lett. **69**(4), 503 (1996)
31.379 T. Mattila, R.M. Nieminen: Point-defect complexes and broadband luminescence in GaN and AlN, Phys. Rev. B **55**(15), 9571 (1997)
31.380 S.O. Kucheyev, M. Toth, M.R. Phillips, J.S. Williams, C. Jagadish, G. Li: Chemical origin of the yellow luminescence in GaN, J. Appl. Phys. **91**(9), 5867 (2002)
31.381 I. Shalish, L. Kronik, G. Segal, Y. Rosenwaks, Y. Shapira, U. Tisch, J. Salzman: Yellow luminescence and related deep levels in unintentionally doped GaN films, Phys. Rev. B **59**(15), 9748 (1999)
31.382 E. Calleja, F.J. Sánchez, D. Basak, M.A. Sánchez-García, E. Muñoz, I. Izpura, F. Calle, J.M.G. Tijero, J.L. Sánchez-Rojas, B. Beaumont, P. Lorenzini,

P. Gibart: Yellow luminescence and related deep states in undoped GaN, Phys. Rev. B **55**(7), 4689 (1997)
31.383 J.L. Lyons, A. Janotti, C.G. Van de Walle: Carbon impurities and the yellow luminescence in GaN, Appl. Phys. Lett. **97**(15), 152108 (2010)
31.384 D. Hofmann, D. Kovalev, G. Steude, B. Meyer, A. Hoffmann, L. Eckey, R. Heitz, T. Detchprom, H. Amano, I. Akasaki: Properties of the yellow luminescence in undoped GaN epitaxial layers, Phys. Rev. B **52**(23), 16702 (1995)
31.385 R. Korotkov, M. Reshchikov, B. Wessels: Transient photoluminescence of defects in undoped GaN prepared by metal organic vapor phase epitaxy, Phys. B Condens. Matter **273/274**, 80 (1999)
31.386 M.A. Reshchikov, H. Morkoç, S.S. Park, K.Y. Lee: Transient photoluminescence of defect transitions in freestanding GaN, Appl. Phys. Lett. **78**(19), 2882 (2001)
31.387 S. Pačesová, L. Jastrabík: Radiative recombination at deep impurity centres in AlN:O, Czechoslov. J. Phys. **29**(8), 913 (1979)
31.388 R.A. Youngman, J.H. Harris: Luminescence studies of oxygen-related defects in aluminum nitride, J. Am. Ceram. Soc. **73**(11), 3238 (1990)
31.389 J.H. Harris, R.A. Youngman, R.G. Teller: On the nature of the oxygen-related defect in aluminum nitride, J. Mater. Res. **5**(08), 1763 (1990)
31.390 R. Collazo, J. Xie, B.E. Gaddy, Z. Bryan, R. Kirste, M. Hoffmann, R. Dalmau, B. Moody, Y. Kumagai, T. Nagashima, Y. Kubota, T. Kinoshita, A. Koukitu, D.L. Irving, Z. Sitar: On the origin of the 265 nm absorption band in AlN bulk crystals, Appl. Phys. Lett. **100**(19), 191914 (2012)
31.391 T. Koyama, M. Sugawara, T. Hoshi, A. Uedono, J.F. Kaeding, R. Sharma, S. Nakamura, S.F. Chichibu: Relation between Al vacancies and deep emission bands in AlN epitaxial films grown by NH_3-source molecular beam epitaxy, Appl. Phys. Lett. **90**(24), 241914 (2007)
31.392 K.B. Nam, M.L. Nakarmi, J.Y. Lin, H.X. Jiang: Deep impurity transitions involving cation vacancies and complexes in AlGaN alloys, Appl. Phys. Lett. **86**(22), 222108 (2005)
31.393 B.N. Pantha, N. Nepal, T.M. Al Tahtamouni, M.L. Nakarmi, J. Li, J.Y. Lin, H.X. Jiang: Correlation between biaxial stress and free exciton transition in AlN epilayers, Appl. Phys. Lett. **91**(12), 121117 (2007)
31.394 W. Rieger, T. Metzger, H. Angerer, R. Dimitrov, O. Ambacher, M. Stutzmann: Influence of substrate-induced biaxial compressive stress on the optical properties of thin GaN films, Appl. Phys. Lett. **68**(7), 970 (1996)
31.395 E. Silveira, J. Freitas, O. Glembocki, G. Slack, L. Schowalter: Excitonic structure of bulk AlN from optical reflectivity and cathodoluminescence measurements, Phys. Rev. B **71**(4), 041201 (2005)
31.396 B. Neuschl, K. Thonke, M. Feneberg, S. Mita, J. Xie, R. Dalmau, R. Collazo, Z. Sitar: Optical identification of silicon as a shallow donor in MOVPE grown homoepitaxial AlN, Phys. Status Solidi B **249**(3), 511 (2012)
31.397 M. Feneberg, B. Neuschl, K. Thonke, R. Collazo, A. Rice, Z. Sitar, R. Dalmau, J. Xie, S. Mita, R. Goldhahn: Sharp bound and free exciton lines from homoepitaxial AlN, Phys. Status Solidi A **208**(7), 1520 (2011)
31.398 H. Ikeda, T. Okamura, K. Matsukawa, T. Sota, M. Sugawara, T. Hoshi, P. Cantu, R. Sharma, J.F. Kaeding, S. Keller, U.K. Mishra, K. Kosaka, K. Asai, S. Sumiya, T. Shibata, M. Tanaka, J.S. Speck, S.P. DenBaars, S. Nakamura, T. Koyama, T. Onuma, S.F. Chichibu: Impact of strain on free-exciton resonance energies in wurtzite AlN, J. Appl. Phys. **102**(12), 123707 (2007)
31.399 L. Chen, B.J. Skromme, R.F. Dalmau, R. Schlesser, Z. Sitar, C. Chen, W. Sun, J. Yang, M.A. Khan, M.L. Nakarmi, J.Y. Lin, H.-X. Jiang: Band-edge exciton states in AlN single crystals and epitaxial layers, Appl. Phys. Lett. **85**(19), 4334 (2004)
31.400 Y. Yamada, K. Choi, S. Shin, H. Murotani, T. Taguchi, N. Okada, H. Amano: Photoluminescence from highly excited AlN epitaxial layers, Appl. Phys. Lett. **92**(13), 131912 (2008)
31.401 E. Silveira, J.A. Freitas, M. Kneissl, D.W. Treat, N.M. Johnson, G.A. Slack, L.J. Schowalter: Near-bandedge cathodoluminescence of an AlN homoepitaxial film, Appl. Phys. Lett. **84**(18), 3501 (2004)
31.402 M. Feneberg, R.A.R. Leute, B. Neuschl, K. Thonke, M. Bickermann: High-excitation and high-resolution photoluminescence spectra of bulk AlN, Phys. Rev. B **82**(7), 075208 (2010)
31.403 T. Onuma, T. Shibata, K. Kosaka, K. Asai, S. Sumiya, M. Tanaka, T. Sota, A. Uedono, S.F. Chichibu: Free and bound exciton fine structures in AlN epilayers grown by low-pressure metalorganic vapor phase epitaxy, J. Appl. Phys. **105**(2), 023529 (2009)
31.404 H. Murotani, T. Kuronaka, Y. Yamada, T. Taguchi, N. Okada, H. Amano: Temperature dependence of excitonic transitions in *a*-plane AlN epitaxial layers, J. Appl. Phys. **105**(8), 083533 (2009)
31.405 R. Phillips, D. Lovering, G. Denton, G. Smith: Biexciton creation and recombination in a GaAs quantum well, Phys. Rev. B **45**(8), 4308 (1992)
31.406 R.A.R. Leute, M. Feneberg, R. Sauer, K. Thonke, S.B. Thapa, F. Scholz, Y. Taniyasu, M. Kasu: Photoluminescence of highly excited AlN: Biexcitons and exciton-exciton scattering, Appl. Phys. Lett. **95**(3), 031903 (2009)
31.407 M. Funato, K. Matsuda, R.G. Banal, R. Ishii, Y. Kawakami: Homoepitaxy and photoluminescence properties of (0001) AlN, Appl. Phys. Express **5**(8), 082001 (2012)
31.408 G. Rossbach, M. Feneberg, M. Röppischer, C. Werner, N. Esser, C. Cobet, T. Meisch, K. Thonke, A. Dadgar, J. Bläsing, A. Krost, R. Goldhahn: Influence of exciton-phonon coupling and strain on the anisotropic optical response of wurtzite AlN around the band edge, Phys. Rev. B **83**(19), 195202 (2011)

31.409 R. Dalmau, B. Moody, R. Schlesser, S. Mita, J. Xie, M. Feneberg, B. Neuschl, K. Thonke, R. Collazo, A. Rice, J. Tweedie, Z. Sitar: Growth and characterization of AlN and AlGaN epitaxial films on AlN single crystal substrates, J. Electrochem. Soc. **158**(5), H530 (2011)
31.410 G.M. Prinz, A. Ladenburger, M. Schirra, M. Feneberg, K. Thonke, R. Sauer, Y. Taniyasu, M. Kasu, T. Makimoto: Cathodoluminescence, photoluminescence, and reflectance of an aluminum nitride layer grown on silicon carbide substrate, J. Appl. Phys. **101**(2), 023511 (2007)
31.411 G.M. Prinz, M. Feneberg, M. Schirra, R. Sauer, K. Thonke, S.B. Thapa, F. Scholz: Silicon-doping induced strain of AlN layers: A comparative luminescence and Raman study, Phys. Status Solidi RRL–Rapid Res. Lett. **2**(5), 215 (2008)
31.412 K.B. Nam, M.L. Nakarmi, J. Li, J.Y. Lin, H.X. Jiang: Photoluminescence studies of Si-doped AlN epilayers, Appl. Phys. Lett. **83**(14), 2787 (2003)
31.413 M. Yoshikawa, M. Kunzer, J. Wagner, H. Obloh, P. Schlotter, R. Schmidt, N. Herres, U. Kaufmann: Band-gap renormalization and band filling in Si-doped GaN films studied by photoluminescence spectroscopy, J. Appl. Phys. **86**(8), 4400 (1999)
31.414 N. Nepal, M.L. Nakarmi, K.B. Nam, J.Y. Lin, H.X. Jiang: Acceptor-bound exciton transition in Mg-doped AlN epilayer, Appl. Phys. Lett. **85**(12), 2271 (2004)
31.415 K.B. Nam, J. Li, M.L. Nakarmi, J.Y. Lin, H.X. Jiang: Deep ultraviolet picosecond time-resolved photoluminescence studies of AlN epilayers, Appl. Phys. Lett. **82**(11), 1694 (2003)
31.416 S.F. Chichibu, T. Onuma, K. Hazu, A. Uedono: Major impacts of point defects and impurities on the carrier recombination dynamics in AlN, Appl. Phys. Lett. **97**(20), 201904 (2010)
31.417 Q. Guo, A. Yoshida: Temperature dependence of band gap change in InN and AlN, Jpn. J. Appl. Phys. **33**(5A), 2453 (1994)
31.418 E. Kuokstis, J. Zhang, Q. Fareed, J.W. Yang, G. Simin, M.A. Khan, R. Gaska, M. Shur, C. Rojo, L. Schowalter: Near-band-edge photoluminescence of wurtzite-type AlN, Appl. Phys. Lett. **81**(15), 2755 (2002)
31.419 X. Tang, F. Hossain, K. Wongchotigul, M.G. Spencer: Near band-edge transition in aluminum nitride thin films grown by metal organic chemical vapor deposition, Appl. Phys. Lett. **72**(12), 1501 (1998)
31.420 F. Chen, A. Cartwright, H. Lu, W.J. Schaff: Ultrafast carrier dynamics in InN epilayers, J. Cryst. Growth **269**(1), 10 (2004)
31.421 K. Osamura, S. Naka, Y. Murakami: Preparation and optical properties of $Ga_{1-x}In_xN$ thin films, J. Appl. Phys. **46**(8), 3432 (1975)
31.422 A. Wakahara, T. Tsuchiya, A. Yoshida: Epitaxial growth of indium nitride, J. Cryst. Growth **99**(1–4), 385 (1990)
31.423 K. Kubota, Y. Kobayashi, K. Fujimoto: Preparation and properties of III–V nitride thin films, J. Appl. Phys. **66**(7), 2984 (1989)
31.424 T.L. Tansley, C.P. Foley: Optical band gap of indium nitride, J. Appl. Phys. **59**(9), 3241 (1986)
31.425 S. Yamaguchi, M. Kariya, S. Nitta, T. Takeuchi, C. Wetzel, H. Amano, I. Akasaki: Anomalous features in the optical properties of $Al_{1-x}In_xN$ on GaN grown by metal organic vapor phase epitaxy, Appl. Phys. Lett. **76**(7), 876 (2000)
31.426 T. Inushima, V. Mamutin, V. Vekshin, S. Ivanov, T. Sakon, M. Motokawa, S. Ohoya: Physical properties of InN with the band gap energy of 1.1 eV, J. Cryst. Growth **227/228**, 481 (2001)
31.427 J. Wu, W. Walukiewicz, W. Shan, K. Yu, J. Ager, E. Haller, H. Lu, W. Schaff: Effects of the narrow band gap on the properties of InN, Phys. Rev. B **66**(20), 201403(R) (2002)
31.428 J. Wu, W. Walukiewicz, K.M. Yu, J.W. Ager, E.E. Haller, H. Lu, W.J. Schaff: Small band gap bowing in $In_{1-x}Ga_xN$ alloys, Appl. Phys. Lett. **80**(25), 4741 (2002)
31.429 V.Y. Davydov, A.A. Klochikhin, R.P. Seisyan, V.V. Emtsev, S.V. Ivanov, F. Bechstedt, J. Furthmüller, H. Harima, A.V. Mudryi, J. Aderhold, O. Semchinova, J. Graul: Absorption and emission of hexagonal InN. Evidence of narrow fundamental band gap, Phys. Status Solidi B **229**(3), r1 (2002)
31.430 J. Wu, W. Walukiewicz, K.M. Yu, J.W. Ager, E.E. Haller, H. Lu, W.J. Schaff, Y. Saito, Y. Nanishi: Unusual properties of the fundamental band gap of InN, Appl. Phys. Lett. **80**(21), 3967 (2002)
31.431 T. Inushima, M. Higashiwaki, T. Matsui: Optical properties of Si-doped InN grown on sapphire (0001), Phys. Rev. B **68**(23), 235204 (2003)
31.432 J. Wu, W. Walukiewicz, S.X. Li, R. Armitage, J.C. Ho, E.R. Weber, E.E. Haller, H. Lu, W.J. Schaff, A. Barcz, R. Jakiela: Effects of electron concentration on the optical absorption edge of InN, Appl. Phys. Lett. **84**(15), 2805 (2004)
31.433 V.Y. Davydov, A.A. Klochikhin, V.V. Emtsev, S.V. Ivanov, V.V. Vekshin, F. Bechstedt, J. Furthmüller, H. Harima, A.V. Mudryi, A. Hashimoto, A. Yamamoto, J. Aderhold, J. Graul, E.E. Haller: Band gap of inN and in-rich $In_xGa_{1-x}N$ alloys ($0.36 < x < 1$), Phys. Status Solidi B **230**(2), R4 (2002)
31.434 J. Thakur, Y. Danylyuk, D. Haddad, V. Naik, R. Naik, G. Auner: Influence of defects on the absorption edge of InN thin films: The band gap value, Phys. Rev. B **76**(3), 035309 (2007)
31.435 I. Mahboob, T. Veal, L. Piper, C. McConville, H. Lu, W. Schaff, J. Furthmüller, F. Bechstedt: Origin of electron accumulation at wurtzite InN surfaces, Phys. Rev. B **69**(20), 201307(R) (2004)
31.436 I. Mahboob, T. Veal, C. McConville, H. Lu, W. Schaff: Intrinsic electron accumulation at clean InN surfaces, Phys. Rev. Lett. **92**(3), 036804 (2004)
31.437 H. Lu, W.J. Schaff, L.F. Eastman, C.E. Stutz: Surface charge accumulation of InN films grown by molecular-beam epitaxy, Appl. Phys. Lett. **82**(11), 1736 (2003)
31.438 H. Lu, W.J. Schaff, L.F. Eastman, J. Wu, W. Walukiewicz, D.C. Look, R.J. Molnar: Growth of thick InN by molecular beam epitaxy, MRS Proc.

743, 317 (2002)
31.439 J. Wu, W. Walukiewicz: Band gaps of InN and group III nitride alloys, Superlattices Microstruct. **34**(1/2), 63 (2003)
31.440 K.S.A. Butcher, M. Wintrebert-Fouquet, S.K. Shrestha, H. Timmers, K.E. Prince, T.L. Tansley: A study of indium nitride films grown under conditions resulting in apparent band-gaps from 0.7 eV to 2.3 eV, MRS Proc. **743**, 707 (2002)
31.441 T. Shubina, S. Ivanov, V. Jmerik, D. Solnyshkov, V. Vekshin, P. Kop'ev, A. Vasson, J. Leymarie, A. Kavokin, H. Amano, K. Shimono, A. Kasic, B. Monemar: Mie resonances, infrared emission, and the band gap of InN, Phys. Rev. Lett. **92**(11), 117407 (2004)
31.442 O. Briot, B. Maleyre, S. Clur-Ruffenach, B. Gil, C. Pinquier, F. Demangeot, J. Frandon: The value of the direct bandgap of InN: A re-examination, Phys. Status Solidi C **1**(6), 1425 (2004)
31.443 B. Monemar, P.P. Paskov, A. Kasic: Optical properties of InN – The bandgap question, Superlattices Microstruct. **38**(1), 38 (2005)
31.444 P. Specht, R. Armitage, J. Ho, E. Gunawan, Q. Yang, X. Xu, C. Kisielowski, E. Weber: The influence of structural properties on conductivity and luminescence of MBE grown InN, J. Cryst. Growth **269**(1), 111 (2004)
31.445 S. Gwo, C.-L. Wu, C.-H. Shen, W.-H. Chang, T.M. Hsu, J.-S. Wang, J.-T. Hsu: Heteroepitaxial growth of wurtzite InN films on Si(111) exhibiting strong near-infrared photoluminescence at room temperature, Appl. Phys. Lett. **84**(19), 3765 (2004)
31.446 A. Wakahara, T. Tsuchiya, A. Yoshida: Epitaxial layers of indium nitride by microwave-excited metalorganic vapor phase epitaxy, Vacuum **41**(4–6), 1071 (1990)
31.447 F. Chen, A. Cartwright, H. Lu, W.J. Schaff: Temperature-dependent optical properties of wurtzite InN, Phys. E Low-Dimens. Syst. Nanostructures **20**(3/4), 308 (2004)
31.448 L. Görgens, O. Ambacher, M. Stutzmann, C. Miskys, F. Scholz, J. Off: Characterization of InGaN thin films using high-resolution x-ray diffraction, Appl. Phys. Lett. **76**(5), 577 (2000)
31.449 T. Peng, J. Piprek, G. Qiu, J.O. Olowolafe, K.M. Unruh, C.P. Swann, E.F. Schubert: Band gap bowing and refractive index spectra of polycrystalline $Al_xIn_{1-x}N$ films deposited by sputtering, Appl. Phys. Lett. **71**(17), 2439 (1997)
31.450 V. Darakchieva, M. Beckers, M.-Y. Xie, L. Hultman, B. Monemar, J.-F. Carlin, E. Feltin, M. Gonschorek, N. Grandjean: Effects of strain and composition on the lattice parameters and applicability of Vegard's rule in Al-rich $Al_{1-x}In_xN$ films grown on sapphire, J. Appl. Phys. **103**(10), 103513 (2008)
31.451 F. Yun, M.A. Reshchikov, L. He, T. King, H. Morkoç, S.W. Novak, L. Wei: Energy band bowing parameter in $Al_xGa_{1-x}N$ alloys, J. Appl. Phys. **92**(8), 4837 (2002)
31.452 N. Nepal, J. Li, M.L. Nakarmi, J.Y. Lin, H.X. Jiang: Temperature and compositional dependence of the energy band gap of AlGaN alloys, Appl. Phys. Lett. **87**(24), 242104 (2005)
31.453 H. Murotani, Y. Yamada, T. Taguchi, A. Ishibashi, Y. Kawaguchi, T. Yokogawa: Temperature dependence of localized exciton transitions in AlGaN ternary alloy epitaxial layers, J. Appl. Phys. **104**(5), 053514 (2008)
31.454 M.A. Khan, J.M. Van Hove, J.N. Kuznia, D.T. Olson: High electron mobility $GaN/Al_xGa_{1-x}N$ heterostructures grown by low-pressure metalorganic chemical vapor deposition, Appl. Phys. Lett. **58**(21), 2408 (1991)
31.455 Y.A. Xi, K.X. Chen, F. Mont, J.K. Kim, E.F. Schubert, W. Liu, X. Li, J.A. Smart: Comparative study of n-type AlGaN grown on sapphire by using a superlattice layer and a low-temperature AlN interlayer, J. Cryst. Growth **299**(1), 59 (2007)
31.456 W.H. Sun, J.W. Yang, J.P. Zhang, M.E. Gaevski, C.Q. Chen, J.W. Li, Z. Gong, M. Su, M. Asif Khan: n-$Al_{0.75}Ga_{0.25}N$ epilayers for 250 nm emission ultraviolet light emitting diodes, Phys. Status Solidi C **2**(7), 2083 (2005)
31.457 M.L. Nakarmi, K.H. Kim, K. Zhu, J.Y. Lin, H.X. Jiang: Transport properties of highly conductive n-type Al-rich $Al_xGa_{1-x}N$ ($x \geq 0.7$), Appl. Phys. Lett. **85**(17), 3769 (2004)
31.458 M. Stutzmann, O. Ambacher, A. Cros, M. Brandt, H. Angerer, R. Dimitrov, N. Reinacher, T. Metzger, R. Höpler, D. Brunner, F. Freudenberg, R. Handschuh, C. Deger: Properties and applications of MBE grown AlGaN, Mater. Sci. Eng. B **50**(1–3), 212 (1997)
31.459 T. Tanaka, A. Watanabe, H. Amano, Y. Kobayashi, I. Akasaki, S. Yamazaki, M. Koike: p-Type conduction in Mg-doped GaN and $Al_{0.08}Ga_{0.92}N$ grown by metalorganic vapor phase epitaxy, Appl. Phys. Lett. **65**(5), 593 (1994)
31.460 S.-R. Jeon, Z. Ren, G. Cui, J. Su, M. Gherasimova, J. Han, H.-K. Cho, L. Zhou: Investigation of Mg doping in high-Al content p-type $Al_xGa_{1-x}N$ ($0.3 < x < 0.5$), Appl. Phys. Lett. **86**(8), 082107 (2005)
31.461 W. Liu, A.A. Balandin: Thermal conduction in $Al_xGa_{1-x}N$ alloys and thin films, J. Appl. Phys. **97**(7), 073710 (2005)
31.462 F.K. Yam, Z. Hassan: InGaN: An overview of the growth kinetics, physical properties and emission mechanisms, Superlattices Microstruct. **43**(1), 1 (2008)
31.463 C.-R. Lee, S.-J. Son, I.-H. Lee, J.-Y. Leem, S.K. Noh: Characteristics of $In_xGa_{1-x}N$/GaN grown by LPMOVPE with the variation of growth temperature, J. Cryst. Growth **182**(1), 6 (1997)
31.464 W. Van der Stricht, I. Moerman, P. Demeester, J. Crawley, E.J. Thrush: Study of GaN and InGaN films grown by metalorganic chemical vapour deposition, J. Cryst. Growth **170**(1–4), 344 (1997)
31.465 H.-C. Lin, C.-K. Shu, J. Ou, Y.-C. Pan, W.-K. Chen, W.-H. Chen, M.-C. Lee: Growth temperature effects on $In_xGa_{1-x}N$ films studied by x-ray and photoluminescence, J. Cryst. Growth **189/190**, 57 (1998)

31.466 K. Kumakura, T. Makimoto, N. Kobayashi: Activation energy and electrical activity of Mg in Mg-doped $In_xGa_{1-x}N$ ($x < 0.2$), Jpn. J. Appl. Phys. **39**(4B), L337 (2000)

31.467 M. Suzuki, J. Nishio, M. Onomura, C. Hongo: Doping characteristics and electrical properties of Mg-doped AlGaN grown by atmospheric-pressure MOCVD, J. Cryst. Growth **189/190**, 511 (1998)

31.468 B.N. Pantha, A. Sedhain, J. Li, J.Y. Lin, H.X. Jiang: Electrical and optical properties of p-type InGaN, Appl. Phys. Lett. **95**(26), 261904 (2009)

31.469 J. Xie, X. Ni, M. Wu, J.H. Leach, U. Özgür, H. Morkoç: High electron mobility in nearly lattice-matched AlInN/AlN/GaN heterostructure field effect transistors, Appl. Phys. Lett. **91**(13), 132116 (2007)

31.470 J.-F. Carlin, M. Ilegems: High-quality AlInN for high index contrast Bragg mirrors lattice matched to GaN, Appl. Phys. Lett. **83**(4), 668 (2003)

31.471 O. Ambacher, J. Majewski, C. Miskys, A. Link, M. Hermann, M. Eickhoff, M. Stutzmann, F. Bernardini, V. Fiorentini, V. Tilak, B. Schaff, L.F. Eastman: Pyroelectric properties of Al(In)GaN/GaN hetero- and quantum well structures, J. Phys. Condens. Matter **14**(13), 3399 (2002)

31.472 R.E. Jones, R. Broesler, K.M. Yu, J.W. Ager, E.E. Haller, W. Walukiewicz, X. Chen, W.J. Schaff: Band gap bowing parameter of $In_{1-x}Al_xN$, J. Appl. Phys. **104**(12), 123501 (2008)

31.473 W. Terashima, S.-B. Che, Y. Ishitani, A. Yoshikawa: Growth and characterization of AlInN ternary alloys in whole composition range and fabrication of InN/AlInN multiple quantum wells by RF molecular beam epitaxy, Jpn. J. Appl. Phys. **45**(21), L539 (2006)

31.474 K. Lorenz, N. Franco, E. Alves, S. Pereira, I.M. Watson, R.W. Martin, K.P. O'Donnell: Relaxation of compressively strained AlInN on GaN, J. Cryst. Growth **310**(18), 4058 (2008)

31.475 W.R. Bryden, T.J. Kistenmacher: Electrical transport properties of InN, GaInN and AlInN. In: *Properties of Group III Nitrides*, ed. by J.H. Edgar (Ed. Inspec, London 1995) p. 910

31.476 M.J. Lukitsch, Y.V. Danylyuk, V.M. Naik, C. Huang, G.W. Auner, L. Rimai, R. Naik: Optical and electrical properties of $Al_{1-x}In_xN$ films grown by plasma source molecular-beam epitaxy, Appl. Phys. Lett. **79**(5), 632 (2001)

31.477 S.N. Mohammad, A.A. Salvador, H. Morkoç: Emerging gallium nitride based devices, Proc. IEEE **83**(10), 1306 (1995)

31.478 S.M. Bedair, F.G. McIntosh, J.C. Roberts, E.L. Piner, K.S. Boutros, N.A. El-Masry: Growth and characterization of In-based nitride compounds, J. Cryst. Growth **178**(1/2), 32 (1997)

31.479 J.-Y. Chang, Y.-K. Kuo: Influence of polarization-matched AlGaInN barriers in blue InGaN light-emitting diodes, Opt. Lett. **37**(9), 1574 (2012)

31.480 M.F. Schubert, J. Xu, J.K. Kim, E.F. Schubert, M.H. Kim, S. Yoon, S.M. Lee, C. Sone, T. Sakong, Y. Park: Polarization-matched GaInN/AlGaInN multi-quantum-well light-emitting diodes with reduced efficiency droop, Appl. Phys. Lett. **93**(4), 041102 (2008)

31.481 M.E. Aumer, S.F. LeBoeuf, B.F. Moody, S.M. Bedair: Strain-induced piezoelectric field effects on light emission energy and intensity from AlInGaN/InGaN quantum wells, Appl. Phys. Lett. **79**(23), 3803 (2001)

31.482 M.-Y. Ryu, C.Q. Chen, E. Kuokstis, J.W. Yang, G. Simin, M.A. Khan: Luminescence mechanisms in quaternary $Al_xIn_yGa_{1-x-y}N$ materials, Appl. Phys. Lett. **80**(20), 3730 (2002)

31.483 W. Walukiewicz: Intrinsic limitations to the doping of wide-gap semiconductors, Proc. Yamada Conf. LIV 9th Int. Conf. Shallow-Level Centers in Semiconductors (2001) p. 123

31.484 N. Koide, H. Kato, M. Sassa, S. Yamasaki, K. Manabe, M. Hashimoto, H. Amano, K. Hiramatsu, I. Akasaki: Doping of GaN with Si and properties of blue m/i/n/n+ GaN LED with Si-doped n+-layer by MOVPE, J. Cryst. Growth **115**(1–4), 639 (1991)

31.485 S. Fritze, A. Dadgar, H. Witte, M. Bugler, A. Rohrbeck, J. Blasing, A. Hoffmann, A. Krost: High Si and Ge n-type doping of GaN doping: Limits and impact on stress, Appl. Phys. Lett. **100**(12), 122104 (2012)

31.486 W.J. Moore, J.A. Freitas, S.K. Lee, S.S. Park, J.Y. Han: Magneto-optical studies of free-standing hydride-vapor-phase epitaxial GaN, Phys. Rev. B **65**(8), 081201 (2002)

31.487 P.J. Dean, J.D. Cuthbert, D.G. Thomas, R.T. Lynch: Two-electron transitions in the luminescence of excitons bound to neutral donors in gallium phosphide, Phys. Rev. Lett. **18**(4), 122 (1967)

31.488 M. Wieneke, H. Witte, K. Lange, M. Feneberg, A. Dadgar, J. Blasing, R. Goldhahn, A. Krost: Ge as a surfactant in metal-organic vapor phase epitaxy growth of *a*-plane GaN exceeding carrier concentrations of 1020 cm^{-3}, Appl. Phys. Lett. **103**(1), 012103 (2013)

31.489 J.K. Sheu, G.C. Chi: The doping process and dopant characteristics of GaN, J. Phys. Condens. Matter **14**(22), 657 (2002)

31.490 H. Amano, M. Kito, K. Hiramatsu, I. Akasaki: P-type conduction in Mg-doped GaN treated with low-energy electron beam irradiation (LEEBI), Jpn. J. Appl. Phys. **28**(12A), L2112 (1989)

31.491 S. Nakamura, M. Senoh, T. Mukai: Highly p-typed Mg-doped GaN films grown with GaN buffer layers, Jpn. J. Appl. Phys. **30**(10A), L1708 (1991)

31.492 S. Nakamura, T. Mukai, M. Senoh, N. Iwasa: Thermal annealing effects on p-type Mg-doped GaN films, Jpn. J. Appl. Phys. **31**(2B), L139 (1992)

31.493 H. Amano, M. Kitoh, K. Hiramatsu, I. Akasaki: Growth and luminescence properties of Mg-doped GaN prepared by MOVPE, J. Electrochem. Soc. **137**(5), 1639 (1990)

31.494 H. Obloh, K.H. Bachem, U. Kaufmann, M. Kunzer, M. Maier, A. Ramakrishnan, P. Schlotter: Self-compensation in Mg doped p-type GaN grown by MOCVD, Proc. Metalorganic Vapour Phase Epitaxy 1998. Ninth Int. Conf (1998) p. 270

31.495 W. Kim, A.E. Botchkarev, A. Salvador, G. Popovici, H. Tang, H. Morkoc: On the incorporation of Mg and the role of oxygen, silicon, and hydrogen in GaN prepared by reactive molecular beam epitaxy, J. Appl. Phys. **82**(1), 219 (1997)

31.496 W. Kim, A. Salvador, A.E. Botchkarev, O. Aktas, S.N. Mohammad, H. Morcoç: Mg-doped p-type GaN grown by reactive molecular beam epitaxy, Appl. Phys. Lett. **69**(4), 559 (1996)

31.497 W. Gotz, N.M. Johnson, J. Walker, D.P. Bour, R.A. Street: Activation of acceptors in Mg-doped GaN grown by metalorganic chemical vapor deposition, Appl. Phys. Lett. **68**(5), 667 (1996)

31.498 I.D. Goepfert, E.F. Schubert, A. Osinsky, P.E. Norris: Demonstration of efficient p-type doping in $Al_xGa_{1-x}N$/GaN superlattice structures, Electron. Lett. **35**(13), 1109 (1999)

31.499 P. Kozodoy, H. Xing, S.P. DenBaars, U.K. Mishra, A. Saxler, R. Perrin, S. Elhamri, W.C. Mitchel: Heavy doping effects in Mg-doped GaN, J. Appl. Phys. **87**(4), 1832 (2000)

31.500 M. Suzuki, J. Nishio, M. Onomura, C. Hongo: Doping characteristics and electrical properties of Mg-doped AlGaN grown by atmospheric-pressure MOCVD, Proc. Second Int. Conf. Nitride Semiconductors (1998) p. 511

31.501 L. Sugiura, M. Suzuki, J. Nishio, K. Itaya, Y. Kokubun, M. Ishikawa: Characteristics of Mg-doped GaN and AlGaN grown by H_2-ambient and N_2-ambient metallorganic chemical vapor deposition, Jpn. J. Appl. Phys. Part 1 **37**(7), 3878 (1998)

31.502 J. Li, T.N. Oder, M.L. Nakarmi, J.Y. Lin, H.X. Jiang: Optical and electrical properties of Mg-doped p-type $Al_xGa_{1-x}N$, Appl. Phys. Lett. **80**(7), 1210 (2002), (1998) p. 511

31.503 H. Yu, E. Ulker, E. Ozbay: MOCVD growth and electrical studies of p-type AlGaN with Al fraction 0.35, J. Cryst. Growth **289**(2), 419 (2006)

31.504 S.N. Mohammed, H. Morkoc: Progress and prospects of group-III nitride semiconductors, Prog. Quantum Electron. **20**(5/6), 361 (1996)

31.505 L.K. Li, M.J. Jurkovic, W.I. Wang, J. Van Hove, P.P. Chow: Surface polarity dependence of Mg doping in GaN grown by molecular-beam epitaxy, Appl. Phys. Lett. **76**(13), 1740 (2000)

31.506 A.J. Ptak, T.H. Myers, L.T. Romano, C.G.J.E. Van de Walle: Northrup: Magnesium incorporation in GaN grown by molecular-beam epitaxy, Appl. Phys. Lett. **78**(3), 285 (2001)

31.507 S. Guha, N.A. Bojarczuk, F. Cardone: Mg in GaN: Incorporation of a volatile species at high temperatures during molecular beam epitaxy, Appl. Phys. Lett. **71**(12), 1685 (1997)

31.508 T.S. Cheng, S.V. Novikov, C.T. Foxon, J.W. Orton: Mechanisms of magnesium incorporation into GaN layers grown by molecular beam epitaxy, Solid State Commun. **109**(7), 439 (1999)

31.509 I.P. Smorchkova, E. Haus, B. Heying, P. Kozodoy, P. Fini, J.P. Ibbetson, S. Keller, S.P. DenBaars, J.S. Speck, U.K. Mishra: Mg doping of GaN layers grown by plasma-assisted molecular-beam epitaxy, Appl. Phys. Lett. **76**(6), 718 (2000)

31.510 R.Y. Korotkov, J.M. Gregie, B.W. Wessels: Codoping of wide gap epitaxial III-nitride semiconductors, Opto-Electron. Rev. **10**(4), 243 (2002)

31.511 H. Reiss, C.S. Fuller, F.J. Morin: Chemical interactions among defects in germanium and silicon, Bell Syst. Tech. J. **35**, 535 (1956)

31.512 H. Reiss, C.S. Fuller, A.J. Pietruszkiewicz: Solubility of lithium in doped and undoped silicon, evidence for compound formation, J. Chem. Phys. **25**(4), 650 (1956)

31.513 U. Kaufmann, P. Schlotter, H. Obloh, K. Kohler, M. Maier: Hole conductivity and compensation in epitaxial GaN: Mg layers, Phys. Rev. B Condens. Matter **62**(16), 10867 (2000)

31.514 Y. Qi, C. Musante, K.M. Lau, L. Smith, R. Odedra, R. Kanjolia: OMVPE growth of p-type GaN using solution Cp_2Mg, Tenth Bienn. Workshop Organomet, Vap. Phase Epitaxy **30**(11), 1382 (2001)

31.515 K.S. Kim, M.S. Han, G.M. Yang, C.J. Youn, H.J. Lee, H.K. Cho, J.Y. Lee: Codoping characteristics of Zn with Mg in GaN, Appl. Phys. Lett. **77**(8), 1123 (2000)

31.516 K.H. Ploog, O. Brandt: Doping of group III nitrides, J. Vac. Sci. Technol. A: Vac. Surf. Films **16**(3), 1609 (1998)

31.517 R.Y. Korotkov, J.M. Gregie, B.W. Wessels: Electrical properties of p-type GaN:Mg codoped with oxygen, Appl. Phys. Lett. **78**(2), 222 (2001)

31.518 G. Kipshidze, V. Kuryatkov, B. Borisov, Y. Kudryavtsev, R. Asomoza, S. Nikishin, H. Temkin: Mg and O codoping in p-type GaN and $Al_xGa_{1-x}N$ ($0 \le x \le 0.08$), Appl. Phys. Lett. **80**(16), 2910 (2002)

31.519 E.F. Schubert, W. Grieshaber, I.D. Goepfert: Enhancement of deep acceptor activation in semiconductors by superlattice doping, Appl. Phys. Lett. **69**(24), 3737 (1996)

31.520 P. Kozodoy, Y.P. Smorchkova, M. Hansen, H. Xing, S.P. DenBaars, U.K. Mishra: Polarization-enhanced Mg doping of AlGaN/GaN superlattices, Appl. Phys. Lett. **75**(16), 2444 (1999)

31.521 A. Saxler, W.C. Mitchel, P. Kung, M. Razeghi: Aluminum gallium nitride short-period superlattices doped with magnesium, Appl. Phys. Lett. **74**(14), 2023 (1999)

31.522 L. Hsu, W. Walukiewicz: Theoretical transport studies of p-type GaN/AlGaN modulation-doped heterostructures, Appl. Phys. Lett. **74**(17), 2405 (1999)

31.523 P. Kozodoy, M. Hansen, S.P. DenBaars, U.K. Mishra: Enhanced Mg doping efficiency in $Al_{0.2}Ga_{0.8}N$/GaN superlattices, Appl. Phys. Lett. **4**(24), 3681 (1999)

31.524 A.D. Bykhovski, B.L. Gelmont, M.S. Shur: Elastic strain relaxation and piezoeffect in GaN-AlN, GaN-AlGaN and GaN-InGaN superlattices, J. Appl. Phys. **81**(9), 6332 (1997)

31.525 E.L. Waldron, J.W. Graff, E.F. Schubert: Improved mobilities and resistivities in modulation-doped p-type AlGaN/GaN superlattices, Appl. Phys. Lett. **79**(17), 2737 (2001)

31.526 F. Bernardini, V. Fiorentini, D. Vanderbilt: Spontaneous polarization and piezoelectric constants of III–V nitrides, Phys. Rev. B **56**(16), R10024 (1997)

31.527 V. Adivarahan, J. Zhang, A. Chitnis, S. Wu, J. Sun, R. Pachipulusu, M. Shatalov, M.A. Khan: Sub-milliwatt power III-N light emitting diodes at 285 nm, Jpn. J. Appl. Phys. Part 2 **41**(4B), 435 (2002)
31.528 M. Stavola: To 40 years of defects in semiconductors: May the problem never be solved!, Phys. B Condens. Matter **273/274**, 1 (1999)
31.529 D.V. Lang: Space-charge spectroscopy in semiconductor. In: *Thermally Stimulated Relaxation in Solids*, Topics in Applied Physics, Vol. 37, ed. by P. Bräunlich (Springer, Berlin 1979) pp. 93–133
31.530 L.C. Kimerling: *Defects in Semiconductors*, Vol. 2 (North-Holland, Amsterdam 1981)
31.531 W. Götz, N.M. Johnson, H. Amano, I. Akasaki: Deep level defects in n-type GaN, Appl. Phys. Lett. **65**(4), 463 (1994)
31.532 P. Hacke, T. Detchprohm, K. Hiramatsu, N. Sawaki, K. Tadatomo, K. Miyake: Analysis of deep levels in n-type GaN by transient capacitance methods, J. Appl. Phys. **76**(1), 304 (1994)
31.533 W.I. Lee, T.C. Huang, J.D. Guo, M.S. Feng: Effects of column III alkyl sources on deep levels in GaN grown by organometallic vapor phase epitaxy, Appl. Phys. Lett. **67**(12), 1721 (1995)
31.534 L. Chernyak, A. Osinsky, H. Temkin, J.W. Yang, Q. Chen, M. Asif Khan: Electron beam induced current measurements of minority carrier diffusion length in gallium nitride, Appl. Phys. Lett. **69**(17), 2531 (1996)
31.535 L. Chernyak, A. Osinsky, V. Fuflyigin, E.F. Schubert: Electron beam-induced increase of electron diffusion length in p-type GaN and AlGaN/GaN superlattices, Appl. Phys. Lett. **77**(6), 875 (2000)
31.536 L. Chernyak, A. Osinsky, G. Nootz, A. Schulte, J. Jasinski, M. Benamara, Z. Liliental-Weber, D.C. Look, R.J. Molnar: Electron beam and optical depth profiling of quasibulk GaN, Appl. Phys. Lett. **77**(17), 2695 (2000)
31.537 R.W. Siegel: Positron annihilation spectroscopy, Ann. Rev. Mater. Sci. **10**, 393 (1980)
31.538 R.W. Siegel, M.J. Fluss, L.C. Smedskjaer: Application of positron annihilation in materials science, Proc. 5th Riso Int. Symp. Metallurgy and Materials Sci., Microstructural Characterization of Materials by Non-Microscopical Techniques (1984) p. 131
31.539 R. Krause-Rehberg, H.S. Leipner: Determination of absolute vacancy concentrations in semiconductors by means of positron annihilation, Appl. Phys. **A64**(5), 457 (1997)
31.540 R. Krause-Rehberg, F. Borner, F. Redmann: Positron beam studies of defects in semiconductors, Mat. Sci. Forum **363–365**, 404 (2001)
31.541 A. Laakso, K. Saarinen, P. Hautojarvi: Positron lifetime beam for defect studies in thin epitaxial semiconductor structures, Phys. B Condens. Matter **308–310**, 1157 (2001)
31.542 R.M. Gwilliam, A.P. Knights, E. Wendler, B.J. Sealy, C.P. Burrows, P.G. Coleman: Development of a novel tool for semiconductor process control, Mat. Sci. Eng. B **80**, 60 (2001)
31.543 A.H. Deng, Y.Y. Shan, S. Fung, C.D. Beling: Application of positron annihilation lifetime technique to the study of deep level transients in semiconductors, J. Appl. Phys. **91**(6), 3931 (2002)
31.544 J. Dekker, R. Aavikko, K. Saarinen: Characterization of superlattices using positron annihilation, Appl. Surf. Sci. **194**, 97 (2002)
31.545 T. Onuma, S.F. Chichibu, A. Uedono, T. Sota, P. Cantu, T.M. Katona, J.F. Keading, S. Keller, U.K. Mishra, S. Nakamura, S.P. DenBaars: Radiative and nonradiative processes in strain-free $Al_xGa_{1-x}N$ films studied by time-resolved photoluminescence and positron annihilation techniques, J. Appl. Phys. **95**(5), 2495 (2004)
31.546 G.P. Karwasz, A. Zecca, R.S. Brusa, D. Pliszka: Application of positron annihilation techniques for semiconductor studies, J. Alloys and Compounds **382**, 244 (2004)
31.547 S.F. Chichibu, A. Uedono, T. Onuma, T. Sota, B.A. Haskell, S.P. DenBaars, J.S. Speck, S. Nakamura: Limiting factors of room-temperature nonradiative photoluminescence lifetime in polar and nonpolar GaN studied by time-resolved photoluminescence and slow positron annihilation techniques, Appl. Phys. Lett. **86**(2), 21914 (2005)
31.548 P. Premchander, S. Abhaya, K. Sivaji, G. Amarendra, K. Baskar, Y.T. Lee: Production of vacancy defects in high-energy Sn-ion irradiated GaN-Positron beam Doppler broadening study, Phys. B Condens. Matter **376/377**, 507 (2006)
31.549 S.F. Chichibu, A. Uedono, T. Onuma, B.A. Haskell, A. Chakraborty, T. Koyama, P.T. Fini, S. Keller, S.P. Denbaars, J.S. Speck, U.K. Mishra, S. Nakamura, S. Yamaguchi, S. Kamiyama, H. Amano, I. Akasaki, J. Han, T. Sotas: Origin of localized excitons in In-containing three-dimensional bulk (Al, In, Ga)N alloy films probed by time-resolved photoluminescence and monoenergetic positron annihilation techniques, Philos. Mag. **87**(13), 2019 (2007)
31.550 P.G. Coleman: Defect profiles in semiconductor structures, Phys. Status Solidi C **4**(10), 3620 (2007)
31.551 A. Uedono, K. Ito, H. Nakamori, K. Mori, Y. Nakano, T. Kachi, S. Ishibashi, T. Ohdaira, R. Suzuki: Annealing properties of vacancy-type defects in ion-implanted GaN studied by monoenergetic positron beams, J. Appl. Phys. **102**(8), 084505 (2007)
31.552 X.L. Yang, W.X. Zhu, C.D. Wang, H. Fang, T.J. Yu, Z.J. Yang, G.Y. Zhang, X.B. Qin, R.S. Yu, B.Y. Wang: Positron annihilation in (Ga, Mn)N: A study of vacancy-type defects, Appl. Phys. Lett. **94**(15), 151907 (2009)
31.553 A. Uedono, S. Ishibashi, T. Ohdaira, R. Suzuki: Point defects in group-III nitride semiconductors studied by positron annihilation, J. Cryst. Growth **311**(10), 3075 (2009)
31.554 A. Uedono: Material characterization by means of positron annihilation, Actual Phys. **79**(4), 307 (2010)
31.555 A. Uedono, S. Ishibashi, S.F. Chichibu, K. Akimoto: Point defects in GaN and related group-III nitrides studied by means of positron annihilation. In: *Gallium Nitride Materials and Devices VI*,

Vol. 7939, ed. by J.-I. Chyi, Y. Nanishi, H. Morkoç, J. Piprek, E. Yoon (SPIE Press, San Francisco 2011)
31.556 A. Zubiaga, J.A. Garcia, F. Plazaola, J. Zuniga-Perez, V. Munoz-Sanjose: Determination of defect content and defect profile in semiconductor heterostructures, J. Phys. Conf. Ser. **265**, 012004 (2011)
31.557 F. Tuomisto, I. Makkonen: Defect identification in semiconductors with positron annihilation: Experiment and theory, Rev. Mod. Phys. **85**(4), 1583 (2013)
31.558 A. Uedono, S. Ishibashi, N. Oshima, R. Suzuki: Positron annihilation spectroscopy on nitride-based semiconductors, Recent Adv. Nitride Semicond. **52**(8), 08JJ02 (2013)
31.559 K. Saarinen, T. Laine, S. Kuisma, J. Nissilä, P. Hautojärvi, L. Dobrzynski, J.M. Baranowski, K. Pakula, R. Stepniewski, M. Wojdak, A. Wysmolek, T. Suski, M. Leszczynski, I. Grzegory, S. Porowski: Observation of native Ga vacancies in GaN by positron annihilation, Phys. Rev. Lett. **79**(16), 3030 (1997)
31.560 F. Tuomisto, K. Saarinen, B. Lucznik, I. Grzegory, H. Teisseyre, T. Suski, S. Porowski, P.R. Hageman, J. Likonen: Effect of growth polarity on vacancy defect and impurity incorporation in dislocation-free GaN, Appl. Phys. Lett. **86**(3), 31915 (2005)
31.561 F. Tuomisto, V. Ranki, D.C. Look, G.C. Farlow: Introduction and recovery of Ga and N sublattice defects in electron-irradiated GaN, Phys. Rev. B **76**(16), 165207 (2007)
31.562 F. Tuomisto: Vacancy Defects in III-nitrides: What does positron annihilation spectroscopy reveal?, Proc. Int. Workshop Positron Studies of Defects (PSD 08) (2011) p. 012003
31.563 S. Hautakangas, I. Makkonen, V. Ranki, M.J. Puska, K. Saarinen, X. Xu, D.C. Look: Direct evidence of impurity decoration of Ga vacancies in GaN from positron annihilation spectroscopy, Phys. Rev. B **73**(19), 193301 (2006)
31.564 J. Oila, J. Kivioja, V. Ranki, K. Saarinen, D.C. Look, R.J. Molnar, S.S. Park, S.K. Lee, J.Y. Han: Ga vacancies as dominant intrinsic acceptors in GaN grown by hydride vapor phase epitaxy, Appl. Phys. Lett. **82**(20), 3433 (2003)
31.565 K. Saarinen, S. Hautakangas, F. Tuomisto: Dominant intrinsic acceptors in GaN and ZnO, Proc. 21st Nordic Semiconductor Meet., 21NSM (2006) p. 105
31.566 F. Tuomisto, S. Hautakangas, I. Makkonen, V. Ranki, M.J. Puska, K. Saarinen, M. Bockowski, T. Suski, T. Paskova, B. Monemar, X. Xu, D.C. Look: Dissociation of VGa-ON complexes in HVPE GaN by high pressure and high temperature annealing, Phys. Status Solidi B **243**(7), 1436 (2006)
31.567 K. Saarinen, T. Suski, I. Grzegory, D.C. Look: Thermal stability of isolated and complexed Ga vacancies in GaN bulk crystals, Phys. Rev. B **64**(23), 233201 (2001)
31.568 T. Paskova, D. Hommel, P.P. Paskov, V. Darakchieva, B. Monemar, M. Bockowski, T. Suski, I. Grzegory, F. Tuomisto, K. Saarinen, N. Ashkenov, M. Schubert: Effect of high-temperature annealing on the residual strain and bending of freestanding GaN films grown by hydride vapor phase epitaxy, Appl. Phys. Lett. **88**(14), 141909 (2006)
31.569 F. Tuomisto, K. Saarinen, T. Paskova, B. Monemar, M. Bockowski, T. Suski: Thermal stability of in-grown vacancy defects in GaN grown by hydride vapor phase epitaxy, J. Appl. Phys. **99**(6), 06610511 (2006)
31.570 F. Tuomisto, T. Suski, H. Teisseyre, M. Krysko, M. Leszczynski, B. Lucznik, I. Grzegory, S. Porowski, D. Wasik, A. Witowski, W. Gebicki, P. Hageman, K. Saarinen: Polarity dependent properties of GaN layers grown by hydride vapor phase epitaxy on GaN bulk crystals, Phys. Status Solidi B **240**(2), 289 (2003)
31.571 N. Faleev, C. Honsberg, O. Jani, I. Ferguson: Crystalline perfection of GaN and AlN epitaxial layers and the main features of structural transformation of crystalline defects, J. Cryst. Growth **300**(1), 246–250 (2007)
31.572 F. Tuomisto, T. Paskova, R. Kröger, S. Figge, D. Hommel, B. Monemar, R. Kersting: Defect distribution in *a*-plane GaN on Al_2O_3, Appl. Phys. Lett. **90**(12), 121915 (2007)
31.573 J. Oila, V. Ranki, J. Kivioja, K. Saarinen, P. Hautojärvi, J. Likonen, J.M. Baranowski, K. Pakula, T. Suski, M. Leszczynski, I. Grzegory: Influence of dopants and substrate material on the formation of Ga vacancies in epitaxial GaN layers, Phys. Rev. B **63**(4), 045205 (2001)
31.574 S. Hautakangas, J. Oila, M. Alatalo, K. Saarinen, L. Liszkay, D. Seghier, H.P. Gislason: Vacancy defects as compensating centers in Mg-doped GaN, Phys. Rev. Lett. **90**(13), 137402 (2003)
31.575 S. Hautakangas, K. Saarinen, L. Liszkay, J.A. Freitas, R.L. Henry: Role of open volume defects in Mg-doped GaN films studied by positron annihilation spectroscopy, Phys. Rev. B **72**(16), 165303 (2005)
31.576 F. Tuomisto, T. Paskova, S. Figge, D. Hommel, B. Monemar: Vacancy defect distribution in heteroepitaxial-plane GaN grown by hydride vapor phase epitaxy, First Int. Symp. Growth Nitrides ISGN-1 (2007) p. 251
31.577 J. Oila, A. Kemppinen, A. Laakso, K. Saarinen, W. Egger, L. Liszkay, P. Sperr, H. Lu, W.J. Schaff: Influence of layer thickness on the formation of In vacancies in InN grown by molecular beam epitaxy, Appl. Phys. Lett. **84**(9), 1486 (2004)
31.578 F. Tuomisto, A. Pelli, K.M. Yu, W. Walukiewicz, W.J. Schaff: Compensating point defects in He^{+4}-irradiated InN, Phys. Rev. B **75**(19), 193201 (2007)
31.579 P. Asoka-Kumar, K.G. Lynn: Applications of positron annihilation spectroscopy, J Phys IV Fr. **05**(C1), C1 (1995)
31.580 A. Pelli, K. Saarinen, F. Tuomisto, S. Ruffenach, O. Briot: Influence of V/III molar ratio on the formation of in vacancies in InN grown by metal-organic vapor-phase epitaxy, Appl. Phys. Lett. **89**(1), 011911 (2006)
31.581 F. Reurings, C. Rauch, F. Tuomisto, R.E. Jones, K.M. Yu, W. Walukiewicz, W.J. Schaff: Defect redistribution in postirradiation rapid-thermal-

annealed InN, Phys. Rev. B **82**(15), 153202 (2010)

31.582 F. Tuomisto, J.-M. Mäki, T.Y. Chemekova, Y.N. Makarov, O.V. Avdeev, E.N. Mokhov, A.S. Segal, M.G. Ramm, S. Davis, G. Huminic, H. Helava, M. Bickermann, B.M. Epelbaum: Characterization of bulk AlN crystals with positron annihilation spectroscopy, Spec. Issue IWBNS-5 Int. Workshop Bulk Nitride Semicond. V (2008) p. 3998

31.583 J.-M. Mäki, F. Tuomisto, B. Bastek, F. Bertam, J. Christen, A. Dadgar, A. Krost: Effect of growth conditions on vacancy defects in MOVPE grown AlN thin layers, Phys. Status Solidi C **6**(11), 2575 (2009)

31.584 Z. Liliental-Weber, X. Ni, H. Morkoc: Structural perfection of laterally overgrown GaN layers grown in polar- and non-polar directions, J. Mater. Sci. Mater. Electron. **19**(8/9), 815 (2008)

31.585 S.K. Mathis, A.E. Romanov, L.F. Chen, G.E. Beltz, W. Pompe, J.S. Speck: Modeling of threading dislocation reduction in growing GaN layers, Phys. Status Solidi A **179**(1), 125 (2000)

31.586 T. Sugahara, H. Sato, M. Hao, Y. Naoi, S. Kurai, S. Tottori, K. Yamashita, K. Nishino, L.T. Romano, S. Sakai: Direct evidence that dislocations are non-radiative recombination centers in GaN, Jpn. J. Appl. Phys. Part 2 Lett. **37**(4A), 398 (1998)

31.587 A. Chakraborty, B.A. Haskell, S. Keller, J.S. Speck, S.P. Denbaars, S. Nakamura, U.K. Mishra: Demonstration of nonpolar *m*-plane InGaN/GaN light-emitting diodes on free-standing *m*-plane GaN substrates, Jpn. J. Appl. Phys. Part 2 Lett. **44**, 173 (2005)

31.588 A. Sakai, H. Sunakawa, A. Usui: Defect structure in selectively grown GaN films with low threading dislocation density, Appl. Phys. Lett. **71**(16), 2259 (1997)

31.589 Z. Liliental-Weber, M. Benamara, W. Swider, J. Washburn, J. Park, P.A. Grudowski, C.J. Eiting, R.D. Dupuis: TEM study of defects in laterally overgrown GaN layers, MRS Internet J. Nitride Semicond. Res. **4S1**, 6d (1999)

31.590 Z. Liliental-Weber, D. Cherns: Microstructure of laterally overgrown GaN layers, J. Appl. Phys. **89**(12), 7833 (2001)

31.591 T.S. Zheleva, S.A. Smith, D.B. Thomson, K.J. Linthicum, P. Rajagopal, R.P. Davis: Pendeo-epitaxy: A new approach for lateral growth of gallium nitride films, J. Electron. Mater. **28**(4), 5 (1999)

31.592 P. Fini, H. Marchand, J.P. Ibbetson, B. Moran, L. Zhao, S.P. Denbaars, J.S. Speck, U.K. Mishra: Maskless lateral epitaxial overgrowth of GaN on sapphire, Proc. 1999 MRS Spring Meet. – Symp. Wide-Bandgap Semiconductors for High-Power, High Frequency and High-Temperature Applications (1999) p. 315

31.593 R.F. Davis, T. Gehrke, K.J. Linthicum, T.S. Zheleva, E.A. Preble, P. Rajagopal, C.A. Zorman, M. Mehregany: Pendeo-epitaxial growth of thin films of gallium nitride and related materials and their characterization, Proc. Twelfth Am. Conf. Crystal Growth and Epitaxy (2001) p. 134

31.594 S. Ruvimov, Z. Liliental-Weber, T. Suski, J.W. Ager III, J. Washburn, J. Krueger, C. Kisielowski, E.R. Weber, H. Amano, I. Akasaki: Effect of Si doping on the dislocation structure of GaN grown on the A-face of sapphire, Appl. Phys. Lett. **69**(7), 990 (1996)

31.595 M.E. Hawkridge, Z. Liliental-Weber, K.M. Yu, L.A. Reichertz, W.J. Schaff, J.W. Ager, W. Walukiewicz: Stacking faults and phase changes in Mg-doped InGaN grown on Si, Phys. Status Solidi C **6**(S2), 421 (2009)

31.596 D. Zubia, S.H. Zaidi, S.R.J. Brueck, S.D. Hersee: Nanoheteroepitaxial growth of GaN on Si by organometallic vapor phase epitaxy, Appl. Phys. Lett. **76**(7), 858 (2000)

31.597 I. Vurgaftman, J.R. Meyer, N. Tansu, L.J. Mawst: (In)GaAsN-based type-II W quantum-well lasers for emission at $\lambda = 1.55\ \mu m$, Appl. Phys. Lett. **83**(14), 2742 (2003)

31.598 Y. Ikenaga, T. Miyamoto, S. Makino, T. Kageyama, M. Arai, F. Koyama, K. Iga: 1.4 μm GaInNAs/GaAs quantum well laser grown by chemical beam epitaxy, Jpn. J. Appl. Phys. **41**(2A), 664 (2002)

31.599 T. Kitatani, K. Nakahara, M. Kondow, K. Uomi, T. Tanaka: A 1.3 μm GaInNAs/GaAs single-quantum-well laser diode with a high characteristic temperature over 200 K, Jpn. J. Appl. Phys. **39**(2A), L86 (2000)

31.600 M. Leroux, N. Grandjean, J. Massies, B. Gil, P. Lefebvre, P. Bigenwald: Barrier-width dependence of group-III nitrides quantum-well transition energies, Phys. Rev. B Condens. Matter **60**(3), 1496 (1999)

31.601 G. Cheng, A. Kolmakov, Y. Zhang, M. Moskovits, R. Munden, M.A. Reed, G. Wang, D. Moses, J. Zhang: Current rectification in a single GaN nanowire with a well-defined p-n junction, Appl. Phys. Lett. **83**(8), 1578 (2003)

31.602 W. Guo, M. Zhang, P. Bhattacharya, J. Heo: Auger recombination in III-nitride nanowires and its effect on nanowire light-emitting diode characteristics, Nano Lett. **11**(4), 1434 (2011)

31.603 T. Kuykendall, P. Ulrich, S. Aloni, P. Yang: Complete composition tunability of InGaN nanowires using a combinatorial approach, Nat. Mater. **6**(12), 951 (2007)

31.604 F. Qian, S. Gradecak, Y. Li, C.-Y. Wen, C.M. Lieber: Core/multishell nanowire heterostructures as multicolor, high-efficiency light-emitting diodes, Nano Lett. **5**(11), 2287 (2005)

31.605 T. Kuykendall, P.J. Pauzauskie, Y. Zhang, J. Goldberger, D. Sirbuly, J. Denlinger, P. Yang: Crystallographic alignment of high-density gallium nitride nanowire arrays, Nat. Mater. **3**(8), 524 (2004)

31.606 H.P.T. Nguyen, S. Zhang, K. Cui, X. Han, S. Fathololoumi, M. Couillard, G.A. Botton, Z. Mi: p-Type modulation doped InGaN/GaN dot-in-a-wire white-light-emitting diodes monolithically grown on Si(111), Nano Lett. **11**(5), 1919 (2011)

31.607 B. Daudin: Polar and nonpolar GaN quantum dots, J. Phys. Condens. Matter **20**(47), 473201

(2008)
31.608 N. Grandjean, J. Massies: GaN/Al$_x$Ga$_{1-x}$N quantum wells grown by molecular beam epitaxy with thickness control at the monolayer scale, Appl. Phys. Lett. **73**(9), 1260 (1998)
31.609 J. Seo Im, H. Kollmer, J. Off, A. Sohmer, F. Scholz, A. Hangleiter: Reduction of oscillator strength due to piezoelectric fields in GaN/Al$_x$Ga$_{1-x}$N quantum wells, Phys. Rev. B **57**(16), R9435–R9438 (1998)
31.610 P. Lefebvre, J. Allègre, B. Gil, H. Mathieu, N. Grandjean, M. Leroux, J. Massies, P. Bigenwald: Time-resolved photoluminescence as a probe of internal electric fields in GaN-(GaAl)N quantum wells, Phys. Rev. B **59**(23), 15363 (1999)
31.611 M. Zamfirescu, B. Gil, N. Grandjean, G. Malpuech, A. Kavokin, P. Bigenwald, J. Massies: Extremely sharp dependence of the exciton oscillator strength on quantum-well width in the GaN/Al$_x$Ga$_{1-x}$N system: The polarization field effect, Phys. Rev. B **64**(12), 121304 (2001)
31.612 F. Yang, M. Wilkinson, E.J. Austin, K.P. O'Donnell: Origin of the stokes shift a geometrical model of exciton spectra in 2-D semiconductors_I, Phys. Rev. Lett. **71**(8), 1287 (1993)
31.613 F. Yang, M. Wilkinson, E.J. Austin, K.P. O'Donnell: Origin of the stokes shift a geometrical model of exciton spectra in 2-D semiconductors, Phys. Rev. Lett. **70**(3), 323 (1993)
31.614 F. Bernardini, V. Fiorentini, D. Vanderbilt: Spontaneous polarization and piezoelectric constants of III–V nitrides, Phys. Rev. B **56**(6), R10024 (1997)
31.615 J. Seo Im, H. Kollmer, J. Off, A. Sohmer, F. Scholz, A. Hangleiter: Effects of piezoelectric fields in GaInN/GaN and GaN/AlGaN heterostructures and quantum wells, Proc. Nitride Semicond. Symp (1997) p. 513
31.616 J.C. Harris, T. Someya, S. Kako, K. Hoshino, Y. Arakawa: Time-resolved photoluminescence of GaN/Al$_{0.5}$Ga$_{0.5}$N quantum wells, Appl. Phys. Lett. **77**(7), 1005 (2000)
31.617 P. Waltereit, O. Brandt, A. Trampert, H.T. Grahn, J. Menniger, M. Ramsteiner, M. Reiche, K.H. Ploog: Nitride semiconductors free of electrostatic fields for efficient white light-emitting diodes, Nature **406**(6798), 865 (2000)
31.618 E. Kuokstis, C.Q. Chen, M.E. Gaevski, W.H. Sun, J.W. Yang, G. Simin, M. Asif Khan, H.P. Maruska, D.W. Hill, M.C. Chou, J.J. Gallagher, B. Chai: Polarization effects in photoluminescence of *c*- and *m*-plane GaN/AlGaN multiple quantum wells, Appl. Phys. Lett. **81**(22), 4130 (2002)
31.619 H.M. Ng: Molecular-beam epitaxy of GaN/Al$_x$Ga$_{1-x}$N multiple quantum wells on *r*-plane $(10\bar{1}\bar{2})$ sapphire substrates, Appl. Phys. Lett. **80**(23), 4369 (2002)
31.620 M.D. Craven, S.H. Lim, F. Wu, J.S. Speck, S.P. DenBaars: Structural characterization of nonpolar $(11\bar{2}0)$ *a*-plane GaN thin films grown on $(1\bar{1}02)$ *r*-plane sapphire, Appl. Phys. Lett. **81**(3), 469 (2002)
31.621 H.M. Ng, A. Bell, F.A. Ponce, S.N.G. Chu: Structural and optical characterization of nonpolar GaN/AlN quantum wells, Appl. Phys. Lett. **83**(4), 653 (2003)
31.622 A. Chakraborty, B.A. Haskell, S. Keller, J.S. Speck, S.P. DenBaars, S. Nakamura, U.K. Mishra: Nonpolar InGaN/GaN emitters on reduced-defect lateral epitaxially overgrown a -plane GaN with drive-current-independent electroluminescence emission peak, Appl. Phys. Lett. **85**(22), 5143 (2004)
31.623 C.Q. Chen, M.E. Gaevski, W.H. Sun, E. Kuokstis, J.P. Zhang, R.S.Q. Fareed, H.M. Wang, J.W. Yang, G. Simin, M.A. Khan, H.-P. Maruska, D.W. Hill, M.M.C. Chou, B. Chai: GaN homoepitaxy on freestanding $(1\bar{1}00)$ oriented GaN substrates, Appl. Phys. Lett. **81**(17), 3194 (2002)
31.624 S. Juršėnas, E. Kuokštis, S. Miasojedovas, G. Kurilčik, A. Žukauskas, C.Q. Chen, J.W. Yang, V. Adivarahan, M. Asif Khan: Increase of free carrier lifetime in nonpolar *a*-plane GaN grown by epitaxial lateral overgrowth, Appl. Phys. Lett. **85**(5), 771 (2004)
31.625 M.D. Craven, P. Waltereit, J.S. Speck, S.P. DenBaars: Well-width dependence of photoluminescence emission from *a*-plane GaN/AlGaN multiple quantum wells, Appl. Phys. Lett. **84**(4), 496 (2004)
31.626 L. Jiawei, Y. Zhizhen, N.M. Nasser: GaN-based quantum dots, Phys. E Low-Dimens. Syst. Nanostructures **16**(2), 244 (2003)
31.627 K. Kato, T. Kusunoki, C. Takenaka, T. Tanahashi, K. Nakajima: Reduction of dislocations in InGaAs layer on GaAs using epitaxial lateral overgrowth, J. Cryst. Growth **115**(1–4), 174 (1991)
31.628 Y. Miyamoto, A. Sano, E. Yoshida, T. Sakano: Ultra-high-capacity digital coherent optical transmission technology, NTT Tech. Rev. **9**(8), 1 (2011)
31.629 M. Kondow, T. Kitatani, S. Nakatsuka, M.C. Larson, K. Nakahara, Y. Yazawa, M. Okai, K. Uomi: GaInNAs: A novel material for long-wavelength semiconductor lasers, IEEE J. Sel. Top. Quant. **3**(3), 719 (1997)
31.630 J.S. Harris: Tunable long-wavelength vertical-cavity lasers: The engine of next generation optical networks?, Sel. Top. Quantum Electron. IEEE J. **6**(6), 1145 (2000)
31.631 K. Yang, C.P. Hains, J. Cheng: Efficient continuous-wave lasing operation of a narrow-stripe oxide-confined GaInNAs-GaAs multiquantum-well laser grown by MOCVD, Photonics Technol. Lett. IEEE **12**(1), 7 (2000)
31.632 M. Kondow, T. Kitatani, K. Nakahara, T. Tanaka: A 1.3 μm GaInNAs Laser Diode with a lifetime of over 1000 hours, Jpn. J. Appl. Phys. **38**(12A), L1355–L1356 (1999)
31.633 N.Y. Li, C.P. Hains, K. Yang, J. Lu, J. Cheng, P.W. Li: Organometallic vapor phase epitaxy growth and optical characteristics of almost 1.2 μm GaInNAs three-quantum-well laser diodes, Appl. Phys. Lett. **75**(8), 1051 (1999)
31.634 S. Sato, S. Satoh: Room-temperature pulsed operation of strained GaInNAs/GaAs double quantum well laser diode grown by metal organic chemical vapour deposition, Electron. Lett. **34**(15), 1495 (1998)
31.635 T. Kitatani, M. Kondow, K. Nakahara, M.C. Larson, K. Uomi: Temperature dependence of the thresh-

old current and the lasing wavelength in 1.3 μm GaInNAs/GaAs single quantum well laser diode, Opt. Rev. **5**(2), 69 (1998)
31.636 S. Nakatsuka, M. Kondow, T. Kitatani, Y. Yazawa, M. Okai: Index-guide GaInNAs laser diode for optical communications, Jpn. J. Appl. Phys. **37**(3B), 1380 (1998)
31.637 A. Ougazzaden, S. Bouchoule, A. Mereuta, E.V.K. Rao, J. Decobert: Room temperature laser operation of bulk InGaAsN/GaAs structures grown by AP-MOVPE using N_2 as carrier gas, Electron. Lett. **35**(6), 474 (1999)
31.638 M. Fischer, M. Reinhardt, A. Forchel: High temperature operation of GaInAsN laserdiodes in the 1.3 μm regime, Proc. Device Res. Conf., Conf. Digest. 58th DRC (2000) p. 119
31.639 H. Shimizu, K. Kumada, S. Uchiyama, A. Kasukawa: High performance CW 1.26 μm GaInNAsSb-SQW and 1.20 μm GaInAsSb-SQW ridge lasers, Electron. Lett. **36**(20), 1701 (2000)
31.640 C. Setiagung, H. Shimizu, Y. Ikenaga, K. Kumada, A. Kasukawa: Very low threshold current density of 1.3 μm-range GaInNAsSb-GaNAs3 and 5 QWs lasers, Sel. Top. Quantum Electron. IEEE J. **9**(5), 1209 (2003)
31.641 S.R. Bank, H.B. Yuen, H. Bae, M.A. Wistey, J.S. Harris: Overannealing effects in GaInNAs(Sb) alloys and their importance to laser applications, Appl. Phys. Lett. **88**(22), 221115 (2006)
31.642 D. Gollub, S. Moses, M. Fischer, A. Forchel: 1.42 μm continuous-wave operation of GaInNAs laser diodes, Electron. Lett. **39**(10), 777 (2003)
31.643 N. Tansu, L.J. Mawst: Low-threshold strain-compensated InGaAs(N) ($\lambda = 1.19-1.31$ μm) quantum-well lasers, Photonics Technol. Lett. IEEE **14**(4), 444 (2002)
31.644 C.S. Peng, T. Jouhti, P. Laukkanen, E.-M. Pavelescu, J. Konttinen, W. Li, M. Pessa: 1.32 μm GaInNAs-GaAs laser with a low threshold current density, Photonics Technol. Lett. IEEE **14**(3), 275 (2002)
31.645 X. Yang, M.J. Jurkovic, J.B. Heroux, W.I. Wang: Molecular beam epitaxial growth of InGaAsN:Sb/GaAs quantum wells for long-wavelength semiconductor lasers, Appl. Phys. Lett. **75**(2), 178 (1999)
31.646 X. Yang, J.B. Héroux, L.F. Mei, W.I. Wang: InGaAsNSb/GaAs quantum wells for 1.55 μm lasers grown by molecular-beam epitaxy, Appl. Phys. Lett. **78**(26), 4068 (2001)
31.647 S.R. Bank, M.A. Wistey, L.L. Goddard, H.B. Yuen, V. Lordi, J.S. Harris: Low-threshold continuous-wave 1.5 μm GaInNAsSb lasers grown on GaAs, Quantum Electron. IEEE J. Of **40**(6), 656 (2004)
31.648 M.O. Fischer, M. Reinhardt, A. Forchel: Room-temperature operation of GaInAsN-GaAs laser diodes in the 1.5 μm range, Sel. Top. Quantum Electron. IEEE J. **7**(2), 149 (2001)
31.649 D.A. Livshits, A.Y. Egorov, H. Riechert: 8 W continuous wave operation of InGaAsN lasers at 1.3 μm, Electron. Lett. **36**(16), 1381 (2000)
31.650 F. Bugge, G. Erbert, J. Fricke, S. Gramlich, R. Staske, H. Wenzel, U. Zeimer, M. Weyers: 12 W continuous-wave diode lasers at 1120 nm with InGaAs quantum wells, Appl. Phys. Lett. **79**(13), 1965 (2001)
31.651 S. Okur, R. Shimada, F. Zhang, S.D.A. Hafiz, J. Lee, V. Avrutin, H. Morkoc, A. Franke, F. Bertram, J. Christen, U. Özgür: GaN-based vertical cavities with all dielectric reflectors by epitaxial lateral overgrowth, Jpn. J. Appl. Phys. **52**(8), 08JH03 (2013)
31.652 E. Wong: Energy efficient passive optical networks with low power VCSELs, Proc. Annu. Conf. Wirel. Optical Commun. (WOCC) (2012) p. 48
31.653 M.A. Khan, J.N. Kuznia, J.M. van Hove, D.T. Olson: Reflective filters based on single-crystal $GaN/Al_xGa_{1-x}N$ multilayers deposited using low-pressure metalorganic chemical vapor deposition, Appl. Phys. Lett. **59**(12), 1449 (1991)
31.654 T. Someya, Y. Arakawa: Highly reflective $GaN/Al_{0.34}Ga_{0.66}N$ quarter-wave reflectors grown by metal organic chemical vapor deposition, Appl. Phys. Lett. **73**(25), 3653 (1998)
31.655 N. Nakada, H. Ishikawa, T. Egawa, T. Jimbo, M. Umeno: MOCVD growth of high reflective GaN/AlGaN distributed Bragg reflectors, 13th Int, Conf. Cryst. Growth Conj. Unction Elev. Int. Conf. Vap. Growth Epitaxy **237–239**, 961 (2002)
31.656 M. Arita, M. Nishioka, Y. Arakawa: InGaN vertical microcavity LEDs with a Si-doped AlGaN/GaN distributed Bragg reflector, Physica Status Solidi C **194**, 403 (2002)
31.657 R. Langer, A. Barski, J. Simon, N.T. Pelekanos, O. Konovalov, R.A. Le Si Dang: High-reflectivity GaN/GaAlN Bragg mirrors at blue/green wavelengths grown by molecular beam epitaxy, Appl. Phys. Lett. **74**(24), 3610 (1999)
31.658 R. Butté, G. Christmann, E. Feltin, A. Castiglia, J. Levrat, G. Cosendey, A. Altoukhov, J.-F. Carlin, N. Grandjean: Room temperature polariton lasing in III-nitride microcavities, a comparison with blue GaN-based vertical cavity surface emitting lasers, Proc. Gallium Nitride Mat. and Devices IV (2009) p. 721619
31.659 C. Holder, D. Feezell, J.S. Speck, S.P. DenBaars, S. Nakamura: Demonstration of nonpolar GaN-based vertical-cavity surface-emitting lasers, Proc. SPIE Vert.-Cavity Surf.-Emitting Lasers XVII, Vol. 8639 (2013) p. 863906
31.660 D. Kasahara, D. Morita, T. Kosugi, K. Nakagawa, J. Kawamata, Y. Higuchi, H. Matsumura, T. Mukai: Demonstration of blue and green GaN-based vertical-cavity surface-emitting lasers by current injection at room temperature, Appl. Phys. Express **4**(7), 072103 (2011)
31.661 H.-Y. Ryu: Extraction efficiency in GaN nanorod light-emitting diodes investigated by finite-difference time-domain simulation, J. Korean Phys. Soc. **58**(4), 878 (2011)
31.662 Y.-J. Liu, C.-C. Huang, T.-Y. Chen, C.-S. Hsu, J.-K. Liou, W.-C. Liu: Improved performance of an InGaN-based light-emitting diode With a p-

GaN/n-GaN barrier junction, IEEE J. Quantum Electron. **47**(6), 755 (2011)
31.663 L.-B. Chang, M.-J. Lai, R.-M. Lin, C.-H. Huang: Effect of electron leakage on efficiency droop in wide-well InGaN-based light-emitting diodes, Appl. Phys. Express **4**(1), 012106 (2011)
31.664 C.-H. Chiu, C.-C. Lin, D.-M. Deng, D.-W. Lin, J.-C. Li, Z.-Y. Li, G.-W. Shu, T.-C. Lu, J.-L. Shen, H.-C. Kuo, K.-M. Lau: Optical and electrical properties of GaN-based light emitting diodes grown on micro- and nano-scale patterned Si substrate, IEEE J. Quantum Electron. **47**(7), 899 (2011)
31.665 S. Gradecak, F. Qian, Y. Li, H.-G. Park, C.M. Lieber: GaN nanowire lasers with low lasing thresholds, Appl. Phys. Lett. **87**(17), 173111 (2005)
31.666 H.-G. Park, F. Qian, C.J. Barrelet, Y. Li: Microstadium single-nanowire laser, Appl. Phys. Lett. **91**(25), 251115 (2007)
31.667 M.A. Zimmler, F. Capasso, S. Muller, C. Ronning: Optically pumped nanowire lasers: Invited review, Semicond. Sci. Technol. **25**(2), 024001 (2010)
31.668 S. Arafin, X. Liu, Z. Mi: Review of recent progress of III-nitride nanowire lasers, J. Nanophotonics **7**(1), 074599 (2013)
31.669 H.-J. Choi, J.C. Johnson, R. He, S.-K. Lee, F. Kim, P. Pauzauskie, J. Goldberger, R.J. Saykally, P. Yang: Self-organized GaN quantum wire UV lasers, J. Phys. Chem. B **107**(34), 8721 (2003)
31.670 D. Saxena, S. Mokkapati, P. Parkinson, N. Jiang, Q. Gao, H.H. Tan, C. Jagadish: Optically pumped room-temperature GaAs nanowire lasers, Nat. Photonics **7**(12), 963 (2013)
31.671 B. Mayer, D. Rudolph, J. Schnell, S. Morkötter, J. Winnerl, J. Treu, K. Müller, G. Bracher, G. Abstreiter, G. Koblmüller, J.J. Finley: Lasing from individual GaAs-AlGaAs core-shell nanowires up to room temperature, Nat. Commun. **4**, 2931 (2013) doi:10.1038/ncomms3931
31.672 J. Treu, M. Bormann, H. Schmeiduch, M. Döblinger, S. Morkötter, S. Matich, P. Wiecha, K. Saller, B. Mayer, M. Bichler, M.-C. Amann, J.J. Finley, G. Abstreiter, G. Koblmüller: Enhanced luminescence properties of InAs–InAsP core-shell nanowires, Nano Lett. **13**(12), 6070 (2013)
31.673 S.J. Chang, S.M. Wang, P.C. Chang, C.H. Kuo, S.J. Young, T.P. Chen, S.L. Wu, B.R. Huang: GaN Schottky barrier photodetectors, IEEE Sens. J. **10**(10), 1609 (2010)
31.674 K.P. Korona: Nitride-based photodetectors containing quantum wells in tunable electric fields, J. Optoelectron. Adv. Mater. **11**(9), 1108 (2009)
31.675 H.C. Lee, Y.K. Su, J.C. Lin, Y.C. Cheng, S.L. Wu, Y.D. Jhou: AlInGaN metal-insulator-semiconductor photodetectors at UV-C 280 nm, Electrochem. Solid-State Lett. **12**(10), 357 (2009)
31.676 E. Muñoz: (Al,In,Ga)N-based photodetectors. Some materials issues, Phys. Status Solidi B **244**(8), 2859 (2007)
31.677 M.-H. Kim, M.F. Schubert, Q. Dai, J.K. Kim, E.F. Schubert, J. Piprek, Y. Park: Origin of efficiency droop in GaN-based light-emitting diodes, Appl. Phys. Lett. **91**(18), 183507 (2007)
31.678 X. Ni, X. Li, J. Lee, S. Liu, V. Avrutin, U. Ozgur, H. Morkoç, A. Matulionis, T. Paskova, G. Mulholland, K.R. Evans: The effect of ballistic and quasi-ballistic electrons on the efficiency droop of InGaN light emitting diodes, Phys. Status Solidi RRL Rapid Res. Lett. **4**(8/9), 194 (2010)
31.679 J. Xie, X. Ni, Q. Fan, R. Shimada, U. Ozgur, H. Morkoç: On the efficiency droop in InGaN multiple quantum well blue light emitting diodes and its reduction with p-doped quantum well barriers, Appl. Phys. Lett. **93**(12), 121107 (2008)
31.680 C. Guthy, C.-Y. Nam, J.E. Fischer: Unusually low thermal conductivity of gallium nitride nanowires, J. Appl. Phys. **103**(6), 064319 (2008)
31.681 J. Zou: Lattice thermal conductivity of freestanding gallium nitride nanowires, J. Appl. Phys. **108**(3), 034324 (2010)
31.682 Z. Wang, X. Zu, F. Gao, W.J. Weber, J.-P. Crocombette: Atomistic simulation of the size and orientation dependences of thermal conductivity in GaN nanowires, Appl. Phys. Lett. **90**(16), 161923 (2007)
31.683 M.L. Colussi, R.J. Baierle, R.H. Miwa: Doping effects of C, Si and Ge in wurtzite [0001] GaN, AlN, and InN nanowires, J. Appl. Phys. **110**(3), 033709 (2011)
31.684 S. Zhao, S. Fathololoumi, K.H. Bevan, D.P. Liu, M.G. Kibria, Q. Li, G.T. Wang, H. Guo, Z. Mi: Tuning the surface charge properties of epitaxial InN nanowires, Nano Lett. **12**(6), 2877 (2012)
31.685 A. Miehr, O. Ambacher, W. Rieger, T. Metzger, E. Born, R.A. Fischer: The first monomeric, volatile bis-azide single-source precursor to Gallium nitride thin films, Chem. Vap. Depos. **2**(2), 51 (1996)
31.686 A.C. Jones, S.A. Rushworth, D.J. Houlton, J.S. Roberts, V. Roberts, C.R. Whitehouse, G.W. Critchlow: Deposition of aluminum nitride thin films by MOCVD from the trimethylaluminum–ammonia adduct, Chem. Vap. Depos. **2**(1), 5 (1996)
31.687 M. Yoshizawa, A. Kikuchi, N. Fujita, K. Kushi, H. Sasamoto, K. Kishino: Self-organization of GaN/$Al_{0.18}Ga_{0.82}N$ multi-layer nano-columns on (0 0 0 1) Al_2O_3 by RF molecular beam epitaxy for fabricating GaN quantum disks, J. Cryst. Growth **189/190**(0), 138–141 (1998)
31.688 T. Karabacak, P.-I. Wang, G.-C. Wang, T.-M. Lu: Growth of single crystal tungsten nanorods by oblique angle sputter deposition, Proc. Contin. Nanophase and Nanostructured Mat. (2003) p. 75
31.689 Y.Y. Kim, B.H. Kong, H.K. Cho: Vertically arrayed Ga-doped ZnO nanorods grown by magnetron sputtering: The effect of Ga contents and microstructural evaluation, J. Cryst. Growth **330**(1), 17 (2011)
31.690 F. Shi: GaN nanowires fabricated by magnetron sputtering deposition. In: *Nanowires – Fundamental Research*, ed. by A. Hashim (InTech 2011) doi:10.5772/16355, available from https://www.intechopen.com/books/nanowires-fundamental-research/gan-nanowires-fabricated-bymagnetron-sputtering-deposition

31.691 M. Junaid: *Magnetron Sputter Epitaxy of GaN Epilayers and Nanorods*, Ph.D. Thesis (Linköping Studies in Science and Technology, Sweden 2012)

31.692 H. Zhuang, S. Xue: GaN nanowires synthesized on Si(111) substrates by magnetron sputtering and ammonification technique, Jpn. J. Appl. Phys. **46**(10R), 6886 (2007)

31.693 R.S. Wagner, W.C. Ellis: Vapour-liquid-solid mechanism of single crystal growth, Appl. Phys. Lett. **4**(5), 89 (1964)

31.694 M. He, I. Minus, P. Zhou, S.N. Mohammed, J.B. Halpern, R. Jacobs, W.L. Sarney, L. Salamanca-Riba, R.D. Vispute: Growth of large-scale GaN nanowires and tubes by direct reaction of Ga with NH_3, Appl. Phys. Lett. **77**(23), 3731 (2000)

31.695 C.C. Tang, S.S. Fan, H.Y. Dang, P. Li, Y.M. Liu: Simple and high-yield method for synthesizing single-crystal GaN nanowires, Appl. Phys. Lett. **77**(13), 1961 (2000)

31.696 C.H. Liang, L.C. Chen, J.S. Hwang, K.H. Chen, Y.T. Hung, Y.F. Chen: Selective-area growth of indium nitride nanowires on gold-patterned Si(100) substrates, Appl. Phys. Lett. **81**(1), 22 (2002)

31.697 H. Parala, A. Devi, F. Hipler, E. Maile, A. Birkner, H.W. Becker, R.A. Fischer: Investigations on InN whiskers grown by chemical vapour deposition, J. Cryst. Growth **231**(1/2), 68 (2001)

31.698 Z.R. Dai, Z.W. Pan, Z.L. Wang: Novel nanostructures of functional oxides synthesized by thermal evaporation, Adv. Funct. Mater. **13**(1), 9 (2003)

31.699 R.-Q. Zhang, Y. Lifshitz, S.-T. Lee: Oxide-assisted growth of semiconducting nanowires, Adv. Mater. **15**(7/8), 635 (2003)

31.700 C.M. Balkaş, R.F. Davis: Synthesis routes and characterization of high-purity, single-phase gallium nitride powders, J. Am. Ceram. Soc. **79**(9), 2309 (1996)

31.701 Y. Zhang, J. Liu, R. He, Q. Zhang, X. Zhang, J. Zhu: Synthesis of aluminum nitride nanowires from carbon nanotubes, Chem. Mater. **13**(11), 3899 (2001)

31.702 J. Liu, X. Zhang, Y. Zhang, R. He, J. Zhu: Novel synthesis of AlN nanowires with controlled diameters, J. Mater. Res. **16**(11), 3133 (2001)

31.703 C.R. Martin: Nanomaterials: A membrane-based synthetic approach, Science **266**(5193), 1961 (1994)

31.704 J. Zhang, X. Peng, X. Wang, Y. Wang, L. Zhang: Micro-Raman investigation of GaN nanowires prepared by direct reaction Ga with NH_3, Chem. Phys. Lett. **345**(5/6), 372 (2001)

31.705 F. Qian, Y. Li, S. Gradecak, D. Wang, C.J. Barrelet, C.M. Lieber: Gallium nitride-based nanowire radial heterostructures for nanophotonics, Nano Lett. **4**(10), 1975 (2004)

31.706 Y.-L. Chang, J.L. Wang, F. Li, Z. Mi: High efficiency green, yellow, and amber emission from InGaN/GaN dot-in-a-wire heterostructures on Si(111), Appl. Phys. Lett. **96**(1), 013106 (2010)

31.707 R. Armitage, K. Tsubaki: Multicolour luminescence from InGaN quantum wells grown over GaN nanowire arrays by molecular-beam epitaxy, Nanotechnology **21**(19), 195202 (2010)

31.708 Y. Kawakami, S. Suzuki, A. Kaneta, M. Funato, A. Kikuchi, K. Kishino: Origin of high oscillator strength in green-emitting InGaN/GaN nanocolumns, Appl. Phys. Lett. **89**(16), 163124 (2006)

31.709 H.-M. Kim, H. Lee, S.I. Kim, S.R. Ryu, T.W. Kang, K.S. Chung: Formation of InGaN nanorods with indium mole fractions by hydride vapor phase epitaxy, Proc. 5th Int. Symp. Blue Laser and Light Emitting Diodes (2004) p. 2802

31.710 H.-M. Kim, W.C. Lee, T.W. Kang, K.S. Chung, C.S. Yoon, C.K. Kim: InGaN nanorods grown on (111) silicon substrate by hydride vapor phase epitaxy, Chem. Phys. Lett. **380**(1/2), 181 (2003)

31.711 A. Kikuchi, M. Kawai, M. Tada, K. Kishino: InGaN/GaN multiple quantum disk nanocolumn light-emitting diodes grown on (111) Si substrate, Jpn. J. Appl. Phys. **43**(12A), L1524 (2004)

31.712 H.-W. Lin, Y.-J. Lu, H.-Y. Chen, H.M. Lee, S. Gwo: InGaN/GaN nanorod array white light-emitting diode, Appl. Phys. Lett. **97**(7), 073101 (2010)

31.713 M. Zervos, D. Tsokkou, M. Pervolaraki, A. Othonos: Low temperature growth of In2O3 and InN nanocrystals on Si(111) via chemical vapour deposition based on the sublimation of NH_4Cl in In, Nanoscale Res. Lett. **4**(6), 491 (2009)

31.714 J. Grandal, M.A. Sánchez-García, E. Calleja, E. Luna, A. Trampert: Accommodation mechanism of InN nanocolumns grown on Si(111) substrates by molecular beam epitaxy, Appl. Phys. Lett. **91**(2), 021902 (2007)

31.715 I. Shalish, G. Seryogin, W. Yi, J.M. Bao, M.A. Zimmler, E. Likovich, D.C. Bell, F. Capasso, V. Narayanamurti: Epitaxial catalyst-free growth of InN nanorods on *c*-plane sapphire, Nanoscale Res. Lett. **4**(6), 532 (2009)

31.716 K.R. Wang, S.J. Lin, L.W. Tu, M. Chen, Q.Y. Chen, T.H. Chen, M.L. Chen, H.W. Seo, N.H. Tai, S.C. Chang, I. Lo, D.P. Wang, W.K. Chu: InN nanotips as excellent field emitters, Appl. Phys. Lett. **92**(12), 123105 (2008)

31.717 M.-S. Hu, G.-M. Hsu, K.-H. Chen, C.-J. Yu, H.-C. Hsu, L.-C. Chen, J.-S. Hwang, L.-S. Hong, Y.-F. Chen: Infrared lasing in InN nanobelts, Appl. Phys. Lett. **90**(12), 123109 (2007)

31.718 P.J. Pauzauskie, P. Yang: Nanowire photonics, Mater. Today **9**(10), 36 (2006)

31.719 R. Yan, D. Gargas, P. Yang: Nanowire photonics, Nat. Photonics **3**(10), 569 (2009)

31.720 D. Saxena, S. Mokkapati, C. Jagadish: Semiconductor nanolasers, IEEE Photonics J **4**(2), 582 (2012)

31.721 D. Vanmaekelbergh, L.K. van Vugt: ZnO nanowire lasers, Nanoscale **3**(7), 2783 (2011)

31.722 C. Ning: Semiconductor nanowire lasers. In: *Advances in Semiconductor Lasers*, ed. by J.J. Coleman, A.C. Bryce, C. Jagadish (Academic, Burlington 2012) p. 455

31.723 L.C. Chen, K.H. Chen, C.C. Chen: Group III- and group IV-nitride nanorods and nanowires. In: *Nanowires and Nanobelts – Materials Properties and Devices: Metal and Semiconductor Nanostructures*, Vol. 1, ed. by Z.L. Wang (Springer, New

York 2003) p. 257
31.724 M. Law, J. Goldberger, P. Yang: Semiconductor nanowires and nanotubes, Annu. Rev. Mater. Res. **34**, 83 (2004)
31.725 G.T. Wang, A.A. Talin, D.J. Werder, J.R. Creighton, E. Lai, R.J. Anderson, I. Arslan: Highly aligned, template-free growth and characterization of vertical GaN nanowires on sapphire by metal-organic chemical vapour deposition, Nanotechnology **17**(23), 5773 (2006)
31.726 L. Cerutti, J. Ristic, S. Fernandez-Garrido, E. Calleja, A. Trampert, K.H. Ploog, S. Lazic, J.M. Calleja: Wurtzite GaN nanocolumns grown on Si(001) by molecular beam epitaxy, Appl. Phys. Lett. **88**(21), 213114 (2006)
31.727 H.-M. Kim, T.W. Kang, K.S. Chung: Nanoscale ultraviolet-light-emitting diodes using wide-bandgap gallium nitride nanorods, Adv. Mater. **15**(7/8), 567 (2003)
31.728 B. Ha, S.H. Seo, J.H. Cho, C.S. Yoon, J. Yoo, G.-C. Yi, C.Y. Park, C.J. Lee: Optical and field emission properties of thin single-crystalline GaN nanowires, J. Phys. Chem. B **109**(22), 11095 (2005)
31.729 T. Kuykendall, P. Pauzauskie, S. Lee, Y. Zhang, J. Goldberger, P. Yang: Metalorganic chemical vapor deposition route to GaN nanowires with triangular cross sections, Nano Lett. **3**(8), 1063 (2003)
31.730 K. Kishino, A. Kikuchi: Highly efficient blue to red emissions of InGaN/GaN nano-disks integrated into GaN nanocolumns, Proc. IEEE LEOS Annu. Meet. (2005) p. 631
31.731 P. Schlotter, R. Schmidt, J. Schneider: Luminescence conversion of blue light emitting diodes, Appl. Phys. Mater. Sci. Process. **64**(4), 417 (1997)
31.732 H.P.T. Nguyen, M. Djavid, K. Cui, Z. Mi: Temperature-dependent nonradiative recombination processes in GaN-based nanowire white-light-emitting diodes on silicon, Nanotechnology **23**(19), 194012 (2012)
31.733 H.P.T. Nguyen, K. Cui, S. Zhang, M. Djavid, A. Korinek, G.A. Botton, Z. Mi: Controlling electron overflow in phosphor-free InGaN/GaN nanowire white light-emitting diodes, Nano Lett. **12**(3), 1317 (2012)
31.734 J.C. Johnson, H.-J. Choi, K.P. Knutsen, R.D. Schaller, P. Yang, R.J. Saykally: Single gallium nitride nanowire lasers, Nat. Mater. **1**(2), 106 (2002)
31.735 F. Qian, Y. Li, S. Gradecak, H.-G. Park, Y. Dong, Y. Ding, Z.L. Wang, C.M. Lieber: Multi-quantum-well nanowire heterostructures for wavelength-controlled lasers, Nat. Mater. **7**(9), 701 (2008)
31.736 Q. Li, J.B. Wright, W.W. Chow, T.S. Luk, I. Brener, L.F. Lester, G.T. Wang: Single-mode GaN nanowire lasers, Opt. Express **20**(16), 17873 (2012)
31.737 H. Xu, J.B. Wright, T.-S. Luk, J.J. Figiel, K. Cross, L.F. Lester, G. Balakrishnan, G.T. Wang, I. Brener, Q. Li: Single-mode lasing of GaN nanowire-pairs, Appl. Phys. Lett. **101**(11), 113106 (2012)
31.738 H. Xu, J.B. Wright, A. Hurtado, Q. Li, T.-S. Luk, J.J. Figiel, K. Cross, G. Balakrishnan, L.F. Lester, I. Brener, G.T. Wang: Gold substrate-induced single-mode lasing of GaN nanowires, Appl. Phys. Lett. **101**(22), 221114 (2012)
31.739 C.-Y. Wu, C.-T. Kuo, C.-Y. Wang, C.-L. He, M.-H. Lin, H. Ahn, S. Gwo: Plasmonic green nanolaser based on a metal-oxide-semiconductor structure, Nano Lett. **11**(10), 4256 (2011)
31.740 Y.-J. Lu, J. Kim, H.-P. Chen, C. Wu, N. Dabidian, C.E. Sanders, C.-Y. Wang, M.-Y. Lu, B.-H. Li, X. Qiu, W.-R. Chang, L.-J. Chen, G. Shvets, C.-K. Shih, S. Gwo: Plasmonic nanolaser using epitaxially grown silver film, Science **337**(6093), 450 (2012)
31.741 J. Heo, W. Guo, P. Bhattacharya: Monolithic single GaN nanowire laser with photonic crystal microcavity on silicon, Appl. Phys. Lett. **98**(2), 021110 (2011)
31.742 P.J. Pauzauskie, D.J. Sirbuly, P. Yang: Semiconductor nanowire ring resonator laser, Phys. Rev. Lett. **96**(14), 143903 (2006)